Università degli Studi di Padova

Dipartimento di Ingegneria dell'Informazione

Ph.D. Course on Information Engineering

Curriculum: Information and Communication Science Technologies

Series: XXXI

Techniques for the Analysis, Design and Simulation of Periodic Surfaces for Space Communications and Antenna Systems for Electrical Appliances

Thesis written with the financial contribution of Electrolux Italia

Coordinator: Prof. Andrea Neviani

Supervisor: Prof. Andrea Galtarossa

Co-Supervisor: Ing. Roberto Giordano

Ph.D. Student: Francesco Rigobello

This thesis is dedicated to my family

Acknowledgments

As I approached writing this paragraph, I suddenly realized how many people I could rely on during this journey. The last three years have been really intense: there were ups and downs, but mostly great moments of fun, hard work and personal growth which left me with cheerful memories of the uni days and expertise for my future professional career.

Firstly, I would like to express my sincere gratitude to my supervisor Prof. Andrea Galtarossa for the continuous support and mentoring of my Ph.D. study. His guidance and motivation helped me in all the time of research and writing of this thesis.

Besides my supervisor, I would like to thank Prof. Antonio-Daniele Capobianco, for his insightful advises and encouragement that stimulated my research.

I would like to thank Electrolux Italia for the financial and technical support to my studies. In particular, a special word of thanks goes to Ing. Roberto Giordano, for being always so helpful and understanding.

I would like to express my gratefulness to Prof. Dimitris Anagnostou and Prof. George Goussetis, who provided me an opportunity to join their team as intern, and who gave access to the laboratory and research facilities. Without they precious support it would not be possible to conduct this research.

A sincere thanks goes to Dr. Salvador Mercader-Pellicer, who demonstrated strong knowledge and passion for the research that were such a meaningful example to follow for me. I could not have imagined having a better collaboration.

Furthermore, I would like to thank people from the PEG group Prof. Marco Santagiustina, Prof. Luca Palmieri, Dr. Luca Schenato, Dr. Elena Autizi, Prof. Domenico de Ceglia, Dr. Saeed Khan, for their discrete but warm presence in everyday life and the thesis committee: Prof. Andrea Locatelli and Prof. Stefano Boscolo.

I thank my fellow labmates from the PEG group: Giulia, for all the time, conversations and adventures spent together, Leonardo, more for the stimu-

lating discussions at Civico then for his advise, Trich, Rong, Ines, Gianluca G., Riccardo, Linda, Gianluca M., Caterina, Simone, Marco for all the fun we had together, inside and outside the lab.

I would like to thank colleagues and friends from the department, so many memories come to my mind about days and nights spent together: Chiara, Federico, Niccolò, Francesco, Michele, Gianluca, Sebastiano, Silvia, Matteo, Daniel, Marco, Nicola, Enrico.

A special thanks goes to the wonderful people that welcomed me in Edinburgh: Rahil, Tasos, Alexis, Spiros, Victoria, Chechu, Julian, Desen, Gabrielis, Salva, Natalia, Rafa, Ruben, Tom, Ben, Niccolò, Arianna, Luis, Victor, Pascual, Adrian, Khaleed, Cesar.

A nostalgic thanks goes to my flatmates (not all of them at the same time) Riccardo, Matteo, Gianfranco, Gianfilippo, Saggio, Stem, Fede, Gaino, Penny, Betta and Giulia, I Tiepidi, that witnessed the hard extra-hour work of a Ph.D. student.

A hearty thanks goes to all my friends, in Verona and in Padova who shared so much with me and to whom I am grateful and strongly attached; I have a specific reason to thank each one of you: Lorenzo, Luca, Marta, Valentina, Laura, Linda, Alessandro, Luca, Roberto, Michele, Francesco, Matteo, Andrea, Andrea, Valerio, Jacopo, Nicole, Michela, Rachele, Ilaria, Marco, Giovanna, Giada, Pippo, Vittorio, Ingrid, Alessia, Eugenio, Marco, Stefano, Paolo, Chiara, Anahita, Gregorio, Luigi, Fabio, Giacomo, Alessia, Gianluca, Federico, Andrea, Lorenzo, Antonino, Zeno, Michele.

Last but not least, I would like to thank my family: my parents and my brother for supporting me patiently throughout this Ph.D. and my life in general.

Finally, thank you Laura, for all the encouragement and love you gave me every day.

Thank you,
Francesco

Festina lente

Contents

List of Figures

List of Tables

Abstract

During the recent years, radio frequency applications for electric appliances have witnessed an huge increase in usage. Large companies as Electrolux Italia expressed the need of relying on electromagnetic simulation tools, in order to aid the designer with accurate models that cancel the necessity of a continuous experimental feedback. The electromagnetic modeling of RF applications has to consider not only the role of the RF components, but also the elements forming the appliance structure. Therfore, an ad-hoc approach for each scenario to be handled has to be followed. In this thesis, a procedure to develop and validate a model for a Wi-Fi connectivity system to be embedded in a smart oven and a wireless system for powering sensing devices is presented. Furthermore, in order to deal with issues that emerged from this analysis, innovative antenna solutions involving adaptive arrays were proposed. The research activity eventually moved to the analysis of periodic surfaces for reflector antenna systems for space communications. A simulation tool based on the spectral domain method of moments was developed. A case study involving a frequency selective surface subreflector was used to experimentally validate the proposed tool.

Durante gli ultimi anni, le applicazioni a radiofrequenza sono entrate prepotentemente nel mondo degli elettrodomestici. Grandi aziende come Electrolux Italia hanno dunque deciso di dotarsi di strumenti di simulazione elettromagnetica al fine di velocizzare la fase di progetto, riuscendo in tal ad evitare lunghe sessioni sperimentali. Lo sviluppo di modelli elettromagnetici dipende dalla specifica applicazione considerata, e diversi approcci vengono applicati per differenti scenari. In questa tesi sono stati realizzate e simulate due applicazioni. La prima riguardava la connettività Wi-Fi per un forno, implementata tramite un sistema di due antenne PIFA mentre nella seconda veniva simulato un sistema di 'Wireless Power Transfer' per trasferire energia a dei sensori posizionati al di sopra di un piano cottura. Entrambi i modelli sono stati analizzati e validati tramite misure sperimentali. Ad alcuni problemi evidenziati dalle nuove tecniche di analisi sono state proposte soluzioni innovative con array di antenne adattative. L'attività di ricerca si è poi spostata sull'analisi di superfici periodiche per sistemi di antenna a riflettore per comunicazioni spaziali. Il lavoro ha riguardato lo sviluppo di uno strumento di simulazione basato sul metodo dei momenti nel dominio spettrale. Quest'ultimo è stato infine validato tramite un caso specifico consistente in una superficie selettiva in frequenza.

Chapter 1

Introduction

1.1 Motivation

In the last few years home appliances have left their traditional role of stand-alone items to transform into multifunctional, smart and highly connected devices. Radio frequency (RF) systems play a major role in the sector and nowadays the implemented technology includes:

- Wireless systems for the connectivity to the home network and to the Internet
- RF systems for wireless and batteryless devices
- RFID systems for the detection and the identification of the elements on which the appliances operate (food, dishes, fabrics, etc.)

The implementation of smart systems for electric appliances present several limitations at the moment of the actual installation of the RF device. In fact, electric appliances are usually stationary elements in an indoor scenario, and the position of the other devices (e.g. a router) involved in the communications is not a-priori known. At the same time, it is not possible for the antenna systems to be installed on the exterior of the appliances. Furthermore, the configuration and the orientation of the antenna system can not be delegated to the user.

The highlighted issues require an approach that is meant to address:

- The modeling and the characterization of the indoor scenario from an electromagnetic point of view
- The modeling and the characterization of the electric appliance
- The design and the analysis of antenna systems suitable for the indoor environment and the placement inside the appliance
- The wireless system optimization

In this regards, electromagnetic modeling and simulation techniques result as a powerful tool in order to optimize the design process and reduce the need of an experimental phase. Simulation techniques may be adopted to assist all the design process phases, from the antenna design to the positioning inside the appliance. Furthermore, the evaluation of the user exposure to electromagnetic fields can be analyzed through accurate models.

Simulation software such as CST [1] or HFSS [2] allow the modeling of the complete configuration and the full-wave solution of the electromagnetic problem under investigation. The behavior of the fields radiated by the wireless device can be accurately predicted and the parameters describing the wireless devices can be modified in order to find improved solutions for the system connectivity. However, since the model has to consider not only the role of the RF components, but also the elements forming the appliance structure, several issues can arise due to the complexity of the overall scenario. Therefore, a specific simulation approach is required to handle each application and a dedicated model has to be developed to study each electric appliance. Beyond RF applications for electric appliances, not all the electromagnetic problems can be solved with full-wave simulation techniques. For instance, this is the case of reflector antenna systems analysis, which may be handled with different approaches, such as ray tracing techniques, physical optics and the physical theory of diffraction. Dedicated commercial software such as GRASP [3] may be used but the actual availability can be very expensive. Therefore, the possibility of developing an in-house tool for handling those kind of problem is very appealing. Clearly, the precision obtained can not be compared to that of a commercial software. However a good accuracy in the analysis can be achieved [4]. Such a simulation tool has to develop a model comprehensive of:

- The source of radiation
- One or more reflecting surfaces
- The analysis of the scattering form the surfaces illuminated by the source

Moreover, nowadays many reflector antenna applications include the presence of periodic surfaces such as reflectarrays or frequency selective surfaces. In this way, it is possible to achieve reconfigurability properties and use efficiently dual-feed subreflector systems. In order to integrate this features, more analysis techniques have to be implemented:

- Exact field reconstruction on the reflector and subreflector surfaces
- Analysis of periodic surfaces

A tool implementing all the described features allows the designer to select and simulate a wide range of configuration, without the need of purchasing a commercial software.

1.2 Survey of the Contents and Scope of the Thesis

The research activity was sponsored by and in collaboration with the company Electrolux Italia, which is currently developing connectivity and sensing solutions for electric appliances. The ultimate aim of this thesis consists in the development of a simulation methodology which needs to be robust to the evolution of the implemented technologies and that may be adapted to future design requirements. It has to be remarked that the main scope of the work is outside the design and the optimization of the antenna systems but, instead, it consists in providing the company with accurately validated analysis tools.

The first RF application for electric appliances analyzed in this work regarded the implementation of the Wi-Fi connectivity for a smart oven. The connectivity is provided by a multiple-input-multiple-output (MIMO) connectivity device which is installed in the appliance. The metallic structure of the oven results to have a strong impact on the electromagnetic behavior of the device, both in terms of resonance detuning and scattering effects, thus drastically modifying the original design of the standing alone antenna system. In this regards, developing an electromagnetic model of the whole configuration results to be a fundamental task, as it allows to anticipate relevant issues that can arise when the free standing device has to be installed in a given apparatus. Commercial software such as CST Microwave Studio can be used to develop a complete model of the scenario under investigation, however a complex configuration as the one considered in this study is not trivial to handle. A good understating of all the components of the system to be simulated results to be necessary, from the source of radiation to the structures surrounding it. Furthermore, different simulation approaches can be employed when considering parts of the overall system that are assumed to be more or less relevant for electromagnetic modeling purposes. In order to develop a complete model of the smart oven, we proceeded by considering increasing levels of complexity for the elements to be simulated. First, the standing alone antenna system was modeled and the field pattern for both antennas was analyzed. After that, the board holding the two PIFAs was placed in a plastic box, which is used as support for the transmitting device to be later embedded in the appliance. The effects of the enclosure on the radiation characteristics of the antennas were examined. Finally, the device is installed in the oven and the radiation pattern of the whole configuration is simulated. For all the considered steps an experimental validation was obtained by measurements in an anechoic chamber.

Innovative solutions for the antenna design can be adopted to overcome issues relative to the non-optimal positioning: this is the case of self-adapting phased array antennas conformal to non-planar surfaces. The research activity involved the PEG group at University of Padova. Self-adapting phased array antennas are designed to adapt to surfaces that change shape in time. This interesting feature allows to increase the coverage of modern wireless devices, but on the other hand it raises the issue of maintaining the radiation

pattern undistorted when the array changes its shape. Moreover, nowadays many applications of phased arrays require beam steering capabilities that are closely related to the possibility of tilting the main beam towards a desired direction or away from an undesired one. The projection method is a cost-effective pattern recovery technique that allows to correct the radiation pattern of the deformed array by just applying a phase compensation to the input signal of each array element. However, the implementation of this methodology can face some limitations that have been investigated: the maximum deformation that can be impressed to the surface and the phase approximation that can be tolerated by the method.

The second application studied was a Wireless Power Transfer (WPT) system designed in order to power sensing devices placed over the surface of an induction hob. A CST model of an induction hob was developed. A transmitting coil was placed on the hob and simulations of wireless power transfer at 13.56 MHz were performed with a receiving coil placed in the space above the structure. Circuits to make the coils resonant were included in the simulation according to the actual configuration. A measurement campaign was carried out in order to validate the model. First, the field distribution generated by the transmitting antenna around the induction hob was measured. This is a crucial information when considering issues related to regulation and user safety. Lately, a measure of the power delivered wirelessly to the receiver load was performed.

Finally, I spent the last months of my PhD at Heriot Watt University, in Edinburgh, where I joined the research group of Prof. Dimitris Anagnostou, Prof. George Goussetis and Doct. Salvador Pelliccer. There the research activity focused on antenna systems for space communications. In detail, I was involved in the development of a software tool for the analysis and the modeling of periodic surfaces, based on the spectral domain method of moments. This tool was used to support the design and simulation phase of Frequency Selective Surfaces (FSS) used as subreflector or reflectarrays. Furthermore, the scattering was investigated when the feed of the system was illuminating surfaces placed in the near field region of the source. In order to do that, a MATLAB code based on the Spherical Wave Expansion (SWE) has been developed. In this way, information about the incident field in terms of amplitude, phase and direction of incidence may be retrieved on any desired surface, considering those in the near field region. A simple case study involving a FSS used as subreflector for a dual feed reflector antenna system was analyzed . The two sources were placed on the two sides of the FSS, at an offset angle, and the scattering from the surface was investigated for both the reflection and the transmission scenarios. Finally, the periodic structure was fabricated and measured, in order to validate with experimental results the developed procedure.

Chapter 2

Wi-Fi Connectivity for a Smart Oven

2.1 Introduction

The first radio frequency (RF) application for electric appliances analyzed in this work regarded the implementation of the Wi-Fi connectivity for a smart oven. The connectivity is provided by a 2-elements MIMO system, composed of two planar inverted-F antennas (PIFA), which was later embedded in the appliance. The metallic structure of the oven results to have a strong impact on the electromagnetic behavior of the device, both in terms of resonance detuning and scattering effects, thus drastically modifying the original design of the standing alone antenna system. In this regards, developing an electromagnetic model of the whole configuration results to be a fundamental task, as it allows to anticipate relevant issues that can arise when the free standing device has to be installed in a given apparatus.

Commercial software such as CST Microwave Studio can be used to develop a complete model of the scenario under investigation, however a complex configuration as the one considered in this study is not trivial to handle. A good understating of all the components of the system to be simulated results to be necessary, from the source of radiation to the structures surrounding it. Furthermore, different simulation approaches can be employed when considering parts of the overall system that are assumed to be more or less relevant for electromagnetic modelling purposes.

In order to develop a complete model of the smart oven, we proceeded by considering increasing levels of complexity for the elements to be simulated. First, the standing alone antenna system was modelled and the field pattern for both antennas was analyzed. After that, the board holding the two PIFAs was placed in a plastic box, which was used as support for the transmitting device to be later embedded in the appliance. The effects of the enclosure on the radiation characteristics of the antennas were examined. Finally, the device is installed in the oven and the radiation pattern of the whole configuration is simulated. For all the considered steps an experimental validation was obtained by measurements in an anechoic chamber. A comparison be-

Figure 2.1: A picture of the PIFA MIMO antenna system

tween simulation and measurement results and a detailed discussion on the critical issues that emerged will be given throughout this Chapter.

It should be remarked that, as several sections of this chapter were initially part of technical reports, some purely practical details are being provided. For example, trivial simulation specifics or details of the measurement setup are given. This is done in order to have a full comprehension of the approach used and to keep an exact track of the procedure to follow for potentially developing an analogous electromagnetic model. Similarly, some critical issues I discovered in the research activity have been highlighted and discussed in this chapter, however some of them have not been solved yet. Anyway, they are clearly addressed in this work for potential future improvement.

2.1.1 PIFA Antenna System

The Wi-Fi connectivity is provided by a 2-elements MIMO system installed on a PCB board, as depicted in Fig. 2.1. In a real life prototype, the electronic modules for signal generation are placed on the board together with the antennas and connected to them through the microstrip lines on the PCB board. However, for this research purposes, the PCB line going to the radiating element for feeding it, is now rerouted towards an SMA connector which is soldered on the board edge. In this way, it will be possible to connect the transmitting device to measurement instruments such as a vector network analyzer (VNA), in order to have information about the resonance frequency of the antennas and their radiation pattern.

The single radiating element considered in this work is a planar inverted-F antenna (PIFA). The two antenna elements are placed on the PCB board as depicted in Fig. 2.1, one rotated of 90° with respect to the other. This is done in order to obtain a degree of pattern diversity [5], [6] for the MIMO system, and it will be investigated in the following of this chapter. We will refer to the two PIFAs, and to the respective feeding lines, as Antenna A (or Channel A) and Antenna B (or Channel B).

A CST model of the board with the antennas is designed and simulated.

The required model accuracy in terms of component details to be included and mesh finesse for the EM solver are investigated. Finally, simulation results are compared to measurements performed in an anechoic chamber for the standing alone board.

2.1.2 PIFA Coordinate System

The reference system we will refer to throughout this chapter is shown in Fig. 2.2. The antenna board is laying in the yz plane, and the direction towards which the antennas on the board are facing is the positive x−axis. The origin of the coordinate system is the geometrical center of the PCB board, and the same point will be kept for all the simulations and measurements, also when the antennas are embedded in the oven. The planes of interest, along whose the radiation pattern of the antennas will be shown, are the xy−plane ($\theta = 90°$), the xz−plane ($\phi = 0°$) and the yz−plane ($\phi = 90°$). The same reference system will be used consistently when measuring the antennas in an anechoic chamber, both for the free standing case and for when it is installed in the appliance.

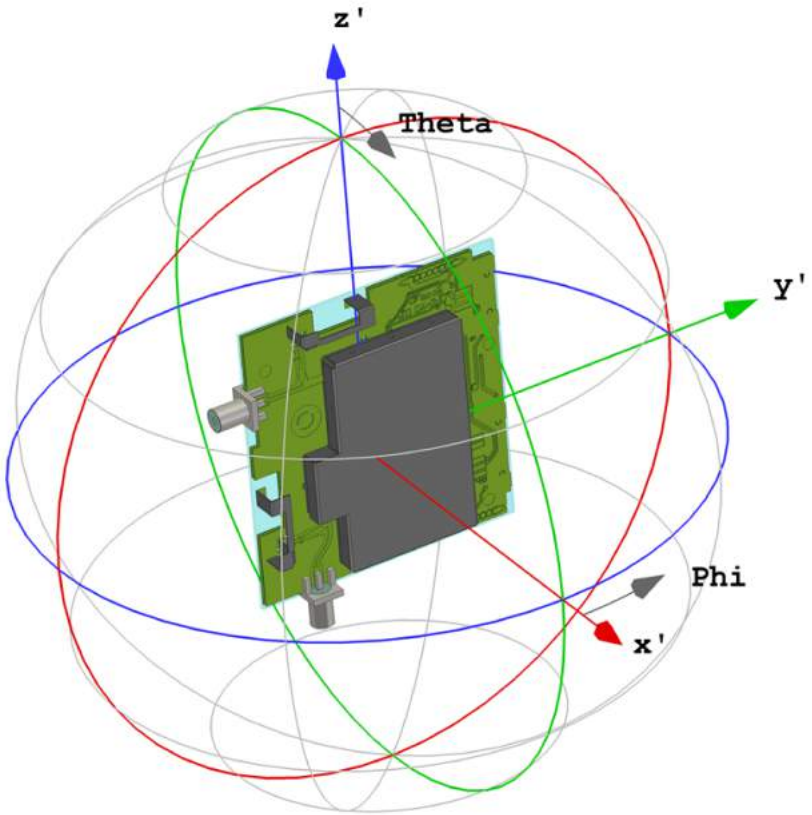

Figure 2.2: Coordinate system considered throughout this chapter

2.2 Antenna System CST Model

The modelling of the antenna system considered, in the first place, only the radiating elements installed on the board. Later, the other elements existing on the PCB board were progressively included, in this way increasing the overall complexity of the model. In detail, we proceeded to analyze, in order of relevance:

- Single PIFA element design
- Two PIFAs on the PCB board
- EMI shielding box
- SMA connectors
- PCB traces

Furthermore, the CST model allowed us investigate the optimal positioning of the antennas on the board by simulating the system while changing the reciprocal displacement between the two PIFAs. At the same time, the PCB substrate material can be studied while varying its dielectric constant in order to reconstruct a model as close as possible to the real life scenario.

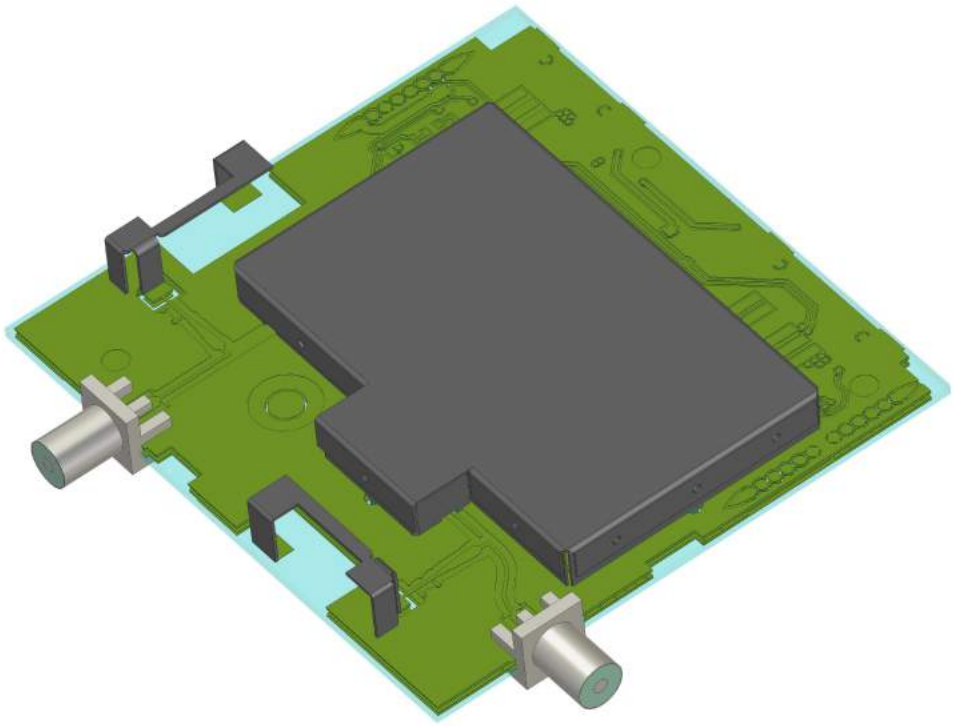

Figure 2.3: CST complete antenna board model

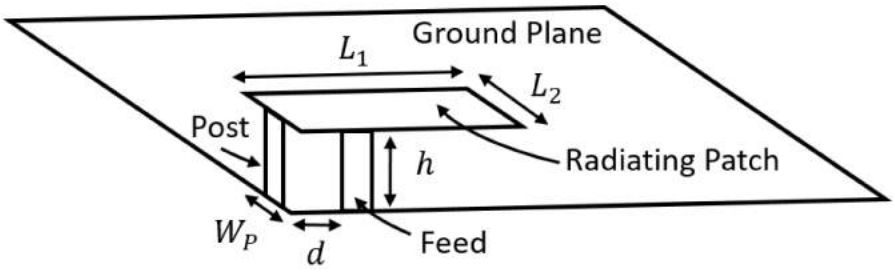

Figure 2.4: PIFA Antenna Schematic

2.2.1 PIFA - Electromagnetic Theory

A brief description of the electromagnetic theory behind the behavior of a PIFA antenna is presented hereafter. Several design of single-[8] and dual-band [9]-[12], PIFAs can be found in the literature, including both planar [13] and printed technologies [14], [15]. PIFA antennas have become widely used for wireless communications for their low profile and omnidirectional pattern properties. The design has two advantages over a simple monopole: the antenna is shorter and more compact, and the impedance matching can be controlled by the designer without the need for extraneous matching components. The structure consists of a radiating patch parallel to a ground plane to which it is shorted at one termination. The feeding pin is placed between the open and shorted end of the patch, and its positioning is used to control the impedance of the antenna. The shorting post allows to reduce the total size of the antenna but on the other hand this results in a narrow bandwidth, which is a limitation of this kind of design. The PIFA is resonant at a quarter-wavelength due to the shorting pin at the end. The distance d of the feed point from the shorting post controls the input impedance of the antenna [16]. Therefore, this parameter is used for tuning without the need of an external matching circuit. A characteristic of a PIFA is the narrower bandwidth if compared to a standard patch antenna. However, the dimensions of the ground plane can be modified in order to improve this figure [17]. The resonance frequency of the PIFA depends on the post width W. If $W = L2$, then the width of the patch is equal to that of the shorting post and the antenna resonates at:

$$L_1 = \frac{\lambda}{4}. \tag{2.1}$$

If now we consider a short with $W = 0$ or a very thin one with $W << L_2$, we have resonance at:

$$L_1 + L_2 = \frac{\lambda}{4}. \tag{2.2}$$

The main parameters controlling the resonance of a PIFA are therefore W, L1 and L2 and they are related by:

$$L_1 + L_2 - W = \frac{\lambda}{4}. \tag{2.3}$$

If the radiating element is placed on a dielectric substrate of thickness h and ϵ_r, then the wavelength in the medium has to be considered.

Table 2.1: PIFA antenna description.

PIFA dimensions (mm)	
l_1	3.1
l_2	3
l_3	3.6
$W_s = W_p$	2.1
h_p	4.55
d_p	10.75

2.2.2 PIFA Element Design

A schematic of the PIFA element used for Wi-Fi connectivity is shown in Fig. 2.5. PIFAs are designed in order to resonate at 2.45GHz when positioned on the PCB board standing alone in free space. The different parts composing the antenna structure are hereby described in detail and they will be referred as follows:

- Feeding plate
- Short circuit post
- Planar radiating element
- Ground plane
- Supporting plate

The latter is for mechanical support and it is not connected to the ground plane. The physical dimensions of the antenna are reported in Table 2.1.

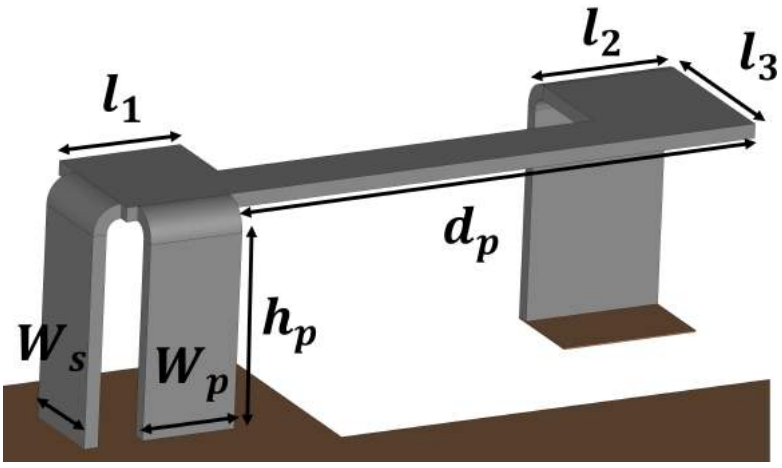

Figure 2.5: Single PIFA antenna element.

Table 2.2: PCB board description.

PCB description	
z_{sub}	1.08 mm
y_{sub}	51.5 mm
h_{sub}	3.6 mm
N_{layers}	4
ε_r	4.3

2.2.3 PIFAs on PCB Board

Initially, a model including only the two antennas placed on the PCB board was considered, as depicted in Fig. 2.6. The board is composed of 4 metallic layers on a FR-4 substrate, as described in Table 2.2. The reflection coefficient for both Antenna A and Antenna B is simulated and shown in Fig. 2.7. It can be observed that the antennas are properly designed to work around 2.45 GHz.

Later, the metallic box used to shield the electronics of the connectivity module on the board is included in the model; see Fig. 2.6. The main effect of its presence is observable in radiation pattern of the antennas. Consider for example the yz-plane cut of the radiation pattern of Antenna B. This plane is where the antenna and the shield are aligned, and therefore a change in the radiation properties is observable. Fig. 2.8 shows how the EMI shield obstructs partially the radiation incoming in its direction.

The tridimensional radiation pattern for Antenna A of the PIFA antenna installed on the PCB board is shown in Fig. 2.9. Considering the yz−plane containing the antenna board as reference, we can observe that the radiation is directional in the elevation plane, while an omnidirectional pattern is observable in the azimuthal plane. The gain peak is around 2.5 dB, and the slot in the ground plane allows some back-radiation to propagate.

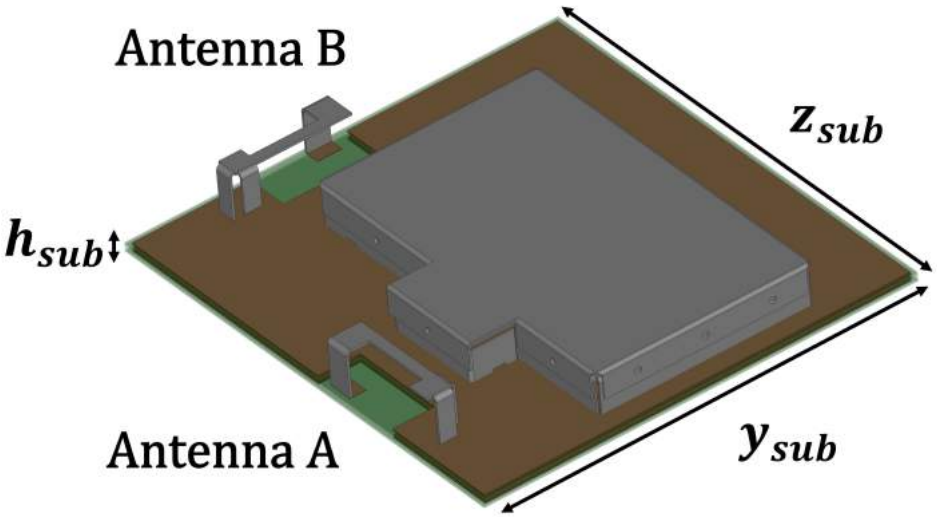

Figure 2.6: Board containing the two PIFAs and the EMI shield.

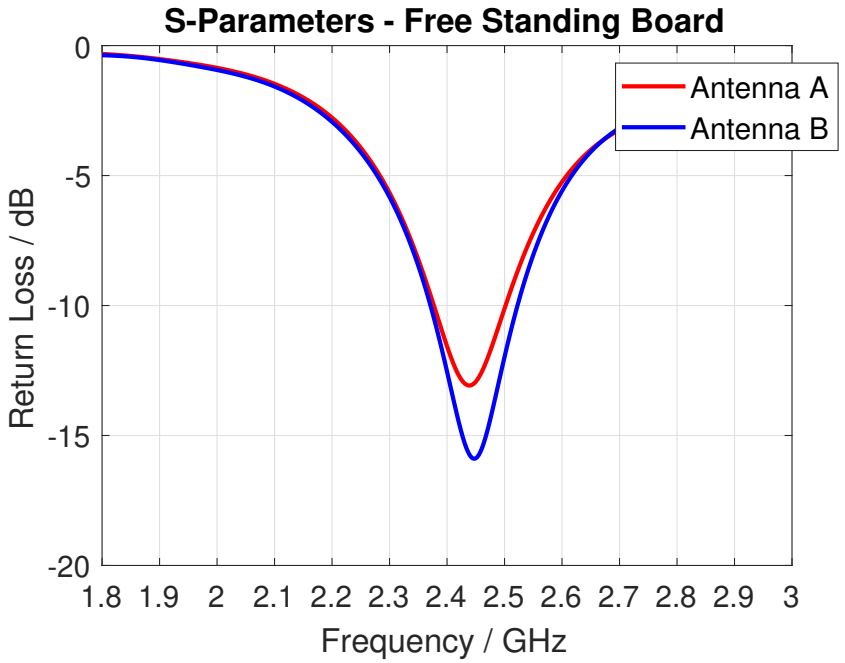

Figure 2.7: Reflection coefficient of the two antennas for the free standing board

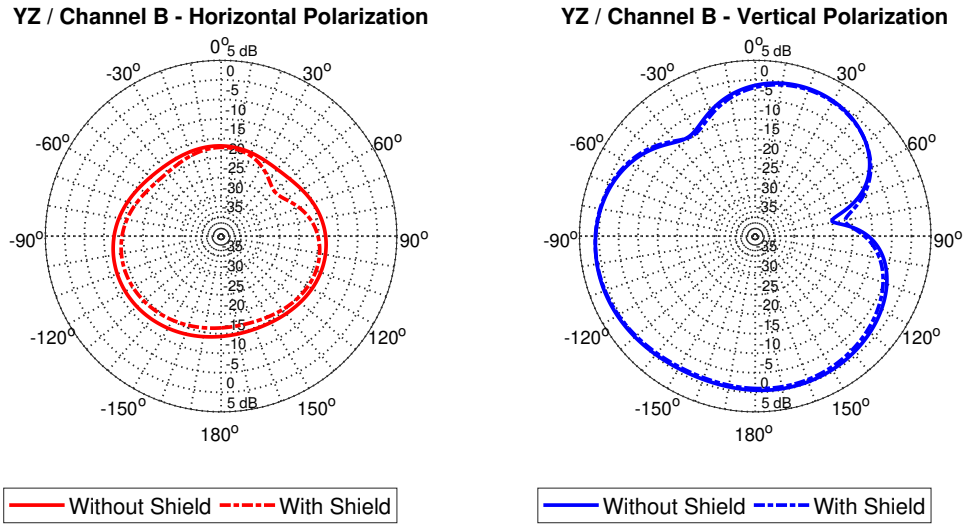

(a) (b)

Figure 2.8: A comparison of the radiation pattern of the free standing board with and without EMI shield

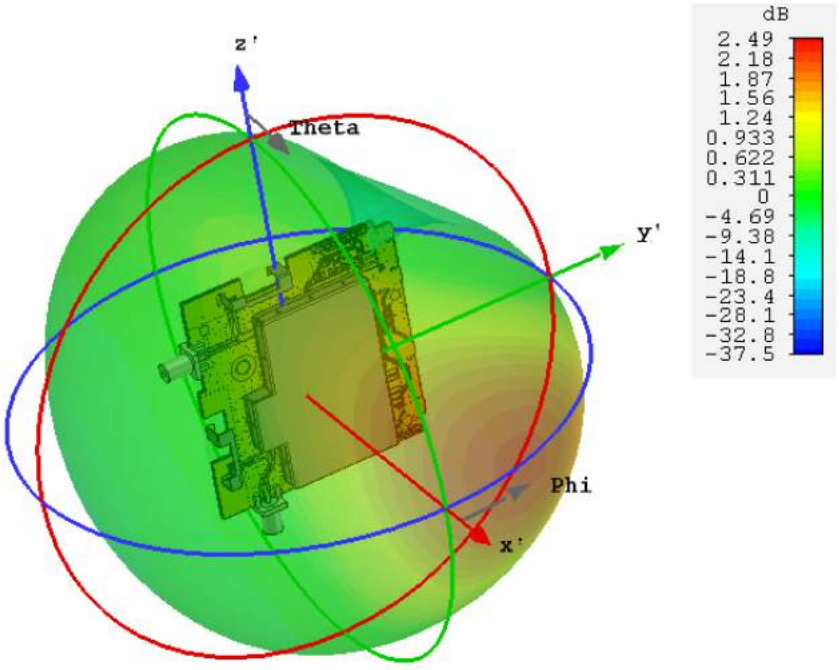

Figure 2.9: Tridimensional gain pattern of Antenna A

2.2.4 Antenna Positioning on the Board

The positioning of the PIFAs on the board is strictly regulated by some constraints like the physical dimension of the substrate and the presence of other electronic components. The space dedicated to the antenna components is therefore very limited and can result in a non optimal configuration. Having said that, a study on the positioning of the antennas for the given space constraints is carried out. The diversity gain (DG) between the two antennas is computed in (2.4) and it is observed while moving them on the board within the dedicated space as depicted in Fig. 2.10. Results are shown in Fig. 2.11. Mutual coupling values [19], [20] do not vary considerably for the considered displacements, and we can conclude that a substantial improvement can not be obtained by considering a new positioning of the PIFAs.

$$\mathrm{DG} = 10\sqrt{1 - |\rho|^2}, \tag{2.4}$$

where:

$$\rho = \frac{|S_{11}^* S_{12} + S_{21}^* S_{22}|^2}{(1 - (|S_{11}|^2 + |S_{21}|^2))(1 - (|S_{22}|^2 + |S_{12}|^2))} \tag{2.5}$$

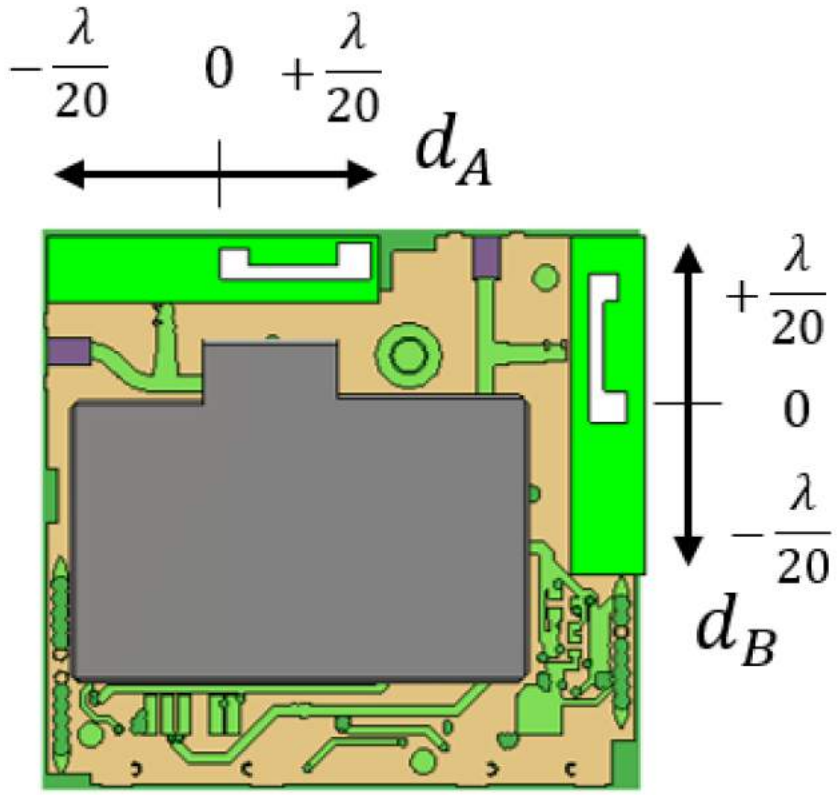

Figure 2.10: Antenna positioning on the board.

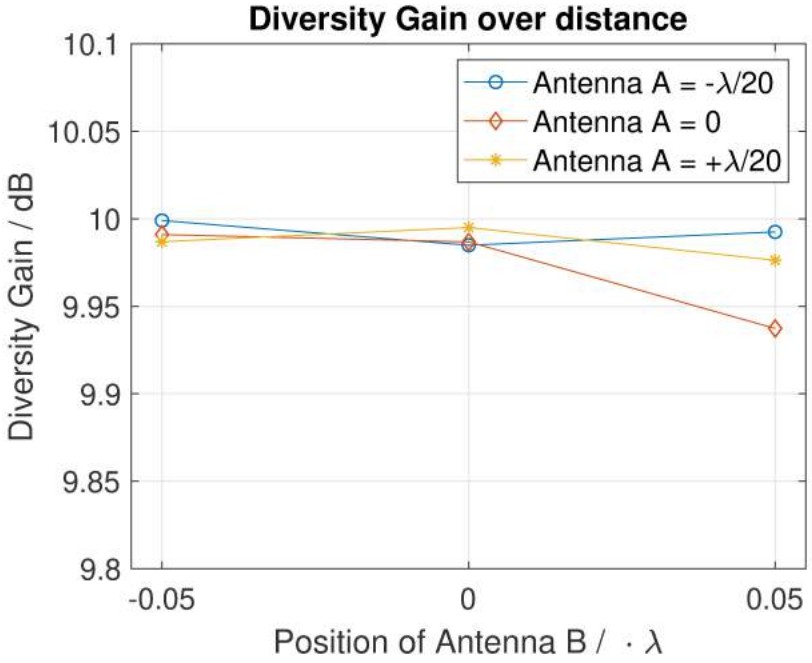

Figure 2.11: Diversity Gain for differerent reciprocal displacement of Antenna A and Antenna B.

2.2.5 SMA Connector

The original design of the PCB board was not equipped with connectors that allowed a link with external instrumentation, for example with a VNA for S-parameters measurement. Therefore, two SMA connectors had to be soldered on the board, one for each Channel. Furthermore, as the electronics for the connectivity on the board is placed under the metallic shield, only a path between it and the antennas exists. A new path between the SMA and the feeding point of the PIFAs had then to be traced. In order to do that, the strip lines were cut and diverted towards the external connection as shown in Fig. 2.12.

The corrections to the circuit topology have been done in the CST model. Two SMA connectors are soldered on the board and are now the new source of signal. A simulation is run in order to verify the impact of the presence of the connectors on the radiation pattern of the two antennas. The radiation pattern in the plane containing the connectors is shown for both Channel A and Channel B in Fig.s 2.13 and 2.14.

It can be observed that there are some discrepancies in the pattern corresponding to the presence of connectors; however, those differences are really small. We can conclude that the SMAs soldered on board do not affect in a significant way the radiation properties of the antennas. Therefore, they can be included in the model in order to have it more similar to the experimental scenario. At the same time, the resulting pattern will not differ from the real-life case, which does not take them into consideration.

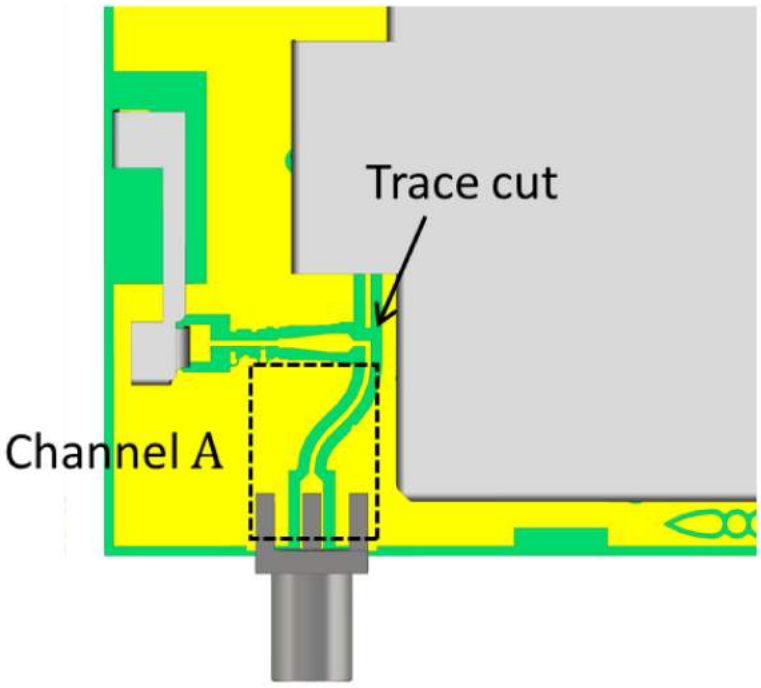

Figure 2.12: PCB trace connecting the antenna to the SMA and excluding the connectivity module.

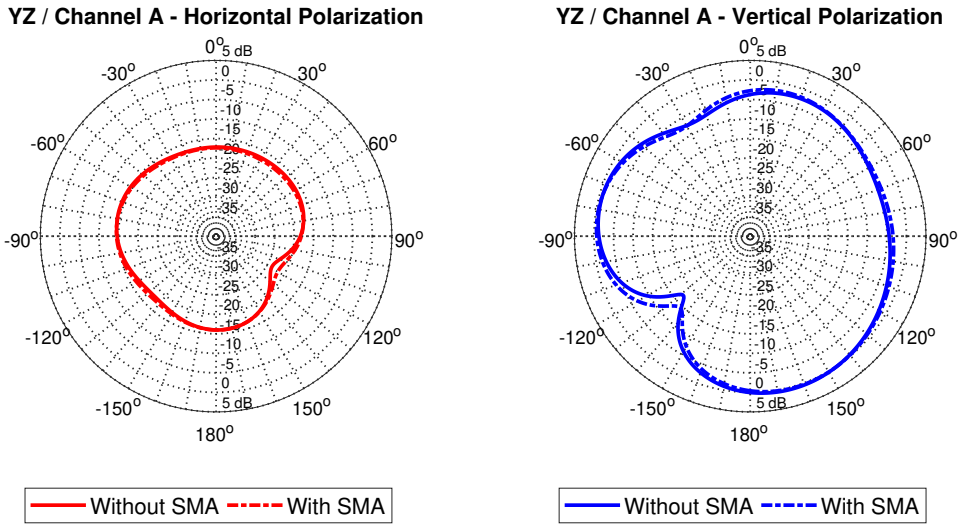

(a) (b)

Figure 2.13: A comparison of the radiation pattern of the free standing board with and without SMA connectors installed.

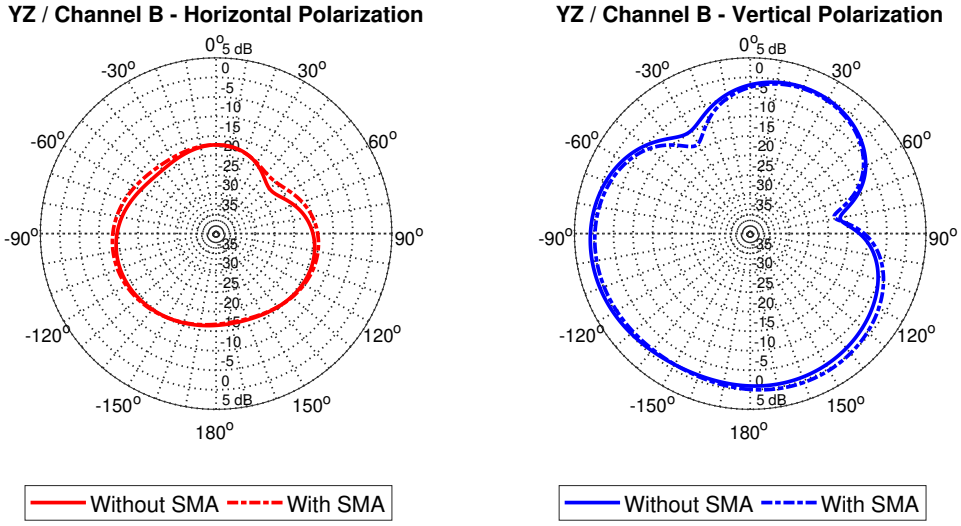

(a) (b)

Figure 2.14: A comparison of the radiation pattern of the free standing board with and without SMA connectors installed

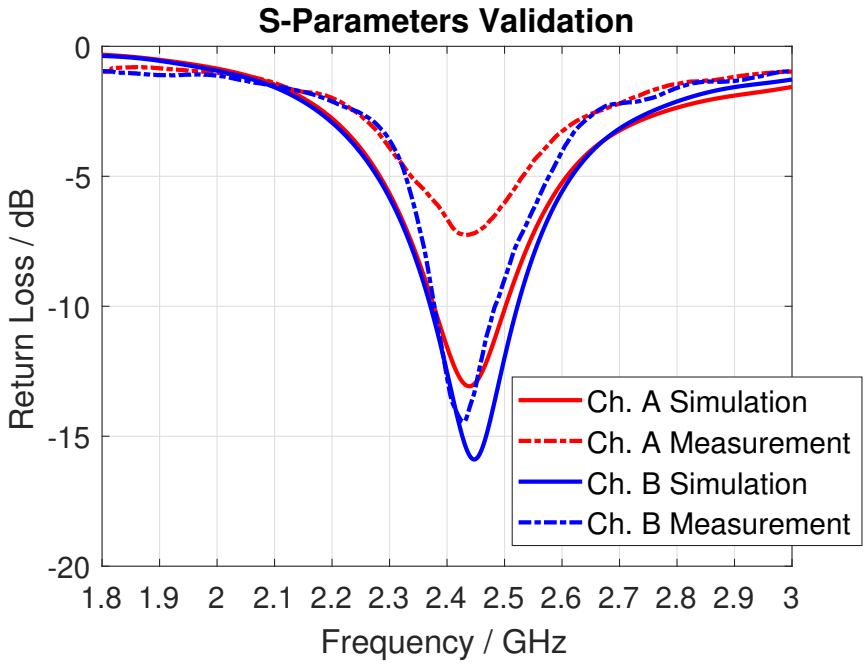

Figure 2.15: Reflection coefficient of the two antennas for the free standing board, simulated and measured

2.2.6 Experimental Validation

The ultimate model obtained using CST is finally validated against measurements. First, measurements of the return-losses are performed using a Vector-Network-Analyzer (VNA) so that the resonance frequency can be checked. A comparison between simulated and measured return losses curves for both ports is shown in Fig. 2.15. A good agreement between simulation and experimental results can be observed, with a resonance for both antennas around 2.45 GHz. This means a good connection was established between the SMA connector and the feeding pin of both antennas.

Later, the radiation pattern of both antennas is measured in an anechoic chamber. The gain of both channels is measured along the three principal Cartesian planes, both for vertical and horizontal orientation of the reference horn antenna. Hereby, only some relevant results will be shown, while a complete pattern characterization of the system was presented in a report for Electrolux. Results shown in Fig.s 2.16 and 2.17 confirm a good matching between the model and the experimental results. Some discrepancies however are noticeable. The main causes can be traced back to the obstruction caused by the cables used to connect the board to the VNA. At the same time, the torsion and some spurious radiations of the cables contribute to some additional noise of the measured gain pattern. Moreover, in the real-life case, the PCB traces on the board that connects the antennas to the SMAs are done through a soldering between the lines. Some further inaccuracies might have appeared due to this reason.

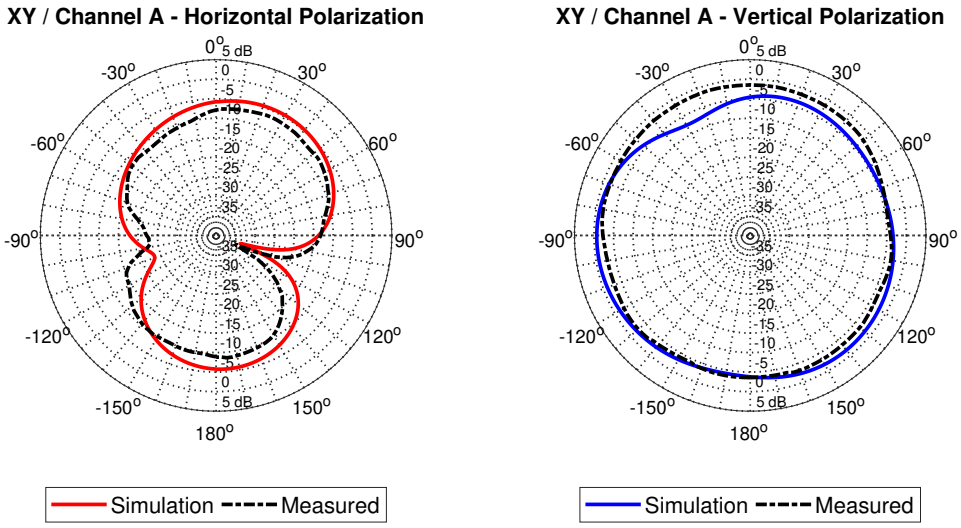

(a) (b)

Figure 2.16: Comparison between simulated and measured gain pattern

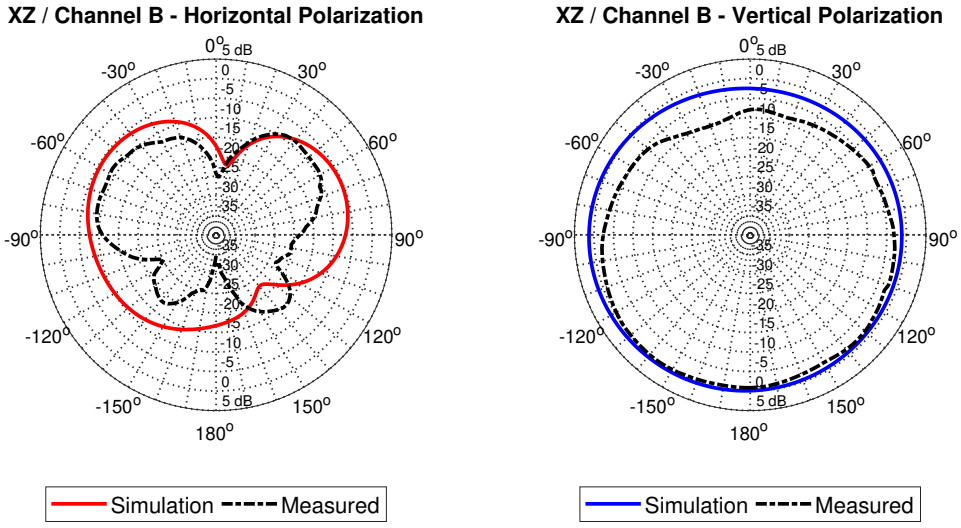

(a) (b)

Figure 2.17: Comparison between simulated and measured gain pattern

2.3 Plastic Casing

The board with the two antennas installed on it is placed in a plastic casing, ready to be installed in the appliance. The enclosure is needed here as mechanical support to the board and to provide protection to the antenna system. The device modeled in CST is pictured in Fig. 2.18. The white box is made of a plastic material with dielectric constant $\epsilon_r = 2.8$. We expect that the presence of the plastic casing in the proximity of the antennas might affect the electromagnetic characteristics of the system.

2.3.1 Detuning Effects of Plastic Enclosure

The effects that the presence of a dielectric material has on the radiation properties of the nearby antennas were evaluated. First, it is observed the frequency detuning that is introduced by the board placement inside the plastic enclosure. In Fig. 2.19 the return loss curves for both Channel A and Channel B are shown before and after enclosing the board in the box. It is easy to observe that Antenna B suffers a bigger detuning with respect to Antenna A. In order to investigate the reason of this difference, we have to observe how the board is placed inside the box: the antenna associated to Channel B is closer to the box edge with respect to the antenna associated to Channel A. To prove that the proximity of the plastic box is the main cause of the detuning, the board was rotated inside the enclosure, in order to place the antenna related to Channel A closer to the edge, as shown in Fig. 2.21. We can observe that a bigger detuning occurs as expected for Antenna A in this configuration.

2.3.2 Casing Effects on Far Field Radiation

The gain pattern for both channels has been simulated when the antenna board was inserted in the plastic enclosure. Figures 2.22 and 2.23 give a visual indication of the effects of the casing on the antenna radiation. Channel B has been chosen for this study, as it proved to be more affected by the plastic proximity. It can be observed that the gain levels are lowered and also the shape of the pattern is changed in some planes.

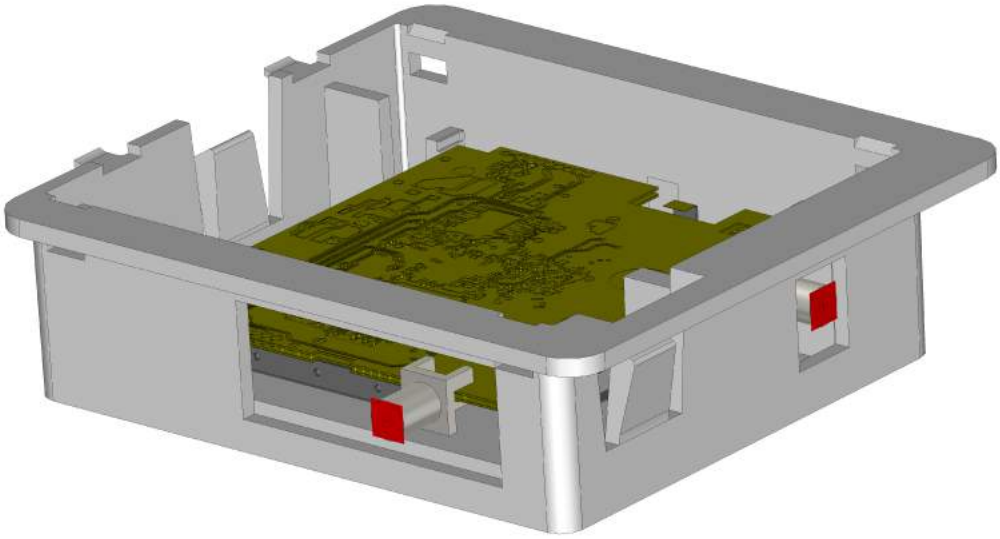

Figure 2.18: The antenna board placed inside the plastic casing.

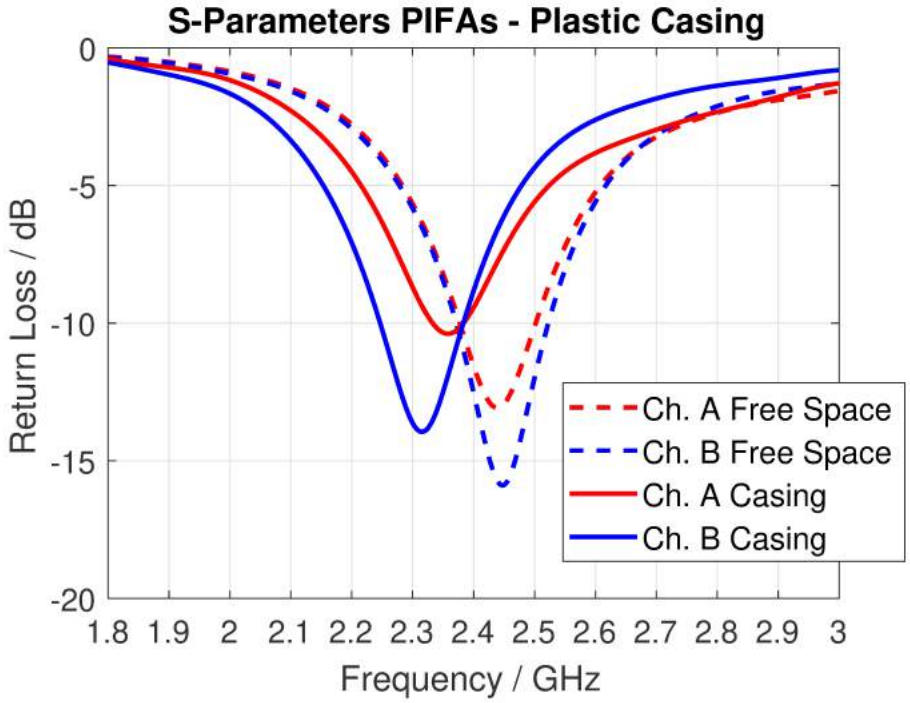

Figure 2.19: A comparison between the reflection coefficients of both channels for the antenna system placed outside and inside the plastic casing.

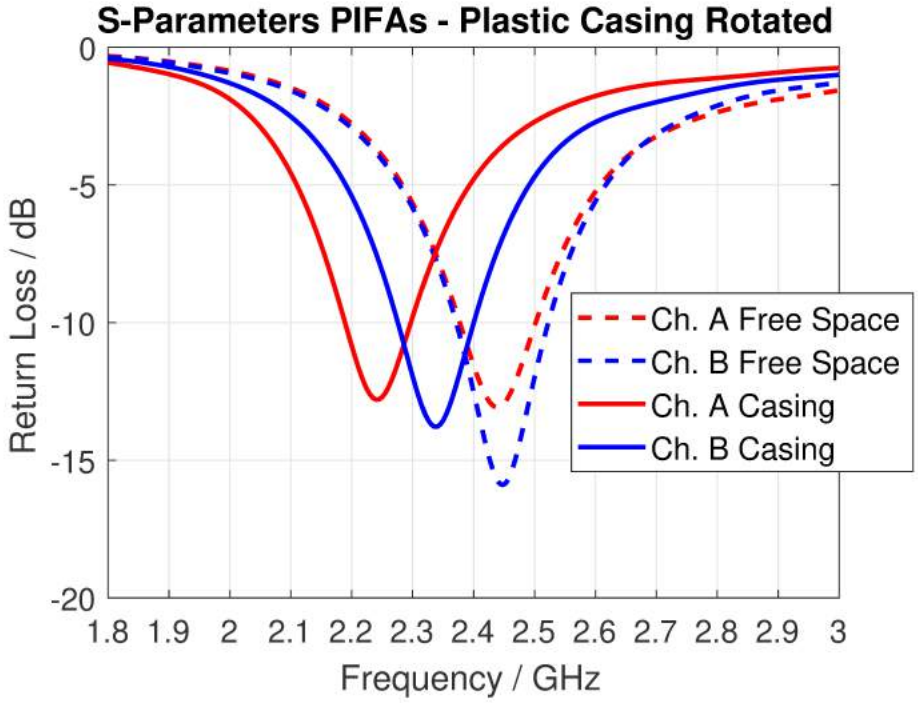

Figure 2.20: A comparison between the reflection coefficients of both channels for the antenna system placed outside and inside the plastic casing. The board is rotated 90° inside the box with respect to the previous case.

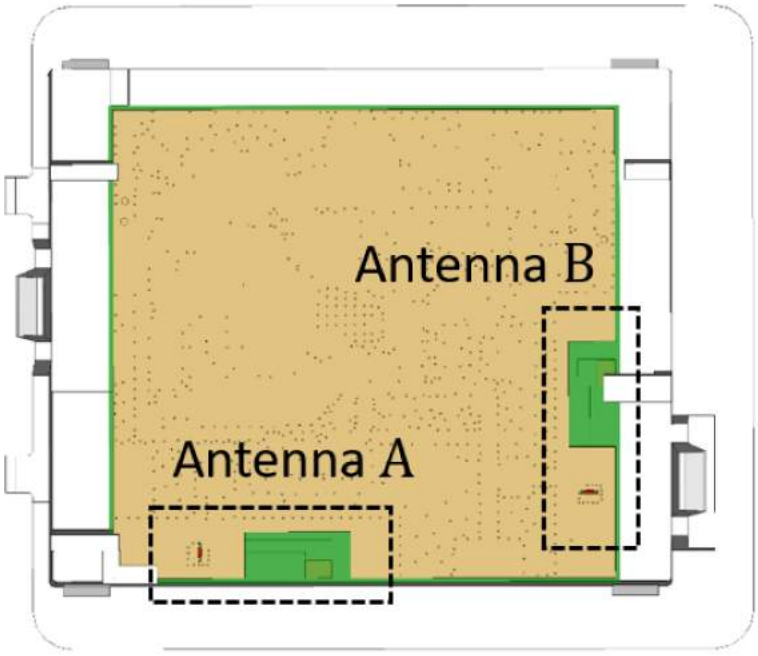

Figure 2.21: PCB board rotated inside the plastic casing.

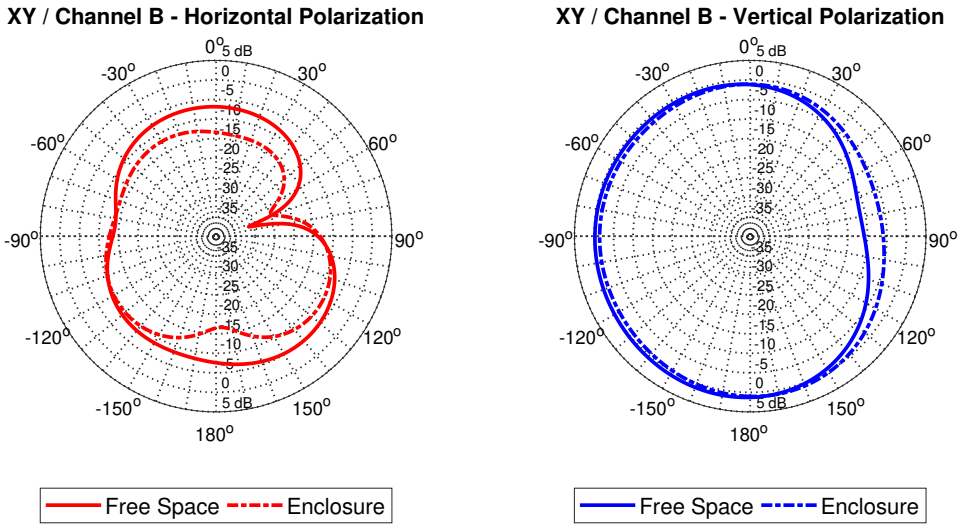

(a) (b)

Figure 2.22: A comparison of the radiation pattern of the antenna system between the free-space and in-casing scenario.

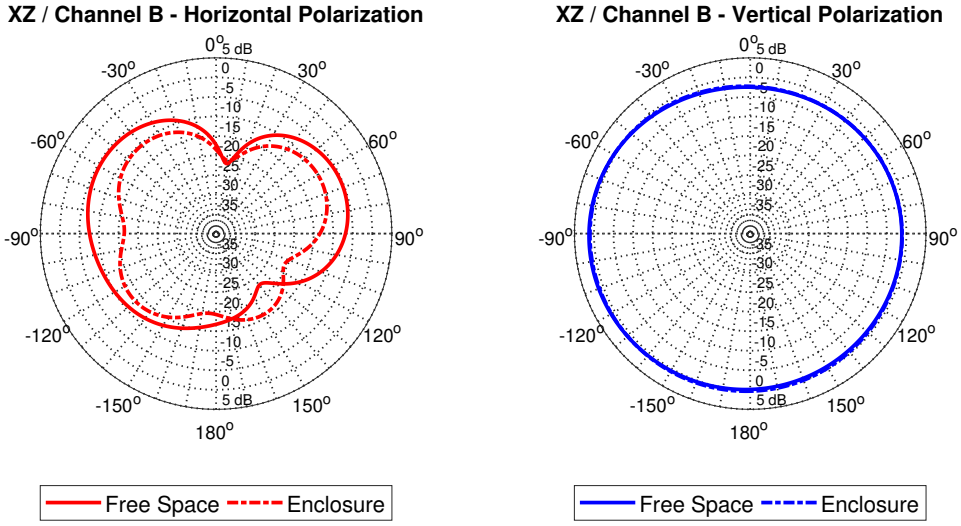

(a) (b)

Figure 2.23: A comparison of the radiation pattern of the antenna system between the free-space and in-casing scenario.

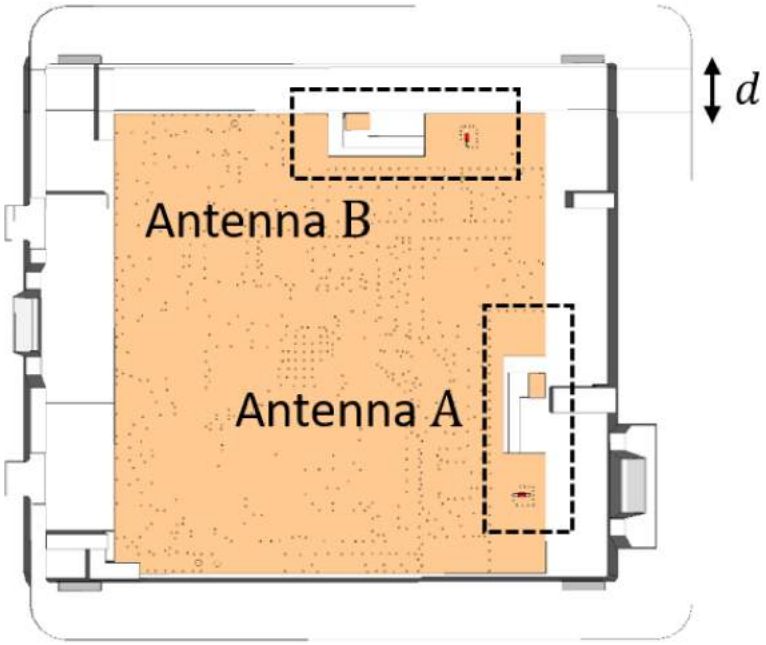

Figure 2.24: A study on the minimum distance between the board and the plastic casing to avoid unwanted detuning.

2.3.3 Avoiding Detuning Effects

As shown in the previous section, the radiation properties of the antenna close to the plastic can get heavily deteriorated, therefore a study on the minimum spacing to be introduced between the board edge corresponding to Antenna B and the box is carried out. Referring to Fig. 2.24, the distance d between the board and the casing is progressively increased and the return loss curves are consequently simulated. In Fig. 2.25, it can be noticed that as the distance is increased the curves move toward the free space scenario case. A minimum distance of $d =$ 3mm is needed to shift the return loss curve to values comparable to the Antenna B case when inserted in the box. A future design of the plastic enclosure has been addressed in this way.

2.3.4 Matching Circuit

The PIFAs are designed to be matched directly to 50 Ω. Therefore, when considering the standing alone board, no external matching components are required. However, as shown in Fig. 2.19, the plastic casing causes a detuning that was not taken into account in the original design. A way to obviate to this low efficiency is designing a matching network [18], [21]. This can be done by using a network of lumped elements to be soldered between the microstrip feeding line and the radiating structure.

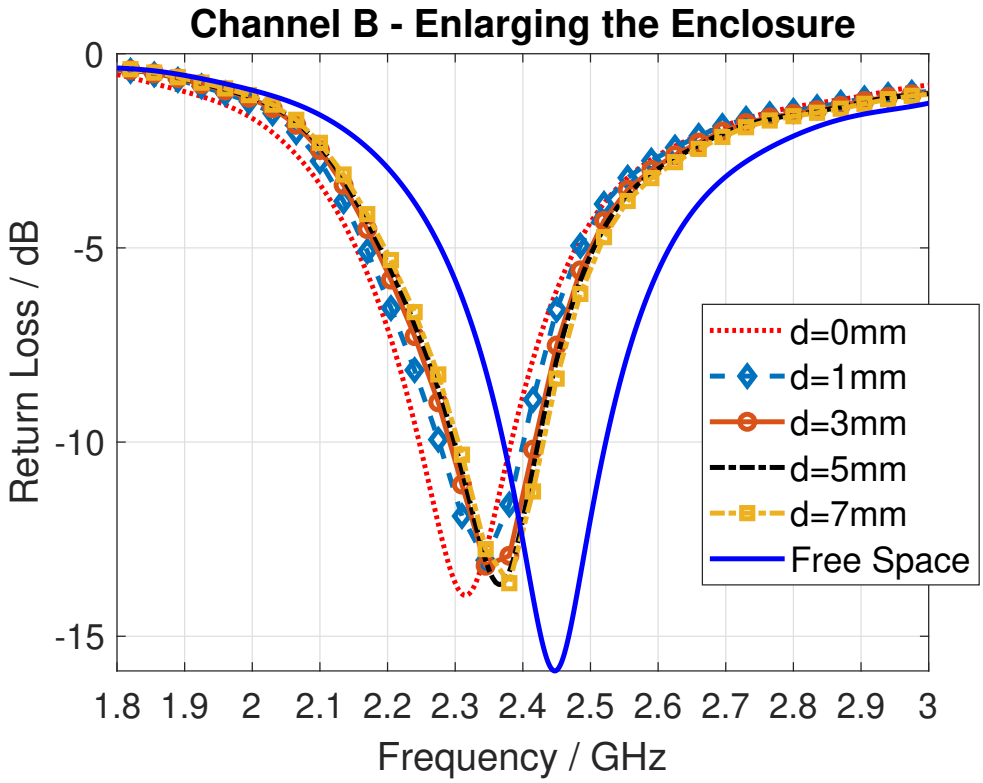

Figure 2.25: A study on the minimum distance between the board and the plastic casing to avoid unwanted detuning.

2.3.5 Study of Material Permittivity Value

Simulation of the return losses have also been used in order to establish the exact value of the relative permittivity ϵ_r of the plastic material composing the enclosure. As only partial data sheets of the material were given, an experimental way to extract it is to run simulations of the antenna behaviour for changing values of ϵ_r until they match with measured results. As the value of ϵ_r is increased it was observed that the return loss curves for Channel B went closer to measurements. A value of $\epsilon_r = 2.8$ has been chosen.

2.3.6 Experimental Validation

Return Loss Measurement

In order to validate our model, we proceeded with measuring the return loss of the antennas when enclosed in the plastic box. In order to do so, we had to trim the box edges to allow the SMA connectors pass through the plastic. The same operation was done in the CST model, to achieve a configuration as close as possible to the real case. The antenna board in the plastic box is shown in Fig. 2.26. Notice that, by doing this operation, some further discrepancies can be introduced. Fig. 2.27 shows a comparison between simulated and measured reflection coefficients, for Channel A and B respectively. A good agreement between the model and experimental results can be observed. At the same time, a bigger detuning for Antenna B is confirmed. Therefore, the efficiency of the antennas when operating around 2.45GHz results to be substantially lowered with respect to the free standing case.

Far Field Radiation Pattern

A measurement campaign was conducted in an anechoic chamber. A picture of the measurement setup is shown in Fig. 2.28. First, from Fig.s 2.29 and 2.30, it can be observed that the gain levels are lowered with respect to the free space case. This is mainly due to the detuning caused by the plastic box. Later, the measured gain pattern of both Antenna A and Antenna B is compared to simulations. An overall good agreement can be noticed; however, some discrepancies mainly due to imperfections in the measurement setup can be noticed. In fact, some drops in the gain are observable in correspondence to the regions where the feeding cables are reaching the board. Those cables connectors have dimensions comparable to the elements on the board and consequently affect the antennas radiation.

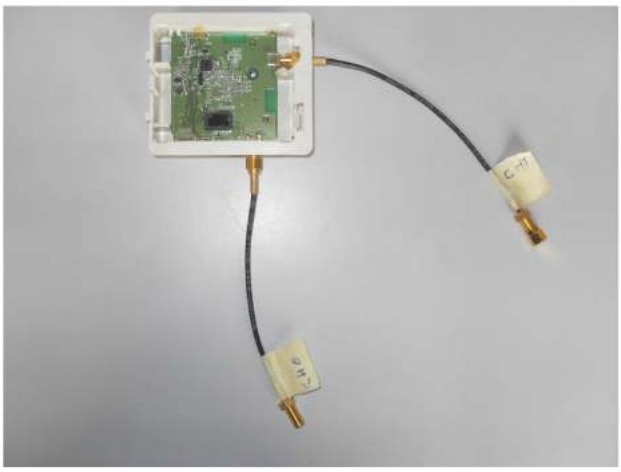

Figure 2.26: The antenna board inserted in the plastic casing and equipped with cables for measurements.

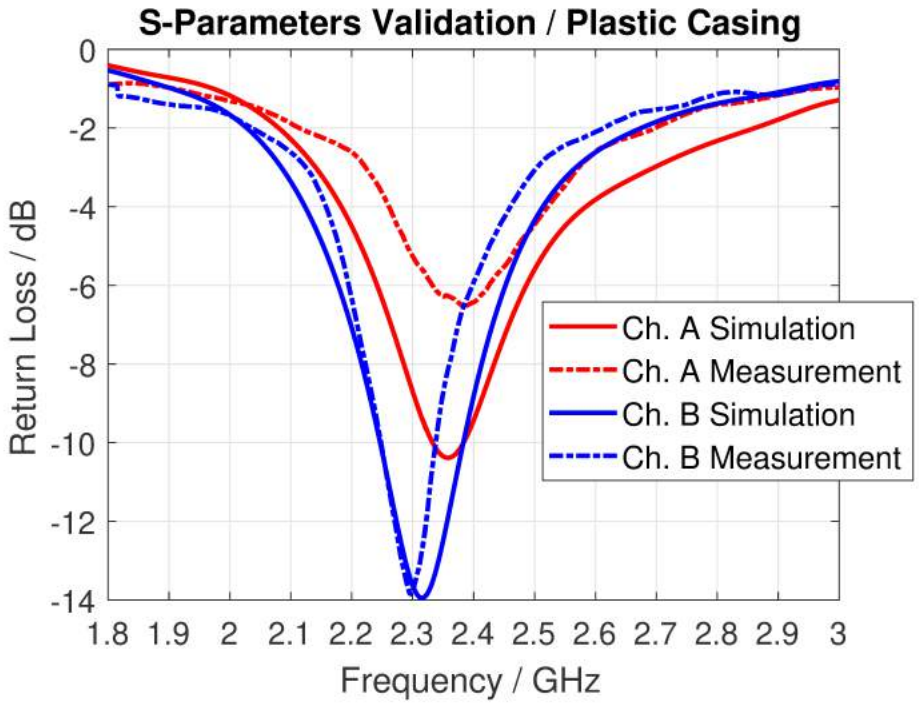

Figure 2.27: Comparison between simulated and measured reflection coefficients when the board is inserted in the plastic box.

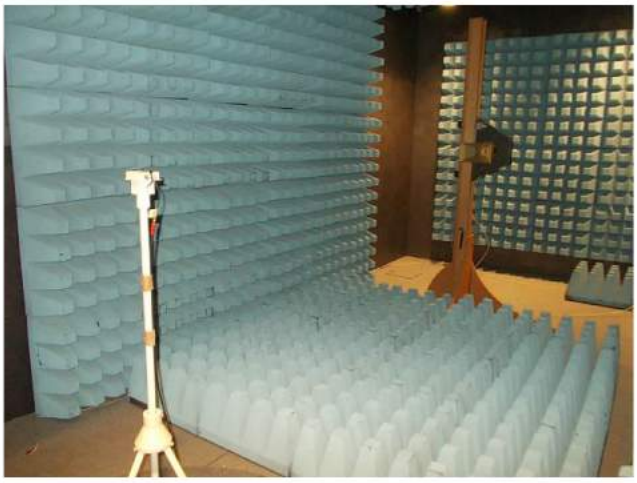

Figure 2.28: The antenna board inserted in the plastic casing in the measurement chamber.

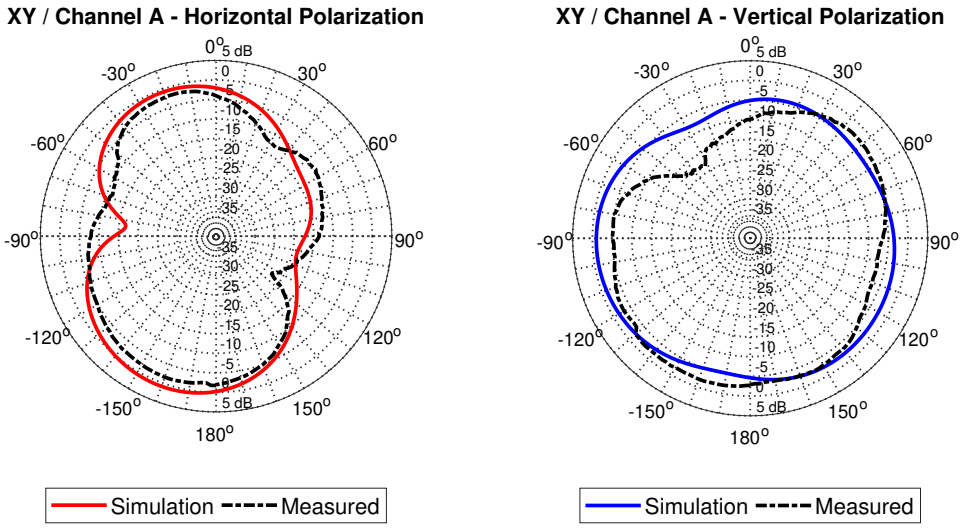

(a) (b)

Figure 2.29: Simulated and measured gain pattern for the antenna system placed in the plastic casing.

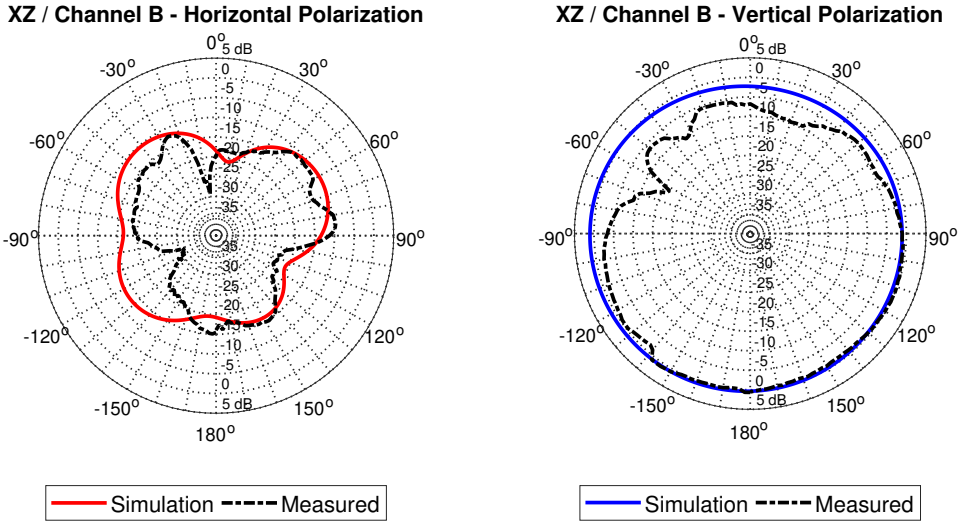

(a) (b)

Figure 2.30: Simulated and measured gain pattern for the antenna system placed in the plastic casing.

2.4 Oven Connectivity

2.4.1 Scenario Description

The board inserted in the plastic enclosure is eventually ready to be installed in the electric appliance. The device considered in this work was a oven. A picture of the configuration is shown in Fig. 2.31. It can be observed that the antenna system is positioned on the left side of the oven structure, lodged in the metallic body of the appliance. A first consideration that can be drawn is that the positioning is not optimal with respect to the initial design of the antenna system. In fact, the metallic components surrounding the antennas might block or distort the original radiation pattern on several sides. Unfortunately, in the design of an electric appliance, the priority is given to the elements contributing to the main scope of the device, while only a minor relevance is left for the connectivity system. Therefore, the physical constraints affect significantly the antenna design and a trade-off between the antenna performances and the positioning has to be accepted. Furthermore, predicting the radiation from the antenna systems when lodged in the oven turns out to be very complicated and the use of experimental measurements in a preliminary phase is burdensome. In this regards, the development of an electromagnetic model allows the engineer to have a fast and easily reconfigurable tool which can provide a reliable support in the design process. Clearly, a complete model of a smart oven is very complicated to handle. Therefore, in this section, a detailed procedure to be followed when dealing with this problem is described.

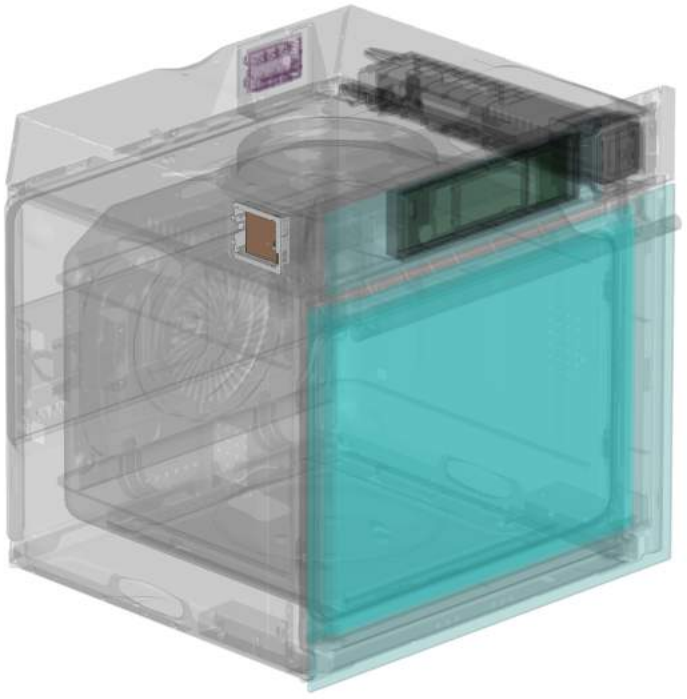

Figure 2.31: Connectivity module installed in the left panel of the oven.

2.4.2 Oven Modelling

The CAD model of the appliance was imported in CST MWS environment. A proper characterization of all the parts composing the oven was done and the correct material was assigned to each component. From an electromagnetic simulation point of view we are interested in two main features with respect to the elements composing the oven:

- Material Type:
  - Dielectric
  - Metallic
- Element size d (with respect to the operating wavelength):
  - Small: $d < \frac{\lambda}{10}$
  - Medium: $\frac{\lambda}{10} < d < \lambda$
  - Large: $d > \lambda$

The operating wavelength is $\lambda = 12.24$ cm. The components to be considered large are the metallic panels, the oven cavity and the front glass. The most relevant medium sized parts are the electronic board, the drawer, and the antenna system itself. All the screws and bolts can be counted in the small elements set.

Some simplifications to the model can be made. In the first place, the very small elements can be excluded from the model. It is important to remark that the removed elements belong to the oven structure while all the small components of the antenna board are entirely included in the model. Secondly, the metallic panels of the oven structure can be approximated by infinitely thin sheets. In this way, no meshing for the thickness dimension is required, thus saving computational resources. This approach and its effectiveness will be studied in the next subsections.

Once the physical model is ready, a fundamental aspect to be analyzed is the meshing of the structure. In fact, this is the main parameter that affects the time required and the accuracy of the simulation. Ideally, we would like to keep the same mesh that was used for the standing alone antenna system, in this way having the same simulation precision obtained in the previous cases. However, using the same mesh resolution would mean having a number of mesh cells that the solver is not able to handle. A view of the described scenario is shown in Fig. 2.32 where the total number of meshcells is around $N_{cell} = 400,000,000$. A solution that can be adopted consists in using two meshing groups: a coarse one for the oven structure and a manually refined one for the antenna system and the components nearby. In this way, a meshing is obtained as depicted in Fig. 2.33. The number of required meshcells drops to $N_{cell} = 25,000,000$, a quantity that can be handled by the simulation tool. Still, the way hexahedral mesh is structured, see Fig. 2.33, implies that the fine meshing of the antenna system due to the small elements on the PCB

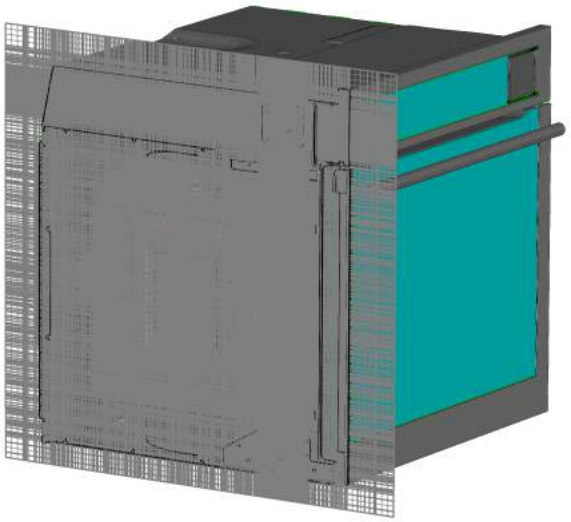

Figure 2.32: Model mesh.

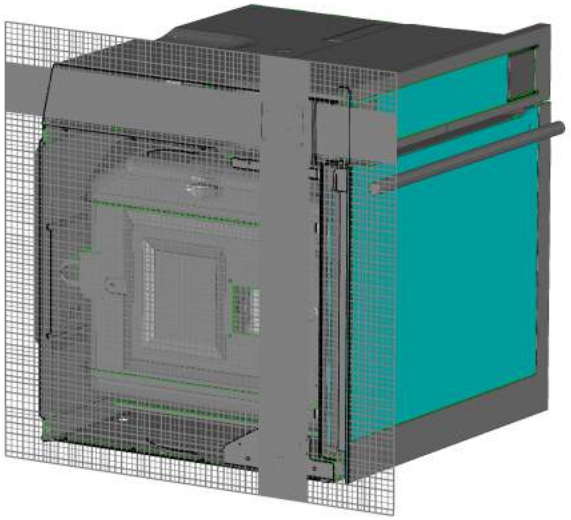

Figure 2.33: Customized model mesh.

board is replicated on its projections along the Cartesian axes. Therefore, an unwanted finer meshing is obtained in some model parts, thus adding complexity to the simulation.

2.4.3 Equivalent Source Model

The critical issues described in the previous section highlight the need of a simulation approach aiming at reducing the problem complexity. In order to limit the overall complexity of the simulation, two solutions can be adopted:

- Equivalent source modelling:
  - Near field equivalent source
  - Near field equivalent source with surrounding structures
- Oven model simplification:
  - Avoiding small elements
  - Zero-thickness and PEC metallic elements
  - Customized mesh accuracy

First, the equivalent source modelling solution was explored [22]-[25]. In order to try this approach, only the upper part of the oven was considered, as depicted in Fig. 2.34. This part was chosen as test case since the antenna system is already completely surrounded by the metallic structure of the appliance.

Consider the standing alone antenna system depicted in Fig. 2.35: a simulation is run and the field distributions are computed on the surface of a rectangular volume surrounding the board [26], [27]. As a consequence, the whole antenna board together with the plastic casing can be represented by its equivalent near field source model. Accordingly, the physical structure of the connectivity system can be replaced in the simulation environment by a rectangular block as shown in Fig. 2.35. In this way, it is possible to avoid the precise meshing required for the small elements on the PCB boards, such as the antennas, the SMA connectors and the copper traces along with all the small features that were included in the model. The antenna system is replaced in the simulation scenario by its equivalent Near Field Source (NFS); the configuration is shown in Fig. 2.36. For a better accuracy, it is possible to include also the antenna structure below the NFS block, but since it has to be

Figure 2.34: Oven components selected for the NFS modelling study.

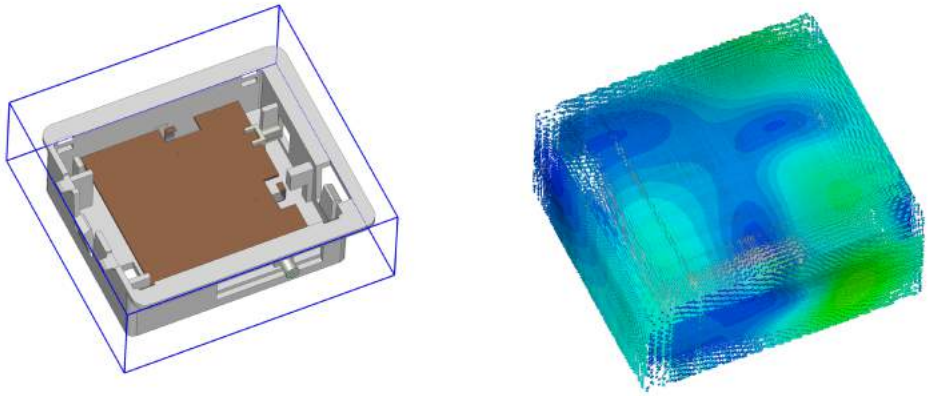

(a) Near field boundaries. (b) NF electric field distribution.

Figure 2.35: Equivalent near field source in CST

Table 2.3: NFS Performance Analysis.

	Simulation Scenario		
	Full-Simulation	NFS FS Board	NFS Board Surrounded
NFS Generation	-	3h	6h
Far Field Simulation	20h	1h	1h

considered only as a passive and not as a radiating element, a coarse meshing can be used in the simulation. A comparison between the radiation pattern considering the real source and using the near field model will be discussed in the following. However, we have to consider that, when embedded in the metallic structure, the frequency behaviour of the antenna is strongly affected by the presence of the surrounding metal. This is not taken into account when the equivalent model is calculated, as the antenna board inserted in the box is considered as standing in free space. Therefore, in order to include effects due to the elements close to the board, the latter have to be, at least partially, included. Consequently, the near field source is calculated for the antenna alone, but considering it not as a standing alone elements, but as part of a more complex environment; see Fig. 2.37.

The radiation pattern of Antenna A is simulated for the three different case described: antenna system entirely simulated, NFS and NFS obtained with the board embedded in the metallic panel. We will refer to the latter as Near Field Source Enhanced (NFSE). The comparison between the three cases is shown in Fig.s 2.38 and 2.39. Considering as reference the red plot, we can observe that there are some differences with the radiation pattern computed with the equivalent source block of the standing alone antenna system. On the other hand, when the second NFS source is considered, an optimal agreement is observable. Therefore, this last approximation can be considered reliable.

Apart from the far field pattern, the variables we are interested in observ-

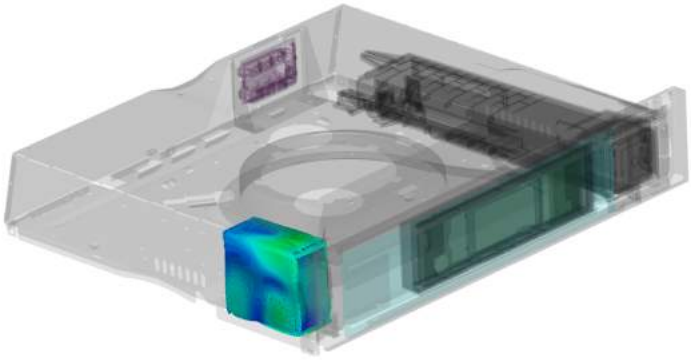

Figure 2.36: NFS embedded in the oven model.

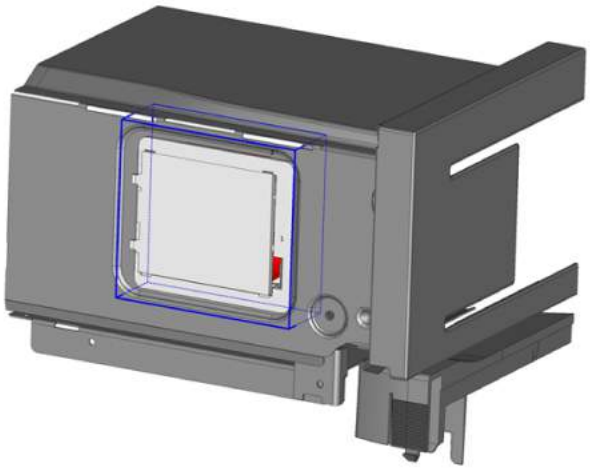

Figure 2.37: Equivalent Near Field Source with part of the oven around it.

ing, to evaluate the goodness of the NFS approach, are the total number of meshcells and the time required for the simulation. Table 2.3 shows the three different cases analyzed. Simulations were run on an Intel-Core i7-4790 CPU @ 3.60GHz with $16,0$ GB of RAM. The NFSE proved to be the most time convenient approach giving reliable results. However, if the time to compute the NFSE itself is added to the time to compute the 3D radiation pattern, the overall time required is comparable to the first case, when the complete model is considered in the simulation. Therefore, we can conclude that this strategy can be more usefully employed for a preliminary study of the radiation of the antennas when embedded in the electric appliance. In other words, if the objective is a quick analysis of the radiation pattern characteristics for different antenna positioning, the NFS approach can be effectively used. In fact, the NFS block can be computed only once and then moved in different positions. Otherwise, if an accurate model is needed, a simulation including all the radiating elements is preferable.

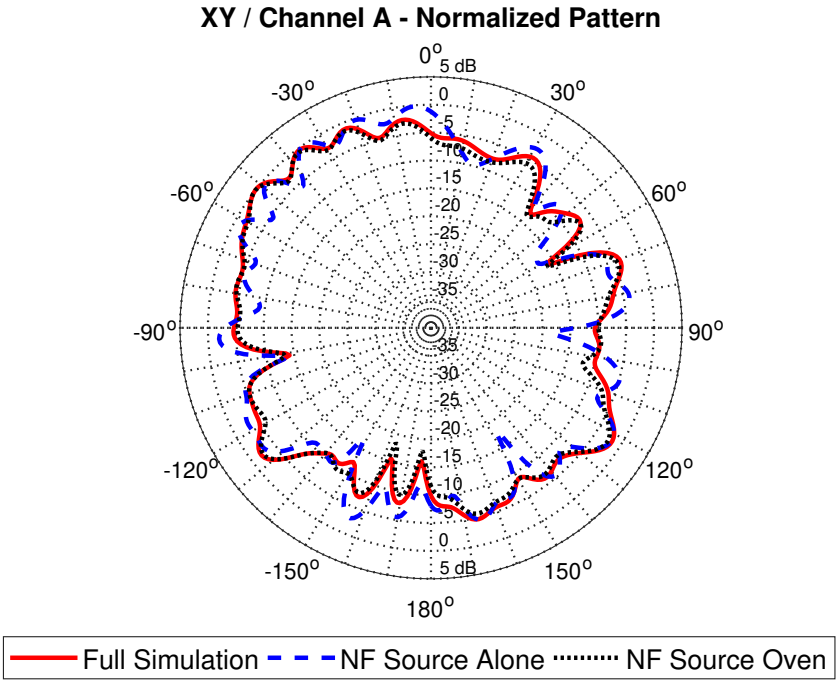

Figure 2.38: Far field comparison between the approaches described in Table 2.3.

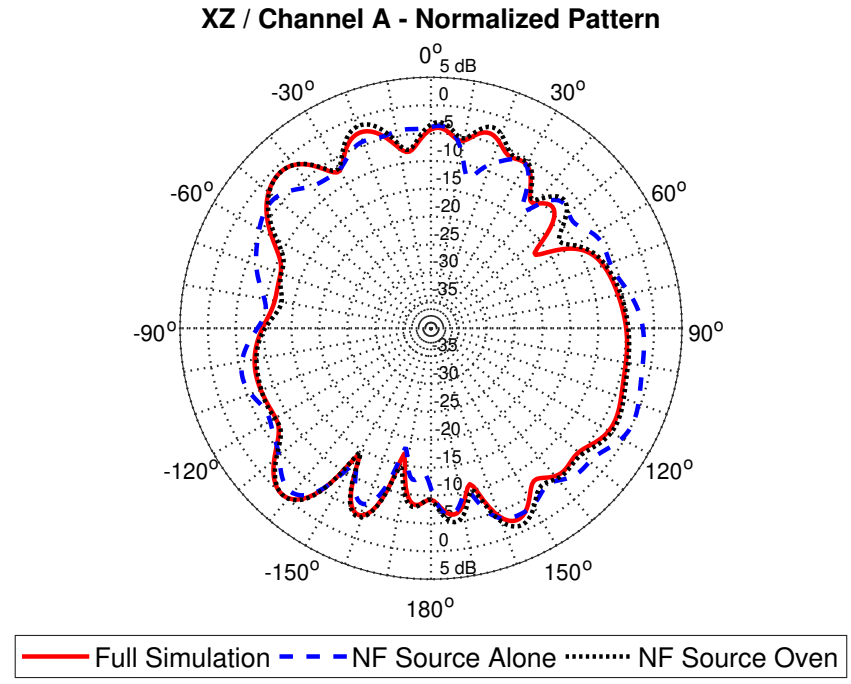

Figure 2.39: Far field comparison between the approaches described in Table 2.3.

A second model simplification approach that can be adopted is considering all the metallic components belonging to the oven structure as infinitely thin sheets. This approximation can hold because the steel thickness is orders of magnitude smaller than the other panel dimensions. Fig. 2.40 illustrates a comparison between the radiation pattern of Channel A in the xz−plane when the steel panels are modeled with a zero or a finite thickness. Results show that the two patterns present some differences, however small. Therefore, this simplification can not be made in this case. This is due to the fact that the radiation pattern of the smart oven is strongly affected and induced by the metallic structures surrounding the antenna system, even more than the original antenna pattern itself. In this regards, even a small change in the metal thickness can have relevant effects on the overall radiation.

Although the presented approaches provided time convenient and acceptable results, we decided to include physically all the elements in the simulation scenario. In fact, as the presence of metals in the nearby of the transmitting system can modify the element resonance and the near field distribution as well, it is more convenient to include all the surrounding structures from the beginning.

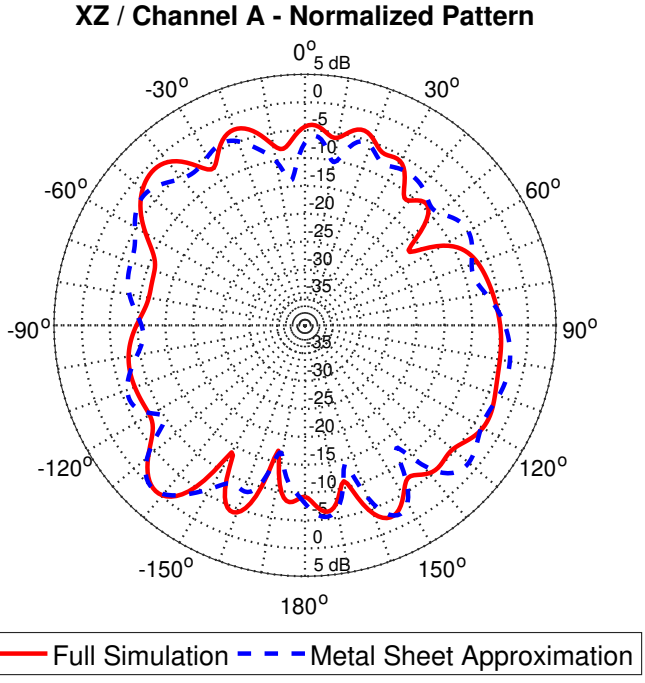

Figure 2.40: Far field comparison between the finite thickness and the zero thickness scenario.

2.4.4 Radiation Characteristics of the Smart Oven

The complete model of the oven is eventually considered for simulation. The sources of radiation are the antennas A and B on the PCB board. It is easy to suppose that the pattern properties shown in the previous sections are going to be lost. In fact, the proximity of metallic structural components and the presence of a closed cavity inside which the antennas are radiating have a strong effect on the radiation characteristics of the antennas by drastically modifying the far field pattern.

Return Losses of the Antennas Installed in the Oven

First, the impact on the resonance for Channel B is hereby analyzed. This antenna was chosen as it was the most critical case when moving from the free space configuration to the plastic casing. A comparison between the return loss curves of the antenna system when in free space and when installed in the oven is shown in Fig. 2.41. The peak of resonance is moved close to 2.4GHz. Other spurious resonances appear, and at the operating frequency of 2.45GHz a return loss of approximately -7dB is observable. This effect is connected to the almost completely metallic cavity to which the antennas are facing, which creates additional resonances that are not caused by the antennas electromagnetic characteristics. In order to overcome this issue, a tuning of the matching network has to be done once the antennas are installed in the oven.

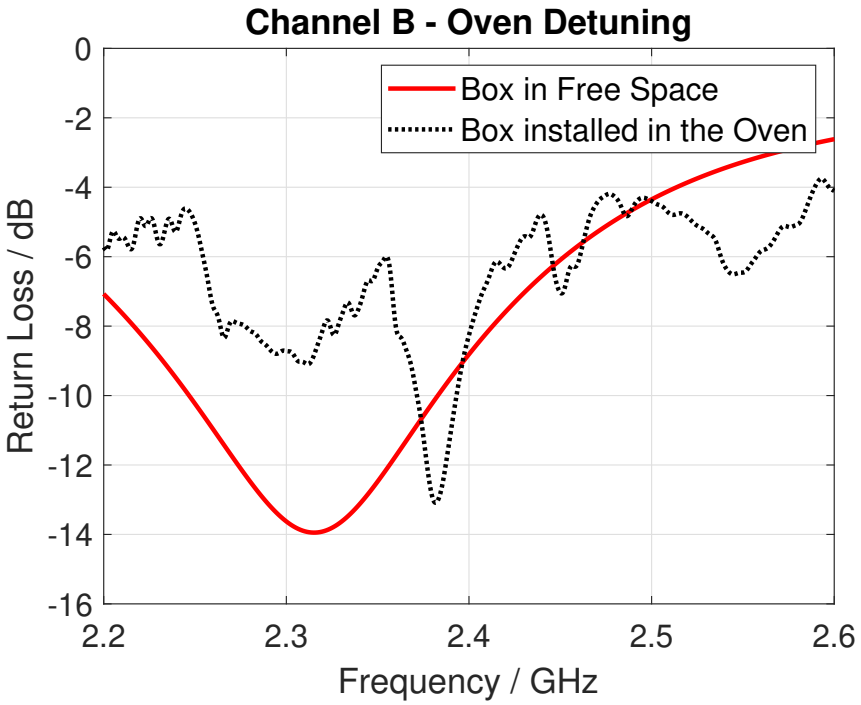

Figure 2.41: Comparison between the reflection coefficients of the antenna board in free space and installed in the oven.

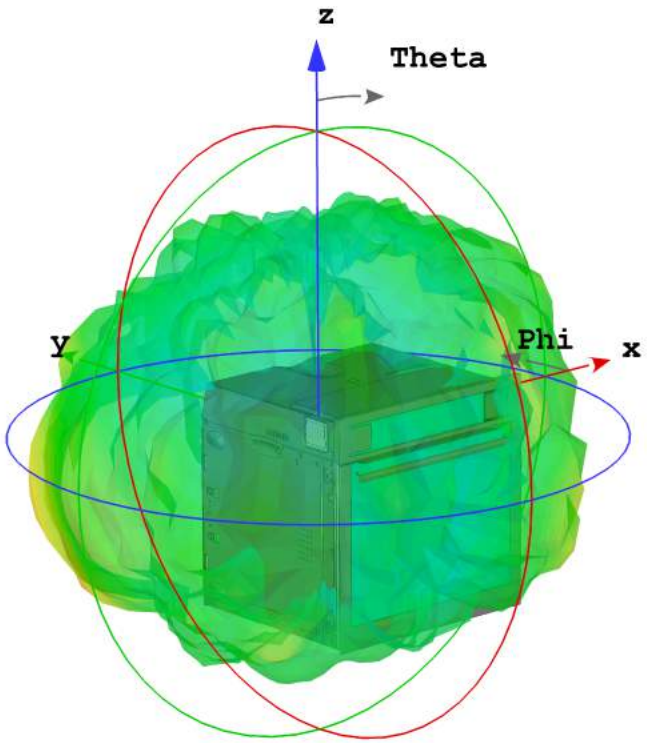

Figure 2.42: 3D radiation pattern for the Antenna B when installed in the appliance.

Radiation Pattern of the Antennas Installed in the Oven

Secondly, the gain pattern of the two antennas is simulated. The 3D radiation pattern of Channel B is shown in Fig. 2.42. The first consideration that can be drawn is that the radiation of the standing alone antenna system turns out to be completely modified when installed in the oven. In fact, the metallic structure surrounding the casing drastically affects and influences its radiation characteristics.

In detail, Fig.s 2.43-2.44 illustrate the gain of Antenna B on the main planes. A comparison with the radiation pattern of the same antenna in free space is shown. At a first sight, it can be observed that the pattern is completely altered after the embedding of the device in the oven. The radiation pattern is strongly distorted by the physical boundaries given by the metallic walls of the oven. In practice, the majority of the far field is radiated towards the directions where the oven panels are interrupted by the front panel glass, a hole in the back side and the free room to be occupied by the casing on the oven side. A good degree of omnidirectionality is preserved in the xy−plane, except for a radiation null corresponding to the right metallic panel. On the other hand, the gain levels are considerably lowered with losses around 10 to 15 dB when considering the xz−plane, thus deteriorating drastically the original pattern of the antenna.

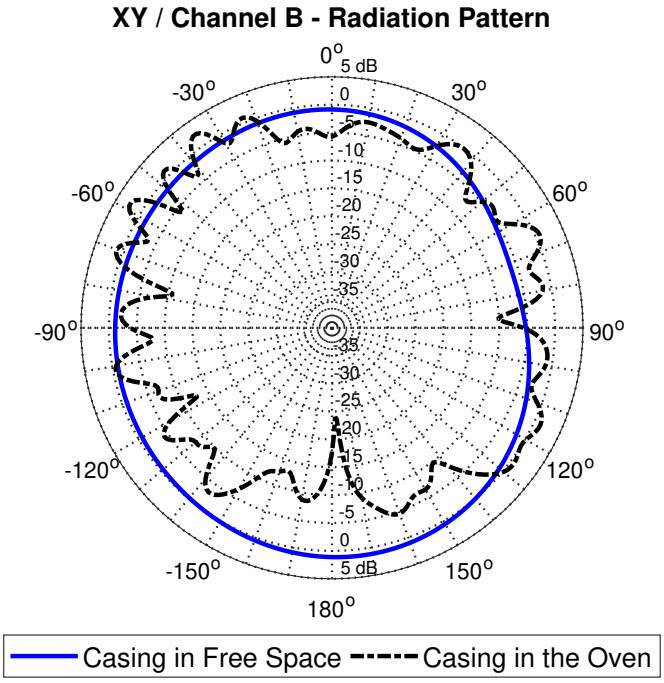

Figure 2.43: Comparison between the gain pattern of the antenna board in free space (with plastic casing) and installed in the oven.

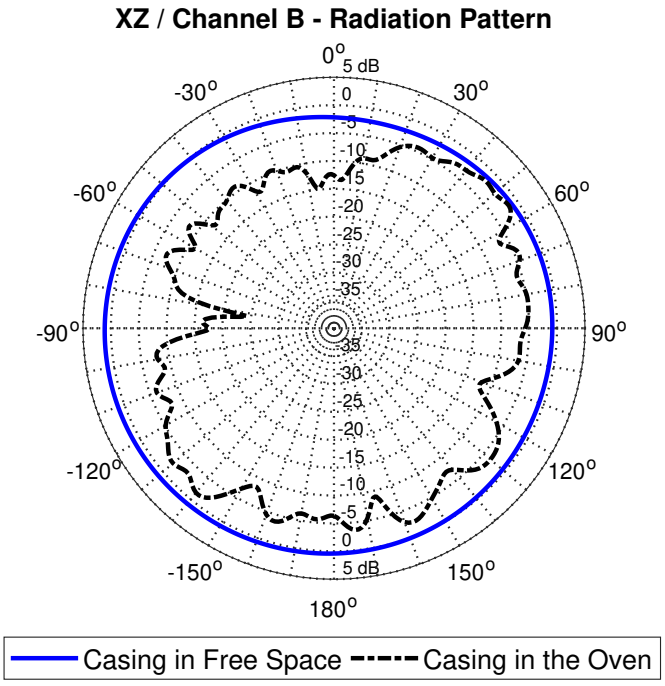

Figure 2.44: Comparison between the gain pattern of the antenna board in free space (with plastic casing) and installed in the oven.

2.4.5 Oven Model Validation

A measurement campaign was eventually carried out in order to validate the whole electromagnetic model of the smart oven developed and presented in the previous sections. The appliance is placed inside an anechoic chamber and the radiation pattern of the radiating elements embedded in the appliance is measured. Measurements were performed, for both channels A and B, on the three main planes depicted in Fig. 2.2. In detail, the oven is rotated around the three Cartesian axes, and for each plane both vertical and horizontal polarization are measured.

When preparing the experimental setup, some critical aspects emerged. For example, the feeding of the antennas, which is done via the SMA connectors, results to be complicated. In fact, as there was no room for the feeding cables, two holes through the metallic structure had to be made in order to let the cables reach the board. Furthermore, some spurious radiation originated by the currents flowing on the cables is responsible of additional noise to the measured pattern. A picture of the experimental setup, when the oven was set to rotate around the z−axis is shown in Fig.s 2.45 and 2.46.

The electromagnetic model of the oven is finally validated against experimental results. Fig.s 2.47-2.50 show a comparison between the simulated and measured antenna gain pattern. In this sections, the radiation pattern will be shown for some planes only, whereas the whole set of results was delivered to Electrolux in a complete report. The plots show a good agreement between measurements and simulation although some discrepancies can be observed. The reduction in the gain levels in some directions can be caused by the feeding system which is not totally stable when the oven is rotating on the mechanical support. At the same time, some noise effects are caused by the cables that have to reach the electronic board. Furthermore, the scattering caused by the metallic structure in the very nearby of the antenna system originates a very indented and noisy pattern for both Channels A and B; see Fig. 2.42. Therefore, even a slightly misalignment in the measurement setup (i.e. the rotation center is not perfectly aligned with the CST model) can produce a considerable difference in the radiation pattern.

It is important to notice that the regions of minima are confirmed by the experimental results and correspond to the areas where the radiation is completely shielded by the oven structure. Considering how the oven will be actually positioned in a domestic environment, the areas of major interest are the regions in front and on the sides of the oven. In this areas, the antenna gain is never higher than 1 dB, thus confirming the overall worsening of the antennas performances due to the installation in the appliance.

Figure 2.45: A picture of the oven in the anechoic chamber on the rotating support: the configuration reported is for measuring the gain in the xz−plane

Figure 2.46: A picture of the oven in the anechoic chamber on the rotating support: the configuration reported is for measuring the gain in the yz−plane

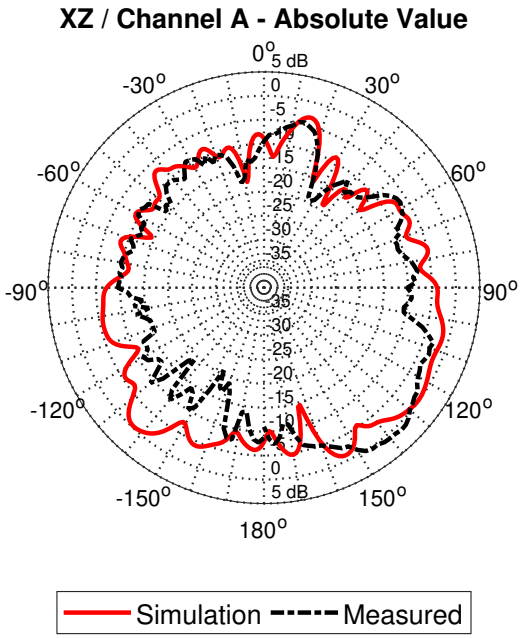

Figure 2.47: Comparison between the simulated and measured gain pattern of the antenna board installed in the oven

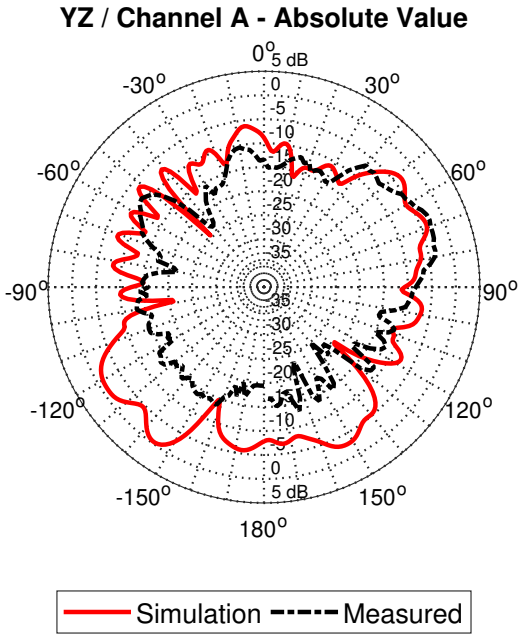

Figure 2.48: Comparison between the simulated and measured gain pattern of the antenna board installed in the oven

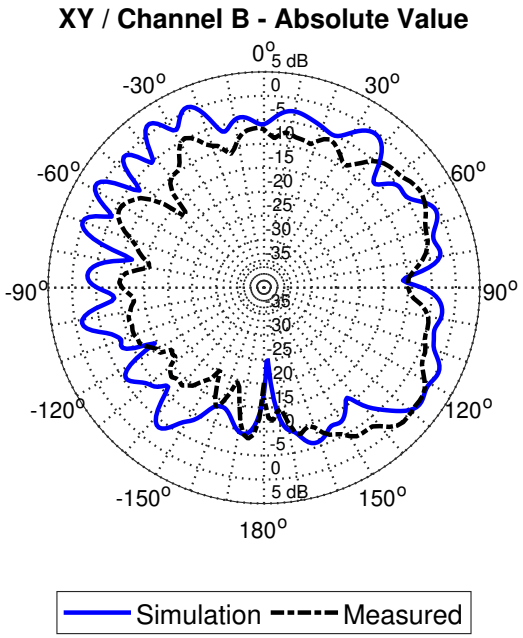

Figure 2.49: Comparison between the simulated and measured gain pattern of the antenna board installed in the oven

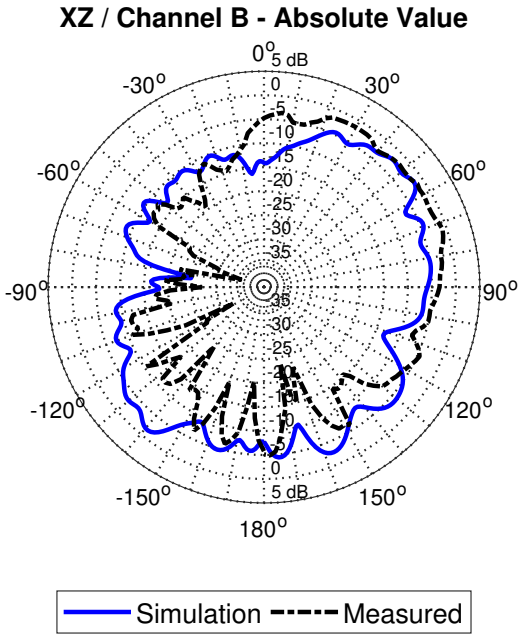

Figure 2.50: Comparison between the simulated and measured gain pattern of the antenna board installed in the oven

Chapter 3

Adaptive Antenna Arrays for Changing Surfaces

3.1 Introduction

The research reported in Chapter 2 highlighted some crucial issues that can arise when developing antenna systems to be embedded in complex structures. First and foremost, as a consequence of the installation inside the appliance, the radiation pattern results to be strongly distorted, thus causing an optimal antenna design to be fruitless.

A first solution that can be adopted in order to overcome these issues is to use phased array antennas, in order to dynamically steer the main beam towards the desired direction. In this way, it is possible to recover the original desired radiation pattern that was deteriorated as a consequence of the structure surrounding the antenna. A second option that can be considered is to use antenna arrays conformal to the surface of the device under analysis. As a result, all the problems related to the scattering due to the metallic structure around the antenna board can be avoided.

A similar problem was addressed in our research, where we considered phased array antennas for which radiation pattern distortion is not due to physical obstacles in its immediate proximity but rather because of a deformation of the surface on which the array is placed. This can be the case of simple wearable devices that monitor health and fitness parameters and that are placed on body parts that move and bend (e.g., wrists, ankles, and knees). In this regards, the control of the radiation pattern is a desirable feature for antennas that have to adapt, with respect to their original free-standing design, to modifications in the structures that surround them. In order to overcome this problem, many different pattern recovery approaches can be adopted, from very accurate and expensive ones to cheaper and simpler ones. We will focus on this second class of techniques that is particularly appealing for simple and cheap wearable devices whose main requirement is to keep the product cost as low as possible.

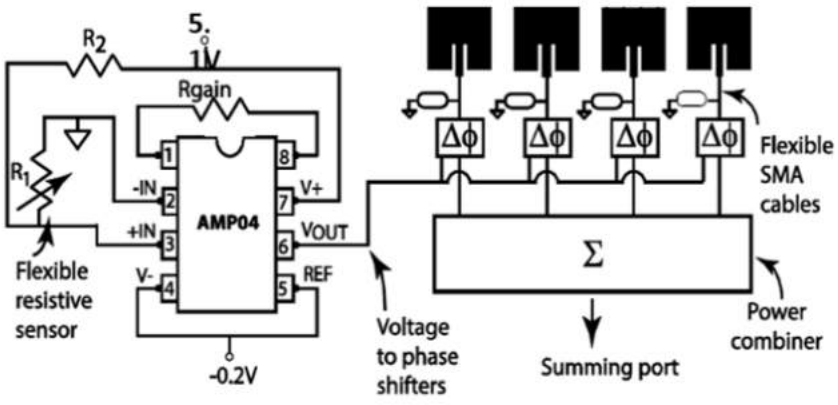

Figure 3.1: Circuit topology for autonomous adaptive conformal antennas.

3.1.1 Problem Statement

Modern wireless communication systems have raised the need of developing antenna arrays capable of adapting to surfaces that change shape in time. The main issue related to the design of this type of antennas, consists in the control of the radiation pattern that results significantly altered as a consequence of the array surface deformation. While the majority of pattern recovery techniques adopted to mitigate this effect, (e.g., mechanical [28] and electrical [29][30] compensation) need extensive signal processing, narrow-band correction algorithms and potentially complex sensor networks, a cheaper and easier-to-implement approach is provided by the projection method [31]. This technique, combined with the use of strain sensors and phase shifters, is a simple but powerful tool for reducing significantly the radiation pattern distortion.

3.1.2 Literature Review

The projection method effectiveness was thoroughly studied for many types of antennas. In [32] this technique was applied to two 1×4 microstrip patch antennas arrays bent on an arc- and on a wedge-shaped surface. In [33] and [34] it was used to recover the radiation pattern of an 1×6 array bent on a spherical surface and a cylindrical surface. Frequency reconfigurable arrays placed on wedge-shaped ans S-shaped surfaces have been considered in [35] and [36]. All the aforementioned works adopt the projection method in order to recover the pattern of broadside arrays, but a common requirement when dealing with phased arrays is to dynamically steer the main lobe towards different desired directions. Some works dealt also with this issue: for example, in [37], the effectiveness of the projection method is evaluated for a beam-tilting linear 1×5 array placed on a wedge-shaped deformable surface.

The pattern recovery technique is autonomously implemented using a simple circuitry as in [32]. Fig. 3.1 shows the operational amplifier and the passive components that, by providing an output voltage that drives the voltage controlled phase shifters, allow to implement the phase compensation.

3.1.3 Original Contribution

Our research was intended to target some critical issues of the pattern recovery technique. In particular, we have evaluated the reliability of the projection method when considering bi-dimensional arrays and surface deformations dramatically more complex with respect to the previous work. This was done in terms of the maximum deformation extent that can be tolerated by the technique both for broad-side and beam-steering arrays. For the latter case, a simplified theory for calculating the compensating phase shifts has been presented and validated. Furthermore, a study on the actual resolution needed by the phase shifters has been carried out, in order to provide useful information when purchasing instruments for an experimental setup.

In detail, in [38] we presented an analytical model for the projection method when considering an asymmetrically deformed bi-dimensional array. In [39] we investigated the projection method application in order to recover the pattern of a bi-dimensional deformed array whose main lobe was steered with respect to the broadside direction. In [40] the same configuration of [39] has been considered. A simplified version of the projection method for beam tilting arrays was introduced in order to provide a simpler and more computationally convenient approach. In [41], we presented a preliminary analysis on the method toleration on the phase compensation approximation. Finally, in [42] the configuration presented in [38] was validated with measurements and a study on the robustness of the recovery technique has been carried out both for a broad-side and a beam-steering configuration. For our study purposes, arrays of patch antennas working in the 2.4 GHz Wi-Fi frequency band have been considered. However, the theory and the applications presented hereafter can easily be transposed for other kind of antennas. Measurements were performed in collaboration with North Dakota State University Laboratories, which we would like to thank.

3.2 The Projection Method

In this section, the projection method, i.e. the technique applied for retrieving the pattern of deformed arrays that has been used in our investigation, is presented in detail. Consider, for sake of simplicity, a linear array composed of four antennas in the spherical coordinates reference system depicted in Fig. 3.2. The array factor (AF) of the array is given by:

$$AF = \sum_{i=1}^{N} w_i \mathrm{e}^{jk\{x_i \sin\theta\cos\phi + y_i \sin\theta\sin\phi + z_i\cos\theta\}} \tag{3.1}$$

where (x_i, y_i, z_i) are the coordinates of the $i-$th element of the array. When a deformation of the array occurs, as displayed in Fig. 3.3, signals coming from misaligned antennas arrive out-of-phase at the reference plane. A compensating phase-shift has to be introduced to each element in order to correct the radiation pattern. The phase correction is proportional to the displacement along the $z-$ axis, and, for each element, it can be computed as:

$$\Delta\phi_i = k\Delta z_i \tag{3.2}$$

As a consequence, the array factor of the array has to take into account the introduced phase term, and it becomes:

$$AF_{\mathrm{C}} = \sum_{i=1}^{N} w_i \mathrm{e}^{jk\{x_i \sin\theta\cos\phi + y_i \sin\theta\sin\phi + z_i\cos\theta\}} \mathrm{e}^{j\Delta\phi_i} \tag{3.3}$$

In a real case scenario, antenna elements are not considered anymore as point sources, and their 3D radiation pattern $D(\theta, \phi)$ has to be considered. As a

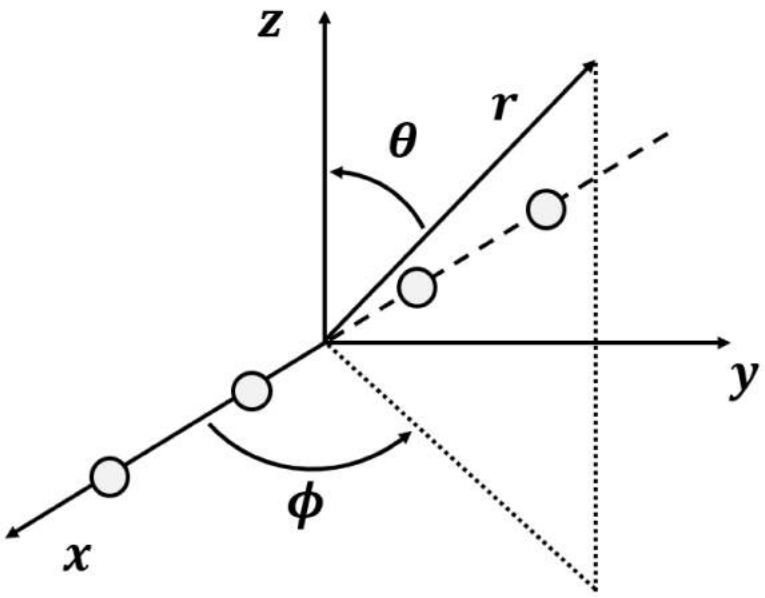

Figure 3.2: A linear array composed of N = 4 elements.

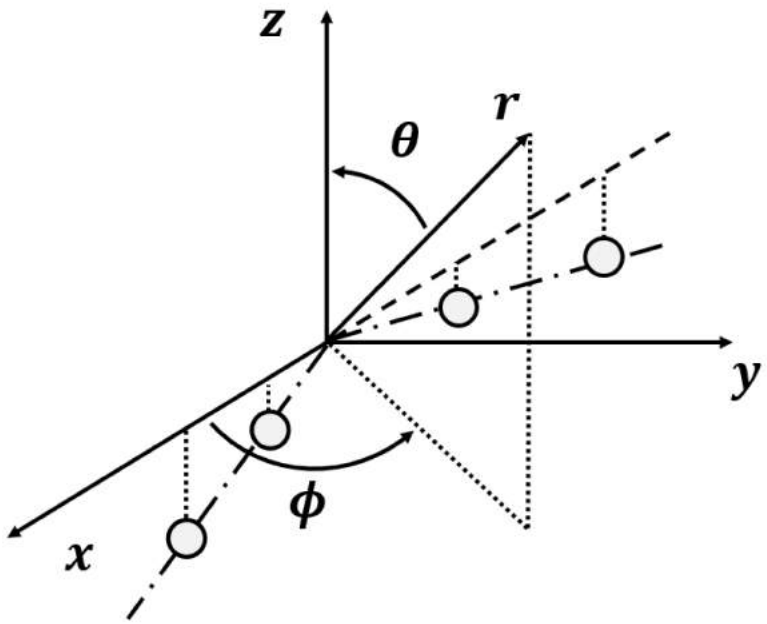

Figure 3.3: A linear array composed of N = 4 elements after a shape deformation.

consequence, the array directivity (AD) is obtained from equation (3.1) that transforms into:

$$AD = \sum_{i=1}^{N} D_i(\theta, \phi) w_i \mathrm{e}^{jk\{x_i \sin\theta\cos\phi + y_i \sin\theta\sin\phi + z_i\cos\theta\}} \tag{3.4}$$

When the structure gets deformed, the array element pattern undergoes to some kind of rotation with respect to the original orientation.

$$AD_{\mathrm{C}} = \sum_{i=1}^{N} D_i(\theta - \theta_i, \phi - \phi_i) w_i \mathrm{e}^{jk\{x_i \sin\theta\cos\phi + y_i \sin\theta\sin\phi + z_i\cos\theta\}} \mathrm{e}^{j\Delta\phi_i} \tag{3.5}$$

where (θ_i, ϕ_i) are the angles each antenna is rotated of, with respect to its original alignment.

As an example, a directive antenna whose main lobe is directed broadside is considered. After the deformation, the main lobe is now pointing towards another direction, and this has to be taken into account for the analysis purposes. Main lobe not broadside anymore can impact on the overall effectiveness of the method, and will be carefully investigated in the following. Equations (3.4) and (3.5) will be used in our studies in order to obtain an analytical model of the array, before and after surface deformation respectively, taking into account at the same time the radiation pattern of the antenna element.

3.3 Main Lobe Control of a Beam Tilting Antenna Array Laid on a Deformable Surface

3.3.1 Problem Statement

The main issue of the projection method when applied to beam-tilting arrays is related to the fact that it requires the correcting phase shifts to be a function of both the surface deformation and the main lobe direction. This is because the phase shifts introduced in the elements have two purposes in this case: compensating the array deformation and steering the beam towards a desired direction. Therefore, it can be seen how the projection method is formulated in order to tilt the beam of an array taking into account (i.e., compensating) the array deformation; it is not used to retrieve the pattern of a deformed array whose main lobe has already been tilted towards a specific direction. This fact complicates the overall system since the phase compensation in this case cannot be simply extracted by the strain sensor data that measure the geometrical deformation (unless this is a priori known): an additional signal processing step is required in order to project the array elements onto a new reference plane every time that the beam is tilted towards a different direction. In [37], this was not an issue since the deformation geometry was quite simple and a priori known, and therefore, also the analytical relation that linked the phase shifts to the geometrical deformation and to the tilting angles was a priori given, but as soon as the deformation becomes slightly more complex (as the one we present here) and/or a priori unknown, the computation of the correcting phase shifts becomes cumbersome. As the shifts cannot be directly computed from the strain sensor data anymore, a new analytical relation

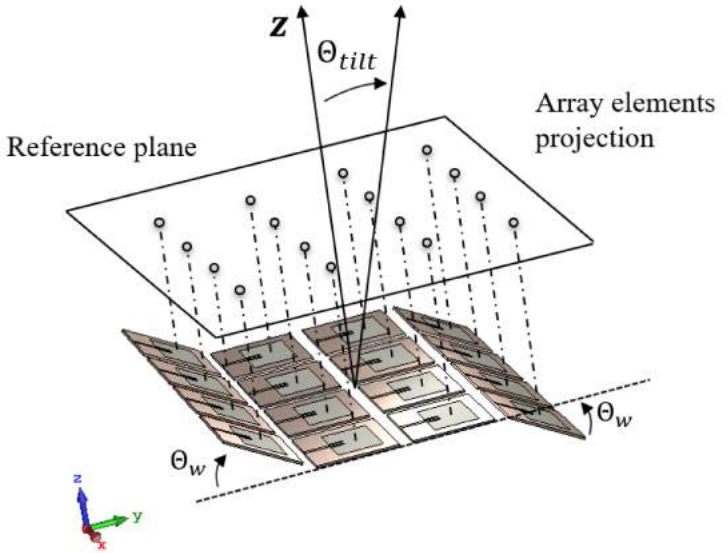

Figure 3.4: Investigated surface deformation for a beam-steering planar array.

between surface deformation and the direction of maximum and compensating phase shifts must be formulated for each main lobe direction and for each possible geometrical deformation. Since this type of arrays is used for simple and cheap devices, we are interested in keeping the overall system complexity and the cost as low as possible. Therefore, the correcting phase shifts is expressed as the sum of two independent terms: one related to the geometrical deformation and one related to the main lobe direction. Doing so, it is possible to simplify the system reducing the amount of signal processing required: in fact, the first term can be directly extracted from strain sensor data that measure surface deformation, while the second component can be easily pre-computed through basic antenna theory. It will be demonstrated that this approach allowed to recover the main radiation properties of a doubly wedge-deformed planar array when its beam is tilted up to 40°.

3.3.2 Theoretical Framework

In order to explain and test the proposed approach, a 4×4 planar array, whose elements are patch microstrip antennas resonating around 2.48 GHz was considerd. Referring to Fig. 3.4, array rows and columns as the sets of array elements sharing, respectively, the same y- or x-coordinate. The array is placed on a surface which is subject to a doubly wedge-like geometrical deformation as depicted in Fig. 3.4: the first and last rows of the array are tilted of Θ_W degrees. As a consequence of the surface deformation, the array radiation pattern is distorted as the main lobe decreases in gain, and shifts in direction. The considered scenario assumes that the array beam is tilted faster than the speed at which the deformation changes shape. Therefore, only a fixed geometry has to be considered for the deformation. The main beam of the array is steered of θ_{tilt} degrees in the yz-plane. In order to do this avoiding excessive pattern distortion, according to the projection method

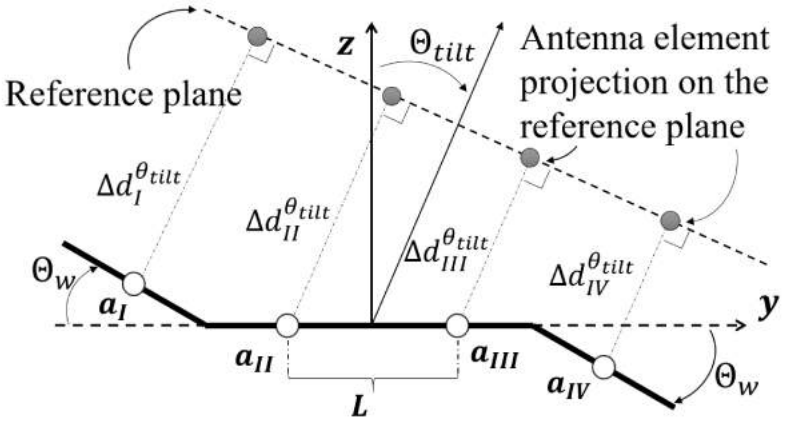

Figure 3.5: yz-plane cut of the deformed array surface. The reference plane is orthogonal to the desired direction of maximum. The compensating phase shifts are computed for each θ_{tilt} from the distance between each array element and its projection on the plane.

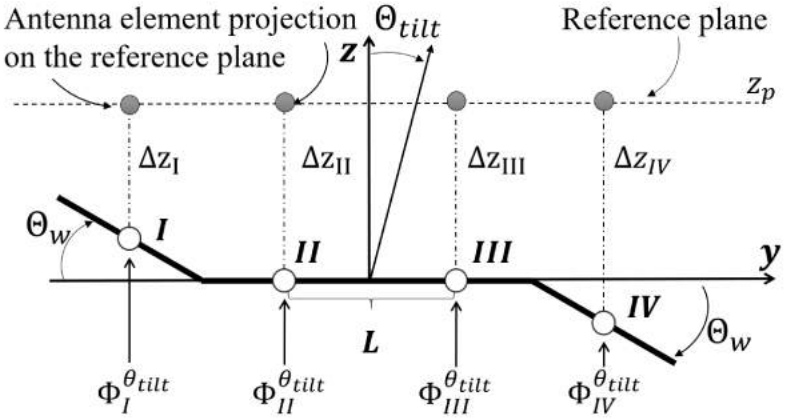

Figure 3.6: yz-plane cut of the deformed array surface. The reference plane is orthogonal to the broadside direction. The compensating phase shifts are computed only once from the distance between each array element and its projection on the plane.

[37], phase shifts have to be applied, so that they take into account both the geometrical deformation of the antenna and the desired main lobe direction . Referring to Fig.s 3.5 and 3.6, the phase shifts are computed projecting the array elements onto the reference plane, that is, the plane chosen among the infinite ones orthogonal to the desired direction of the maximum. In other words, they are proportional to the distance of the elements from the reference plane.Assuming now that $\theta_{\text{tilt}} = 0°$, the deformed array is operating in broadside mode, and therefore, the reference plane must be chosen among the planes that are parallel to the xy-plane: for example, in Figure 3.6, the reference plane is represented above this plane in order to stress the fact that any of these planes can be chosen as the reference one. For example, a straightforward choice is to pick exactly the xy-plane: in this way, the distances of the array elements from it are simply given by their z-coordinates. In particular, if strain sensors between adjacent antennas are used to measure the surface deformation, then the distance of the elements from the xy-plane can be directly computed from the sensor data [36]: no analytical expression of this distance in the function of the deformation geometry must be provided.

However, if the main lobe is tilted towards a different direction, as depicted in Fig. 3.5, then the reference plane will be tilted as well, and this implies that the distances between the elements and the new reference plane cannot be simply evinced from the information provided by the strain sensors. Consequently, an analytical relation linking the correcting phase shifts to the geometrical deformation and to the tilted reference plane must be introduced as it has been done in [37]. Now, this can be easily done if the geometrical deformation is simple or a priori known, but if this is not the case, then it can be difficult to evaluate the compensating phase shifts, since an analytical expression of these quantities must be available for each geometrical deformation and for each steering angle. The goal of this work is to keep the system complexity as low as possible, and therefore, it is shown that it is possible to

retrieve the array radiation pattern even if skipping the last signal processing step that requires the computation of a new analytical relation every time that either the steering angle or the surface deformation changes. In order to do this, the overall phase-shift to be introduced into the nth element (see Figure 3.6) is expressed as the sum of two terms:

$$\psi_i = \Delta\phi_i^0 + \Phi_i^{\theta_{tilt}} \tag{3.6}$$

where $\Delta\phi_i^0 = k \cdot \Delta z_i$ are the terms that have the function of correcting the surface deformation and coincide with the phase shifts required by the projection method to retrieve the pattern of the broadside array (they are given by the product between the wave vector k and Δz_i in Fig. 3.6), while $\Phi_i^{\theta_{\text{tilt}}}$ is simply the phase-shift that must be introduced into the $i-$th element of the undeformed planar array in order to steer its main lobe into the desired direction. The first term can be directly computed from the strain sensor data that measure surface deformation, while the second term can be easily pre-computed for a set of angles of interest according to basic antenna theory [43] and stored in a small memory or look-up table into the device. For the scenario depicted in Fig. 3.6, the phase shifts are obtained from:

$$\begin{aligned}
&\Delta\phi_I^0 = -k \cdot \frac{L}{2} \cdot \sin\theta_W \\
&\Delta\phi_{II}^0 = 0 \\
&\Delta\phi_{III}^0 = 0 \\
&\Delta\phi_{IV}^0 = k \cdot \frac{L}{2} \cdot \sin\theta_W
\end{aligned} \tag{3.7}$$

Therefore, with this approach, no analytical expression of the phase shifts in the function of the geometrical deformation and of the steering angle is required and no further processing steps are necessary. A comparison between the two approaches in terms of correcting phase-shift is made. Among the infinite planes orthogonal to the direction of the maximum, the reference plane is chosen as the one touching element a_{IV}. The correcting phase shifts $\psi_i,\ i = I, \ldots, IV$ to be introduced into elements $a_I, \ldots, a_{IV}$, respectively, are a function both of the geometry of the deformation and of the steering angle, and they are given by:

$$\begin{aligned}
&\psi_{IV} = k \cdot \Delta d_{IV} = 0 \\
&\psi_{III} = k \cdot \Delta d_{III} = \psi_{IV} + \frac{L}{2[\sin(\theta_{\text{tilt}} - \theta_W) + \sin(\theta_{\text{tilt}})]} \\
&\psi_{II} = k \cdot \Delta d_{II} = \psi_{III} + L \cdot \sin(\theta_{\text{tilt}}) \\
&\psi_I = \psi_{II} + \frac{L}{2[\sin(\theta_{\text{tilt}} - \theta_W) + \sin(\theta_{\text{tilt}})]}
\end{aligned} \tag{3.8}$$

The expressions (3.8) can be cumbersome to evaluate, especially considering that the geometrical deformation may not be a priori known and that it

(a) Single patch element (b) Antenna array

Figure 3.7: A picture of the patch element and of the fabricated prototype of the array placed on the doubly-edge deformed surface.

could further change in shape and become even more complex than the one presented here (e.g., it could change to a three-dimensional deformation as the one studied in [38]]). According to the proposed approach instead, the overall phases to be applied to the elements are given by the sum of two terms that can be evinced from sensors data and pre-computed. The terms responsible for the deformation compensation are given by: $\Delta\phi_{IV} = -\Delta\phi_I = 45°$, $\Delta\phi_{II} = -\Delta\phi_{II} = 0°$ while those responsible of tilting the beam towards a set of sample directions are given in Table 3.1 and have been computed according to [43]. As it will be shown in the next section, this approach proves to be effective in recovering the radiation pattern of the conformal array when the main lobe is tilted from $\theta_{\text{tilt}} = 0°$ up to $\theta_{\text{tilt}} = 40°$.

3.3.3 Experimental Validation

The experimental set-up consisted of a planar array capable of steering the beam along the $y-$direction of θ_{tilt} degrees. The array is then placed on a surface that is deformed in a doubly-wedge shape with $\theta_W = 30°$, as it can be seen in Fig. 3.4. The radiation pattern of the planar array for different tilt angles ($\theta_{\text{tilt}} = 15°,\ 25°,\ 40°$) is taken as the reference pattern to be retrieved. Full-wave numerical simulations were performed in CST Microwave Studio and a prototype of the 4×4 array was fabricated and measured in an

Table 3.1: Beam steering phases $\Phi_i^{\theta_{tilt}}$ (°).

		Main lobe direction θ_{tilt}			
		0°	15°	25°	40°
Array $i-$th row	I	0	70	155	200
	II	0	20	65	65
	III	0	-20	-65	-65
	IV	0	-70	-155	-200

anechoic chamber. Fig. 3.7 shows a picture of the fabricated prototype. The phase of each patch antenna was controlled through a phase shifter (Hittite: HMC928LP5E). Figures 3.8, 3.9 and 3.10 contain four graphs: the radiation pattern of the planar array (i.e., the target to retrieve), the distorted pattern of the deformed array, the pattern corrected according to proposed approach and the pattern corrected according to the current formulation of the projection method. For the last three graphs, both numerical and measurement results are shown. From all the three figures it can be seen how the geometrical deformation results in pattern distortion with respect to the planar array: the main lobe is shifted of approximately 10° and its magnitude is reduced of about 1dB; moreover at some frequencies where the planar array has a null, the deformed array has instead a considerably high gain value (e.g., when $\theta_{\text{tilt}} = 15°$ the planar array gain has a zero at $\theta = 45°$, the one of the deformed array is still between 5 dB and 10 dB). The proposed approach is compared to the projection method by noting that it is still effective in retrieving the main radiation feature of the deformed array, i.e. it is able to shift the main lobe back to the desired direction. It is also able to reduce the gain value in correspondence of the nulls of the planar array, even if in this case the projection method performs better. As far as mutual coupling is concerned, this depends on the reciprocal distance and orientation of adjacent elements in the array, and therefore it is expected that it will depend also on the deformation geometry. For instance, if the deformation is such that the main lobes of two adjacent antennas are tilted towards each other (as in the case of elements I and II in Fig. 3.6) a higher coupling is expected (i.e., a higher value of $S_{I,II}$) with respect to the planar array; in a similar way, if the deformation is such that the main lobes of two adjacent antennas are tilted away from each other (as in the case of elements III and IV in Fig. 3.6) a lower value of $S_{I,II}$ with respect to the planar array is expected. The guess is confirmed by the results reported in Fig. 3.11. From this plot, it can be noticed that, in this particular case, the mutual coupling level in the deformed array are similar to those of the undeformed array: this is again as expected since adjacent antennas are not strongly tilted towards/away from each other. Therefore, mutual coupling is negligible in a relative way, i.e. with respect to the planar array, recalling that the goal was not to get low coupling levels, but to get coupling levels similar to the ones of the undeformed array.

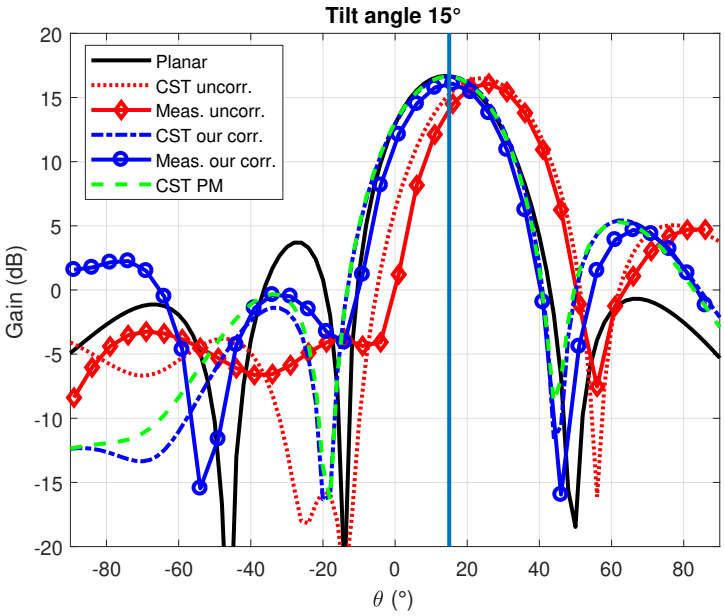

Figure 3.8: Simulated and measured 4×4 antenna gain: planar, uncorrected, corrected with our approach and with the projection method patterns on the $yz-$plane for $\theta_{\text{tilt}} = 15°$.

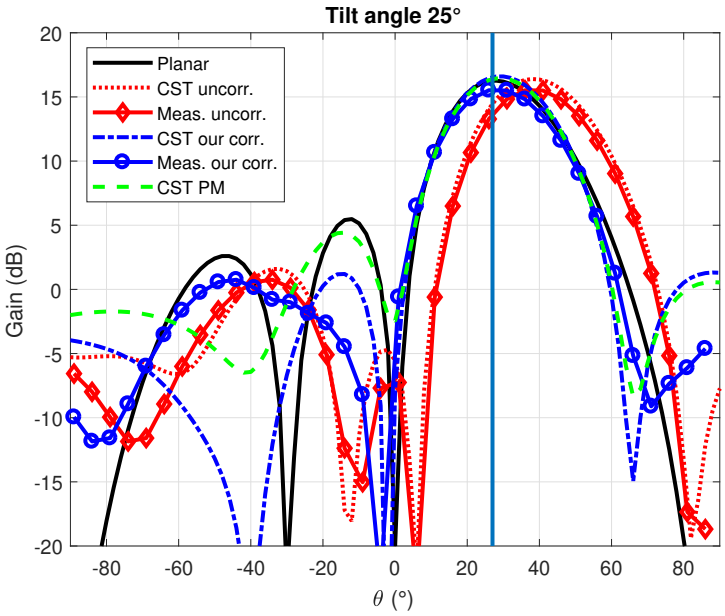

Figure 3.9: Simulated and measured 4×4 antenna gain: planar, uncorrected, corrected with our approach and with the projection method patterns on the $yz-$plane for $\theta_{\text{tilt}} = 25°$.

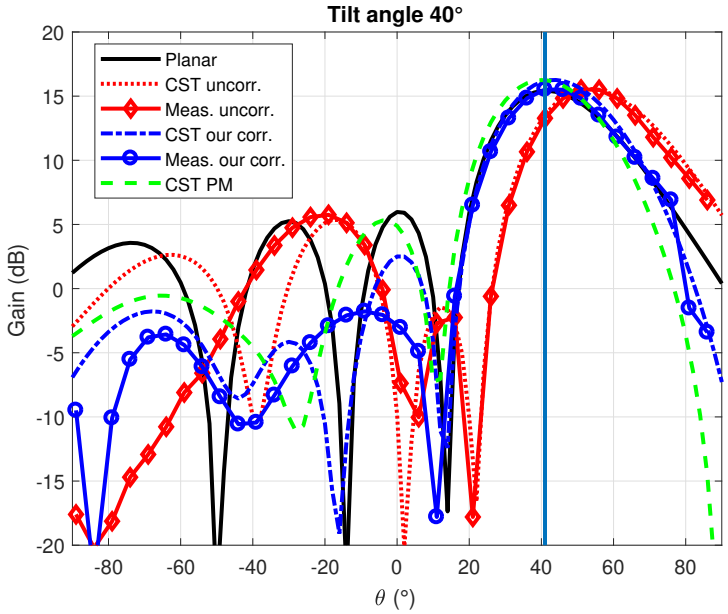

Figure 3.10: Simulated and measured 4×4 antenna gain: planar, uncorrected, corrected with our approach and with the projection method patterns on the $yz-$plane for $\theta_{\text{tilt}} = 40°$.

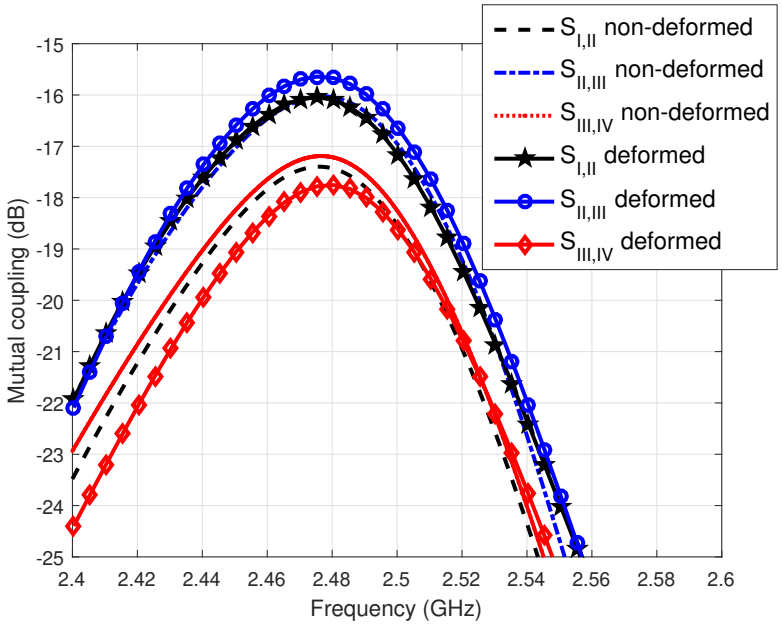

Figure 3.11: Relevant changes in mutual coupling effects after surface deformation of 4×4 array.

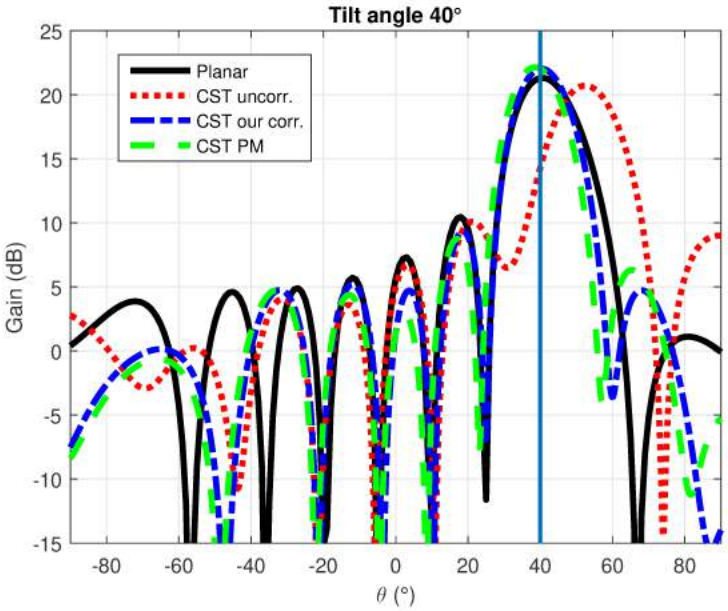

Figure 3.12: Gain pattern of the 8×8 beam steering array in the $yz-$plane.

Figure 3.13: The 8×8 doubly wedge-deformed array.

3.3.4 Projection Method Application to Larger Arrays

The pattern recovery approach is valid also when dealing with larger beam-tilting arrays placed on a deformed surface. This has been proven through full-wave numerical simulations on an 8×8 array, depicted in Fig. 3.13, shaped according to a similar geometry with respect to the one presented in the previous section. When beam-tilting weights are applied to the 64-elements array, the radiation pattern is distorted and the main beam is not tilted towards the desired direction. Therefore the proposed pattern recovery technique was applied to this configuration and compared it with the projection method in order to assess its effectiveness. In Fig. 3.12 the results are reported for the worst case scenario among the three discussed above: this is when the beam is tilted towards 40°. The reference pattern is the one of a planar 8×8 array that steers the beam in the desired direction: it can be seen again how the proposed approach can retrieve the radiation pattern and it is still valid when compared to the projection method

3.4 Phase Sensitivity of the Projection Method for a Beam Tilting Deformed Array

3.4.1 Issues of the Projection Method Implementation

When moving to the experimental validation of the projection method for a given scenario, a principal role is played by the instruments that allow the practical implementation of the system. In fact, equipment costs can variate considerably as the desired precision increases, affecting in this way the overall convenience of the approach: phase shifters are the critical part of the setup, as their market price is strictly connected with the phase step they can provide. The purpose of this work is the analysis of the phase approximation that can be tolerated by the compensations derived with the projection method, in order to optimize the expenses at the moment of purchasing the items. A deformed linear array whose main lobe angle of tilt is progressively increased is considered. The array was modeled in CST environment and a numerical evaluation of the phase sensitivity of the method is provided.

In order to evaluate the phase sensitivity of the projection method, we considered a 1×4 linear array, whose elements are patch microstrip antennas, half-wavelength spaced, resonating at 2.5 GHz. The array is placed on a surface which is subject to an half wedge-like geometrical deformation as depicted in Fig. 3.14: half of the array is rotated of θ_W degrees. As a consequence of the surface deformation, the array radiation pattern is distorted. A schematic of the scenario is depicted in Fig. 3.15. θ_W indicates the angle of the wedge deformation while θ_{tilt} represents the angle of the desired main lobe maximum. $\Phi(\theta_{tilt})$ and Δz_i are, respectively, the phases to be applied to tilt the beam of the linear 1×4 array of θ_{tilt} degrees and the distances that separate each array element from the reference plane. Phase corrections $\Delta\phi_i,\ i = I, \ldots, IV$ to be applied to each antenna, following the projection

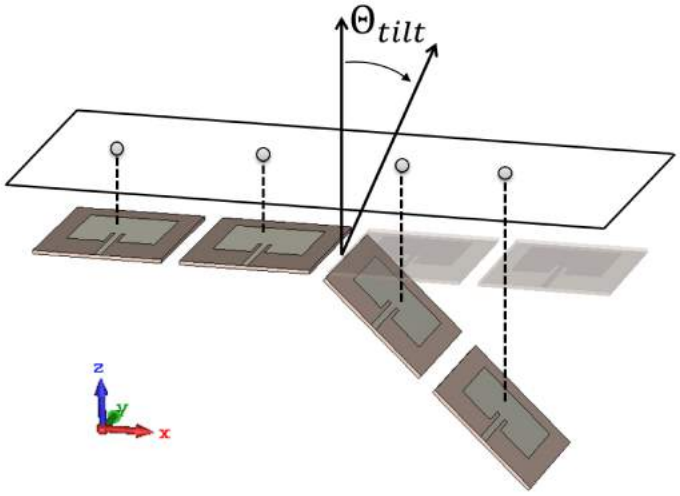

Figure 3.14: Investigated 1×4 array surface deformation.

method as in [12], are computed simply from the parameters describing the surface deformation, i.e. phase shifts are proportional to the distance of the elements from the reference plane:

$$\begin{aligned}
\Delta\phi_I &= k\Delta z_I = 0^\circ \\
\Delta\phi_{II} &= k\Delta z_{II} = 0^\circ \\
\Delta\phi_{III} &= k\Delta z_{III} = k\frac{L}{2}\sin(\theta_W) \\
\Delta\phi_{IV} &= k\Delta z_{IV} = k\frac{3L}{2}\sin(\theta_W)
\end{aligned} \tag{3.9}$$

In the proposed study, in order to simplify the process, we assumed the xy plane as reference. The total phase $\psi_i,\ i = I, \ldots, IV$ to be applied to each antenna element in order to retrieve the main beam of the non-deformed array consists in adding phases calculated in (3.9) to $\Phi_i(\theta_{tilt})$, for $i = I, \ldots, IV$, to obatain:

$$\psi_i(\theta_{tilt}) \quad = \quad \Phi_i(\theta_{tilt}) + \Delta\phi_i \tag{3.10}$$

From a simulation point of view, the exact value of the phase as computed in (3.10) can be imposed to array input signals; however, when moving to a practical implementation of the system, only discrete values of phases can be set. The latter are indeed determined by the resolution of the chosen phase shifter. In order to investigate the phase sensitivity of the projection method within which is still possible to recover the pattern, input phases are approximate to the closest multiple of 5.625°, 11.25° and 22.5° and the respective main lobe gain is evaluated and compared to the one obtained using the exact phase compensating values.

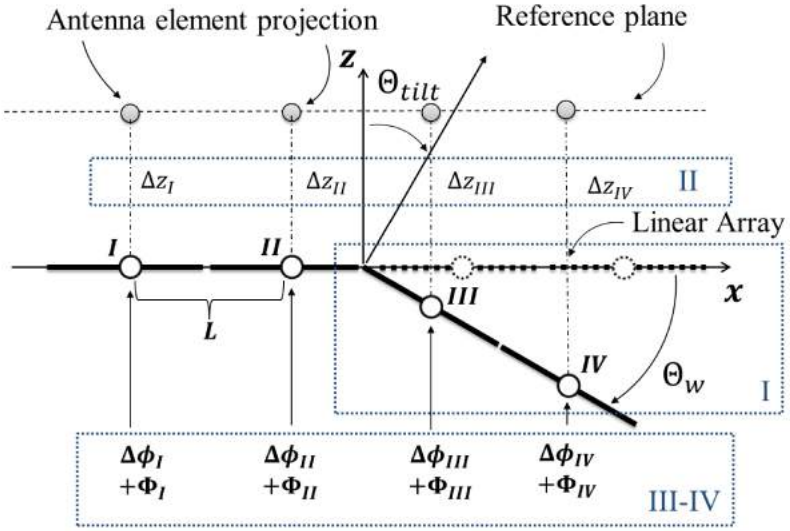

Figure 3.15: Schematic of the projection method application.

3.4.2 Results and Discussion

Table 3.2 shows phase corrections computed following the projection method to be applied for a deformation angle of $\theta_W = 45°$, when the main lobe is tilted up to $\theta_{tilt} = 40°$ with respect to the broadside direction. As stated before, input signal phases ψ_i^{δ} are given by the sum of $\Delta\phi_i$ and Φ_i contributions for each θ_{tilt}. The superscript $\delta(°)$ indicates the approximation made on the phases imposed to array elements, i.e. it represents the desired phase shifter precision. Rows with $\delta = 0°$ indicate the ideal case, where continuum phase values can be applied. Results relative to the latter are assumed as reference for comparison. $\delta = 5.625°$, $11.25°$ and $22.5°$ refer, respectively, to a phase shifter step of 5.625, 11.25, and 22.5 degrees. CST full wave simulations are performed on the deformed array and phases, as reported in Table 3.2, are applied to the $i-$th antenna.

In Fig. 3.17 we can observe a comparison between the gain of the main lobe evaluated with different phase precision δ, for increasing angle of tilt θ_{tilt}. Simulation results show that a phase approximation of $\delta = 22.5°$ is still sufficient to retrieve the gain with the same accuracy of the $\delta = 0°$ case. In fact, for all the considered θ_{tilt}, the distance between points related to different phase shifter precision is almost null for the considered case of study. Moreover, the fact that the main lobe gain of the recovered pattern has not a regular behaviour is explained by simple considerations on the antennas reciprocal orientation, as the elements have themselves a directive pattern.

In detail, Fig. 3.16 shows a comparison between radiation patterns retrieved with different phase tolerance δ and the pattern of the linear array, for $\theta_{tilt} = 40°$. Furthermore, the pattern of the deformed array, when no phase compensation is applied, is plotted in order to appreciate visually the goodness of the method. We can notice that the main lobe is retrieved in amplitude and correctly directed; at the same time side lobe levels are lowered. This holds for any of the considered phase approximations. Again, the geometry of the array and the directivity of the single antenna cause the radiation pattern of the deformed array to have an higher gain with respect to the linear case. Considerations about the reciprocal orientation of the array elements and the relative main lobe recovery are outside the scope of this work, which focuses instead on the analysis of the phase precision needed, assuming in principle the validity of the projection method.

Table 3.2: Compensating phase shifts for $\theta_{tilt} = 40°$

Phase corrections to be applied (°)

$\theta_{tilt} = 40°$	**Array Element**			
	I	II	III	IV
$\delta = 0°$	0	-116	-168	-157
$\delta = 5.625°$	0	-118.25	-168.75	-157.5
$\delta = 11.25°$	0	-112.5	-168.75	-157.5
$\delta = 22.5°$	0	-112.5	-180	-157.5

Numerical results proved that phase shifters with a phase step of 22.5° are sufficient for an accurate implementation of the system. Therefore, the overall cost of the setup can be kept low since an extreme precision, while imposing phase corrections, is not required.

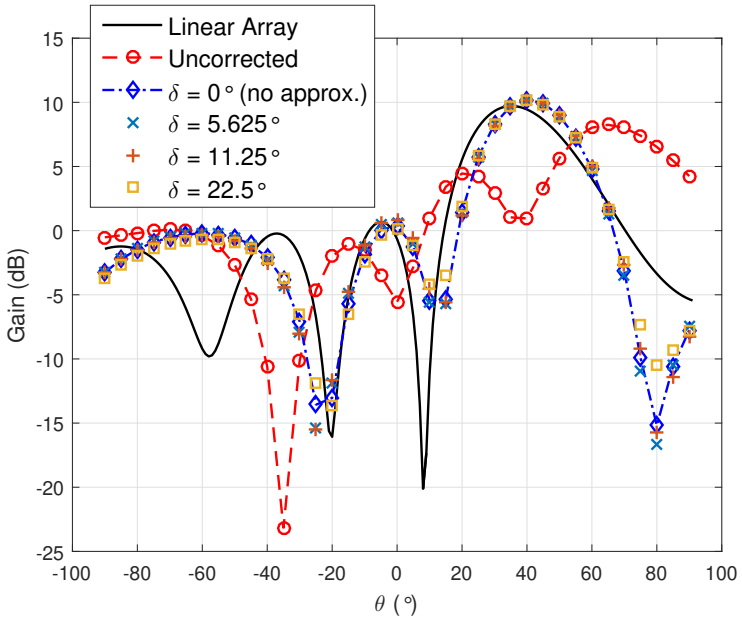

Figure 3.16: Gain pattern comparison in the xz-plane for different phase-shift approximation δ.

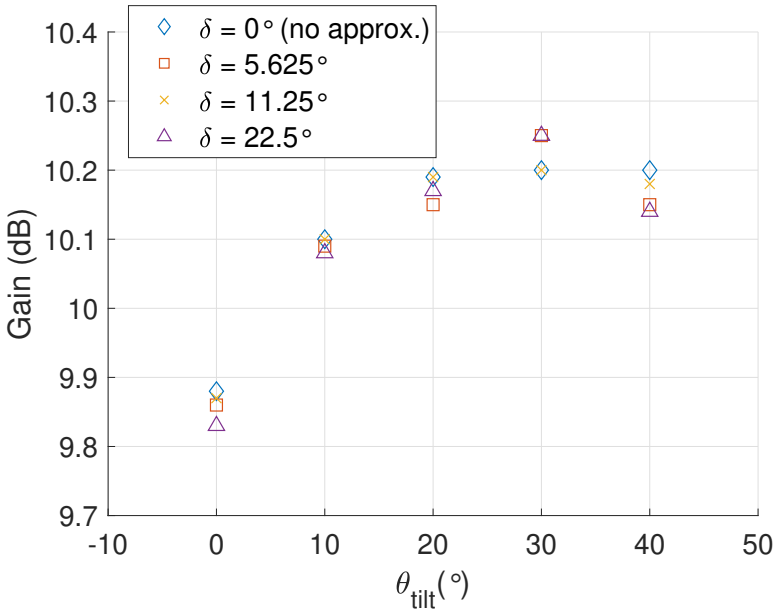

Figure 3.17: Main lobe gain for growing maximum direction θ_{tilt} and phase-shift approximation δ, considering a fixed deformation angle $\theta_W = 45°$.

3.5 Robustness of the Projection Method for an Asymmetrically Deformed Planar Antenna Array

3.5.1 Scenario Description

Following the analysis presented in Section 3.4, a square planar array composed of 16 patch antennas resonating at 2.48 GHz is considered. Each element is fabricated on a Rogers TMM-4 substrate of thickness $t = 1.52$ mm, with the antenna physical dimensions reported in Fig. 3.18. Again, the antenna structure was placed on a surface whose shape can be deformed. The array under investigation is depicted in Fig. 3.19: this kind of deformation is particularly relevant with respect to those analysed in the previous works, as it implies a pattern degradation along both the $\phi = 0°$ (yz)- and the $\phi = 90°$ (xz)-plane. As a consequence of the surface deformation, radiation properties of the array result to be strongly degraded. According to the projection method, pattern distortion is mainly caused by a relative phase change in the signals coming from different elements of the array; with the introduction of a proper phase-shift in some of the elements of the array, radiation pattern distortion can be mitigated.

Parameters controlling the deformation are the wedge angle θ_W, and the radii of curvature of the two cylinders r_1 and r_2. Array rows indicate elements sharing the same y-coordinate and are numbered with an increasing index $i = I, \ldots, IV$. Analogously, array columns indicate elements sharing the same x-coordinate and are numbered with an increasing index $j = I, \ldots, IV$. The surface presents an asymmetrical deformation along the x-axis, given by the juxtaposition of an half wedge- and an half cylindrical-shaped surfaces. Along the y-axis, the array is bent on a cylindrical-shaped surface, giving rise to a remarkably complex geometrical configuration. The conformal array can be seen along the y-axis as a 4×1 linear array bent over a cylindrical surface of radius r_2. Elements composing the array are the rows R_i with $i = I, \ldots, IV$.

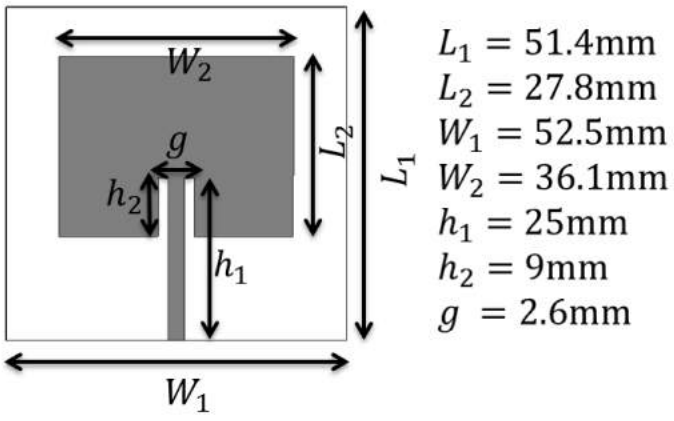

Figure 3.18: Patch antenna with physical dimensions.

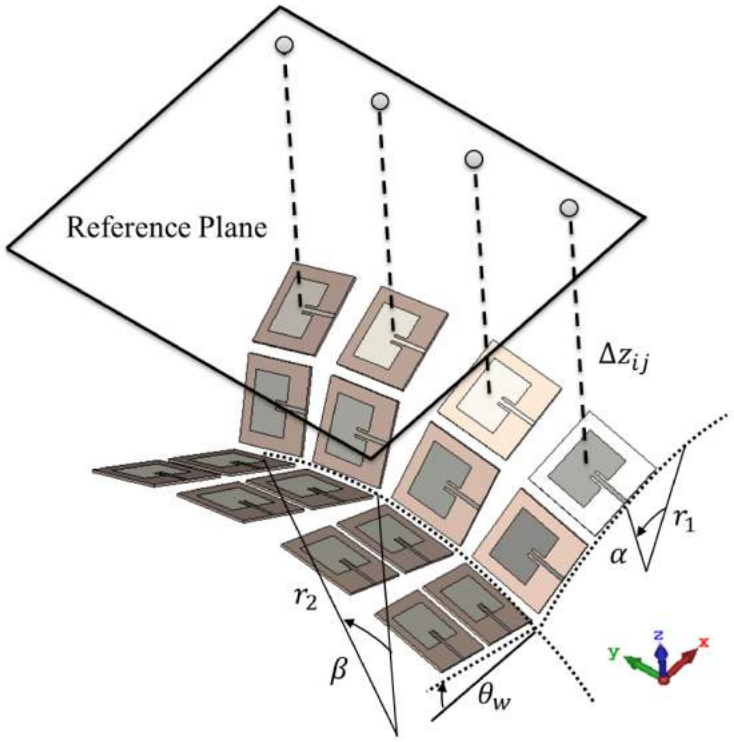

Figure 3.19: Bi-dimensional asymmetrical deformation.

With respect to the configuration represented in Fig. 3.20, equations (3.11) are used to derive the phase-shift to be applied to elements belonging to each array row, in order to recover the original pattern of the flat array.

$$\begin{aligned} \Delta\phi_{R_{I,IV}} &= k \cdot \Delta z_{R_{I,IV}} = k \cdot r_2 \cdot |\sin\beta_{II} - \sin\beta_I| \\ \Delta\phi_{R_{II,III}} &= k \cdot \Delta z_{R_{II,III}} = 0 \end{aligned} \tag{3.11}$$

Each element of the array is an 1×4 array itself, oriented along the x-axis, characterized by an asymmetrical deformation given by the juxtaposition of an half wedge- and an half cylindrical-shaped structure. We refer to the latter as column C_i with $i = I, \ldots, IV$. With respect to the configuration depicted

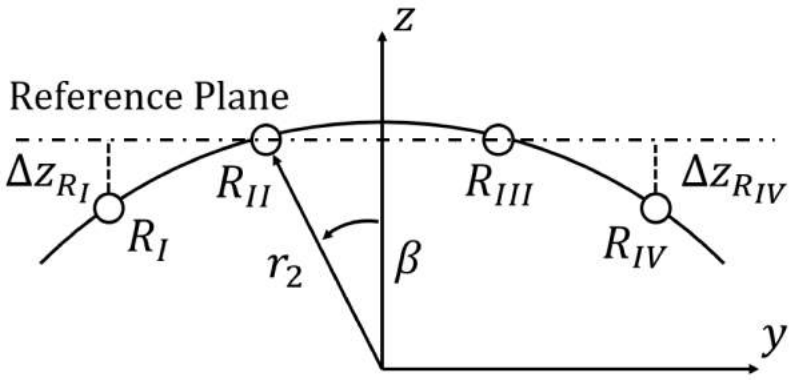

Figure 3.20: The $yz-$ plane cut of the deformed array.

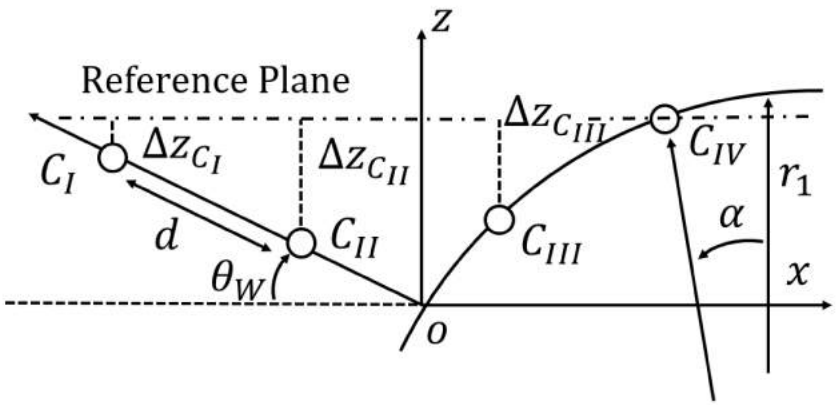

Figure 3.21: The $xz-$ plane cut of the deformed array.

in Fig. 3.21, equations (3.12) are used to evaluate phase shifts required for internal elements of the wedge-shaped part, external elements of the wedge-shaped part and elements on the cylindrical-shaped surface respectively.

$$\begin{aligned}
&\Delta\phi_{C_{IV}} = k \cdot \Delta z_{C_{IV}} = 0 \\
&\Delta\phi_{C_{III}} = k \cdot \Delta z_{C_{III}} = k \cdot r_2 \cdot |\sin\alpha_{IV} - \sin\alpha_I II| \\
&\Delta\phi_{C_{II}} = k \cdot \Delta z_{C_{III}} = k \cdot r_2 \cdot |\sin\alpha_{IV} - \sin\alpha_O| + \frac{1}{2} d \cdot \sin\theta_W \\
&\Delta\phi_{C_I} = k \cdot \Delta z_{C_{III}} = k \cdot r_2 \cdot |\sin\alpha_{IV} - \sin\alpha_O| + \frac{3}{2} d \cdot \sin\theta_W
\end{aligned} \tag{3.12}$$

where the spacing between patch antennas is $d = \lambda/2$. For sake of clearness, configurations depicted in Fig.s 3.20 and 3.21 are just to give an idea of the scenario: proportions and distances do not respect the real-life case.

3.5.2 Robustness Analysis

As the deformation gets more accentuated, limitations of the recovery technique have been evaluated. Afterwards, the phase sensitivity of the projection method has been examined: with the main lobe tilted towards 40° along the xz-plane, the radiation pattern has been retrieved imposing phases values with different precision. Consequently, the accuracy of the equipment needed, i.e., the required phase shifters, can be established.

Main Lobe Gain - Parametrical Study

The projection method has been applied in order to recover the radiation pattern of the deformed antenna array. In this section, the performances of the approach are stressed: the limitations in retrieving the main lobe pattern have been investigated for increasing levels of deformation of the array. Initially, a CST numerical study has been performed, where geometrical parameters controlling the deformation were progressively increased and the correcting phase shifts consequently computed using equations (3.11)-(3.12). The gain

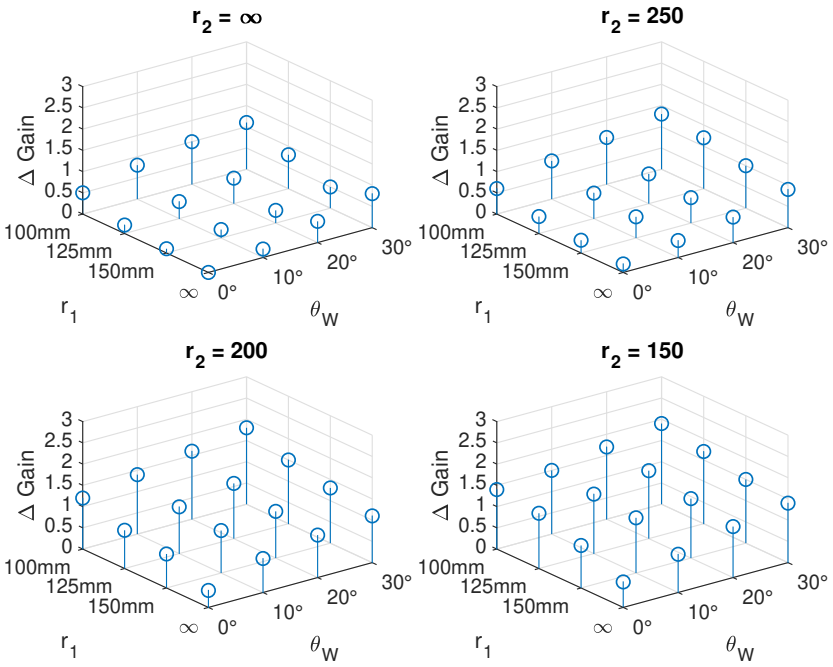

Figure 3.22: Peak gain difference between planar array and conformal array with phase corrections.

of the main lobe has been accordingly evaluated and a threshold has been chosen to define a limit of the projection method effectiveness. Figure 3.22 illustrates the difference between the peak gain of the retrieved pattern with the one of the planar array, i.e., the one we ideally wanted to retrieve, when the main lobe direction is broadside. As the deformation increases, it can be observed how the performances of the projection method are deteriorated; the gain of the antenna attached to the conformal surface drops below the one of the flat array. Parameters controlling the deformation have been swept in the ranges defined in Table 3.4. Further, the planar case ($r_1 = \infty$ and $r_2 = \infty$) was considered. A reasonable threshold value of $\Delta\text{Gain} = 1.5$ dB has been chosen, which corresponds to a deformation defined by $\theta_W = 30°, r_1 = 200$ mm, $r_2 = 125$ mm, as it can be observed in Fig. 3.22. This was set as the limit deformation that can be recovered using the projection method for the considered configuration.

Phase Sensitivity Analysis

When moving to a practical implementation of the projection method, phase corrections as derived from equations (3.11)-(3.12) cannot be applied with the same degree of precision of a simulation scenario. In fact, depending on the phase shifter used in a real-life system, a certain degree of approximation should be assumed. Therefore, the resolution of the phase shifter may influence the effectiveness of the method. For example, if digital phase shifters are used in the setup under consideration, only discrete phase steps are allowed.

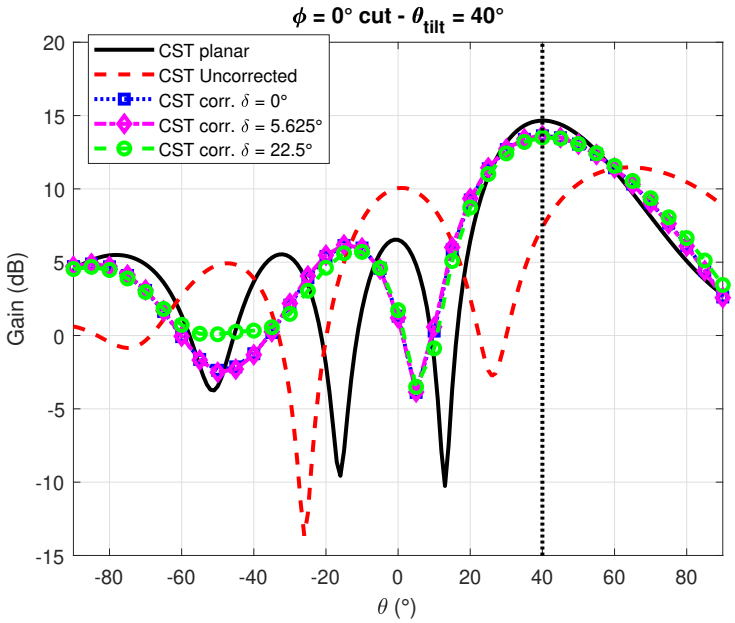

Figure 3.23: Gain pattern of the array retrieved for different phase shifter precision.

In this section, a numerical analysis supported by CST simulations is carried out in order to study the phase sensitivity of the projection method for different approximations of the correcting phase shifts. A comparison between the retrieved pattern with different precision induced phases is shown. An evaluation in this regard is believed to be necessary since the equipment costs can vary dramatically as the desired precision increases, affecting in this way the overall convenience of the method. The surface deformation obtained in Section 3.5.1 was maintained while the main lobe direction was tilted towards $\theta = 40°$ in the xz-plane. As stated in [11], in order to retrieve the pattern, it is sufficient to add to the phases imposed to steer the beam, the compensation phases for the broadside configuration. CST simulations have been performed using phase shifts described in Table 3.3. The superscript $\delta(°)$ indicates the rounding made on the phase impressed to array elements with respect to its exact value as derived by the previous analysis. Rows with $\delta = 0°$ indicate the ideal case, where continuum values can be applied, which is assumed as reference for comparison. $\delta = 5.625°$ and $\delta = 22.5°$ refer, respectively, to phase steps of 6-bit or 4-bit digital phase shifters. Results are depicted in Fig. 3.23. Marked lines represent radiation patterns retrieved with different phase precision δ. In order to visually appreciate the effectiveness of the method, the red dashed line shows the simulated radiation pattern of the deformed array while the black solid line is the gain of the planar array (i.e., the one we ideally want to recover). We can conclude that any of the considered phase precision allows to recover the pattern with a good degree of accuracy. In fact, main lobe direction and gain are successfully recovered. At the same time the side lobe levels are substantially lowered and only small differences can be noticed between patterns retrieved with different δ.

3.5.3 Experimental Validation

A prototype of the array was manufactured and placed on a deformable surface; a picture of the experimental setup is shown in Fig. 3.25. The patch antenna element is resonating at 2.48 GHz: a comparison between the simulated and measured reflection coefficient is shown in Fig. 3.24. The maximum surface deformation obtained after the numerical analysis is shown on the right-hand side of the picture. In order to control the input phase of each patch antenna, a network of phase shifters was connected to it. Accordingly with the study taken in the previous section, phase shifter steps of $\delta = 22.5°$ have been used for the experimental validation of the method. Figures 3.26 and 3.27 show the radiation pattern for the broadside case in the yz- and xz-planes, before and after the phase correction. A comparison with the radiation pattern of the initial planar array can be evaluated. Simulated and measured results are plotted respectively with solid/dashed and marked lines. Dashed red lines represent the radiation pattern of the deformed array. A substantial improvement can be appreciated when the correcting phase shifts are applied (blue lines): the main lobe gain figure is retrieved and the broadside direction is restored. At the same time, side lobe levels are lowered and nulls around $\theta = \pm 30°$ are re-established as well as the half-power bandwidth (HPBW). Furthermore, an experimental validation for the beam steering case is shown in Fig. 3.28. The red dashed lines show the distortion induced on the gain pattern when the array was deformed and the main lobe had been tilted of $\theta_{tilt} = 40°$. The blue lines represent the retrieved radiation pattern. A substantial mitigation of the distortion effects can be observed by comparing the latter to the black lines showing the radiation pattern of the planar, undeformed array. Measurements confirmed simulation results and proved the overall effectiveness of the method.

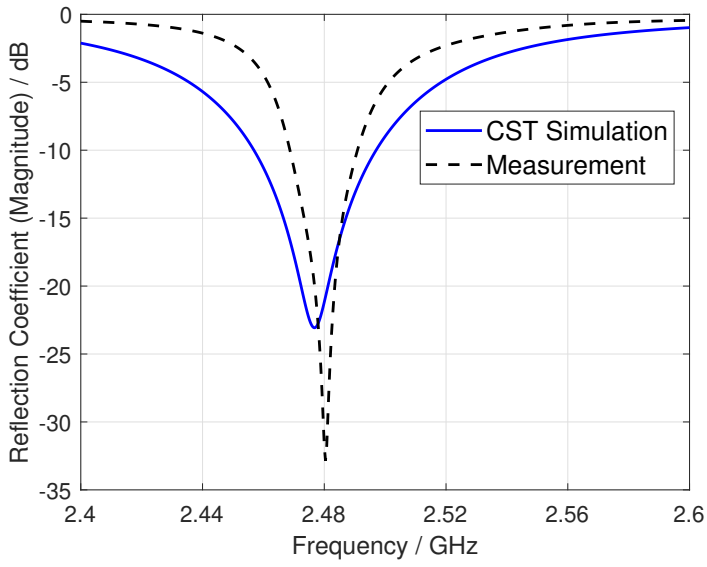

Figure 3.24: Reflection coefficient of the patch antenna element.

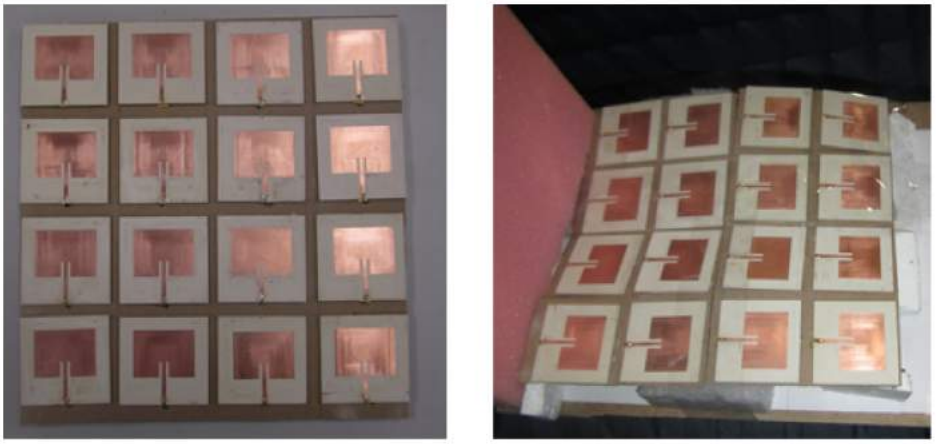

Figure 3.25: Fabricated prototype in planar configuration and deformed configuration.

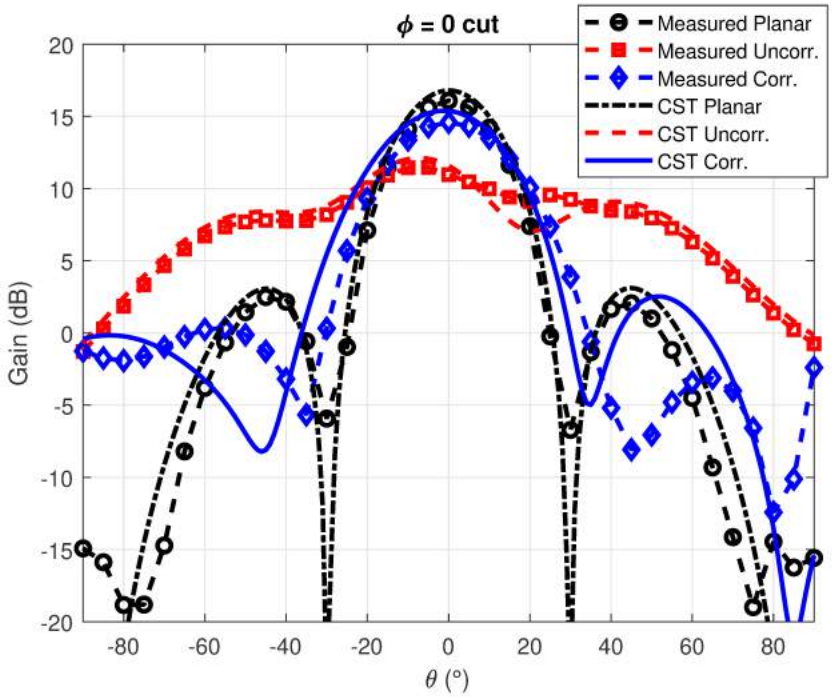

Figure 3.26: Gain pattern of the array in the $yz-$plane.

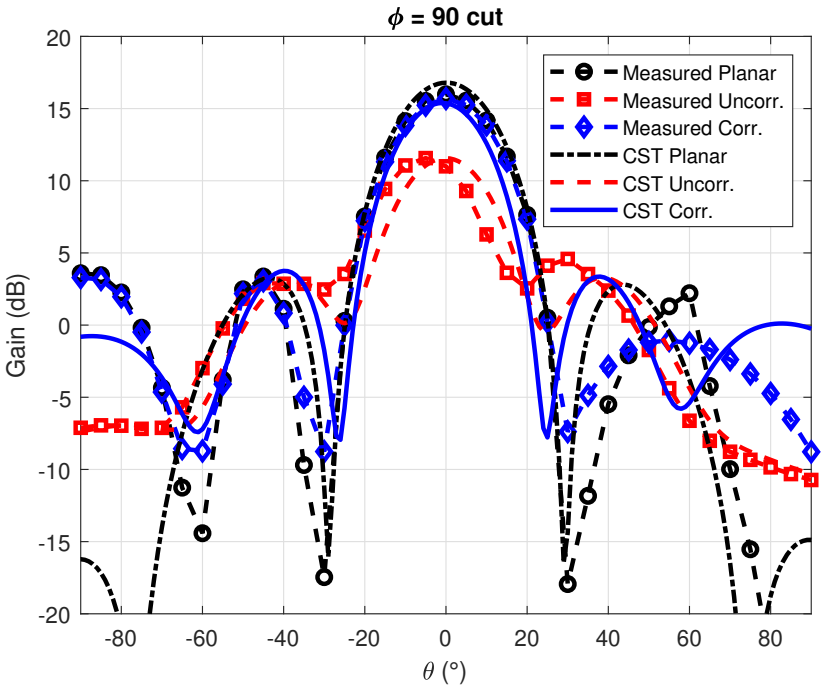

Figure 3.27: Gain pattern of the array in the $xz-$plane.

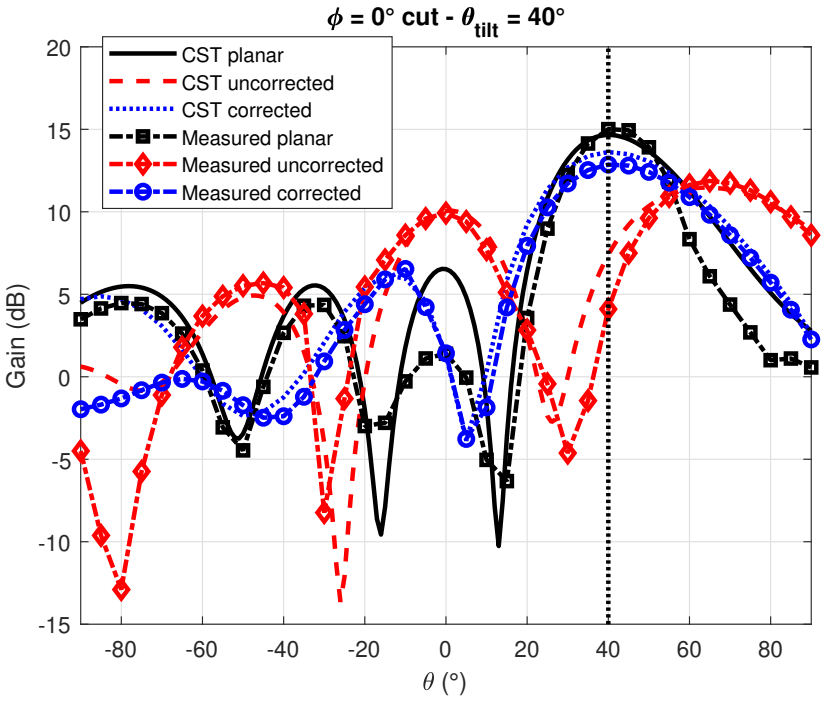

Figure 3.28: Gain pattern of the beam steering array in the $yz-$plane.

Table 3.3: Compensating phase shifts for resolution $\delta = 0°$, $\delta = 5.625°$ and $\delta = 22.5°$.

		Phase Compensation $\Delta\phi_{ij}$				
Phase Shifter Resolution	$\delta = 0°$	i, j	**I**	**II**	**III**	**IV**
		I	102.21°	186.78°	159.81°	54.78°
		II	49.71°	138.36°	110.07°	0°
		III	49.71°	138.36°	110.07°	0°
		IV	102.21°	186.78°	159.81°	54.78°
	$\delta = 5.625°$	i, j	**I**	**II**	**III**	**IV**
		I	101.25°	185.625°	157.5°	56.25°
		II	50.625°	140.625°	112.5°	0°
		III	50.625°	140.625°	112.5°	0°
		IV	101.25°	185.625°	157.5°	56.25°
	$\delta = 22.5°$	i, j	**I**	**II**	**III**	**IV**
		I	112.5°	180°	157.5°	45°
		II	45°	135°	112.5°	0°
		III	45°	135°	112.5°	0°
		IV	112.5°	180°	157.5°	45°

Table 3.4: Parameters describing the conformal surface.

θ_W	r_1	r_2
$0° - 30°$	150mm − 100mm	250mm − 150mm

3.6 Conclusion

The research presented in this chapter was intended to propose a simplification of the projection method in order to retrieve efficiently the radiation pattern of beam-tilting antennas. Since the projection method requires that the phase-shifts are functions of both the deformation geometry and the main lobe direction, an analytical formulation would be required for every geometrical deformation and for every steering angle. This introduces a further processing step and complicates the overall system. The proposed approach, instead, expresses the computation of the phase-shifts as the sum of two components. The first one, is responsible for deformation compensation while the second one tilts the beam of the planar array towards the desired direction. The first term can be directly linked to the data acquired by simple sensors that measure surface deformation and the second one can be computed according to basic antenna theory. Therefore, analytical expressions are not required anymore. Full-wave numerical simulations and measurements proved the approach effectiveness in retrieving the radiation properties of a deformed array, providing a straightforward and cheap pattern recovery technique suitable for simple low-cost systems.

Furthermore, the effectiveness of the projection method technique has been analyzed with respect to two metrics: the level of surface deformation that affects the antenna array and the precision of the phase-shifters that are used to implement the phase compensations. A limit on the surface deformation that the projection method can effectively compensate can be established: the threshold was set in such a way that the peak gain of the retrieved pattern does not drop below 1.5 dB with respect to the pattern of the planar array. Finally, the required precision of the phase shifters used for a practical implementation of the correction technique has been evaluated. A 4-bit digital phase shifter can be used effectively, thus maintaining the overall setup cost low. For the deformation considered as case of study, experimental results have confirmed the suitability of the method in retrieving the radiation pattern both for a broadside and a 40° tilted beam, even considering a considerable phase shifts approximation.

3.6.1 Future Work

An exhaustive research has already been conducted on the topic introduced in this Chapter. However, some open issues have remained, such as the overall system miniaturization and the mathematical formulation of the computational complexity of the developed algorithms. Furthermore, the antenna design can be moved from rigid to flexible substrates, in order to allow the implementation of wearable technologies adopting the proposed beam-recovery technique.

Chapter 4

Wireless Powering of Sensing Devices Positioned Over an Induction Hob

4.1 Introduction

The second RF application for electric appliances investigated in this thesis work regarded a wireless system for transferring power to sensing devices placed over an induction hob. The sensors are designed to be positioned on the pots and the data collected is delivered to the network using a connectivity module embedded in the same smart device. The devices are battery-less, and therefore, the power had to be delivered from the underlying hob through a wireless system. A picture of the configuration is shown in Fig. 4.1.

Three types of wireless power transfer (WPT) exist:

- Radiative transfer [44], [45]: microwave power transfer has usually a very low efficiency as the majority of radiation is wasted into free space. Highly directional antennas can be used to improve the efficiency, but an uninterrupted line-of-sight is required.

Figure 4.1: Wireless power transfer configuration: receiver antenna.

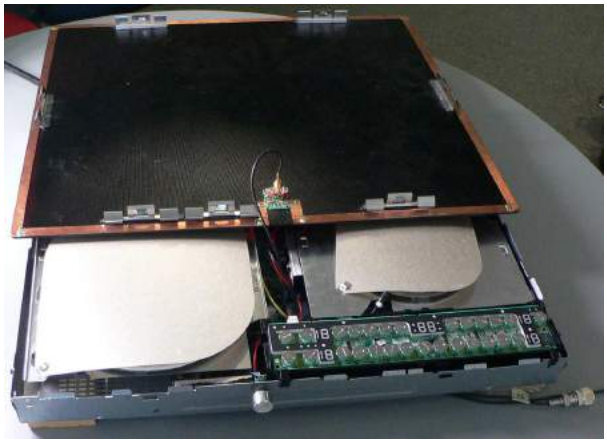

Figure 4.2: Wireless power transfer configuration: transmitter antenna.

- Inductive coupling [46]-[48]: this technique is characterized by a high efficiency but a very short range.
- Resonant coupling: for the first time in [49], authors proposed WiTricity, a mid-range WPT technology that exploits electromagnetic resonant coupling.

Magnetic resonant coupling allows power to be transmitted between two antennas at the resonance frequency. [50]-[52]. An exhaustive literature can be found on resonant circuits for wireless transmission and several solutions are deeply investigated for parallel and series configurations [53]-[55] and for hybrid solutions [56], [57]. The efficiency of the link can be improved using impedance matching techniques, both at the transmitter and at the receiver side [58], [59].

In a wireless power transfer (WPT) system, a transmitter antenna, driven by electric power from a power source, generates a time-varying electromagnetic field, which transmits power across space to a receiver device that extracts power from the field and supplies it to an electrical load. The term antenna is used loosely here, as the electromagnetic resonance coupling involves creating a resonance and transferring the power with electromagnetic inductive coupling without radiating electromagnetic waves.

In this regards, it clearly appears that the development of an electromagnetic model of the WPT system has to follow a different approach [60], [61] with respect to the one used in Chapter 2 for the smart oven . The focus is concentrated on the near field distribution and on the coupling properties of inductive coils, whereas the far field characterization loses interest in this context. Furthermore, the full-wave simulation of the physical configuration has to be followed by a significant study of the matching and resonating circuits to be connected to the antennas, which practically allow the wireless power transfer. WPT systems can be studied using equivalent circuit representations [62]-[64] or the coupled mode theory [65]. Electromagnetic modeling software like CST allows the results coming from a full-wave simulation to be extracted and used as part of a schematic circuit [66], in order to obtain

together the geometry of the physical system components and the possibility of a quick circuital analysis.

Simple design of antennas operating at 13.56 GHz can be adopted for consumer devices, both at the transmitter [67], [68] and at the receiver side [69], as loops and coils in printed technology [70] are nowadays successfully adopted as antenna components for WPT systems. The WPT system designed for the application investigated in this Chapter considered a large rectangular coil as transmitting antenna, see Fig. 4.2 and a four-turn spiral coil as tag. The evaluation of the transfer efficiency as well as the field levels to which the user is exposed is done by simulating the ad-hoc developed model. A measurement campaign was eventually performed, in order to validate the models with experimental results.

4.1.1 Theory Review for Antenna Coil Design

A brief review of the basic theory for antenna coil design [71] is presented in this Section. According to Ampere's law, the magnetic field produced by a current element, see Fig. 4.3, on a round conductor of finite length can be expressed as:

$$B = \frac{\mu_0 I}{4\pi r}\Delta L = \frac{\mu_0 I}{4\pi r}(\cos\alpha_2 - \cos\alpha_1) \tag{4.1}$$

where:

I = current intensity

r = distance from the center wire

The magnetic field originated by a circular loop antenna as in Fig. 4.3 is given by:

$$B = \frac{\mu_0 I N a^2}{2(a^2 + r^2)^{3/2}} \tag{4.2}$$

where:

a = radius of loop

r = distance from the loop center

It can be noticed from Eq. 4.2, that the field intensity decreases with $1/r^3$.

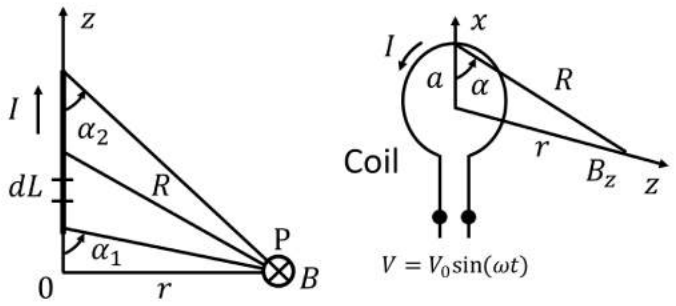

Figure 4.3: Schematic of currents and magnetic fields for conducting wires and loops.

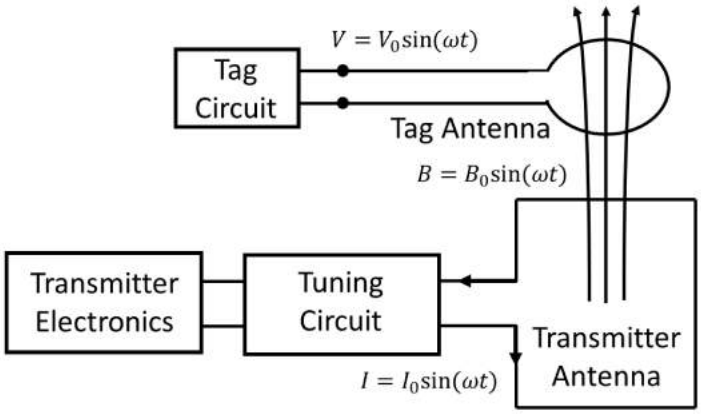

Figure 4.4: Schematic of a transmitter and tag antennas configuration for WPT.

4.1.2 WPT System Schematic

The representation of a basic configuration of reader and tag antennas, i.e. respectively the transmitter and the receiver for WPT applications, is given in Fig. 4.4. Faraday's law states that the time-varying magnetic field B generated by the transmitter antenna coil induces a voltage in the tag, that, in turn, originates a flow of current on the coil. The induced voltage is given by the formula:

$$V = -N\frac{d\Psi}{dt} \tag{4.3}$$

where:

N = number of coil turns
Ψ = magnetic flux through each turn

The minus sign indicates that the direction of the induced current is such that the consequently magnetic field generated is opposite to the original magnetic field. The magnetic flux is expressed as:

$$\Psi = \int B \cdot dS \tag{4.4}$$

where:

B = magnetic field
S = coil area
$\cdot$ = inner product

The inner product in 4.4 indicates that the maximum magnetic flux is obtained when the transmitter and the receiver are positioned parallel to each other.

4.2 Transmitter Antenna Modeling

The transmitter antenna consists in a rectangular copper tape positioned on the bottom surface of the hob upper glass. The coil is connected to the power source around the midpoint of the hob longer side. At the beginning, the copper tape alone was modelled in CST; the antenna, together with the hob structure, is depicted in Fig. 4.5. A simulation was run and the values of the complex impedance at the coil terminals were extracted at the WPT operating frequency f_{WPT} = 13.56 MHz. Afterwards, the hob components were progressively added to the model: first, the glass on which the tape is attached and secondly the whole induction hob structure. The complex impedance was computed and the coil parameters R and L were extracted. Fig.s 4.6 and 4.7 show the different resistance and inductance values at the operating frequency while adding more complexity to the simulation.

An equivalent circuit model may consequently be developed. Fig. 4.8 shows the phase of the input complex impedance of the transmitter antenna. The phase value is close to 90°; therefore, the behavior of the coil is purely inductive at f_{WPT} = 13.56 MHz and the physical structure of the antenna can be modeled as a series of a resistance and an inductance taking values extracted from the 3D simulation. The equivalent circuit for the transmitting coil is represented in Fig. 4.9, and is given by a series of a resistance and an inductance connected to an AC signal source. If the copper tape alone is considered, a formulation for expressing the inductance of the rectangular loop composed of a thin plate element is given by [72]:

$$L = 4\left\{ l_b \ln\left(\frac{2A}{a(l_b + l_c)}\right) + l_a \ln\left(\frac{2A}{a(l_a + l_c)}\right) + 2\left[a + l_c - (l_a + l_b)\right] \right\} \quad (4.5)$$

where:

$$\begin{aligned} A &= l_a \times l_b \\ l_c &= \sqrt{l_a^2 + l_b^2} \end{aligned} \quad (4.6)$$

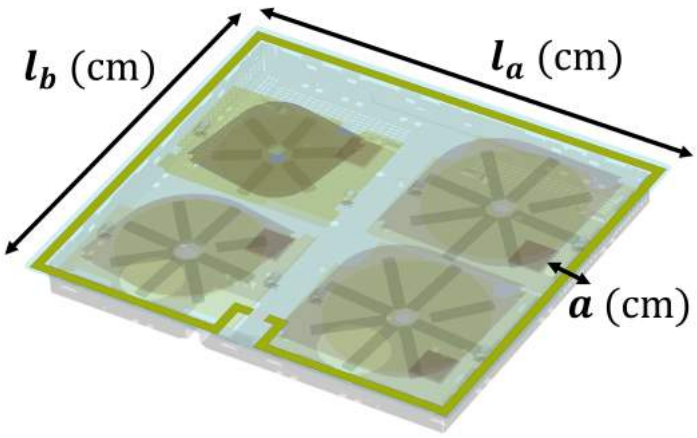

Figure 4.5: Transmitter antenna modeled in CST.

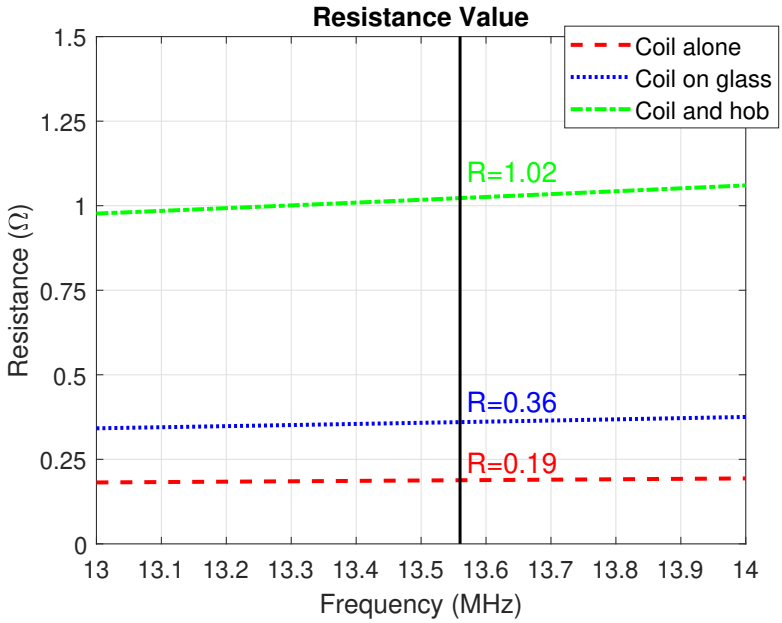

Figure 4.6: Resistance values at the transmitter terminals for increasing model detail.

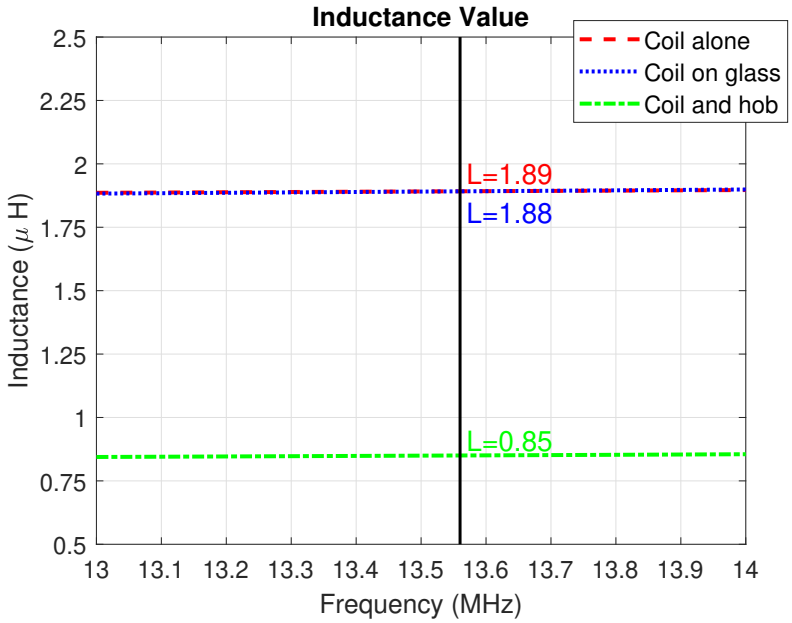

Figure 4.7: Inductance values at the transmitter terminals for increasing model detail.

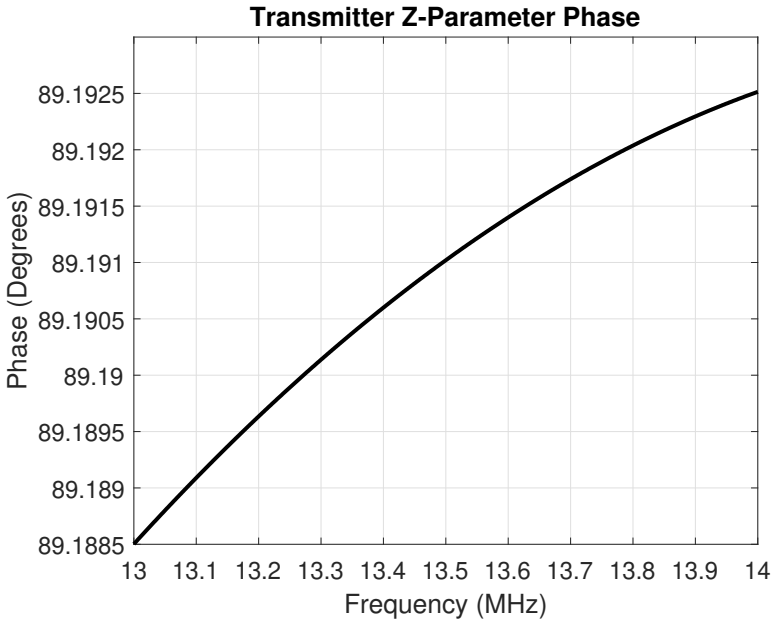

Figure 4.8: Phase of the simulated complex impedance observable at the transmitter antenna terminals. The value close to 90° confirms the inductive behavior.

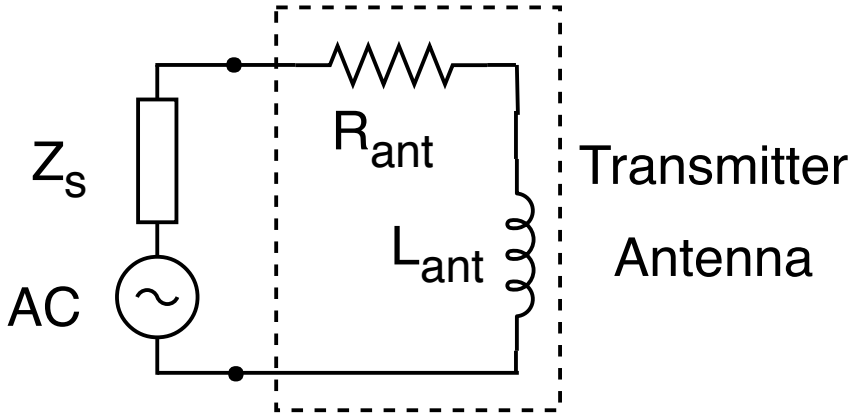

Figure 4.9: Equivalent circuit of the transmitting antenna connected to the power source.

4.2.1 Matching Circuit

The efficiency of a power transfer system can be improved by using impedance matching techniques. The resonance frequency of the transmitter antenna can be tuned to the desired value by designing a proper network [68]. A capacitance matching network was implemented for the considered transmitting system, according to [68]. A schematic of the capacitor matching circuit, to be placed in between the power source and the radiating element, is shown in Fig. 4.10.

The capacitive matching considered in this work is particularly critical when considering large antennas where only small pF capacitance values are required for matching. Small changes in capacitance can make large differences to the matching, so it is easy to miss the window when using trial and error methods. The values of L_{ant} and R_{ant} extracted form CST simulation were used to model the transmitter input impedance. The capacitance C_{tot} required to obtain resonance at $f_{res} = 13.56$ MHz is derived as:

$$C_{tot} = \frac{1}{\omega^2 L_{ant}} \tag{4.7}$$

where

$$\omega = 2\pi f_{res} \tag{4.8}$$

The performance of an antenna is related to its Quality (Q) factor. For a circuit as in Fig. 4.11 this is given by:

$$Q = \frac{R_{ant}}{2\pi f L_{ant}} \tag{4.9}$$

The total input resistance of the antenna is computed setting a required value of Q.

$$R_{par} = 2\pi f L_{ant} Q \tag{4.10}$$

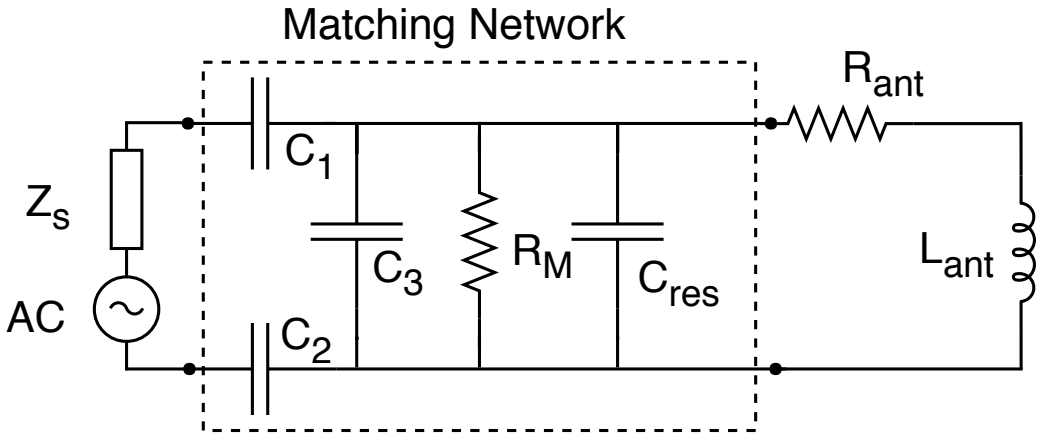

Figure 4.10: Equivalent circuit representation of the transmitting antenna with the matching network implemented.

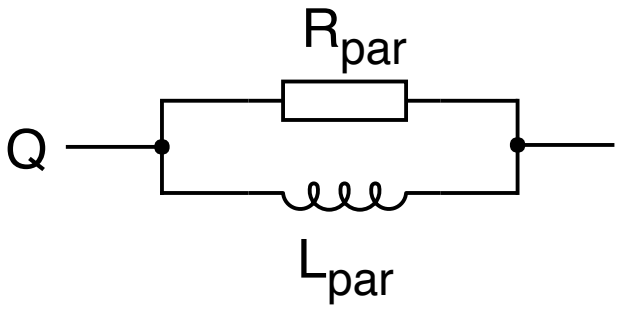

Figure 4.11: Q-factor schematic for an inductive coil.

For the case under analysis, R_{par} is given by the parallel of R_M and $R_{p,ant}$ where $R_{p,ant}$ is obtained from the equivalent parallel circuit of transmitter antenna and R_M is the resistor to be used in the matching network design. Consequently, the required resistance R_M can be obtained using the following formula:

$$\frac{1}{R_M} = \frac{1}{R_{par}} - \frac{1}{R_{par,ant}} \tag{4.11}$$

In general, the higher the Q, the higher the power output for a given antenna. On the other hand, a too high Q may conflict with the band-pass characteristics of the transmitter. For these reasons Q is chosen to be 20 or less. From C_{tot}, C_3 can be computed:

$$C_3 = C_{tot}\sqrt{\frac{R_{par}}{Z_{in}}} \tag{4.12}$$

and C_{T12} from

$$C_{T12} = \frac{1}{\frac{1}{C_{tot}} - \frac{1}{C_3}} \tag{4.13}$$

Finally, the value of C_{T12} is doubled and added to both sides, so:

$$C_1 = 2 \cdot C_{T12} \tag{4.14}$$

and

$$C_2 = 2 \cdot C_{T12} \tag{4.15}$$

Referring to Fig. 4.10, the capacitor C_{res} can be used to modify the reactance of the original design in order to achieve the desired resonance frequency, when some undesired detuning effect occurs. For example, when the receiver is placed over the hob, the mutual inductance between the two coils has to be considered, thus changing the impedance seen at the terminals of the transmitter antenna. This effect will be depicted in Fig. 4.36 in Section 4.5.2.

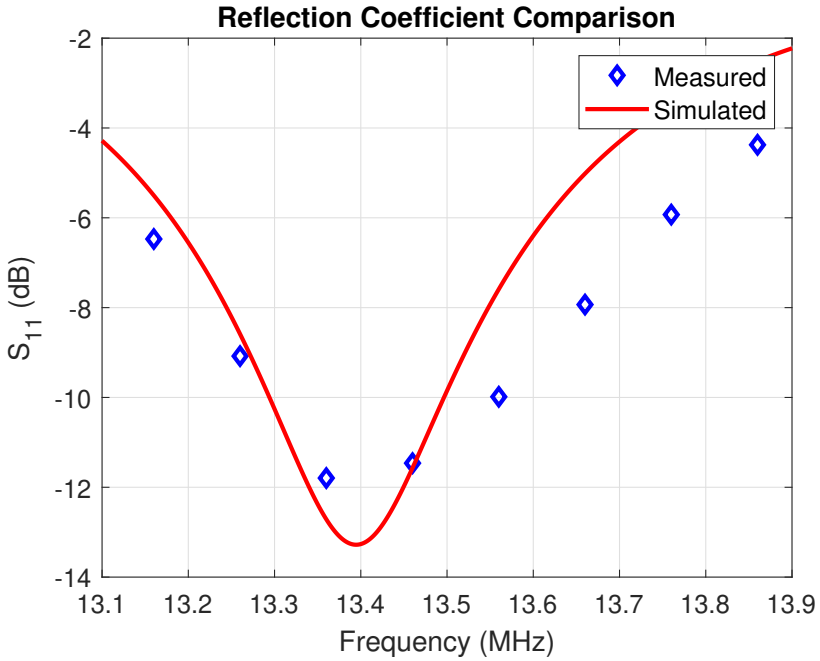

Figure 4.12: Simulated and measured return loss curves for the transmitting antenna.

4.2.2 Transmitter Antenna Reflection Coefficient

The matching circuit was implemented at the copper coil terminals and the reflection coefficient was measured using an impedance analyzer that spanned in the frequency interval $[13.16 - 13.86]$ MHz. Later, the same matching network was implemented in CST. In order to do so, the 3D simulation block was attached to a schematic circuit which was not included physically in the full wave simulation, thus allowing an easy reconfigurability for the simulation phase.

Reflection coefficient curves are displayed in Fig. 4.12. The comparison between simulation and measurement shows a good agreement between the curves, and the capacitance values of the matching network in CST were slightly re-tuned according to the analysis. From the plots, we can observe that the center frequency is around 13.40 MHz, but an acceptable return loss value of -10 dB is still present at 13.56 MHz, which is the WPT operating frequency. The shift of the operating frequency is motivated by the fact that, in the practical scenario implemented, capacitance values were subject to the availability of the components. The design presented fulfills the specification requirements regardless.

4.3 Electromagnetic Radiation Evaluation

When designing RF systems for electric appliances, it is fundamental to control the levels of electromagnetic radiation to which the users are exposed. In this regards, we are interested in evaluating the intensity of the radiated electric and magnetic field in the surroundings of the transmitting antenna. A CST simulation of the transmitting coil, including the matching circuit components, is run, and the oscillating fields at $f_{res} = 13.56$ MHz are evaluated. The considered schematic is shown in Fig. 4.16: a circuit is attached to the 3D results obtained by the full-wave simulations, and the radiation obtained considering the matching circuit can be straightforwardly obtained. A view of the 3D distribution of the magnetic field in the CST environment is shown in Fig. 4.13.

4.3.1 Radiated Field Measurement Campaign

A measurement campaign was conducted in the Electrolux facilities, in order to evaluate the intensity of the magnetic and electric field generated by the transmitting coil in the surrounding space. The source was connected to the output of a signal generator in series with a power amplifier. The input power was fixed, $P_{in} = 2$ W at $f = 13.56$ MHz, while a ROS-meter was used to have an indication of the reflected power, see Fig. 4.15. It should be noted that all the power and field intensity values reported in this chapter refer to peak values. A schematic of the setup is shown in Fig. 4.14. A triaxial probe was used to measure the intensity of the EM field at $f = 13.56$ MHz. The physical dimensions of the probe ($9\text{ cm} \times 9\text{ cm} \times 9\text{ cm}$) are not negligible when performing measurements close to the hob structure. In fact, it was observed that values shown by the probe are strongly sensitive to small misalignment or rotation when considering areas close to the hob surface (i.e. where the field is rapidly varying). Therefore, accurate results are observable mainly in spatial regions that are not critical with respect to the field distribution.

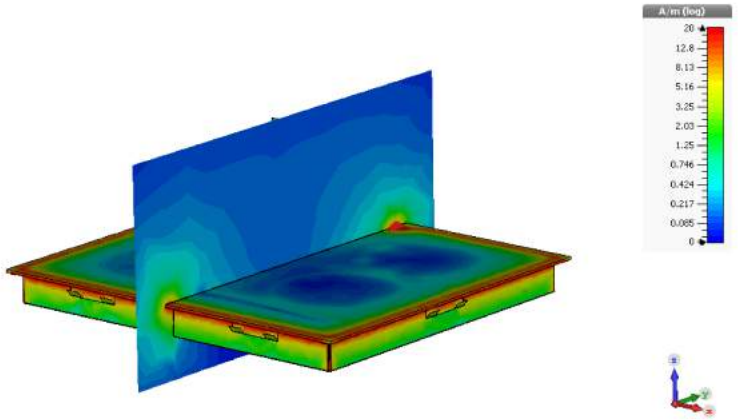

Figure 4.13: Oscillating magnetic field at $f_{res} = 13.56$ MHz in the hob surroundings.

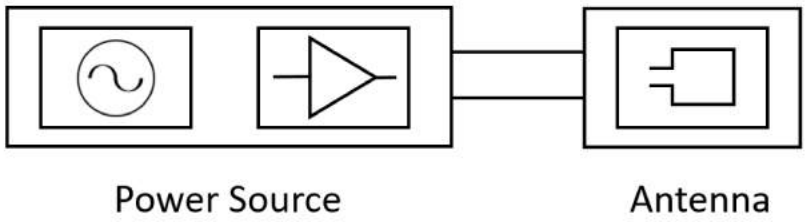

Figure 4.14: Power source schematic.

4.3.2 Electromagnetic Field Around the Hob

First, the field intensity was evaluated in correspondence of four points 30 cm apart from the hob border, for different heights. The points correspond to the midpoint of the hob glass edges. Referring to Fig. 4.22, in this chapter the field distribution was analyzed in P_B and P_C, which are respectively the midpoint of the shorter and the longer hob dimension.

Figures 4.18-4.21 show the E- and H-field behaviour for varying heights. The intensity maximum is found for height = 0 mm, which corresponds to the plane containing the transmitting coil. When the point of observation is moved away from that plane, the field intensity decreases similarly both along the positive and the negative direction of the vertical axis. A picture of the experimental setup is shown in Fig. 4.17. The probe was moved around the hob and the field intensity was measured at three different heights: height = 0, -500, 1000 mm. The measured results are reported in Fig.s 4.18-4.21; a good agreement with simulations can be observed. In detail, for the points measured above the hob plane the comparison with simulations gives more accurate results with respect to the points taken along the negative axis direction. A reason for this discrepancy can be found in the measurement setup; in fact, when measuring the lower points, the probe is brought very close to a table whose presence can affect, even if in a marginal way, the field distribution.

Figure 4.15: Power source picture.

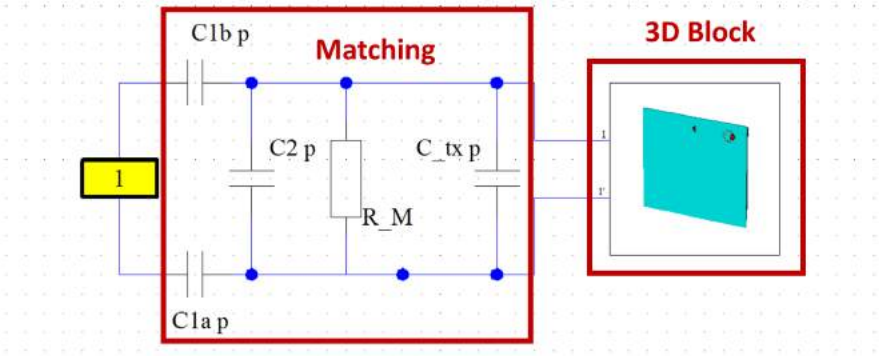

Figure 4.16: CST scenario of the transmitter antenna with the schematic matching network implemented.

Figure 4.17: Measurement setup for oscillating EM fields around the hob.

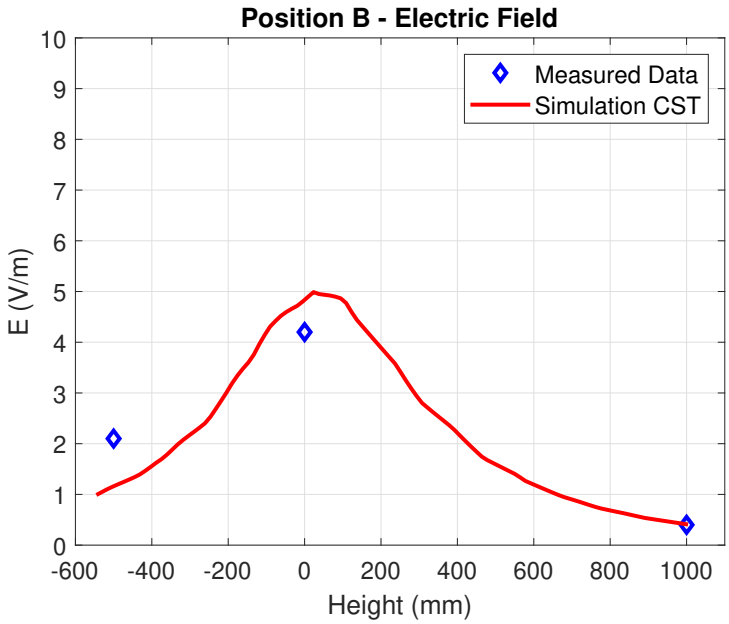

Figure 4.18: Electric field distribution 30 cm apart from the hob side.

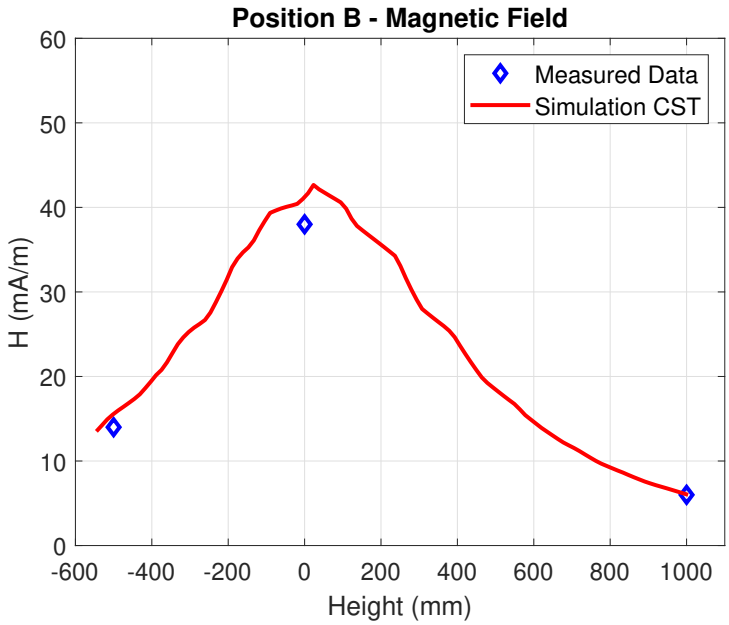

Figure 4.19: Magnetic field distribution 30 cm apart from the hob side.

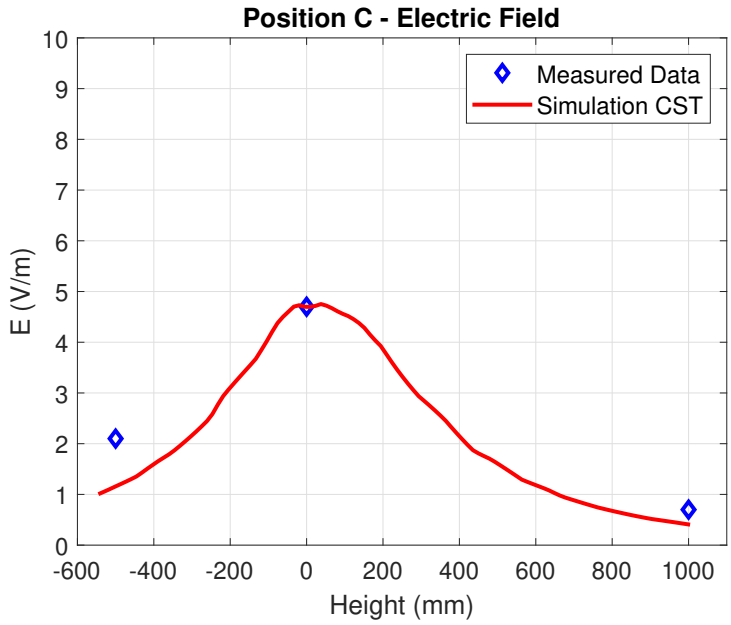

Figure 4.20: Electric field distribution 30 cm apart from the hob side.

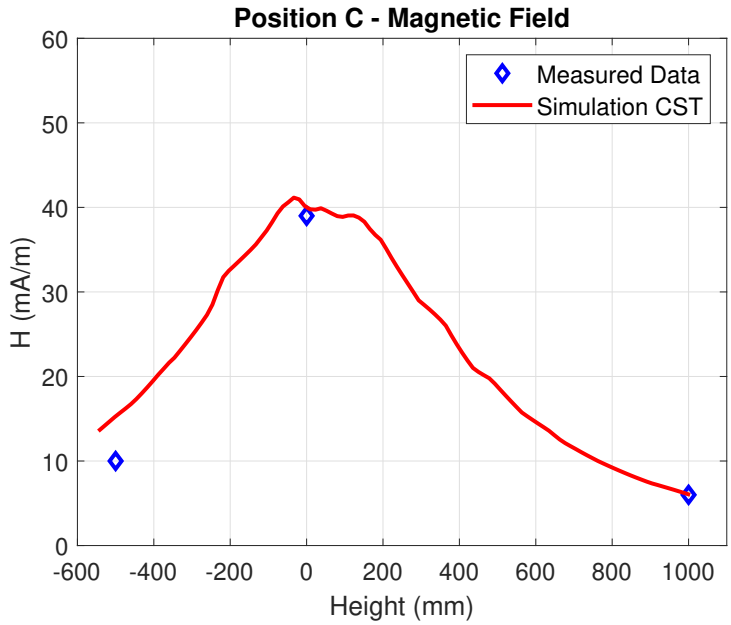

Figure 4.21: Magnetic field distribution 30 cm apart from the hob side.

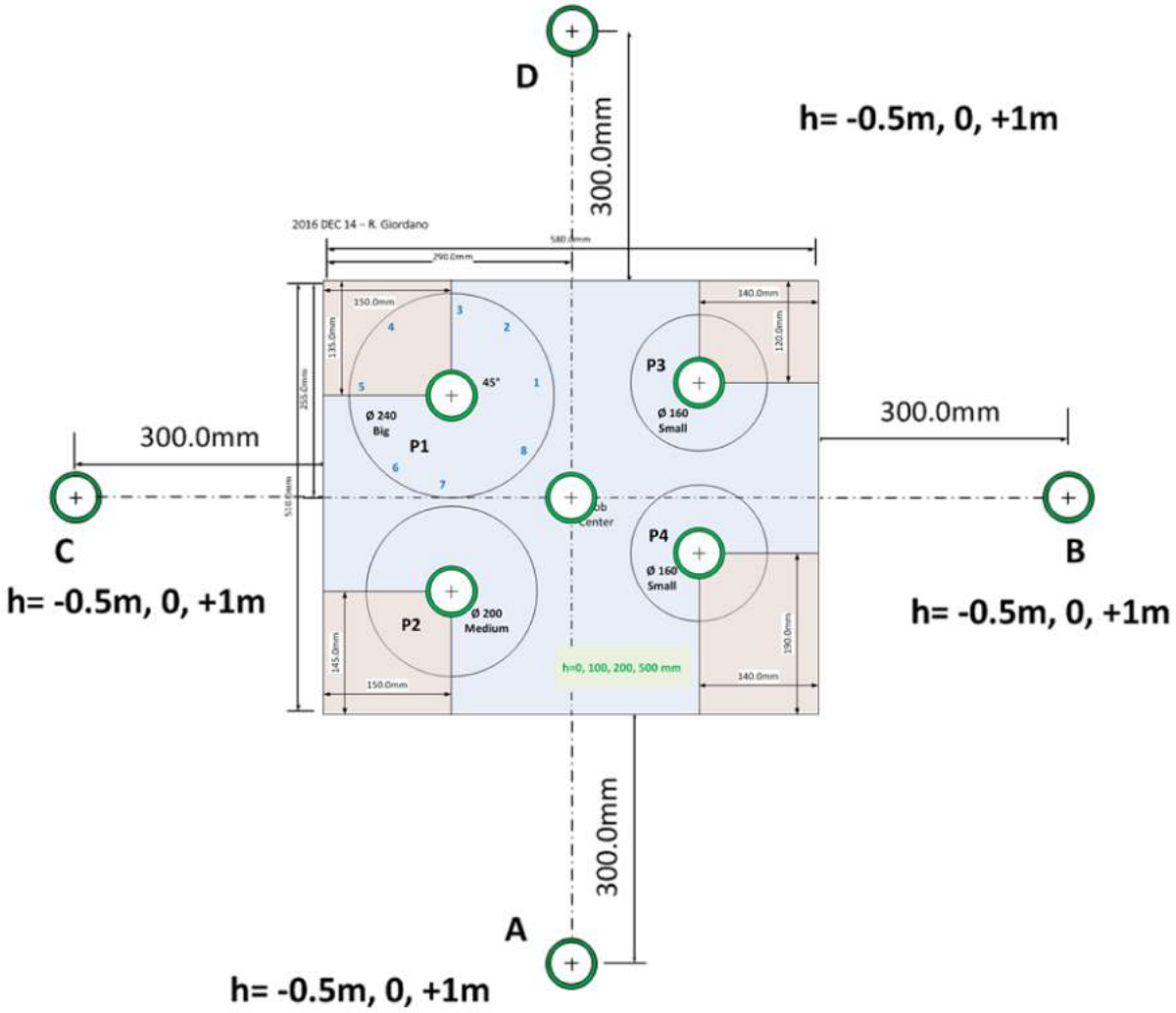

Figure 4.22: Positions considered for the measurement probe.

4.3.3 Electromagnetic Field Over the Hob Surface

The intensity of the electric and the magnetic field was calculated in the region above the hob surface. The behaviour of the fields was investigated for five positions on the on the upper glass plane for varying heights. We will refer to the positions as P_i, $i = 0, \ldots, 4$. Positions P_i refer respectively to:

- P_0, the middle point of the hob surface
- $P_1 - P_4$, the four hotplates

It is important to notice that for positions associated to the hotplates, the inner structure of the hob presents the cooking inductive coil and the ferrite blocks. On the other hand, below the position P_0, there are no relevant components. Consequently, a different field evolution for the two cases is expected. The positions P_0 and P_3 have been chosen for this chapter analysis. The evolution of the E− and the H−field is shown in Fig.s 4.23-4.26.

For position P_0, the fields have a maximum at height = 0 mm, which corresponds to the transmitting antenna plane. When moving to negative values of the vertical axis, i.e. the inward of the hob, a dramatic drop in the intensity values occurs. For increasing values of height in the positive axis region, the fields decrease rapidly: at height = 1000 mm, the field intensity is lower than 1/10 of the peak value.

On the other hand, if position P_3 is considered, the field distribution has a different shape. In detail, the fields have an intensity peak in the hob inward, in the region corresponding to the presence of the ferrite blocks. When moving away from the glass surface, the field intensity gradually decreases. A similar behavior has been observed for the position related to the other three cooking hotplates.

The main region of interest for this analysis purposes is the space above the induction hob, i.e. where the pots with the sensors will be placed in a real life scenario. The probe was moved at four different heights (h = [0, 200, 400, 550] mm) and the electric and magnetic field were measured. Experimental data were used to validate the CST model, and a optimal agreement can be observed, for both E and H, in Fig.s 4.23-4.26.

The physical dimensions of the probe affect the accuracy of the measurements around the zero-height, i.e. the glass surface; however, as the receiver will never be positioned at that level, those small discrepancies can be neglected.

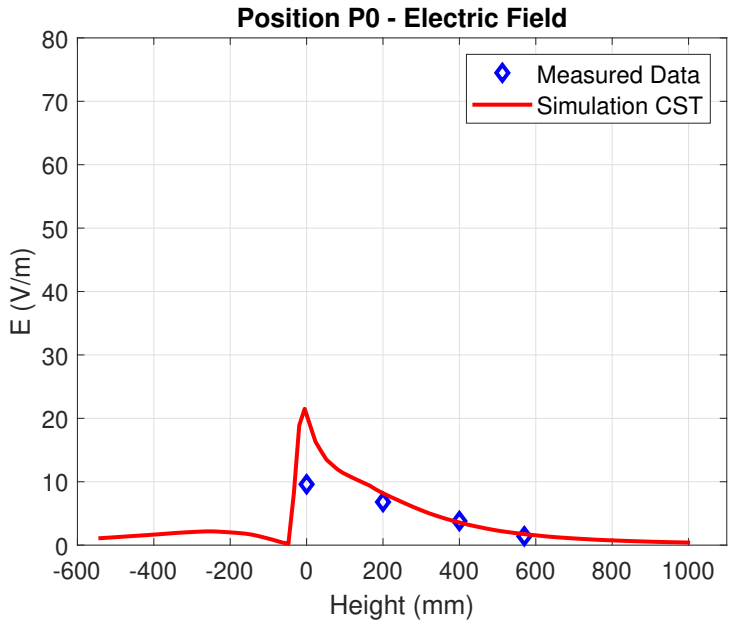

Figure 4.23: Electric field distribution over the hob glass surface.

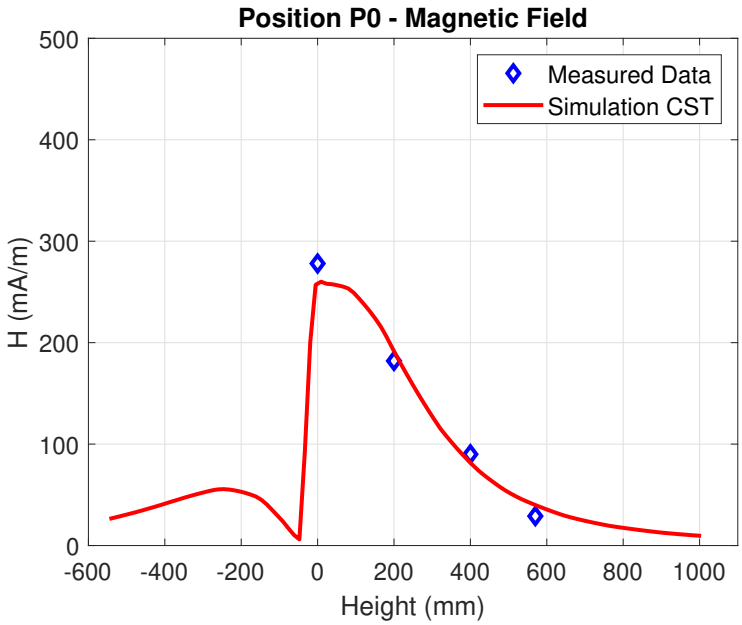

Figure 4.24: Magnetic field distribution over the hob glass surface.

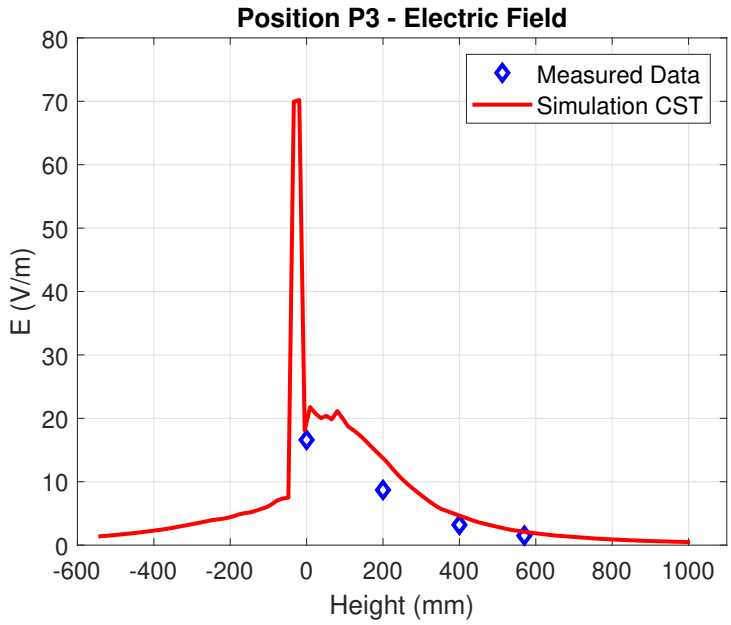

Figure 4.25: Electric field distribution over the hob glass surface.

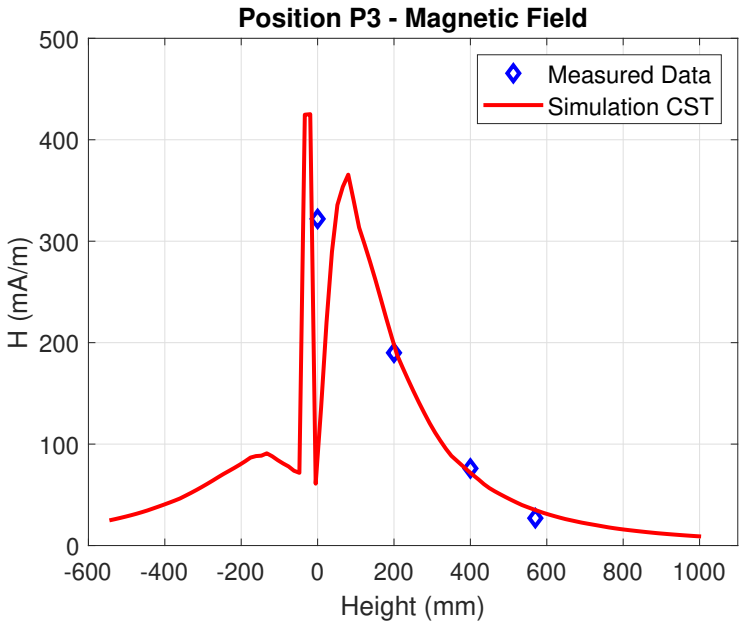

Figure 4.26: Magnetic field distribution over the hob glass surface.

Figure 4.27: Receiver antenna modelled in CST.

4.4 Receiver Antenna

The receiver antenna consists in a 4-turns copper coil placed on a FR-4 substrate. A model of the tag antenna was prepared in CST Microwave Studio and it is shown in Fig. 4.27. The tag is responsible for concatenating the oscillating field generated by the transmitter and delivering power to the load. The receiving antenna is held in a plastic casing attached to a clamp used to fix the whole apparatus to a pot standing on the hob. The whole smart device is used for sensing purposes, however, as far as the WPT model is concerned, only the tag will be of interest, while all the other structures connected to it will be included in the simulation only as standing elements.

4.4.1 Coil Impedance

A first simulation was performed on the tag alone without any circuit attached, in order to evaluate its input impedance. The result was compared to the impedance value extracted from an actual prototype of the receiver at the frequency of operation f = 13.56 MHz using a Vector Network Analyzer. The impedance is given by two terms, a real part, the resistance, and an imaginary part, the reactance, which, as expected, is purely inductive. A good agreement is observable in Fig. 4.28, therefore we can conclude that the electromagnetic representation of the structure is accurate.

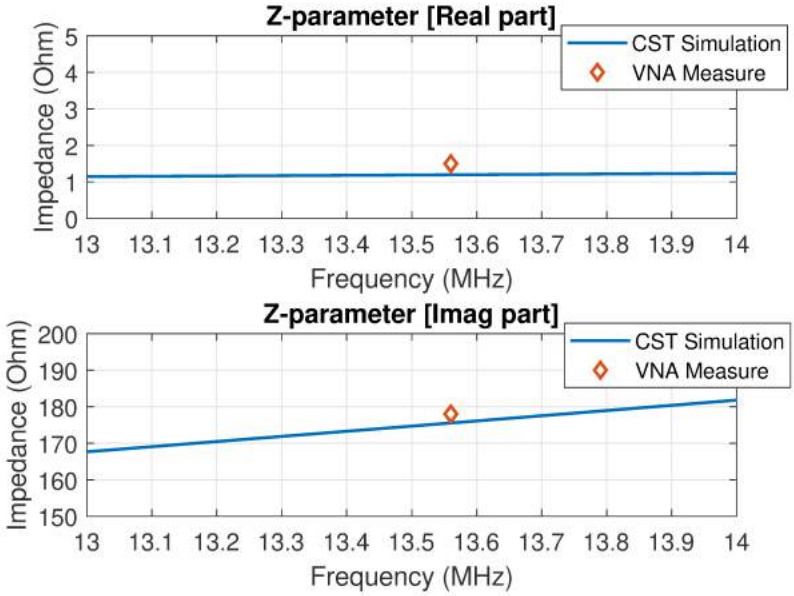

Figure 4.28: Input impedance of the receiver tag.

4.4.2 Analytical model

An analytical model can be used to obtain the inductance of a spiral conductor [71]. Referring to Fig. 4.29, the inductance is given by:

$$\mathrm{L_{coil}} = \frac{0.3937 \cdot (a\mathrm{N})^2}{8a + 11b} \ (\mu\mathrm{H}) \tag{4.16}$$

where:

$$\begin{aligned} a &= (r_i + r_o)/2 \\ b &= r_o - r_i \\ r_i &= \text{Inner radius of the spiral} \\ r_o &= \text{Outer radius of the spiral} \\ \mathrm{N} &= \text{Number of turns} \end{aligned} \tag{4.17}$$

The analytical model is accurate when considering the coil standing alone. However, when other parts of the receiver have to be included, the model

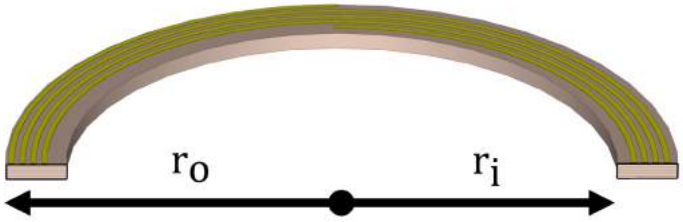

Figure 4.29: A view of the inductive coil used at the receiver side.

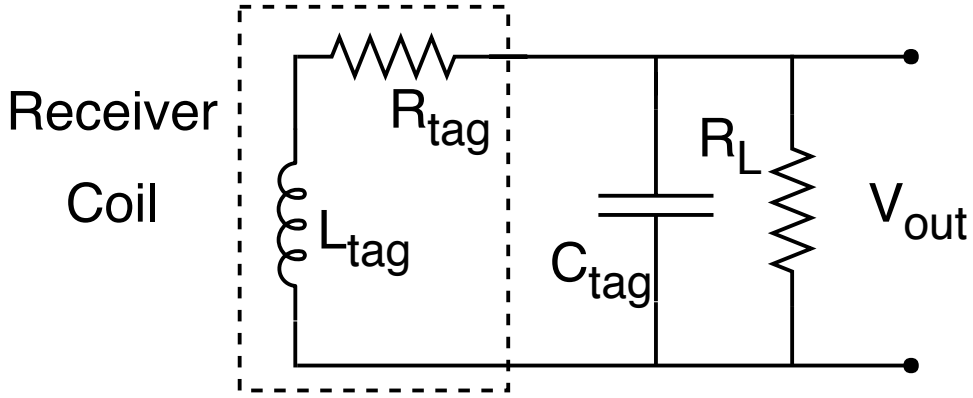

Figure 4.30: Equivalent circuit representation of the receiver antenna system.

validity does not hold anymore and full-wave simulation techniques have to be adopted.

4.4.3 Resonant Coil

Referring to Fig. 4.30, the equivalent circuit of the spiral coil is highlighted with a dashed rectangle. In the same schematic, the circuit attached to the receiver to achieve resonance is represented. The capacitor C_{tag} is tuned in order to obtain resonance at $f = 13.56$ MHz. The output voltage is evaluated at the load terminals. The latter is a resistor R_{Load} and the Q-factor of the resonating circuit is controlled by its value. When the capacitor is properly tuned to have resonance, the input impedance of the TAG is expected to be purely resistive.

The circuit tuning is performed when the tag is considered as a standing alone element. Obviously, the presence of the hob and the inductive coupling with the transmitter antenna will affect the resonant behaviour of the tag. However, in a practical application, it is not possible to tune the receiver for each configuration. Therefore, the capacitance value can be changed in the design and simulation phase, but it has to be considered fixed in a real life scenario. Consequently, a R_{Load} value is chosen in order to get a Q-factor of the resonant circuit that allows a functioning of the WPT system within an acceptable bandwidth.

4.4.4 Resonant Circuits

Once the equivalent inductance of the coil is computed, the capacitance value to obtain resonance at a given frequency f_0 is given by:

$$\mathrm{C} = \frac{1}{\mathrm{L}(2\pi f_0)^2} \tag{4.18}$$

Two different resonant circuit topologies can be adopted: series and parallel [71].

The series resonance gives an impendance minimum corresponding to the frequency f_0. Consequently, a maximum current is avaliable in the circuit. In contrast, a maximum impedance at the resonance frequency is obtained for a parallel circuit resonance. As a result, a minimum current and a maximum voltage is available at the resonance. For this reason, since a maximum voltage delivered to the load is usually desired, the parallel topology is chosen for the tag circuit.

Parallel Resonant Circuit

For a parallel resonant circuit as the one depicted in Fig. 4.31, the input impedance of the circuit is obtained from the formula:

$$Z(\omega) = \frac{j\omega L}{(1-\omega^2 LC) + j\frac{j\omega L}{R}} \tag{4.19}$$

The maximum impedance is obtained when the denominator is minimized. At the resonance condition the impedance is purely real:

$$Z_{in} = R \tag{4.20}$$

The Q-factor in a parallel resonant circuit is given by:

$$Q = R\sqrt{\frac{C}{L}} \tag{4.21}$$

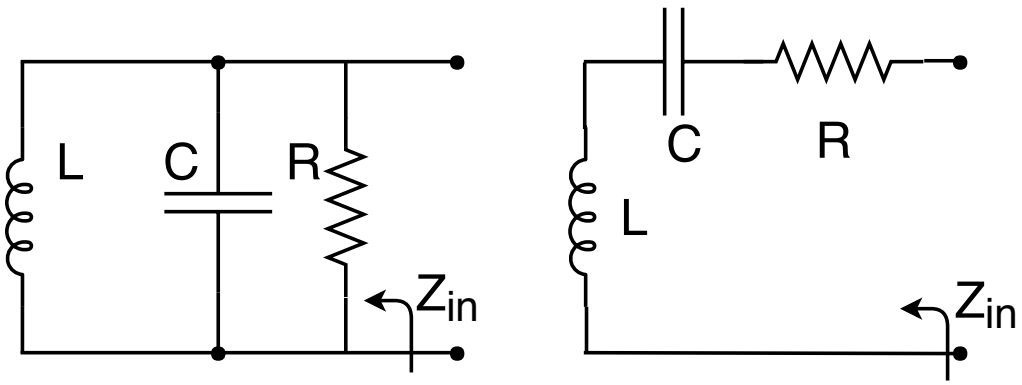

Figure 4.31: Resonant circuit topologies.

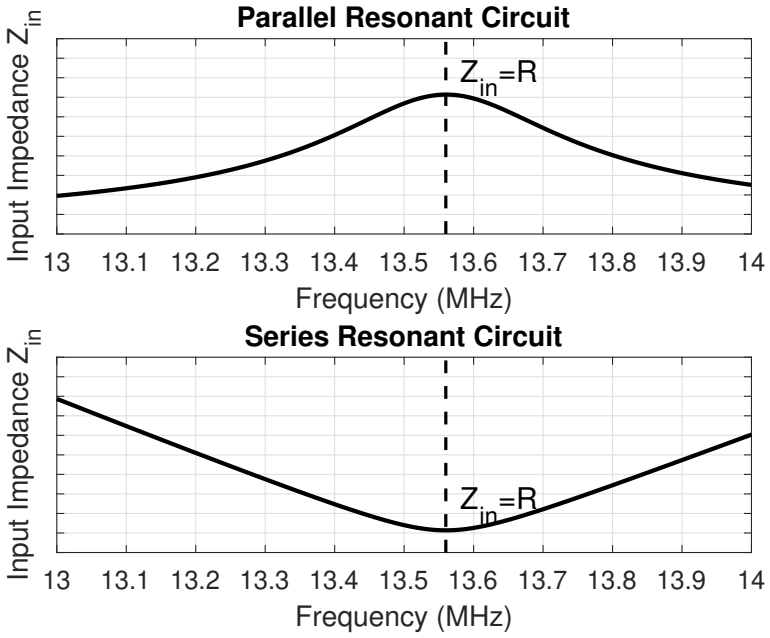

Figure 4.32: Input impedance for the resonating circuits shown in Fig. 4.31. At the resonance, the impedance is purely real, i.e. resistive.

Series Resonant Circuit

If a series resonant circuit is considered, see Fig. 4.31, the input impedance of the circuit is obtained from the formula:

$$Z(\omega) = R + j(X_L - X_C) \tag{4.22}$$

At the resonance condition, i.e. when $X_L = X_C$, the impedance is minimized as the reactance components get canceled out.

Fig. 4.32 shows the impedance response for the two topologies of resonant circuits discussed above. It can be observed that, at the resonance frequency of $f = 13.56$ MHz, the curves have a positive or a negative peak, which corresponds to a purely real input impedance, $Z_{in} = R$, i.e. the resonant circuit has a purely resisitive behavior.

4.5 Wireless Power Transfer System

The final aim of this study is to evaluate the wireless power transfer efficiency, i.e. the amount of radiation generated by the transmitter antenna that can be delivered to the receiver load. Since the WPT system is designed to feed sensing devices to be installed on the cooking pots, it is of interest the calculation of the efficiency while moving the tag in the region over the hob glass surface.

4.5.1 CST Scenario

The transmitter device and the receiver tag are both included in the same CST simulation scenario. A full-wave simulation is run and the 3D system, see Fig. 4.33, can be represented in the CST Schematic environment as a 2-ports block to which the circuits implemented on the transmitter and the receiver antenna side may be attached. This is represented in Fig. 4.34: the power source is connected to the Port 1 and the passive resonant circuit on the receiver side is attached at the Port 2 terminals. The power transfer is permitted by the inductive coupling that originates from the interactions between the transmitter and the receiver coil. The mutual inductance gives a measure of the amount of coupling that is established. For the scenario depicted in Fig. 4.33, where the tag, referring to 4.22, is placed in the position P_2 at h = 100 mm, the mutual coupling is shown in Fig. 4.35.

4.5.2 WPT Modelling

The equivalent circuit of the whole WPT system was designed. This is represented in Fig. 4.36, and it is comprehensive of both the transmitting and the receiving circuits. In between, the mutual inductance is modeled by the coupling coefficient k. The coupling coefficient k between the two coils can be calculated from:

$$k = -\frac{M}{\sqrt{L_1 L_2}} \tag{4.23}$$

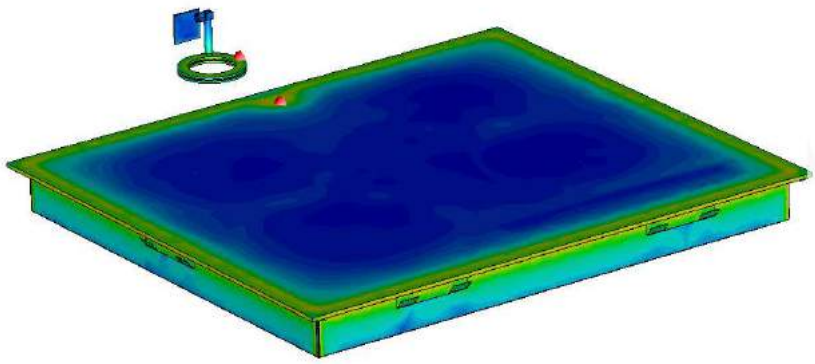

Figure 4.33: 3D WPT simulated in CST.

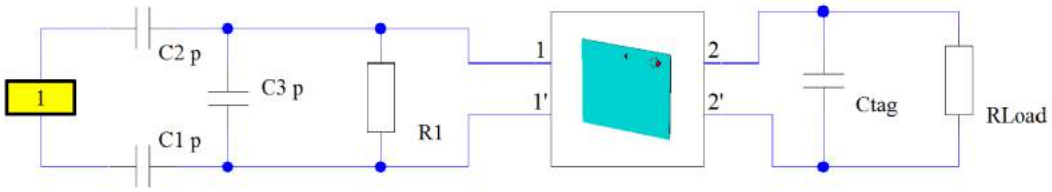

Figure 4.34: CST schematic of the WPT system.

where M is the mutual inductance, extracted from the CST simulation at the resonance frequency in the same way the self-inductance values L_{ant} and L_{tag} were computed. The coupling coefficient k, for the example considered, results to be very low: $k = 0.27 \cdot 10^{-3}$.

4.5.3 Output Voltage Evaluation

We are interested in evaluating the voltage at the load R_{Load} terminals. The output voltage curves in frequency are plotted in Fig. 4.37. A comparison between the receiving circuits including or excluding the capacitor C_{tag} is shown. Without the capacitor, the voltage values are low within all the considered bandwidth, with a maximum corresponding to the frequency the transmitter is matched to, i.e. to the S_{11} minimum. On the contrary, when the resonating circuit is implemented on the receiver side, this allows a considerable output level values improvement. A peak around the resonance frequency f_{res} = 13.56 MHz can be noticed, thus proving the effectiveness of the presented approach. However, it can be noticed that the maximum

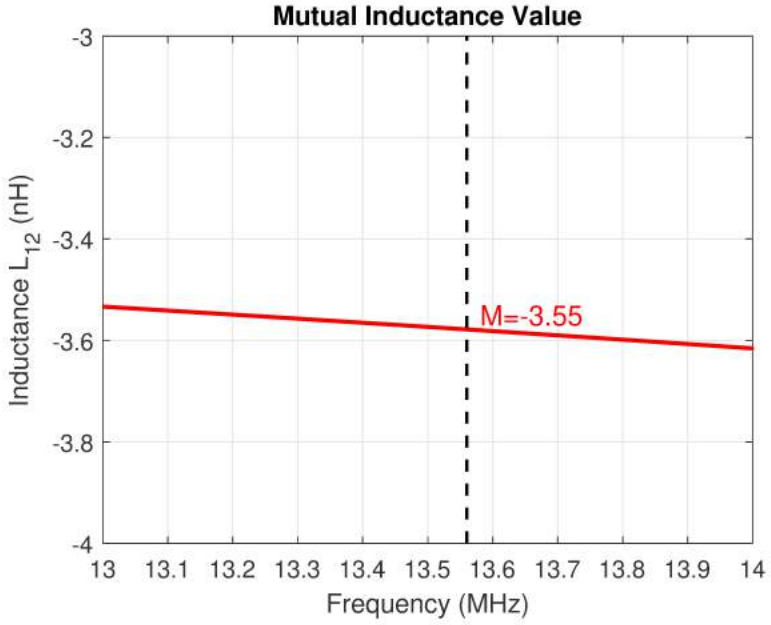

Figure 4.35: Mutual inductance between transmitter and receiver coil.

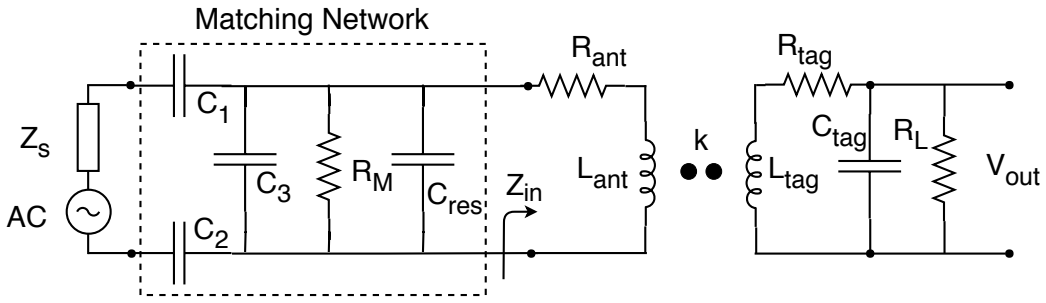

Figure 4.36: Equivalent circuit representation of the wireless power transfer system.

does not correspond exactly to the operating frequency, but it results to be slightly shifted. As stated before, the detuning occurs since the capacitance value was tuned according to the equivalent inductance of the standing alone coil. Consequently, when the transmitter is included in the model, the mutual inductance changes, even if in a very slightly way, the overall inductance computed from the receiver side.

While moving the resonant receiver at different heights over the hob surface, it can be observed in Fig. 4.38 that the output voltage curve has a peak that progressively shifts towards lower frequencies. As explained before, this happens because the tuning capacitance is kept fixed, i.e. as if the tag was standing alone, $h_2 = \infty$, while the mutual inductance changes when the tag is moved closer to the hob plane. At the same time, as the coupling coefficient values grow, the maximum voltage delivered to the load is increased.

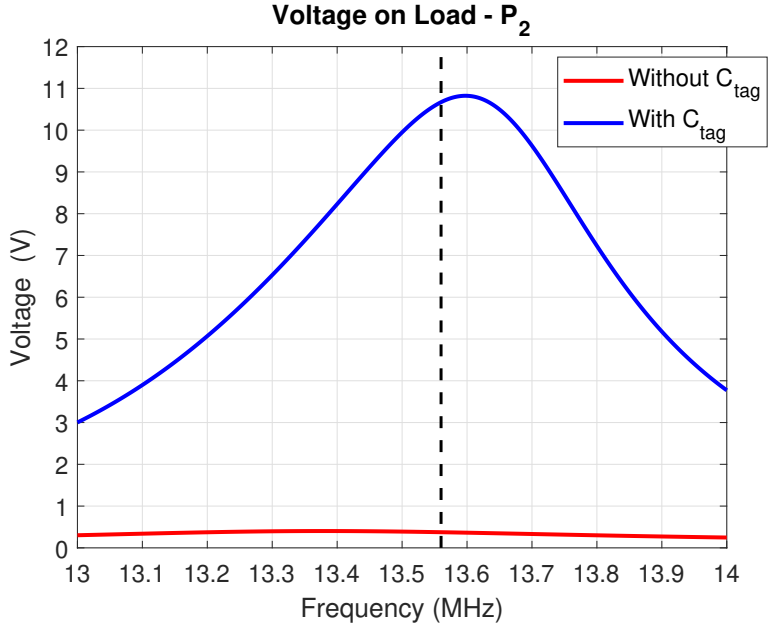

Figure 4.37: Output Voltage simulated with and without the shunt capacitance that makes the receiving circuit resonant.

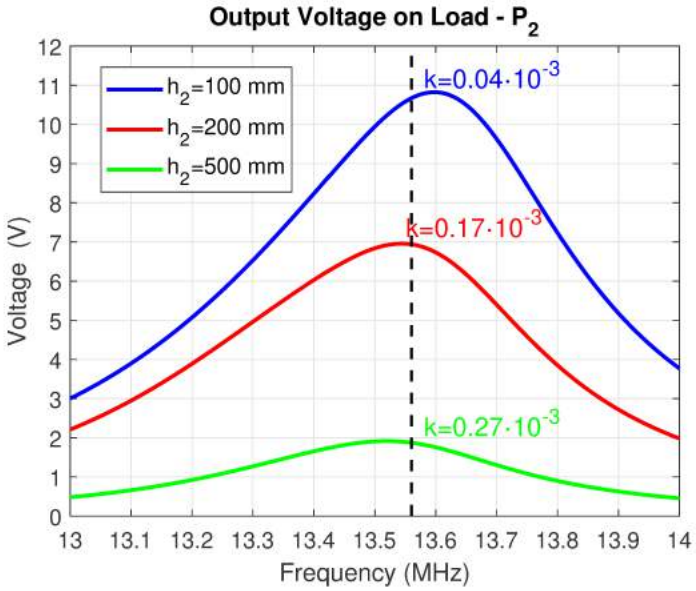

Figure 4.38: Output Voltage curves simulated with the receiver placed at different heights over the hob. As the coupling coefficient values decrease the peak is shifted towards lower frequencies.

4.5.4 Tag Antenna Measurement

Finally, the model developed to simulate the WPT system was validated in terms of the voltage delivered to the receiver load. The circular antenna is kept parallel to the horizontal plane while moved in five positions over the hob at three different heights. An oscilloscope probe is connected to the device and the AC voltage is measured at the load terminals. A picture of the experimental setup is shown in Fig. 4.39.

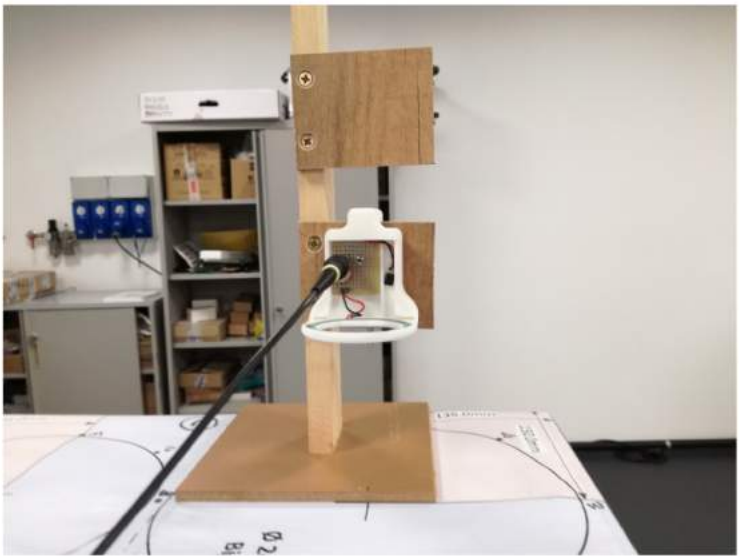

Figure 4.39: Measurement setup for evaluating the voltage delivered to the tag load.

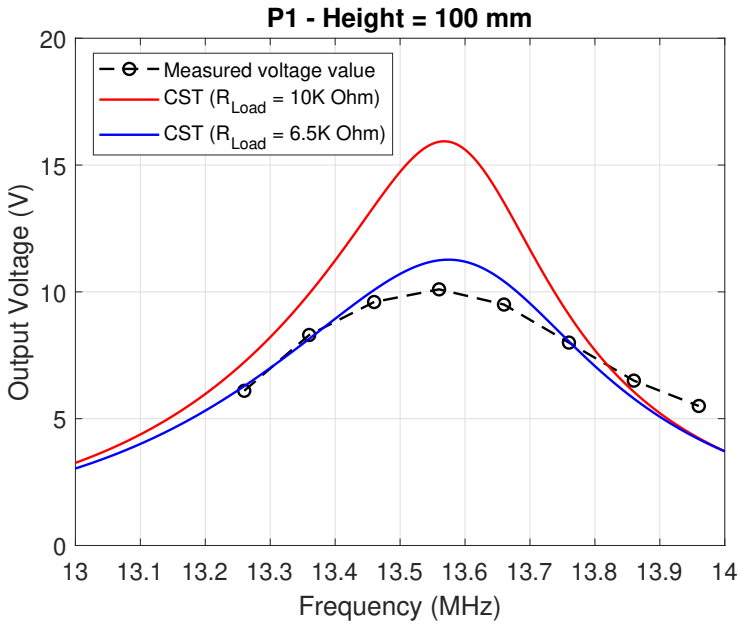

Figure 4.40: Comparison between measured and simulated output voltage.

Considering as case study the position P_1, the voltage at the load terminals was measured for a tag height of $h_1 = 100$ mm. The receiving circuit was tuned by modifying the parallel capacitance value, in order to have the maximum output voltage available at $f_{res} = 13.56$ MHz. The same configuration was simulated and the relative results are plotted in Fig. 4.40. The nominal value of the load resistor in the original design is $R_{Load} = 10$ kΩ. However, as it can be observed from the figure, a large discrepancy happens between the red and the black curves. This is an emblematic case where the availability of an accurate model allowed to highlight a problematic, otherwise hard to spot. In fact, according to the doubts raised by this analysis, a further investigation was carried out on the circuit components. The input impedance of the resonating circuit was evaluated: referring to Fig. 4.41, at the resonance frequency, as expected, the impedance is purely resistive. However, the measured real part is considerably lower than the simulated one for the same R_{Load} value. It was found out that the shunt capacitor has a parasitic resistance of $R_{cap} = 22$ kΩ.

By including the latter in the CST schematic, the correct value of input impedance was established, see the red plot of Fig. 4.41, and the blue curve representing the output voltage of Fig. 4.40 was computed. The output voltage curves, simulated and measured, exhibit a good agreement. The measured peak value, corresponding to the operating frequency, is about 1 V lower with respect to the CST results. The inaccuracies are mainly caused by the effects of the oscilloscope probe on the voltage output and by the uncertainties regarding the exact amount of input power, which was not easy to control in the measurement setup.

Later, the position P_2 on the hob glass surface was considered and the tag was moved at three different heights. The wireless power efficiency was

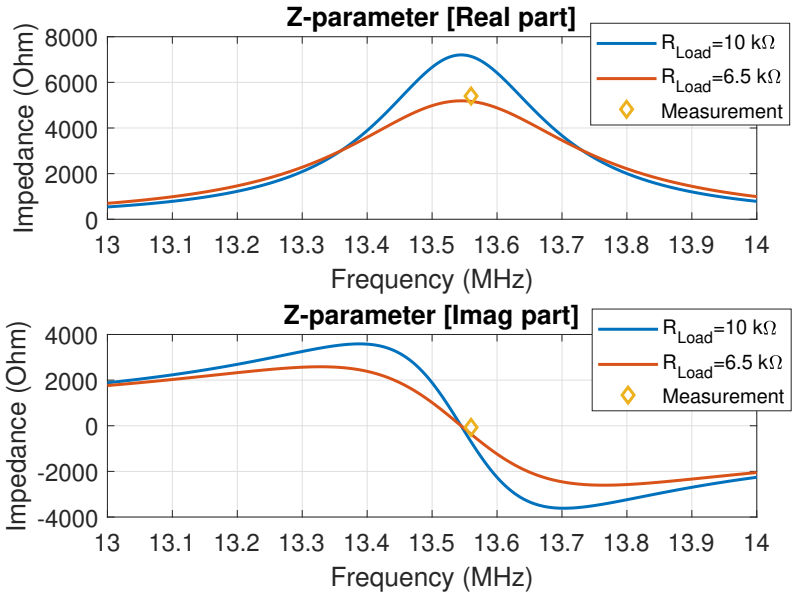

Figure 4.41: Impedance of the receiver tag calculated at the load terminals.

evaluated in terms of peak voltage delivered to the receiver. A CST simulation was run and compared to experimental data; the comparison of the results is shown in Fig. 4.42. Again, a good agreement can be appreciated, with the received voltage that is decreasing for growing distance between the tag and the hob plane. The small differences in the output voltage values are due to the fact that the oscilloscope probe and cable are not properly characterized in the simulation environment.

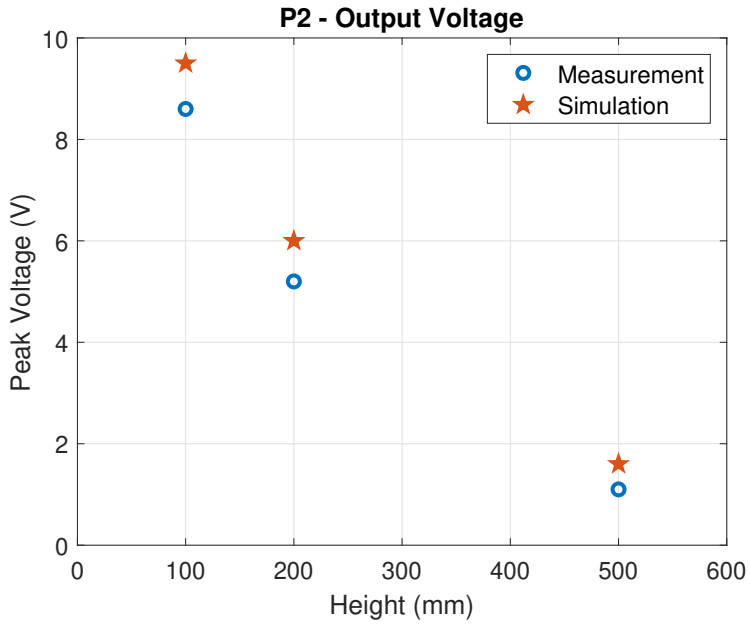

Figure 4.42: Output voltage on load, for the tag position P_2.

4.5.5 Pot Placement Effects on WPT Performances

A real-life scenario expects the sensors, and consequently the receiver antenna, to be installed on a pot standing on the hob, as depicted in Fig. 4.43. The effects on the WPT efficiency due to the pot structure are studied in this section.

Transmitter Reflection Coefficient

First, the detuning at the transmitter side is analyzed. In Fig. 4.44, the effects of placing a pot on the hob are evaluated in terms of the transmitter antenna frequency response shift. It can be noticed that no relevant changes in the curve take place; therefore, no further matching circuit modification is required.

Power Delivered to the Load

Later, the wireless power transfer efficiency is investigated in terms of voltage delivered to the receiver with and without the pot holding it. In picture 4.45, it could be observed that when the tag is attached to the pot, the voltage delivered to the load increases in value. Moreover, a slight detuning of the frequency of maximum voltage can be noticed when the pot is placed on the hob. Therefore, a further correction on the tuning capacitance would be required. However, as the receiver is designed to work in a generic environment, a-priori assumptions on the pot typology or on the presence of other appliances can not be made, and, consequently, the tuning is done only once.

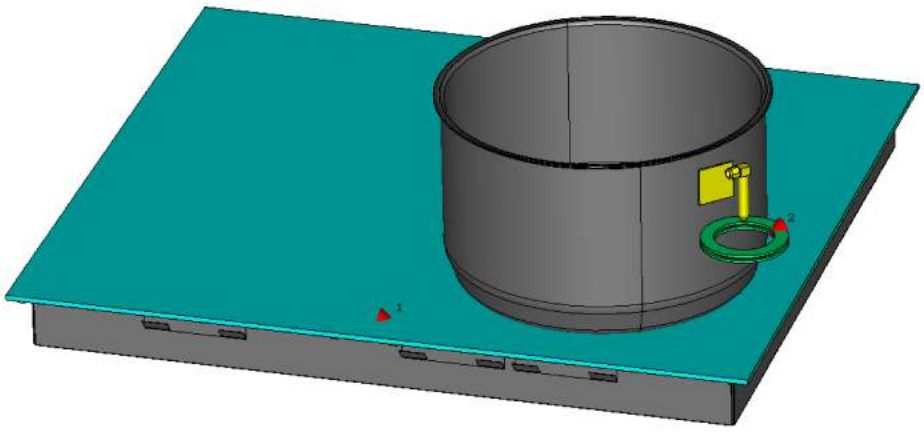

Figure 4.43: WPT configuration with the receiver antenna installed on a pot placed on the induction hob.

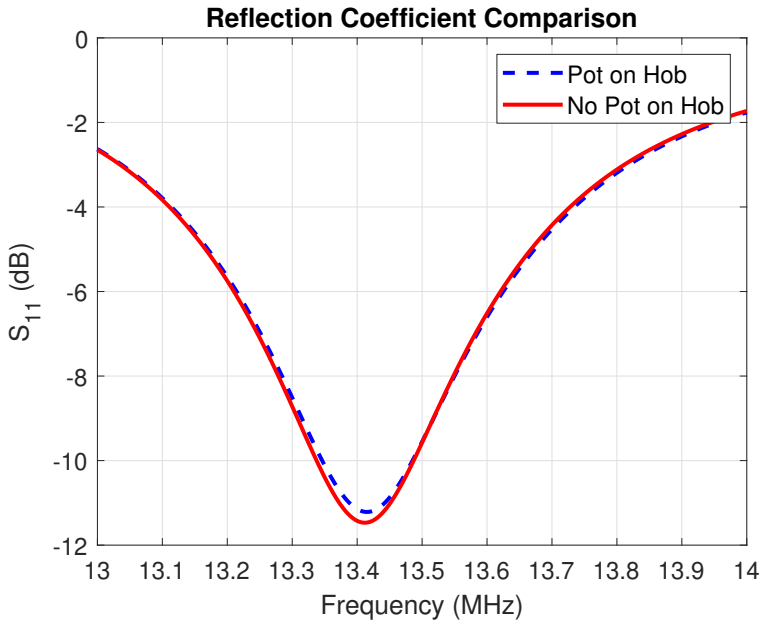

Figure 4.44: Detuning effects on transmitter antenna due to the pot presence.

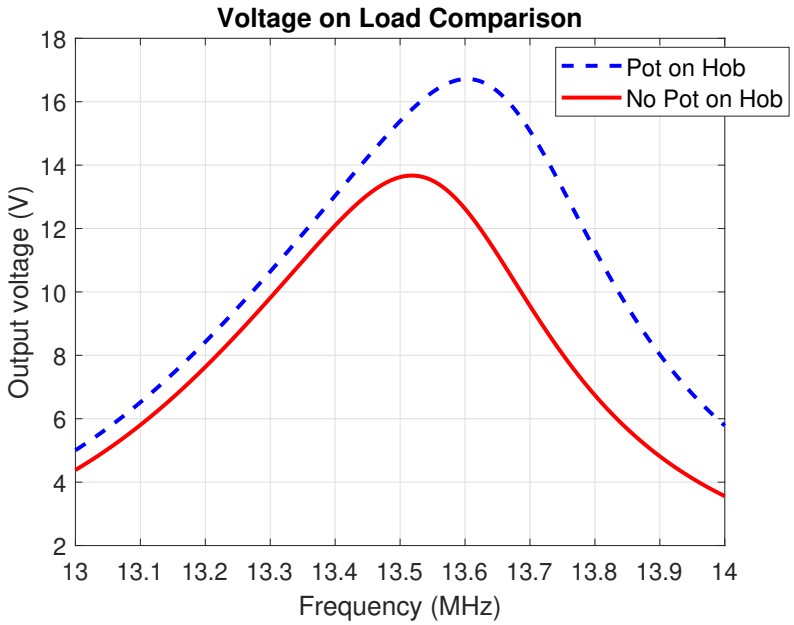

Figure 4.45: WPT efficiency variations due to the pot presence.

Chapter 5

Development of a Simulation Tool for the Analysis of Periodic Surfaces with near field Incidence

5.1 Introduction

The research presented in this Chapter was intended to integrate and improve the simulation tool developed by S. Mercader-Pellicer during his PhD Thesis work in [4]. Author in [4] has developed a reflector antenna analysis tool, based on the physical optics (PO) approach, whose soundness was proved by several works within the Heriot-Watt-University Antenna group [73].

The simulation tool was used also for the analysis of a polarizing reflectarray [74]. However, the analysis relative to the periodic surface was still done using the commercial software CST. In this regards, a MATLAB code for the analysis of frequency selective surfaces (FSS) and reflectarrays was developed. The analysis is based on a spectral domain method of moments (SD-MOM) and the integration in the simulation tool of this new functionality allowed to explore new configurations for reflector antenna systems. For instance, a FSS with frequency discrimination properties can be used as subreflector in a dual feed reflector antenna system, allowing the radiation incoming from one feed to be transmitted while reflecting the illumination from the second one.

Furthermore, many reflector antenna configurations contemplate the possibility of placing the reflecting surface in the Fresnel region of the radiating source. The actual field illuminating the surface can be reconstructed using a spherical-wave expansion (SWE) based algorithm. A significant improvement in the reflector antenna analysis can be achieved by considering the near field (NF) incidence instead of the far field (FF) approximation. The SWE feature was integrated in the code, providing an universal tool for the incidence analysis on arbitrarily-shaped surfaces. The proposed technique is particularly suited for configurations where the common far field model of the horn is not valid, which happens in many practical configurations, for example, when the

focal distance is small or when the reflector or the FSS surface is illuminated by a large horn.

In order to validate the new functionalities implemented in the simulation tool a case of study was selected. A frequency discriminating FSS, placed in the Fresnel region of the sources, was used as offset fed subreflector for a dual feeding system. A schematic of the analysis approach presented in this Chapter is depicted in Fig. 5.1. The far field radiation scattered by the surface had to be computed using the analysis tool and a validation against experimental results is provided along this Chapter. As a result, an in-house developed code for the reflector antenna analysis, totally independent from external tools such as CST, was obtained.

The Chapter will be subdivided as follows:

- Investigation on the reflector antenna feed modeling solutions
- Development of the SWE tool
- Description of the physical optics technique for the scattering analysis
- Implementation of the FSS analysis tool using the spectral domain method of moments approach
- Accurate study on the Fourier domain representation of the Rao-Wilton-Glisson sub-domain basis functions
- Validation of the tool with a practical configuration comprehensive of a FSS subreflector with linearly polarized near field system

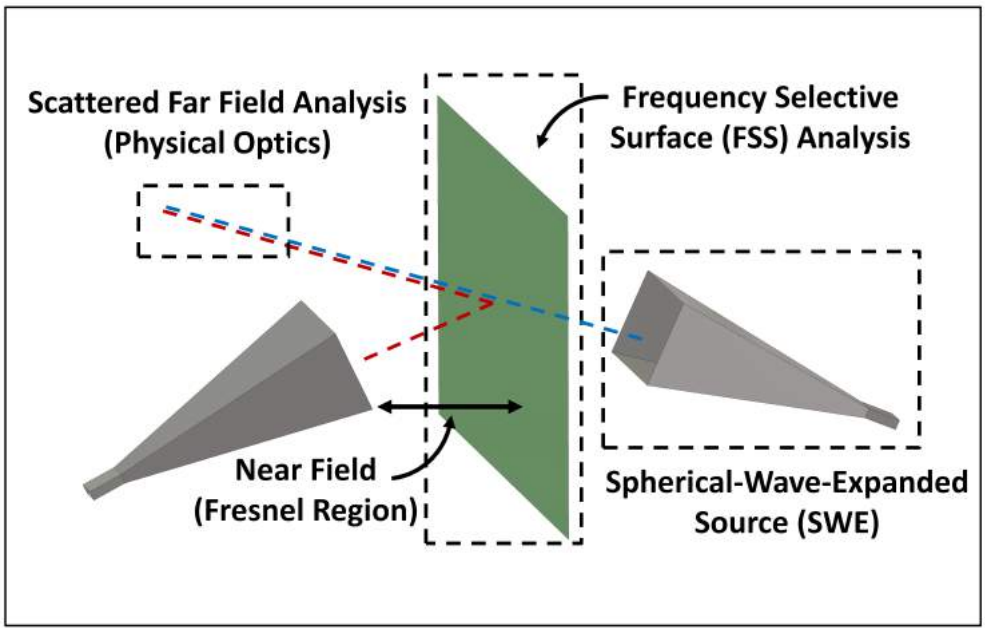

Figure 5.1: Schematic of the simulation tool features.

5.2 Field Regions Around an Antenna

The electromagnetic field generated by an antenna in the surrounding space has a behavior which has complex and varying shape and therefore hard to predict. In particular, if considering the region closer to the antenna structure, very little can be told from an analytical expression point of view about the EM field shape. On the other hand, while moving further from the antenna, a more regular field shape can be observed. At larger distances, for example, the field can be modeled with spherical waves, that can be handled with simple mathematical operations.

A representation of the subdivision of the space surrounding an antenna is provided in Fig. 5.2. Three regions can be identified [75]:

- Reactive Near Field region
- Radiating Near Field (Fresnel) region
- Far Field (Fraunhofer) region

The subdivision is not meant to provide exact boundaries between different regions, but rather to give an identification of the field structure to which some simplifications can be applied.

Reactive Near Field Region

In the region immediately surrounding the antenna, the reactive components of the field predominate. Electric and magnetic components are not in phase and the angular field distribution is highly dependent upon the distance and direction from the antenna. The behaviour of the field in this region can be predicted only by using complex numerical methods, unless very simple antenna configurations are considered.

Radiating Near Field (Fresnel) Region

The region following the reactive field zone, is a region where almost all the field radiates, but the different parts of the antenna contribute to a complex field structure. In the Fresnel zone, the electric and the magnetic component of the field are in phase but the angular field distribution is still dependent upon the distance from the antenna.

Far Field (Fraunhofer) Region

The region surrounding the radiating near field zone and extending to infinity is called far field region. There, all the field radiates, electric and magnetic components are in phase and perpendicular to each other, and perpendicular also to the direction of propagation. This allows using simple mathematical equations to describe the field behavior. In the Fraunhofer region, the angular field distribution is essentially independent of the distance from the antenna and can be approximated with spherical wave-fronts. Furthermore, as the

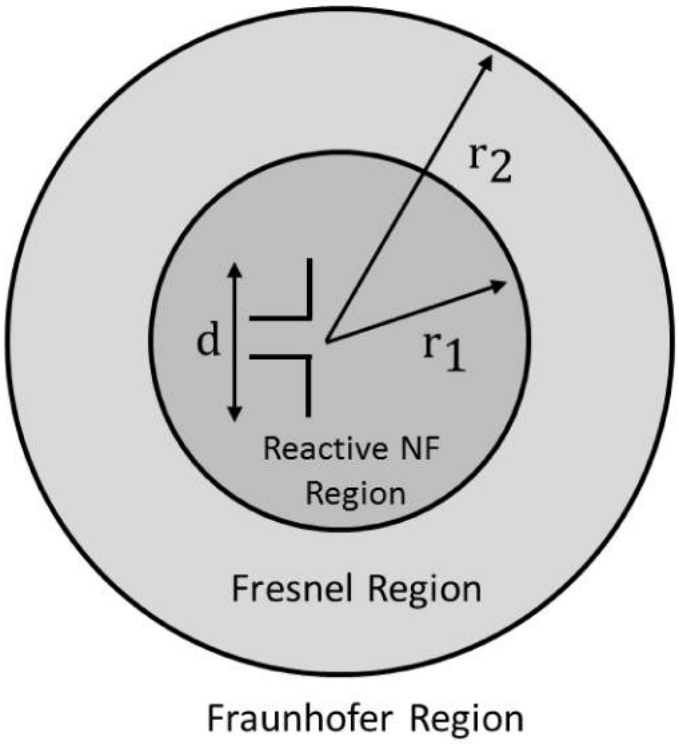

Figure 5.2: Field regions around an antenna.

distance from the antenna becomes large, the physical size of the radiating element does not influence anymore the field shape, and can therefore be approximated by a point source.

Referring to Fig. 5.2, the regions are separated according to:

- $r_1 = 0.62\left(d^2/\lambda\right)^{1/2}$, where d is the maximum between the antenna dimensions and λ is the operating wavelength,
- $r_2 = (2d^2/\lambda)$.

5.3 Source Feed Modeling

First of all, The analysis of a reflector antenna system has to take into account the modeling of the source of the electromagnetic radiation. The radiation source will be referred to as the feed element. Many approaches can be adopted in order to provide a model of the source, and a brief summary is reported in this section.

Ideal sources such as the point source [76], a Gaussian Beam or the Cosine Feed Pattern [77] can be modeled with mathematical closed equations. On the other hand, when considering real life sources, such as horn feeds, a mathematical model is most of the time not available and therefore the radiation pattern of the source has to be obtained by simulations or measurements.

5.3.1 The Huygens Source

A Huygens source consists of an electrical x-directed short dipole (a Hertzian dipole) and an y-directed short magnetic dipole. Such a point source has the advantage that in any direction its polarisation is co-polar to the linear x-polarisation, as defined according to Ludwig's 3rd definition [78].

Hereby, only the mathematical expression for the Huygens source at large distances r will be reported:

$$\boldsymbol{E}(\theta, \phi, \rho) = E_0 \frac{e^{-jkr}}{r}(1 + \cos\theta)(\cos\theta\hat{\theta} - \sin\phi\hat{\phi}) \tag{5.1}$$

5.3.2 Gaussian Beam

The Gaussian feed is a point source radiating a tapered beam. This is obtained by locating a source at a point with the complex position $(x, y, z) = (0, 0, jb)$: it will generate a Gaussian beam in the positive z -direction [79]. The distance b is the imaginary displacement.

Consider the field from a scalar point source:

$$u = \frac{e^{-jkR}}{R} \tag{5.2}$$

where R is the distance separating the source to the field point P. For practical applications, only field points in real space are of interest. Therefore $R(x, y, z)$ will be a real valued function. The distance R can be written as:

$$R = \sqrt{x^2 + y^2 + z^2 - b^2 + jbz} \tag{5.3}$$

In spherical coordinates, P is expressed as $P(\rho, \theta, \phi)$ and in the far field R becomes:

$$R \simeq \sqrt{r^2 + j2br\cos\theta} \simeq r + jb\cos\theta \tag{5.4}$$

Expression 5.2 becomes

$$u = e^{kb\cos\theta}\frac{e^{-jkR}}{R} \tag{5.5}$$

It can be noticed that the width of the beam radiated by the complex point source along the positive z-axis is controlled by the parameter b.

5.3.3 Cosine Feed Pattern

In reflector antenna analysis, the radiation pattern of a practical feed is usually well-approximated near the main beam region by cosine functions [80]. For example, the radiation from an $x-$polarized feed can be expressed as:

$$\boldsymbol{E}(\boldsymbol{r}) = \frac{e^{-ikr}}{4\pi r}[\hat{\theta}U_1 - \hat{\phi}U_2] \tag{5.6}$$

where

$$U_1 = (\cos\theta)^{q_1}\cos\phi,\ U_2 = (\cos\theta)^{q_2}\sin\phi \tag{5.7}$$

with U_1 and U_2 being the field patterns in the E- and H-plane respectively. Values q_1 and q_2 are chosen to achieve a desired aperture taper over the reflector surface. The directivity of the pattern presented in (5.6) can be expressed as:

$$D = \frac{4\pi[U_1^2 + U_2^2]_{\theta=0}}{\int_0^{2\pi} d\phi \int_0^{\pi/2} [U_1^2 + U_2^2] \sin\theta d\theta} \tag{5.8}$$

that can analogously be written as:

$$D = \frac{2(2q_1 + 1)(2q_2 + 1)}{(q_1 + q_2 + 1)} \tag{5.9}$$

If we consider the case of equal E- and H- plane patterns, $q_1 = q_2 = q$, we obtain:

$$D = 2(2q + 1). \tag{5.10}$$

If the feed is a rectangular waveguide, the directivity from [81] is:

$$D = 10.19 \frac{\text{aperture area}}{\lambda^2} = 8.82 \Big(\frac{d}{\lambda}\Big)^2 \tag{5.11}$$

and from equations (5.10) and (5.11) the following can be obtained:

$$q = 2.21(d/\lambda)^2 - 0.5 \tag{5.12}$$

for the rectangular aperture.

5.3.4 Realistic Feed Source

A typical feed in a real-life scenario consists of a rectangular horn antenna. A horn is a high-directive antenna which is typically used as a feed antenna (feed horn) for larger antenna structures such as parabolic reflectors. This kind of radiation source is usually modeled by its far field pattern approximation. The far field pattern is described by the tangential components of the field (E_θ, E_ϕ), while the radial component E_ρ is assumed to be zero. This means that once the tangential components are known, the field can be expressed for every point of the space ($\theta.\ \phi\ , \rho$) in spherical coordinates according to:

$$\mathbf{E}(\theta, \phi, \rho) = [\mathrm{E}_\theta\ \hat{\theta} + \mathrm{E}_\phi\ \hat{\phi}]\ \frac{e^{-jk\rho}}{\rho} \tag{5.13}$$

However, when the reflector or subreflector surface is positioned in the near field of the horn, this approximation is no longer valid, and some considerations have to be drawn. First, as just mentioned, the far field approximation gives no information about the radial component of the electromagnetic field illuminating the source. Secondly, it is important to remark that in many scenarios, the far field pattern of the source is the only information available about the source. This can come from an analytical model, from a simulation or from a pattern measurement. Therefore, a tool that allows to recover the near field radiation is an extremely useful tool needed for an accurate analysis of the system under observation.

5.4 Spherical Wave Expanded Feed

In the reflector antenna analysis, when the scattering surfaces are positioned in the Fresnel region of the source feed, the far field approximation of the incident field can cause anomalies that might lead to an incorrect analysis of the scattered radiation from the reflector [82]. A Spherical-Wave representation of the incident field can be developed in order to eliminate these errors. In fact, this technique allows an exact representation of the incident fields in any region of the space surrounding the source of radiation.

5.4.1 Sine-Cosine Modes

The formulation of the Spherical-Wave Expansion (SWE) was first introduced in [83]. Referring to Fig 5.3, assume that an electromagnetic field $\boldsymbol{E}(\rho,\theta,\phi)$, $\boldsymbol{H}(\rho,\theta,\phi)$ exists in a region outside a sphere (which encloses all radiating sources) of $\rho > 0$; given the tangential $\boldsymbol{E}_{tan}$ field on the surface of any sphere of radius $\rho_1 \geq \rho_0$, we can determine coefficients a^e_{omn} (TE waves) b^e_{omn} (TM waves) such that for all $\rho \geq \rho_0$:

$$\begin{aligned}\boldsymbol{E}(\rho,\theta,\phi) &= -\sum_m \sum_n a^e_{omn}\boldsymbol{m}^e_{omn} + b^e_{omn}\boldsymbol{n}^e_{omn} \\ \boldsymbol{H}(\rho,\theta,\phi) &= \frac{k}{j\omega\mu}\sum_m \sum_n a^e_{omn}\boldsymbol{n}^o_{emn} + b^e_{omn}\boldsymbol{m}^o_{emn}\end{aligned} \tag{5.14}$$

where $\boldsymbol{m}^o_{emn}$ and $\boldsymbol{n}^o_{emn}$ are the spherical-wave solutions of Maxwell's equations in a source-free, homogeneous, isotropic medium as given by [85]:

$$\begin{aligned}\boldsymbol{m}^e_{omn} = {} & \mp z_n(k\rho)\frac{mP^m_n(\cos\theta)}{\sin\theta}\sin m\phi\ \hat{\theta} \\ & -z_n(k\rho)\frac{\partial}{\partial\theta}P^m_n(\cos\theta)\sin m\phi\ \hat{\phi}\end{aligned} \tag{5.15}$$

$$\begin{aligned}\boldsymbol{n}^e_{omn} = {} & n(n+1)\frac{z_n(k\rho)}{k\rho}P^m_n(\cos\theta)\sin m\phi\ \hat{\rho} \\ & +\frac{1}{k\rho}\frac{\partial}{\partial\rho}\big[\rho z_n(k\rho)\big]\frac{\partial}{\partial\theta}P^m_n(\cos\theta)\sin m\phi\ \hat{\theta} \\ & \pm +\frac{1}{k\rho}\frac{\partial}{\partial\rho}\big[\rho z_n(k\rho)\big]\frac{mP^m_n(\cos\theta)}{\sin\theta}\sin m\phi\ \hat{\phi}\end{aligned} \tag{5.16}$$

where:

$$\begin{aligned}&k = \text{propagation constant} \\ &z = n(k\rho) = \text{any solution of the spherical Bessel equation} \\ &P^m_n(\cos\theta) = \text{associated Legendre function}\end{aligned} \tag{5.17}$$

Since sources are assumed to be of finite extent, only solutions involving outward traveling waves are considered. Therefore, only the spherical Hankel functions of the second kind $h^{(2)}_n$ have to be included.

If a far field pattern is chosen as input, the asymptotic relations for the Hankel functions can be introduced:

$$\lim_{\rho_{in}\to\infty} h_n^{(2)}(k\rho_{in}) = j^{n+1}\frac{\exp(-jk\rho_{in})}{k\rho_{in}} \tag{5.18}$$

and

$$\lim_{\rho_{in}\to\infty} \frac{1}{k\rho_{in}}\frac{\partial}{\partial\rho}[\rho h_n^{(2)}(k\rho_{in})]_{\rho=\rho_{in}} = j^{n}\frac{\exp(-jk\rho_{in})}{k\rho_{in}} \tag{5.19}$$

Expressions for the associated Legendre functions [86] and recurrence relations for the Hankel functions, as implemented in the code, are provided in Section 5.4.2. We will refer to functions 5.15 and 5.16 as Sine-Cosine modes, for their azimuthal dependence on the sinusoidal functions.

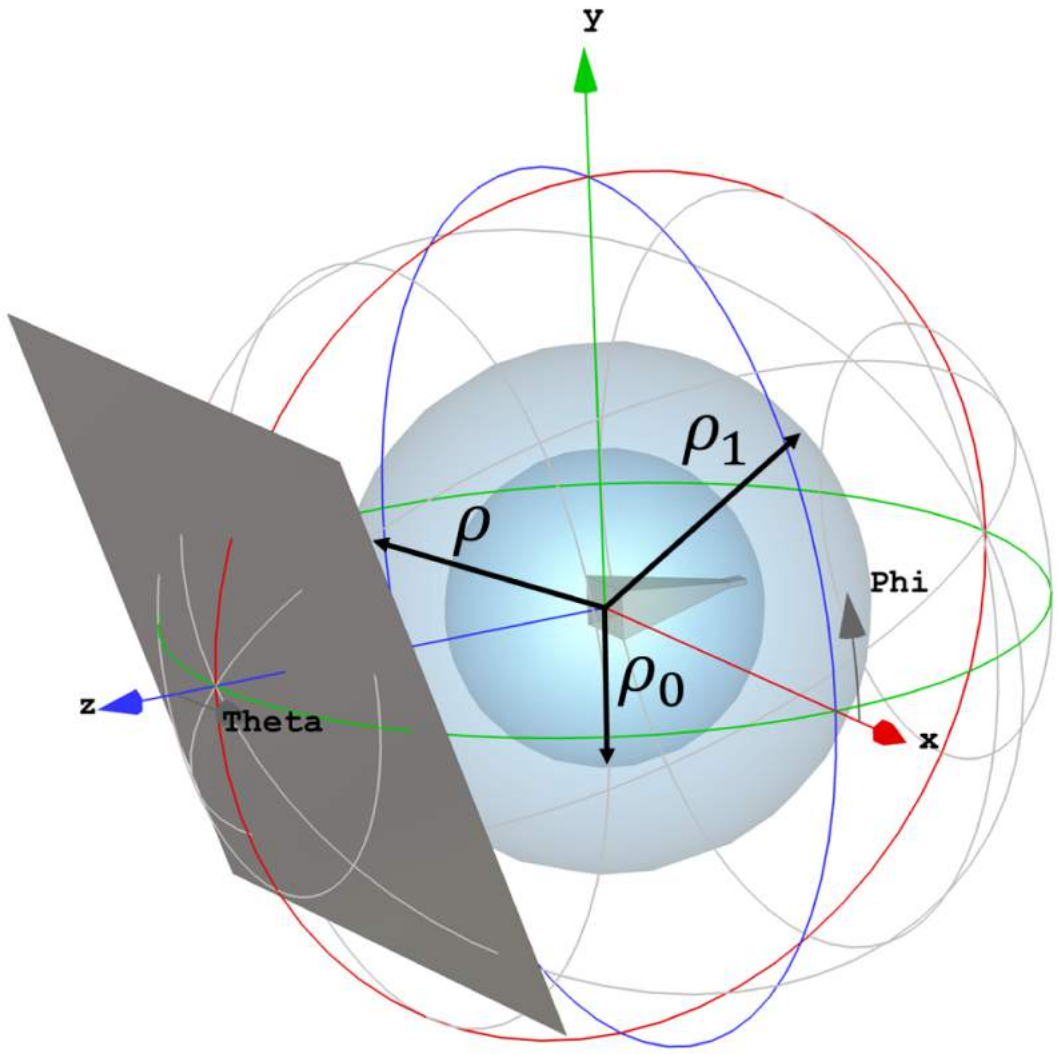

Figure 5.3: Schematic of the SWE coefficients extraction configuration. A metallic screen is used for validating the reconstruction of the near field illuminating it.

According to [87], the formula to compute the coefficients is given by:

$$a^e_{omn} = \frac{1}{[(z_n(k\rho_1)]^2}\frac{2n+1}{\pi 2n(2n+1)}\frac{(n-m)!}{(n+m)!}\times \\ \times \int_0^{2\pi}\int_0^{\pi} -\boldsymbol{m}^e_{omn}\cdot \boldsymbol{E_i}(\rho_1,\theta,\phi)_{tan}\sin\theta\, d\theta\, d\phi \quad (5.20)$$

$$b^e_{omn} = \frac{1}{\left\{\frac{1}{k\rho_1}\frac{\partial}{\partial\theta}[\rho_1 z_n(k\rho_1)]\right\}^2}\frac{2n+1}{\pi 2n(2n+1)}\frac{(n-m)!}{(n+m)!}\times \\ \times \int_0^{2\pi}\int_0^{\pi} -\boldsymbol{n}^e_{omn}\cdot \boldsymbol{E_i}(\rho_1,\theta,\phi)_{tan}\sin\theta\, d\theta\, d\phi \quad (5.21)$$

5.4.2 Exponential Modes

Another formulation of the spherical wave expansion can be obtained by using a set of exponential basis functions [88]. This formulation does not differentiate anymore between even and odd modes, in this way reducing the computational resources needed. The $\phi-$ dependence is now controlled by exponential functions. The spherical wave functions $\boldsymbol{m}_{mn}(r,\theta,\phi)$ and $\boldsymbol{n}_{mn}(r,\theta,\phi)$ are now defined as:

$$\begin{aligned}\boldsymbol{m}_{mn}(r,\theta,\phi) = &- h_n^2(kr)\frac{jmP_n^{|m|\cos\theta}}{\sin\theta}e^{-jm\phi}\ \hat{\theta} \\ &- h_n^2(kr)\frac{dP_n^{|m|\cos\theta}}{d\theta}e^{-jm\phi}\ \hat{\phi},\end{aligned} \quad (5.22)$$

and

$$\begin{aligned}\boldsymbol{n}_{mn}(r,\theta,\phi) =&\frac{n(n+1)}{kr}h_n^2(kr)P_n^{|m|\cos\theta}e^{-jm\phi}\ \hat{r} \\ &+ \frac{1}{kr}\frac{d}{d(kr)}(kr)h_n^2(kr)\frac{dP_n^{|m|\cos\theta}}{d\theta}e^{-jm\phi}\ \hat{\theta} \\ &- \frac{1}{kr}\frac{d}{d(kr)}(kr)h_n^2(kr)\frac{jmP_n^{|m|\cos\theta}}{\sin\theta}e^{-jm\phi}\ \hat{\phi}.\end{aligned} \quad (5.23)$$

where $P_n^{|m|}(\cos\theta)$ are the associated Legendre functions:

$$P_n^{|m|}(\cos\theta) = (\sin\theta)^{|m|}\frac{d^{|m|}P_n(\cos\theta)}{d(\cos\theta)^{|m|}},\ |m|\leq n \quad (5.24)$$

with

$$P_n(\cos\theta) = \frac{1}{2^n n!}\frac{d^n}{d(\cos\theta)^n}((\cos\theta)^2-1)^2,\ n\geq 0 \quad (5.25)$$

5.4.3 Theoretical Number of Modes

The number of modes in which the field should be expanded is a crucial parameter to be considered, as the overall simulation time is influenced by the indexes of the summations in 5.14. The spherical modes have an azimuthal index m and a polar index n. The maximum value, N, of the polar index is determined by $k\rho_0$ where ρ_0 is the radius of the minimum sphere containing the source. From [89], a sufficient accuracy is generally obtained when

$$N = k\rho_0 + max(3.6(k\rho_0)^{1/3}, 10) \tag{5.26}$$

The azimuthal index m is limited by

$$-n \leq m \leq n \tag{5.27}$$

For each pair of indices (m, n) two modes given by the coefficients a_{mn} and b_{mn} exist. Therefore, the total number of modes is $2N(N+2)$ [84].

The summations 5.14 can be formulated for the possible n for each m:

$$\sum_{m=-N}^{N} \sum_{\substack{n=|m|,\\ n>0}}^{N} \tag{5.28}$$

This notation gives the possibility of excluding high order modes with negligible power. The m-modes index may be limited to $|m| \leq M \leq N$ where M is given as input to the code, recalling that antennas with an high degree of rotational symmetry will often have a low value of M while N is found in 5.26. For each m, the number of n-modes with significant power might be lower than N and therefore the summation can be truncated to an m value which is function of the considered n: $N(m)$. For instance, the highly rotational antenna will often have $N(m)$ low for m even but $N(m) = N$ for odd m. M and $N(m)$ are determined once the spherical modes are calculated by observing the energy associated within each coefficient. Finally, the summation becomes:

$$\sum_{m=-M}^{M} \sum_{\substack{n=|m|,\\ n>0}}^{N(m)} \tag{5.29}$$

5.4.4 MATLAB Code Implementation

In conclusion, the Spherical-Wave Expansion is a technique that allows to express a generic source of radiation uniquely by a series of coefficients. When used for expanding a horn antenna, used as source for a reflector system, it allows to have the field recovered in any point of the surrounding space. However, a practical implementation is not trivial. In this thesis work, a MATLAB tool was developed in order to implement the SWE: it will be presented and validated in the following sections. The tool presented includes both the Sine-Cosine and the Exponential SWE formulations and proved to be efficient and reliable.

5.4.5 SWE Tool Validation

Following to the theory presented in Section 5.4, a spherical wave expansion tool was developed in this thesis work. In order to validate the SWE code, the Ka-band Flann rectangular horn represented in Fig. 5.4 operating at $f = 21.7$ GHz was considered as the source feed to be expanded. A CST simulation was carried out in order to obtain the far field pattern to be given as input to the code. In detail, the tangential components (E_θ, E_ϕ) of the electric field at $\rho_{in} = 1$ m were used as input.

Output Field on a Sphere in the Fresnel Region - Far Field Approximation

First, the code was used to reconstruct the electric field on a full-sphere of radius $\rho_{out} = 0.5$ m. The sphere belongs to the Fresnel region of the source, therefore the far field approximation in not longer valid. This is proved in Fig.s 5.5 and 5.6, where a comparison between the simulated exact field and the FF approximation is shown. The Theta− and Phi−components of the electric field are plotted on the $\phi = 90°$ and $\phi = 0°$ planes respectively. Some discrepancies between the two incident field representations can be noticed, therefore giving rise to the need of a more accurate model. Obviously, the field extracted from CST without using the FF approximation could be correctly used, however this proved to be computationally timely more expensive and longer to be calculated with respect to the SWE approach.

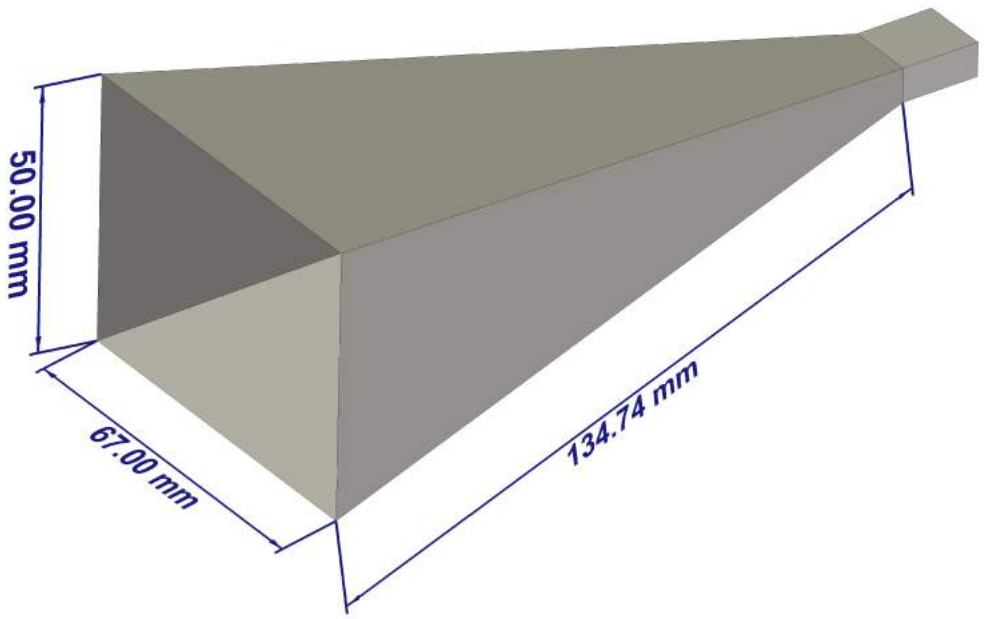

Figure 5.4: A Flann horn antenna geometry.

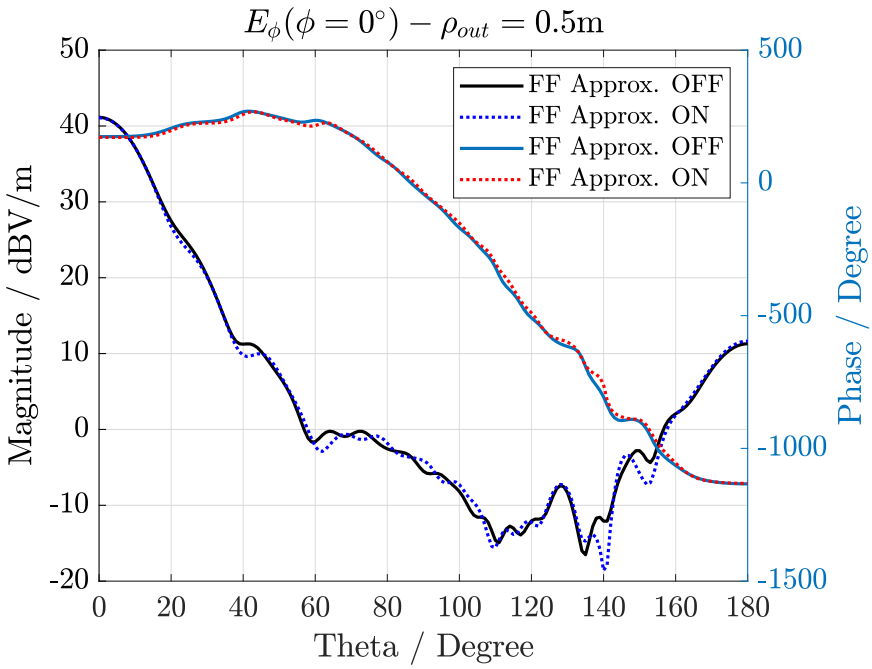

Figure 5.5: Comparison between the FF and NF tangential component (E_ϕ) of the electric field on a sphere of radius $\rho = 0.5$ m. The black and the blue lines are relative to the magnitude while the purple and the red lines are relative to the phase.

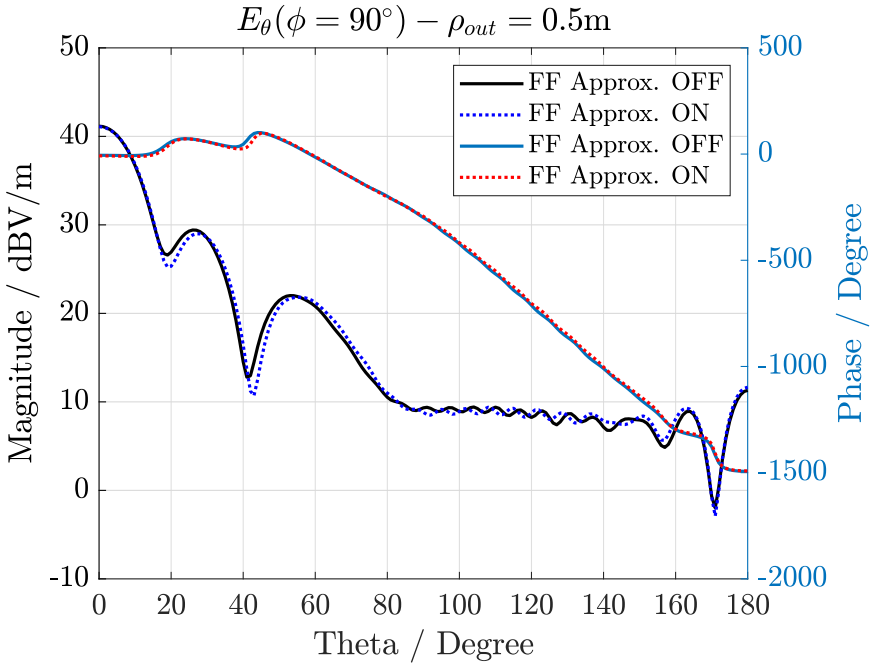

Figure 5.6: Comparison between the FF and NF tangential component (E_θ) of the electric field on a sphere of radius $\rho = 0.5$ m. The black and the blue lines are relative to the magnitude while the purple and the red lines are relative to the phase.

Output Field on a Sphere in the Fresnel Region - SWE Field

The need of having a feed modeling more accurate than the FF approximation was ultimately proved. The SWE code was used to compute a field output for $\rho_{out} = 0.5$ m and the results were compared to the field extracted from the CST simulation for the same ρ. The comparison between the Theta− and Phi−components of the electric field, on the $\phi = 90°$ and $\phi = 0°$ planes respectively, is shown in Fig.s 5.7 and 5.8. The field reconstructed with the SWE code perfectly agrees with the full-wave simulation results. Moreover, Fig. 5.9 shows that a significant radial component E_ρ of the field arises. The latter is completely ignored if the FF approximation is considered, since only the tangential components are considered to be relevant. This assumption is valid as long as the far field region is considered, however, when moving closer to the source, also the radial components have to be considered. It is important to remark that CST simulations are used as benchmark here for the validation of the code developed. However, extracting the field without the far field approximation in CST can take several minutes, while with our code only few seconds are required.

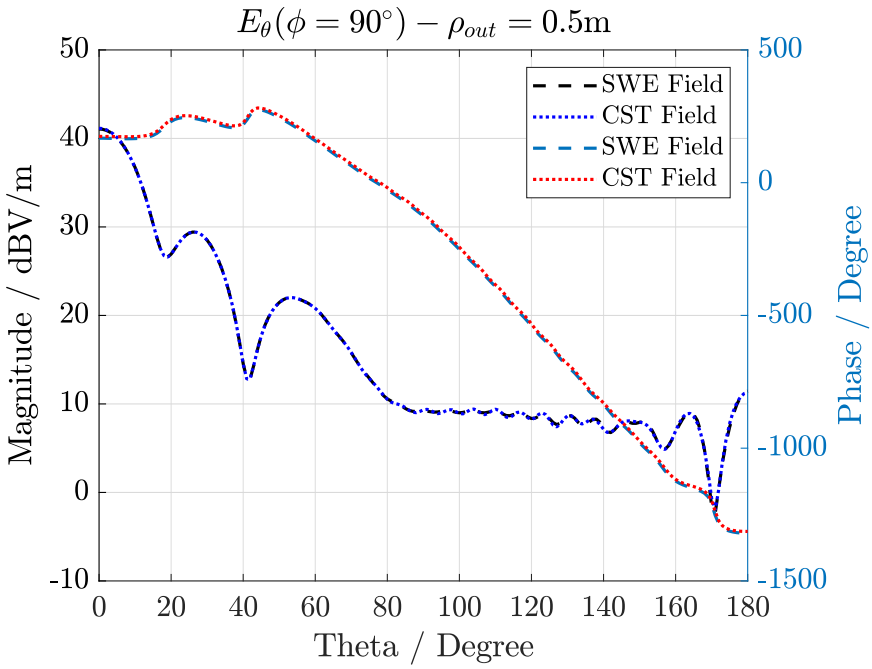

Figure 5.7: Comparison between the E_θ component of the exact field reconstructed using CST and the SWE code on a sphere of radius $\rho = 0.5$ m. The black and the blue lines are relative to the magnitude while the purple and the red lines are relative to the phase.

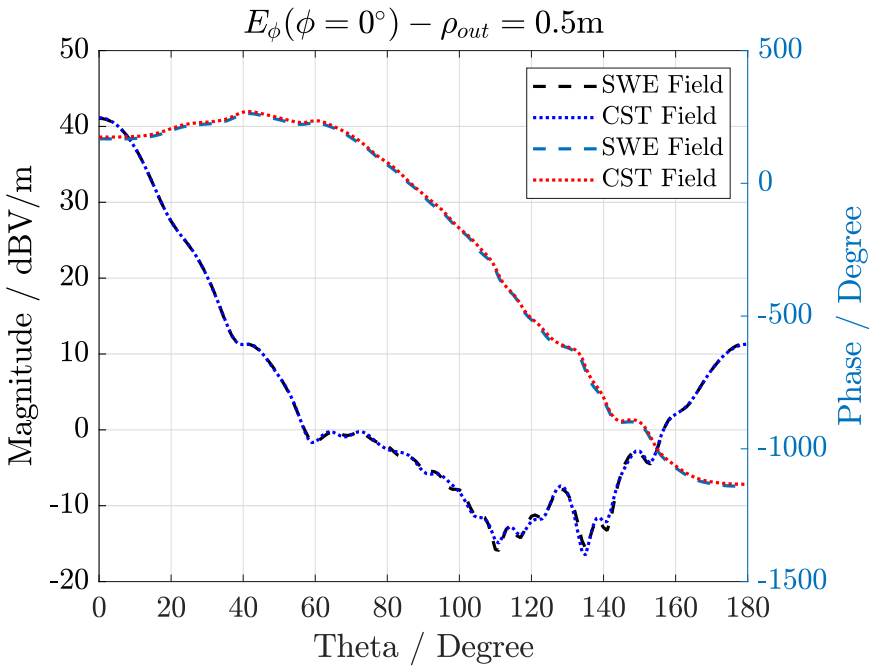

Figure 5.8: Comparison between the E_ϕ component of the exact field reconstructed using CST and the SWE code on a sphere of radius $\rho = 0.5$ m. The black and the blue lines are relative to the magnitude while the purple and the red lines are relative to the phase.

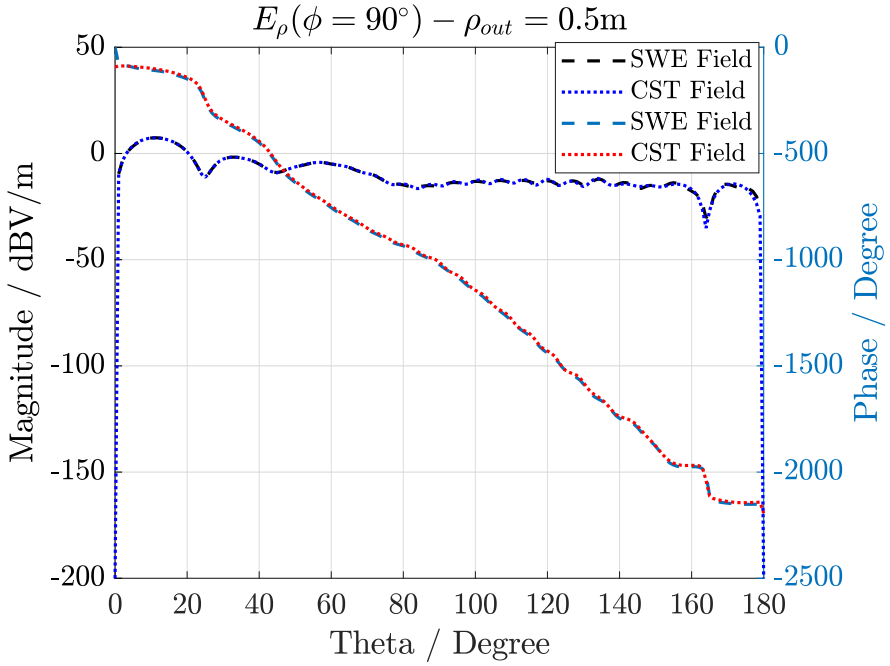

Figure 5.9: Comparison between the E_ρ component of the exact field reconstructed using CST and the SWE code on a sphere of radius $\rho = 0.5$ m. The black and the blue lines are relative to the magnitude while the purple and the red lines are relative to the phase.

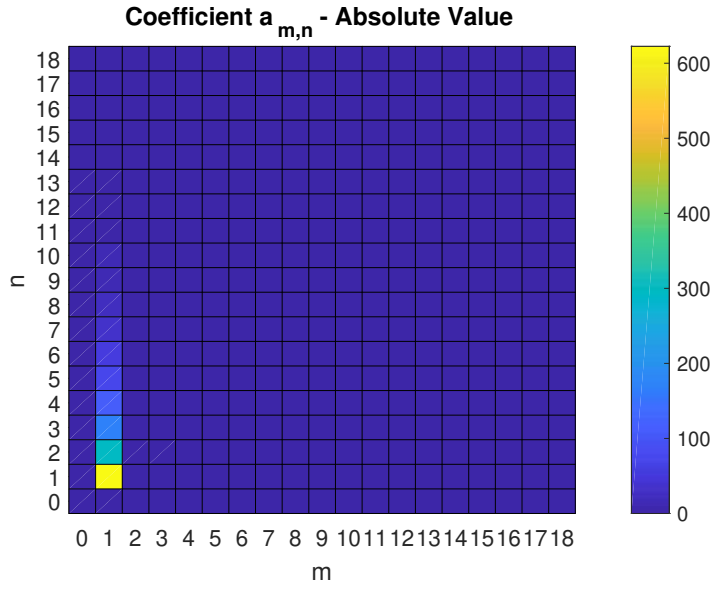

Figure 5.10: Magnitude of the a_{mn} SWE coefficient in function of the mode indexes m, n.

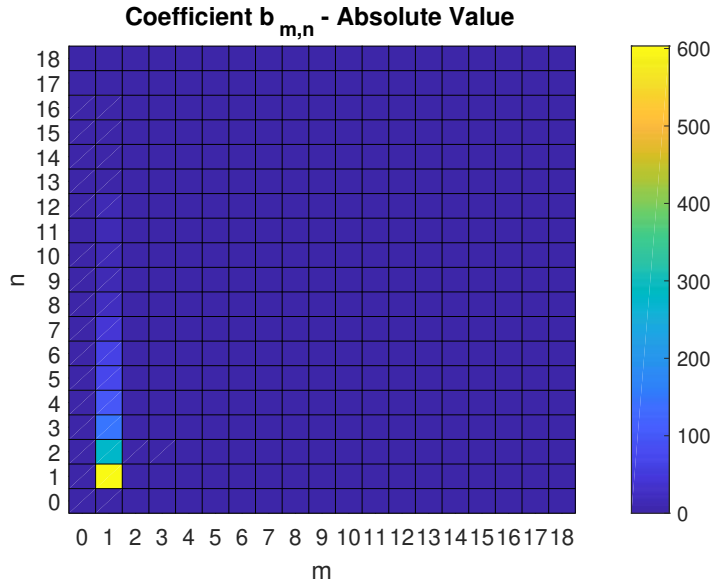

Figure 5.11: Magnitude of the b_{mn} SWE coefficient in function of the mode indexes m, n.

Spherical Wave Coefficients

The number of modes required to properly reconstruct the field is studied for the horn used in this section. The a and b coefficients values for increasing values of indexes m, n are plotted in Fig.s 5.10 and 5.11. It can be observed that only coefficients with $m = 1$ are present. This is due to the fact that for far field pattern with circular or quasi-circular symmetries, the orthogonality properties of sine and cosine cancel out the remaining components [82].

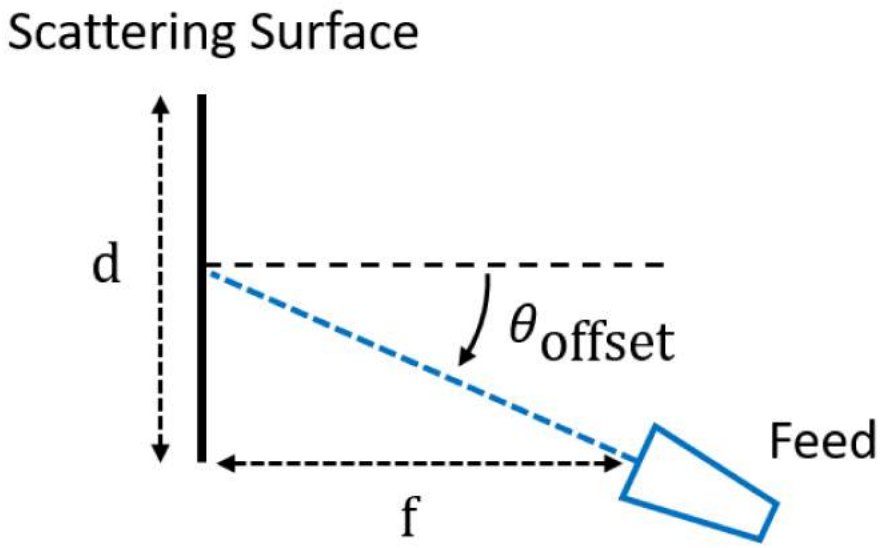

Figure 5.12: Schematic of the offset configuration for a feed illuminating a surface in its Fresnel region.

Incident Field on a Reflector Surface - Magnitude

When dealing with reflector antenna systems the reconstruction of the incident field on the reflector or subreflector surface coming from the source feed is usually of interest. This can be easily done using our tool. A scenario where the horn feed was placed f = 250 mm apart from the reflector surface at an offset angle of 30° was considered for validation against CST, see Fig. 5.12. The electric field, in magnitude and phase, is reconstructed on a d × d = 300 mm × 300 mm surface. The same configuration, see Fig. 5.13 is simulated in CST and the field is extracted on the same surface. A comparison is shown in Fig. 5.14: again, a perfect matching can be appreciated. This case is even more relevant than the one presented before: by using only CST, a full-wave simulation would be required for each reciprocal displacement between feed and reflector. The tool instead only requires the knowledge of the far field on any sphere surrounding the source, the field on any surface can be reconstructed by just summing the expansion coefficients by the proper weighted spherical functions. The comparison with the CST extracted field shows that the tool provides smoother and more regular results: this is due to the interpolation done by the commercial software when extracting the results that can obviously be improved at the cost of a longer computational time. In contrast, the tool gave promising results in a shorter time and the additional use of the software can be avoided.

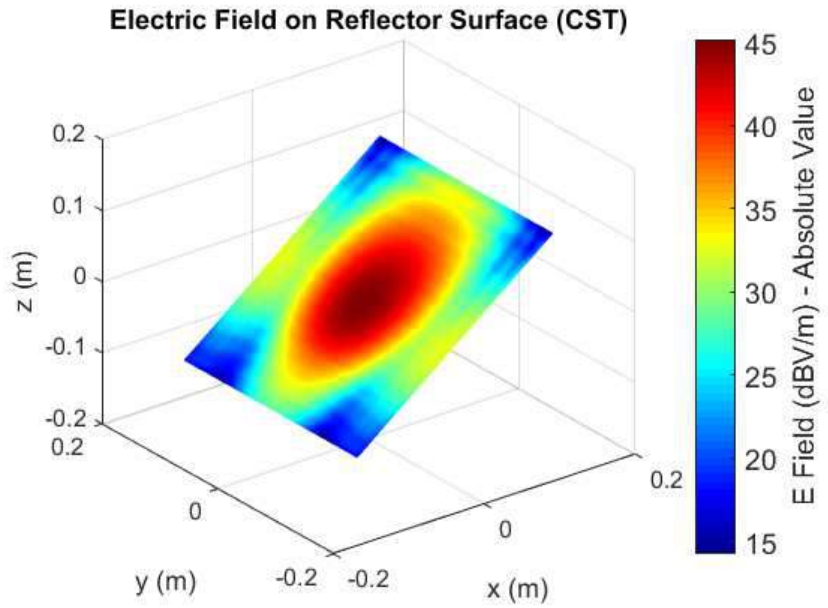

Figure 5.13: Electric field computed on the scattering surface using CST.

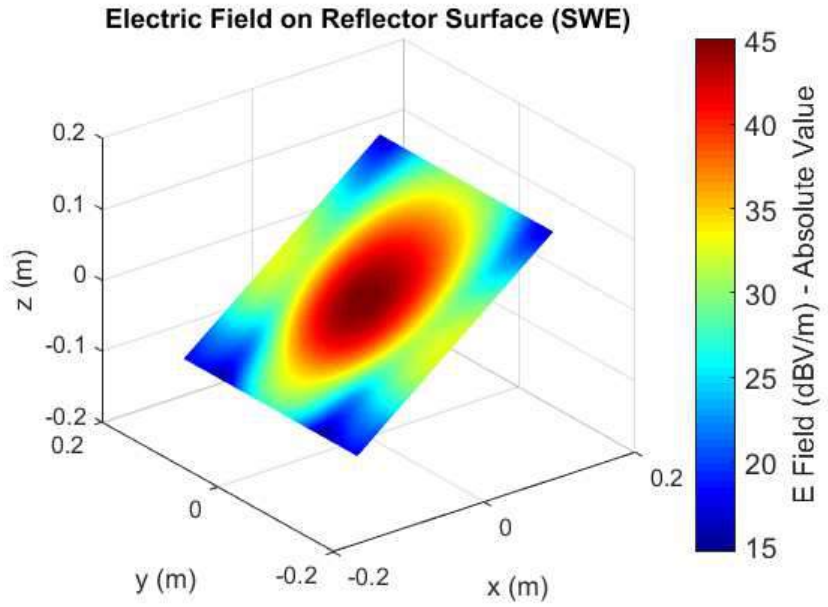

Figure 5.14: Electric field computed on the scattering surface using the SWE tool.

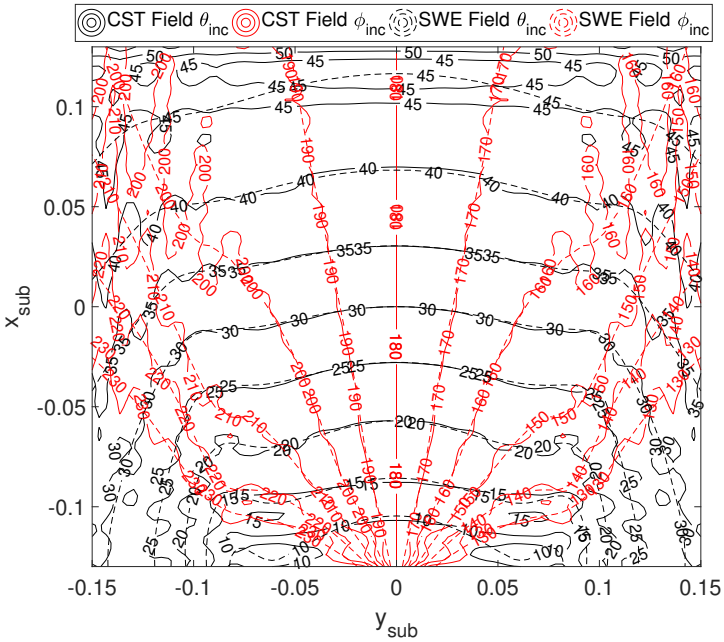

Figure 5.15: A comparison between the angle of incidence on a rectangular surface computed through a CST simulation and the SWE tool.

Incident Field on a Reflector Surface - Angle of Incidence

Another important parameter to check for validation is the actual angle of incidence of the field on the reflector surface. In fact, when considering near field illumination, the angle of incidence can not be approximated anymore as the one from a point source. This is a fundamental information that is required when calculating scattering from the surface. In particular, if a periodic surface is placed in correspondence of the reflector, which is the case of reflectarrays or FSS-subreflectors, the scattering matrix of each unit-cell composing the lattice depends on the actual angle of incidence. For each point on the reflector surface (x_s, y_s) the angle of incidence is calculated as the direction of the real part of the Poynting vector:

$$\mathbf{S}(x_s, y_s) = \frac{1}{2}\mathrm{Re}\{\mathbf{E}(x_s, y_s) \times \mathbf{H}^*(x_s, y_s)\} \tag{5.30}$$

The spherical angles of incidence (θ_{inc} and ϕ_{inc}) along the surface for the configuration represented in Fig. 5.12 are shown in Fig. 5.15. It can be observed that for points closer to the source the angles have an irregular behaviour, e.g. $\theta = 10°$ and ϕ lines intersections. On the other hand, when moving further from the source, the incidence angles resemble those of spherical waves, i.e. as originated by the point source. Again, the comparison with the CST extracted field shows that the tool provides the same results, but smoother and more regular: this is due to the interpolation done by the commercial software when extracting the results. In conclusion, no more use of the CST software is required for retrieving field distributions around the source.

5.5 Scattering Analysis - Physical Optics

In this section, the formulation of the physical optics approach for the analysis of scattering from perfectly conducting surfaces is presented as in [79]. A scattering problem consists of a known incident field and a scatterer with known geometry and electrical surface properties. The fields are related by:

$$\mathbf{E} = \mathbf{E}_i + \mathbf{E}_s \tag{5.31}$$

where $\mathbf{E}_i$ is the incident electrical field, $\mathbf{E}$ is the total field and $\mathbf{E}_s$ is the scattered field. If the surfaces of the scatterer are perfectly conducting the scattered field is generated by the induced surface currents on the scatterer. For non-perfectly conducting surfaces a set of equivalent electric and magnetic surface currents can be computed. The scattering analysis can be considered as a three step procedure where the first step is to calculate the induced or equivalent surface currents, the second step is to calculate the field radiated by these currents and the third step is to add the incident and the scattered field to obtain the total field.

5.5.1 Currents Induced on the Surface

The physical optics analysis assumes that the surface current in a point of a perfectly conductive surface is the same as the surface current flowing on infinite planar scatterer which is tangent to the surface at that point. The currents induced on a perfectly conductive infinite plane surface by an incident arbitrary field are expressed by the physical optics approximation [90] as

$$\boldsymbol{J}_e = 2\hat{n} \times \boldsymbol{H}^{inc} \tag{5.32}$$

where $\boldsymbol{J}_e$ is the electric current induced on the scatterer surface, $\hat{n}$ is a unit vector normal to the surface and $\boldsymbol{H}^{inc}$ is the incoming magnetic field. The equation is straightforward to derive for an incident plane wave and it is valid for any kind of incident field. The formula presented in 5.32 is valid for perfectly conducting scatterers. For reflectors with material properties the PO formulation is modified, and an approach using both electric and magnetic equivalent currents is adopted.

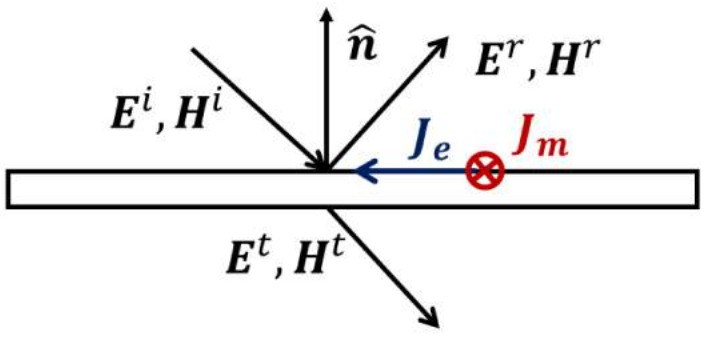

Figure 5.16: Fields and currents on a non-perfectly conducting scatterer.

Consider the configuration depicted in Fig. 5.16, where an incident wave is illuminating a non perfectly conducting screen. A procedure similar to the physical optics approach can be adopted to compute a set of equivalent electric and magnetic currents which approximate the exact equivalent currents radiating the scattered field. The reflection and transmission coefficients are known quantities used to express a relationship between the incident, reflected and transmitted electric and magnetic fields, denoted respectively with E^i, E^r, E^t and H^i, H^r, H^t. The equivalent currents can be computed from the electromagnetic boundary conditions, thus giving:

$$\boldsymbol{J}_e = \hat{n} \times (\boldsymbol{H}^i + \boldsymbol{H}^r - \boldsymbol{H}^t) \tag{5.33}$$

$$\boldsymbol{J}_m = -\hat{n} \times (\boldsymbol{E}^i + \boldsymbol{E}^r - \boldsymbol{E}^t) \tag{5.34}$$

It is important to remark that for the non-perfectly conducting surfaces, the reflection and transmission coefficients usually depend on the angle of incidence which means that it is necessary to know the direction of propagation of the incident. As shown in the following of the thesis, the derivation of the exact direction of incidence is a feature that was implemented in the developed tool and will be discussed and motivated in detail.

5.5.2 Radiation from a set of Currents

The radiated field from a set of equivalent currents running over a scatterer surface S can be computed from:

$$\mathbf{A}_e = \frac{\mu}{4\pi} \iint_S \mathbf{J}_e(\mathbf{r'}) \frac{e^{-jkR}}{R}\, ds' \tag{5.35}$$

$$\mathbf{A}_m = \frac{\epsilon}{4\pi} \iint_S \mathbf{J}_m(\mathbf{r'}) \frac{e^{-jkR}}{R}\, ds' \tag{5.36}$$

$$\mathbf{E} = -j\omega \left(\mathbf{A}_e + \frac{1}{k^2} \nabla\nabla \cdot \mathbf{A}_e \right) - \frac{1}{\epsilon} \nabla \times \mathbf{A}_m \tag{5.37}$$

$$\mathbf{H} = \frac{1}{\mu} \nabla \times \mathbf{A}_e - j\omega \left(\mathbf{A}_m + \frac{1}{k^2} \nabla\nabla \cdot \mathbf{A}_m \right) \tag{5.38}$$

where $\mathbf{A}_m$ and $\mathbf{A}_e$ are, respectively, the magnetic and electric vector potentials. The distance R is given by $R = |\mathbf{r} - \mathbf{r}'|$ where $\mathbf{r}$ is the point of observation and $\mathbf{r}'$ is the integration variable.

Following from equations (5.35)-(5.38), the formula for the radiated electric and magnetic field is given by:

$$\begin{aligned} \mathbf{E}(\mathbf{r}) = & \frac{\eta}{4\pi} \iint_S (\mathbf{J}_e(-\frac{j}{kR} - \frac{1}{k^2R^2} + \frac{j}{k^3R^3}) \\ & + (\mathbf{J}_e \cdot \hat{\mathbf{R}})\hat{\mathbf{R}}(\frac{j}{kR} - \frac{3}{k^2R^2} - \frac{3j}{k^3R^3}))e^{-jkR}k^2 ds' \\ & - \frac{1}{4\pi} \iint_S \mathbf{J}_m \times \hat{\mathbf{R}} \frac{1}{k^2R^2}(1 + jkR)e^{-jkR}k^2 ds' \end{aligned} \tag{5.39}$$

$$\begin{aligned}\mathbf{H}(\mathbf{r}) =& \frac{1}{4\pi}\iint_S \mathbf{J}_e \times \hat{\mathbf{R}}\frac{1}{k^2R^2}(1+jkR)e^{-jkR}k^2ds' \\ &+ \frac{\eta}{4\pi}\iint_S (\mathbf{J}_m(-\frac{j}{kR}-\frac{1}{k^2R^2}+\frac{j}{k^3R^3}) \\ &+ (\mathbf{J}_m\cdot\hat{\mathbf{R}})\hat{\mathbf{R}}(\frac{j}{kR}-\frac{3}{k^2R^2}-\frac{3j}{k^3R^3}))e^{-jkR}k^2ds'\end{aligned} \tag{5.40}$$

where

$$\hat{\mathbf{R}} = \frac{\mathbf{R}}{\mathrm{R}} = \frac{\mathbf{r}-\mathbf{r}'}{|\mathbf{r}-\mathbf{r}'|}. \tag{5.41}$$

The far field radiation is obtained from:

$$\mathbf{E}_{ff} = \lim_{r\to\infty}(\mathbf{E}(\mathbf{r})kre^{jkr}) \tag{5.42}$$

$$\mathbf{H}_{ff} = \lim_{r\to\infty}(\mathbf{H}(\mathbf{r})kre^{jkr}) \tag{5.43}$$

where

$$r = |\mathbf{r}| \tag{5.44}$$

From equations 5.39 and 5.40 one can obtain:

$$\begin{aligned}\mathbf{E}_{ff} =& -\frac{j\eta}{4\pi}\iint_S(\mathbf{J}_e-(\mathbf{J}_e\cdot\hat{r})\hat{r})e^{jk\mathbf{r}\cdot\hat{r}}k^2ds' \\ &+\frac{j}{4\pi}\hat{r}\times\iint_S\mathbf{J}_me^{jk\mathbf{r}\cdot\hat{r}}k^2ds'\end{aligned} \tag{5.45}$$

$$\begin{aligned}\mathbf{H}_{ff} =& -\frac{j}{4\pi}\hat{r}\times\iint_S\mathbf{J}_ee^{jk\mathbf{r}\cdot\hat{r}}k^2ds' \\ &-\frac{j}{4\pi\eta}\iint_S(\mathbf{J}_m-(\mathbf{J}_m\cdot\hat{r})\hat{r})e^{jk\mathbf{r}\cdot\hat{r}}k^2ds'\end{aligned} \tag{5.46}$$

where $\hat{r}$ is the direction of propagation $\hat{r} = \mathbf{r}/|\mathbf{r}|$.

In order to obtain an efficient procedure these surface integrals must be transformed into standard two-dimensional integrals on a plane. Integration techniques are discussed in detail in [4] where the related part of the simulation tool developed is described.

5.5.3 Physical Optics Application

For the aim of the research presented in this Chapter, the physical optics approach was used to compute the field scattered from a surface placed in the Fresnel zone of the feed source. The field was first reconstructed on the surface using a SWE-based code and then, from the knowledge of the currents distribution over the aperture, the far field radiation could be obtained using the equations described in Section 5.5.2

Depending on the surface considered, whether a purely metallic, an aperture or a periodic structure, different sets of currents can be used in order to obtain the scattered field. The differences between the approaches will be shown and discussed in detail for a practical case of study in Section 5.7

5.6 Spectral Domain Method of Moments with RWG sub-domain basis Functions for the Analysis of Frequency Selective Surfaces

5.6.1 Introduction

A frequency selective surface (FSS) is a periodic structure given by the infinite repetition of a basic element, called unit-cell, arranged along a plane and comprised between one or more dielectric layers. Unit-cells are typically composed of metallic patch or aperture elements. When excited by an incident plane wave, the structure response allows to achieve beam splitting [95] and polarizers properties [94] as well as frequency discrimination [93]. They are often used as subreflector in reflector antenna systems [96] which corresponds to the application of interest for this thesis work.

Electromagnetic problems associated with planar periodic structures, are often addressed with the method of moments (MOM) analysis conducted in the spectral domain. First, Green's functions in the spatial domain have not a closed-form representation, while an exact formulation is given in the spectral domain. Second, as the periodic structures are assumed to be infinitely extended, electrical quantities can be represented, in the spectral domain, as a summation of a continuum of modes over the considered surface. [97]

In this section, a tool based on the spectral domain method of moments (SD-MOM) has been developed in order to analyze a FSS. The domain of integration was divided in triangular sub-domains and the Rao-Wilton-Glisson (RWG) [98] basis functions were used to model the current distribution across the unit-cell. The spectral formulation for this function was investigated in detail and a methodology to establish the number of modes to truncate the

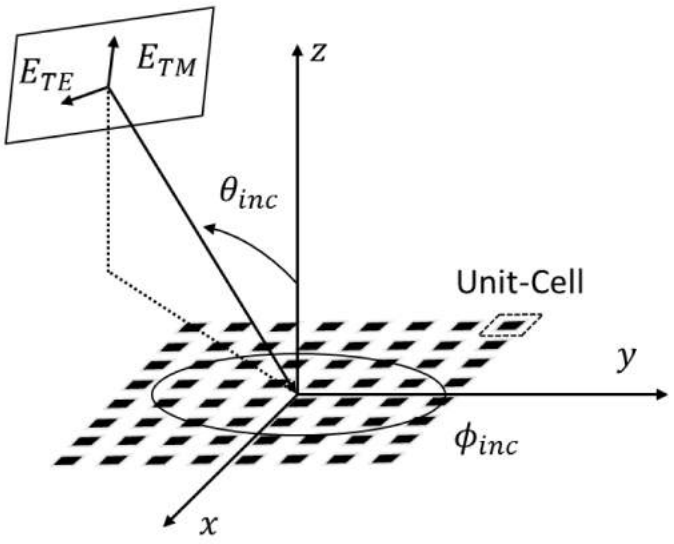

Figure 5.17: Schematic representation in spherical coordinates of a plane wave illuminating a periodic surface.

infinite sums was provided. A simple unit-cell design was chosen case of study and the tool is validated against CST by comparing the resulting scattering parameters. Results extracted using the code can easily be embedded in the rest of the tool. Therefore, the scattering analysis presented in Section 5.5 can be extended to calculate the radiation from a set of currents flowing on a FSS.

5.6.2 Floquet Analysis for Periodic Structures

A periodic structure is given by the uniformly spaced repetition of a geometry that will be referred to as unit-cell. When dealing with those kind of structures, the comprehension of the Floquet Theorem is fundamental, as it allows to express the fields interacting with the structure in function of the element periodicity.

Let Θ be an operator representing an electromagnetic quantity, electric or magnetic field, that interacts with the periodic structure. Assuming a time-dependence $e^{j\omega t}$ and a wave propagation along the z−direction, the wave equation to be solved is:

$$(\nabla^2 + k^2)\Theta(x, y, z) = 0 \tag{5.47}$$

with:

$$\Theta(x, y, z) = \Theta_t(x, y)e^{-jk_z z} \tag{5.48}$$

Referring to the schematic depicted in Fig. 5.17, considering the double periodicity along both the x− and the y−axis, one can obtain:

$$\Theta(x + d_x, y + d_y, z) = \Theta_t(x, y)e^{-j(k_x^i d_x + k_y^i d_y)}e^{-jk_z z} \tag{5.49}$$

where:

- d_x and d_y are the spatial periodicities
- $\boldsymbol{k}_t = \begin{bmatrix} k_x^i & k_y^i \end{bmatrix}$
- $k_x^i = k_{x,pq}^i = k\sin(\theta_{inc})\cos(\phi_{inc})$
- $k_y^i = k_{y,pq}^i = k\sin(\theta_{inc})\sin(\phi_{inc})$
- $k = 2\pi/\lambda$ is the magnitude of the wavevector of the incident wave

On the FSS surface, the field for each unit-cell is the same apart for a phase factor. It is fundamental to remark that the formulation presented allows to restrict the analysis of a periodic array to the analysis of the single unit-cell, assuming it part of a periodic lattice. Later, all the contributes are summed considering the relative phase shifts in order to find the total solution. Mathematics reported in [103] derives the following expression for the modal field solution of eq. 5.47:

$$\Theta_{pq}(x, y, z) = e^{jk_{xp}x}e^{jk_{yp}y}e^{-jk_z z} \tag{5.50}$$

where the indexes p, q represent the considered Floquet mode, and $k_x,\ k_y$ are given by:

$$\begin{aligned} k_x &= k_x^i - \frac{2\pi p}{d_x} \\ k_y &= k_y^i - \frac{2\pi q}{d_y} \end{aligned} \tag{5.51}$$

The waves can be classified in:

- propagating waves: $k^2 \geq k_x^2 + k_y^2$ and k_{zpq} is a real positive number: $k_{zpq} = \sqrt{k^2 - (k_x^2 + k_y^2)}$
- evanescent waves: $k^2 \leq k_x^2 + k_y^2$ and k_{zpq} is an imaginary negative number: $k_{zpq} = -j\sqrt{(k_x^2 + k_y^2) - k^2}$

Each component of the electric and magnetic field can finally be expressed as a Fourier series, for example:

$$E_z(x, y, z) = \sum_{p=-\infty}^{\infty} \sum_{q=-\infty}^{\infty} a_{pq} \Theta_{pq}(x, y, z) = \sum_{pq} a_{pq} e^{-jk_x x} e^{-jk_y y} e^{-jk_z z} \tag{5.52}$$

where a_{pq} refers to the modal amplitude. In conclusion, the total field will be obtained by the contributions of each unit-cell (p, q) with the proper phase-shift (exponential terms).

TE/TM Modes

The field can be expressed in a compact form with modal vectors of TE/TM Floquet components [106]. Recalling that a field can generally be expressed by the TE and TM components, the scattered field from a FSS surface is given by:

$$\mathbf{E}(\mathbf{r}, z) = \sum_{ipq} a_{ipq} e^{\pm jk_{zpq} z} \Psi_{pq}(\mathbf{r}) \mathbf{K}_{ipq} \tag{5.53}$$

$$\mathbf{H}(\mathbf{r}, z) = \mp \sum_{ipq} \eta_{ipq} a_{ipq} e^{\pm jk_{zpq} z} \Psi_{pq}(\mathbf{r}) \hat{z} \times \mathbf{K}_{ipq} \tag{5.54}$$

where:

- η_{ipq} is the modal admittance for TM ($i = 1$) or TE ($i = 2$) modes;
- $\Psi_{pq} = e^{-j\mathbf{k}_{tpq} \cdot \mathbf{r}}$ is the Floquet phasor;
- $\mathbf{K}_{1pq} = \frac{k_{tx}\hat{x} + k_{ty}\hat{y}}{k_{tpq}}$ and $\mathbf{K}_{2pq} = \hat{z} \times \mathbf{K}_{1pq}$ are parallel or orthogonal to $\mathbf{k}_{tpq}$ for TM and TE modes respectively.

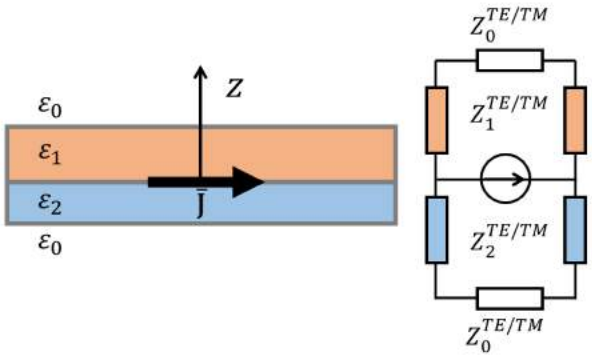

Figure 5.18: Equivalent transmission line representation of a metallich patch unit-cell in a layered media.

5.6.3 Analysis of a Frequency Selective Surface

The technique used to analyze a FSS is the so called equivalent modal transmission line theory. The FSS of metallic patches is represented as an impedance in parallel with the equivalent transmission lines of the two dielectric layers that enclose it, see Fig. 5.18. The field is expressed as an infinite sum of Floquet modes, each one given by the superimposition of a TM and a TE component. The analysis in the spectral domain (SD) is a general technique that is used for the study of planar periodic structures for which the thickness of the metallizations can be neglected. This formulation results to be convenient since the Green's functions can be expressed in closed form, while this is not possible in the spatial domain. In order to study the behaviour of a FSS, consider the scenario depicted in Fig. 5.17, where a plane wave (TE or TM polarized) is illuminating an infinitely periodic structure composed of metallic patch elements. In this Section, the analysis will be restricted only to arrays of metallic elements, since the configuration chosen later for experimental validation will be of this kind. The FSS analysis formulation for an array of slots is similar and exhaustive literature for this case can be found in [92], [107]. The first step in formulating the problem of electromagnetic scattering from a frequency selective surface is to relate the fields scattered from the FSS to the surface currents induced on the screen by the incident field. The electric field scattered by the periodic metallizations is given by [91]:

$$\boldsymbol{E}(x,y) = \sum_{pq} \tilde{\boldsymbol{G}} \cdot \tilde{\boldsymbol{J}}(k_{xpq}, k_{ypq}) e^{j(k_{xpq}x+)k_{ypq}y} \tag{5.55}$$

where $\tilde{\boldsymbol{J}}$ and $\tilde{\boldsymbol{G}}$ are respectively the electric currents impressed on the FSS surface and the dyadic Green function, both in the spectral domain. Due to the planar nature of the FSS, the induced surface current $\boldsymbol{J}(k_{xpq}, k_{ypq})$ has only nonzero transverse components $\boldsymbol{J}_t$. The field is expressed as the sum of the field contributions given by each unit-cell, which are accounted in the p, q sum indexes. The boundary conditions for the electric field require that the tangential component is zero on the perfect electric conductor (PEC)

element surface. The formulation is given by the electric field integral equation (EFIE):

$$\boldsymbol{E}_t + \boldsymbol{E}_{imp} = 0 \tag{5.56}$$

This is the equation to be solved by method of moments (MOM) [101].

5.6.4 Sub-domain Basis Functions

The method of moments formulation begins by expressing the unknown current distribution as an infinite summation of unknown coefficients multiplied by a set of basis functions:

$$\boldsymbol{J}(\boldsymbol{r}_t) = \sum_{n=1}^{N} \mathrm{I}_n \boldsymbol{J}_n(\boldsymbol{r}_t) \tag{5.57}$$

where $\boldsymbol{t} = x\hat{x} + y\hat{y}$ is a generic point on the surface, N is the number of basis functions, I_n are the coefficients to be determined and $\boldsymbol{J}_n(\boldsymbol{r}_t)$ are the chosen basis functions.

Two main families of basis function exist: entire-domain basis functions and sub-domain basis functions. Typically, the first ones are well suited for structures with a regular shape. However, if an arbitrary geometry is considered for the metallic patch element of the unit-cell, the second approach has to be adopted.

Entire-Domain Basis Functions

The first class of basis functions considered are the so-called entire domain basis functions. They are used to model current distributions for specific geometries of the patch or the aperture of an FSS. Authors in [92] give an exhaustive list of entire-domain basis functions for typical geometries such as rectangular and circular patches or apertures, dipoles and crosses. The use of entire-domain basis functions results in a smaller size of the MOM matrix, thus providing faster results.

Sub-Domain Basis Functions

Sub-domain basis functions allow the analysis of arbitrarily shaped FSS unit-cells. The periodic element is discretized and a function is associated to each sub-domain element. Obviously, depending on the number of basis functions used, a better accuracy can be obtained at the cost of larger matrices to be solved. Typical sub-domain basis functions used in the literature are:

- Roof-top [99]
- Surface-patch [109]
- Rao-Wilton-Glisson [98]

In [118], the Fourier transform of the three presented sub-domain basis functions is given.

5.6.5 RWG Sub-Domain Basis Function

In order to describe arbitrary geometry FSS, the sub-domain function introduced by Rao-Wilton-Glisson (RWG) can be employed for its ability to model arbitrarily shaped structure. RWG basis functions were first introduced in [98], for analyzing problems of scattering from structures of arbitrary shape. Referring to Fig. 5.19, each RWG is associated to a pair of adjacent triangles having a common edge. The function is defined as:

$$\boldsymbol{f}_n(\boldsymbol{r}) = \begin{cases} \frac{l_n}{2A_n^+}\boldsymbol{\rho}_n^+ & \text{if } \mathbf{r} \text{ in } T_n^+ \\ \frac{l_n}{2A_n^-}\boldsymbol{\rho}_n^- & \text{if } \mathbf{r} \text{ in } T_n^- \\ 0 & \text{otherwise} \end{cases} \tag{5.58}$$

where $A_n^{\pm}$ is the area of the triangle $T_n^{\pm}$. The vector $\boldsymbol{\rho}_n^{\pm}$ connects the associated vertex to the point of observation: $\boldsymbol{\rho}_n^{\pm} = \pm(\boldsymbol{\rho}_n^{\pm} - \boldsymbol{r})$. RWG functions allow to represent arbitrary current distributions, and it is possible to design a non-uniform meshing in order to provide better detailing in proximity of critical points.

5.6.6 Fourier Transform of RWG Basis Functionss

In order to have an efficient code for analyzing frequency selective surfaces using the spectral domain MOM, the Fourier transform of the RWG function has to be expressed in an analytical form. Authors in [118] present an analytical formula for expressing a triangular-patch discretization in the spectral domain, and compare it to other sub-domain formulation such as the roof-top [99] and the surface-patch [109]. However, this formulation is valid only for a uniform discretization and becomes not ideal for meshing an arbitrarily shaped metallization.

Two alternative formulations for obtaining an analytical expression of the RWG function in the spectral domain have been investigated in [111] and [112]. In [111], the formulas introduced in [113][114] for the Fourier transform of functions on polygon were used to compute the Fourier transform of the RWG functions in a triangular domain. Authors in [114] give an expression

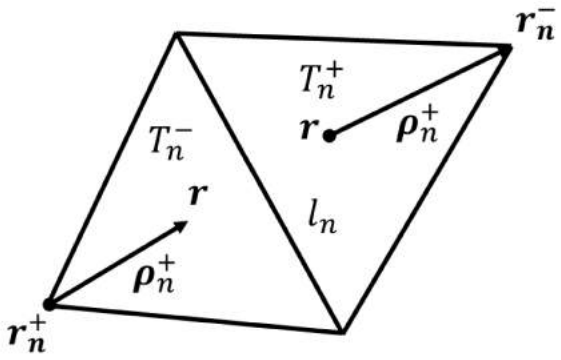

Figure 5.19: Rao-Wilton-Glisson (RWG) basis function.

for transforming a function $\mathbf{t}(\boldsymbol{r}) = (\boldsymbol{r} - \overline{\boldsymbol{r}})$ over a polygonal domain Σ, where $\overline{\boldsymbol{r}}$ is a generic point in the plane:

$$\begin{aligned}\boldsymbol{T}(\boldsymbol{k};\overline{\boldsymbol{r}}) &= \iint_{\Sigma}(\boldsymbol{r}-\overline{\boldsymbol{r}})e^{j\boldsymbol{k}\cdot\boldsymbol{r}}dA \\ &= \frac{1}{|\boldsymbol{k}|^2}\sum_{n=1}^{N} e^{j\boldsymbol{k}\cdot\boldsymbol{r}_{nc}}\cdot\{[\hat{\boldsymbol{z}}\times\boldsymbol{l}_n + (j\boldsymbol{r}_{nc} - j\overline{\boldsymbol{r}} - \frac{2\boldsymbol{k}}{|\boldsymbol{k}|^2})\hat{\mathbf{z}}\cdot\boldsymbol{l}_n\times\boldsymbol{k}]\cdot \\ &= j_0(\frac{\boldsymbol{k}\cdot\boldsymbol{l}_n}{2}) - \boldsymbol{l}_n\frac{\hat{\boldsymbol{z}}\cdot\boldsymbol{l}_n\times\boldsymbol{k}}{2}j_1(\frac{\boldsymbol{k}\cdot\boldsymbol{l}_n}{2})\}\end{aligned} \tag{5.59}$$

where

$$\begin{aligned}&\boldsymbol{l}_n = \boldsymbol{r}_{n+1} - \boldsymbol{r}_n \\ &\boldsymbol{r}_{nc} = (\boldsymbol{r}_{n+1} + \boldsymbol{r}_n)/2 \\ &\boldsymbol{r} = x\hat{\boldsymbol{x}} + y\hat{\boldsymbol{y}} \\ &\boldsymbol{k} = k_x\hat{\boldsymbol{x}} + k_y\hat{\boldsymbol{y}}\end{aligned} \tag{5.60}$$

and $\boldsymbol{r}_n$ represents the $n-$th vertex of the triangle, $\overline{\boldsymbol{r}}$ is the free vertex of the basis function, $A^{\pm}$ is the area of the triangle $T^{\pm}$, $\boldsymbol{l}_n$ is the length of the common edge and j_n denotes the spherical Bessel function of the first kind of order n. Fourier transforms are taken in both T^+ and T^- and then summed to obtain the overall transform for each function $\boldsymbol{f}_n(\boldsymbol{r})$.

Another formulation to obtain the spectral domain representation of RWG basis functions on non-uniform triangular domains is provided in [112]. For instance, considering the triangle T^+ of Fig. 5.19, a change of variables has to be performed:

$$\boldsymbol{r} = \boldsymbol{r}_n^+ + \boldsymbol{J}_+\cdot\overline{\boldsymbol{r}} \tag{5.61}$$

where

$$\boldsymbol{J}_{\pm} = \begin{bmatrix} x_{1^{\pm}} - x_{3^{\pm}} & x_{2^{\pm}} - x_{3^{\pm}} \\ y_{1^{\pm}} - y_{3^{\pm}} & y_{2^{\pm}} - y_{3^{\pm}}\end{bmatrix} \tag{5.62}$$

and

$$\overline{\boldsymbol{r}} = \begin{bmatrix}\xi \\ \eta\end{bmatrix} \tag{5.63}$$

The variable $\tilde{\boldsymbol{k}}_t$ has to be introduced:

$$\tilde{\boldsymbol{k}}_t = \boldsymbol{k}\cdot\boldsymbol{J}_+ = \begin{bmatrix}\tilde{k}_x & \tilde{k}_y\end{bmatrix} \tag{5.64}$$

The Fourier transform of a RWG basis function defined on a triangular domain is finally given by the formula:

$$\begin{aligned}\boldsymbol{T}(\boldsymbol{k};\overline{\boldsymbol{r}}) &= \iint_{T_{\pm}}(\boldsymbol{r}-\overline{\boldsymbol{r}})e^{j\mathbf{k}\cdot\boldsymbol{r}}dA \\ &= l_{edge}e^{j\boldsymbol{k}\cdot\boldsymbol{r}_{fv}^{\pm}}\boldsymbol{J}_{\pm}\cdot\begin{bmatrix}\frac{\Psi(\tilde{k}_x))+(\tilde{k}_y-\tilde{k}_x)\frac{d\Psi(\tilde{k}_x)}{d\tilde{k}_x}-\Psi(\tilde{k}_y))}{(\tilde{k}_x-\tilde{k}_y))^2} \\ \frac{\Psi(\tilde{k}_y))+(\tilde{k}_x-\tilde{k}_y)\frac{d\Psi(\tilde{k}_y)}{d\tilde{k}_y}-\Psi(\tilde{k}_x))}{(\tilde{k}_x-\tilde{k}_y))^2}\end{bmatrix}\end{aligned} \tag{5.65}$$

The complete expression for the function $\Psi(\tilde{k}_x, y)$ and its derivatives can be found in [115].

5.6.7 Spectral Domain Method of Moments (SD-MOM)

Recalling the EFIE in eq. (5.56), it can be rewritten as:

$$\boldsymbol{E}_t = -\boldsymbol{E}_{imp} \tag{5.66}$$

The electric currents flowing on the surfaces of the metallizations are expanded in basis functions:

$$\boldsymbol{J}(\boldsymbol{r}_t) = \sum_{n=1}^{N} \mathrm{I}_n \boldsymbol{J}_n(\boldsymbol{r}_t) \tag{5.67}$$

Eq. 5.67 can be expressed in the transform domain as:

$$\tilde{\boldsymbol{J}}(\boldsymbol{k}_t) = \sum_{n=1}^{N} \mathrm{I}_n \tilde{\boldsymbol{J}}_n(\boldsymbol{k}_t) \tag{5.68}$$

From eq. 5.55, one can obtain:

$$\boldsymbol{E}_t(\boldsymbol{J}) = \sum_{n=1}^{N} I_n \boldsymbol{E}_t(\boldsymbol{J}_n) = \sum_{n=1}^{N} I_n \sum_{pq} \tilde{\boldsymbol{G}}_t^{ee}(\boldsymbol{k}_{t,pq}) \tilde{J}_n(\boldsymbol{k}_{t,pq}) e^{-j(\boldsymbol{k}_{t,pq}\cdot\boldsymbol{r})} \tag{5.69}$$

where

$$\boldsymbol{k}_t = k_{x,pq}\hat{x} + k_{y,pq}\hat{y} \tag{5.70}$$

The quantities $k_{x,pq}$ and $k_{y,pq}$ are the transverse components of the wavevector relative to the Floquet mode of indexes (p, q). The unit-vectors in the spectral domain are defined as:

$$\hat{u}_{pq} = \frac{\boldsymbol{k}_{t,pq}}{|\boldsymbol{k}_{t,pq}|} \tag{5.71}$$

$$\hat{v}_{pq} = \hat{z} \times \hat{u}_{pq} \tag{5.72}$$

The inner product between two functions $\boldsymbol{A}$ and $\boldsymbol{b}$ is defined as:

$$\langle \boldsymbol{A}, \boldsymbol{B} \rangle = \iint_{patch} \boldsymbol{A}^* \cdot \boldsymbol{B} \; dS \tag{5.73}$$

The Galerkin method of moments is applied [100] to obtain the MOM algeabric system:

$$\boldsymbol{Z}_{MOM}\boldsymbol{I} = \boldsymbol{V} \tag{5.74}$$

where $\boldsymbol{V} = \{V_m\}^T_{m=1,\ldots,N}$ is the column vector of the electric field components impressed along the basis function transforms, i.e. V_m given by:

$$V_m = -\tilde{\boldsymbol{J}}_m^*(\boldsymbol{k}_t) \cdot \boldsymbol{E}_{imp}(\boldsymbol{k}_t) \tag{5.75}$$

The set of coefficients to be determined using the MOM is represented by $\boldsymbol{I} = \{V_n\}_{n=1,\ldots,N}$. The elements of the impedance matrix $\boldsymbol{Z}_{MOM}$ are obtained from:

$$Z_{MOM}^{mn} = \iint_{patch} \boldsymbol{J}_m^* \cdot \boldsymbol{E}_t(\boldsymbol{J}_n) \; dS = \sum_{pq} \boldsymbol{J}_m^*(\boldsymbol{k}_{t,pq}) \cdot \tilde{\boldsymbol{G}}_t^{ee}(\boldsymbol{k}_{t,pq}) \boldsymbol{J}_n(\boldsymbol{k}_{t,pq}) \tag{5.76}$$

By expressing the $\tilde{\boldsymbol{G}}_t^{ee}$ as in [102], one can obtain:

$$Z_{MOM}^{mn} = \sum_{p,q} \tilde{\boldsymbol{J}}_m^*(\boldsymbol{k}_{t,pq}) \cdot \left[-Z_{GF}^{TM}(\mathbf{k}_{t,pq}) \hat{u}_{pq} \hat{u}_{pq} - Z_{GF}^{TE}(\boldsymbol{k}_{t,pq}) \hat{v}_{pq} \hat{v}_{pq} \right] \cdot \tilde{\boldsymbol{J}}_n(\boldsymbol{k}_{t,pq}) \tag{5.77}$$

where $Z_{GF}^{TM/TE}$ are the TM/TE components of the Green's function for the electric field in the spectral domain. The $Z_{GF}^{TM/TE}$ components can be obtained by solving the equivalent transmission line of the considered dielectric layer. For a patch embedded between two semi-infinite dielectrics, which is the case of interest for this thesis, they are given by:

$$Z_{GF}^{TM/TE}(\boldsymbol{k}_{t,pq}) = \left[Y_1^{TM/TE}(\boldsymbol{k}_{pq}) + Y_1^{TM/TE}(\boldsymbol{k}_{pq}) \right] \tag{5.78}$$

with:

$$Y_i^{TM}(\boldsymbol{k}_{t,pq}) = \frac{\omega \varepsilon_i}{k_{z_i pq}} \tag{5.79}$$

and

$$Y_i^{TE}(\boldsymbol{k}_{t,pq}) = \frac{k_{z_i pq}}{\omega \mu_0} \tag{5.80}$$

where:

$$k_{z_i pq} = \sqrt{\varepsilon_i k_o^2 - k_{xpq}^2 - k_{ypq}^2} \tag{5.81}$$

The MOM matrix expression can be written in a more compact form:

$$\boldsymbol{Z}_{MOM} = \boldsymbol{Q}^H \boldsymbol{Z}_{GF} \boldsymbol{Q} \tag{5.82}$$

The $\boldsymbol{Z}_{GF}$ is a $2M \times 2M$ diagonal matrix of the Green's function sampled at the Floquet wave (FW)-numbers, where M is the total number of considered modes. $\boldsymbol{Q}$ is a $2M \times N$ matrix; the elements composing the i-th line of $\boldsymbol{Q}$ are given by:

$$Q_{pq,n}^{TM} = \tilde{\boldsymbol{J}}_m(\boldsymbol{k}_{t,pq}) \cdot \hat{u}_{pq} \tag{5.83}$$

$$Q_{pq,n}^{TE} = \tilde{\boldsymbol{J}}_m(\boldsymbol{k}_{t,pq}) \cdot \hat{v}_{pq} \tag{5.84}$$

Following the procedure of [104][105], the vector of unknown coefficients $\boldsymbol{I}$ can be expressed in terms of the floquet wave voltage vector:

$$\boldsymbol{I}_{FW} = \boldsymbol{Q}_A \boldsymbol{I} \tag{5.85}$$

where $\boldsymbol{Q}_A$ is a $2M_A \times N$ matrix related to the first M_A TM/TE modes considered. The index M_A refers to the numbers of accessible modes [108]. Since for our analysis only the fundamental mode ($p = 0,\ q = 0$) will be of interest, we will assume $M_A = 1$. The incident electric field is projected on the Floquet wave-vectors, thus obtaining:

$$\boldsymbol{V} = \boldsymbol{Q}_A^H \boldsymbol{V}_{FW}^{imp} \tag{5.86}$$

where $\boldsymbol{V}_{FW}^{imp}$ is the incident field. The MOM system can finally be expressed as:

$$\begin{aligned} \boldsymbol{I}_{FW}^{FSS} &= \boldsymbol{Y}_{FW} \boldsymbol{V}_{FW}^{imp} \\ \boldsymbol{Y}_{FW} &= \boldsymbol{Q}_A \boldsymbol{Z}_{MOM}^{-1} \boldsymbol{Q}_A^H \end{aligned} \tag{5.87}$$

Equations in (5.87) give a relationship between the impressed mode voltages and the modal currents associated to the Floquet wave modes. For the FSS composed of metallic patch elements the following equations can be derived:

$$\begin{aligned} \boldsymbol{V}_{FW} &= \boldsymbol{V}_{FW}^{imp} - \boldsymbol{Z}_{GF}\boldsymbol{I}_{FW}^{FSS} = \left[\boldsymbol{I} - \boldsymbol{Z}_{GF}\boldsymbol{Y}_{FW}\right]\boldsymbol{V}_{FW}^{imp} \\ \boldsymbol{Y}_{FSS} &= \boldsymbol{Y}_{FW}\left[\boldsymbol{Y}_{GF} - \boldsymbol{Y}_{FW}\right]^{-1}\boldsymbol{Y}_{GF} \end{aligned} \tag{5.88}$$

The matrix $\boldsymbol{Y}_{FSS}$ is the admittance matrix that describes the FSS and $\boldsymbol{Z}_{FSS} = (\boldsymbol{Y}_{FSS})^{-1}$ is the relative impedance matrix. Recalling the relationship:

$$\boldsymbol{S} = (\boldsymbol{Z} - \boldsymbol{I}) \cdot (\boldsymbol{Z} + \boldsymbol{I})^{-1} \tag{5.89}$$

the quantities of interest to be extracted are the reflection and the transmission coefficients for the TM and TE components of the fundamental mode. In order to compute the scattering parameters at the interfaces between the dielectric layers and the air, a translation has to be applied. This corresponds to a phase-shift which is function of the layer thickness and dielectric properties:

$$\boldsymbol{S}_{FSS,diel} = \boldsymbol{S}_{diel} \cdot \boldsymbol{S}_{FSS} \cdot \boldsymbol{S}_{diel} \tag{5.90}$$

where $\boldsymbol{S}_{diel}$ is diagonal matrix with elements expressed in the form

$$\boldsymbol{S}_{diel,i} = e^{-j\boldsymbol{z}_i h_i} \tag{5.91}$$

where the index i refers to the upper or lower dielectric layer.

The reader can refer to [102] for the complete derivation of the scattering parameters. In this Chapter, only the fundamental steps of the spectral domain method of moments were reported, as the the work was more focused on the actual implementation of the SD-MOM allowed by the RWG sub-domain basis functions. For our analysis purposes it is important to point out that for a plane wave incidence, two sets of S-parameters have to be computed:

$$\mathbf{S}_{refl} = \begin{pmatrix} R_{TETE} & R_{TETM} \\ R_{TMTE} & R_{TMTM} \end{pmatrix} \tag{5.92}$$

$$\mathbf{S}_{trans} = \begin{pmatrix} T_{TETE} & T_{TETM} \\ T_{TMTE} & T_{TMTM} \end{pmatrix} \tag{5.93}$$

The first set, eq. (5.92), refers to the scattering parameters describing the portion of radiation that gets reflected by the periodic structure. The second set, eq. (5.93), corresponds to the fields that get transmitted through the FSS. Cross-parameters such as S_{TETM} describe the quantity of TM polarized incident field that gets reflected/transmitted on the orthogonal polarization (TE).

5.6.8 Investigation on RWG Basis Function in Spectral Domain

The two ways of obtaining an expression for the RWG functions in the spectral domain were both implemented in MATLAB. They proved to give similar results, however, the second one was found to be faster and therefore it was the one chosen to be implemented in the tool. From a practical point of view, a triangular meshing is obtained for the metallic patches of the FSS; an example is illustrated in Fig. 5.20. A RWG basis function is associated to each mesh element. The total number of mesh elements corresponds to the number of inner edges: N_{edges}. Recalling the expression to obtain the MOM matrix, for each couple of basis function of indexes m, n with $m, n = 1, \ldots, N_{edges}$.

$$Z_{MOM}^{mn} = \sum_{p,q} \tilde{\mathbf{J}}_m^*(\mathbf{k}_{t,pq}) \cdot \left[-Z_{GF}^{TM}(\mathbf{k}_{t,pq}) \hat{u}_{pq} \hat{u}_{pq} - Z_{GF}^{TE}(\mathbf{k}_{t,pq}) \hat{v}_{pq} \hat{v}_{pq} \right] \cdot \tilde{\mathbf{J}}_n(\mathbf{k}_{t,pq}) \tag{5.94}$$

where $\tilde{\mathbf{J}}_m(\mathbf{k}_{t,pq})$ and $\tilde{\mathbf{J}}_n(\mathbf{k}_{t,pq})$ are the Fourier transform of the n-th and m-th basis function, sampled at the Floquet wave-numbers. The expression in 5.94 can be written in a more compact form:

$$\mathbf{Z}_{MOM} = \mathbf{Q}^H \mathbf{Z}_{GF} \mathbf{Q} \tag{5.95}$$

the elements composing the i-th line of Q are given by:

$$Q_{pq,n}^{TM} = \tilde{\mathbf{J}}_m(\mathbf{k}_{t,pq}) \cdot \hat{u}_{pq} \tag{5.96}$$

$$Q_{pq,n}^{TE} = \tilde{\boldsymbol{J}}_m(\boldsymbol{k}_{t,pq}) \cdot \hat{v}_{pq} \tag{5.97}$$

where $\hat{u}_{pq}$ and $\hat{v}_{pq}$ are the unit-vectors in the spectral domain, and they are given by:

$$\hat{u}_{pq} = \frac{\boldsymbol{k}_{t,pq}}{|\boldsymbol{k}_{t,pq}|} \tag{5.98}$$

$$\hat{v}_{pq} = \hat{z} \times \hat{u}_{pq} \tag{5.99}$$

The convergence of the sum in 5.94 depends on the decay rate of the functions $\tilde{\boldsymbol{J}}_m(\boldsymbol{k}_{t,pq})$, for increasing mode indexes p, q. The maximum mode number M to which the Floquet expansion has to be truncated is chosen in order to have the majority of energy contained in the first $(2M + 1)^2$ modes. In this way, the contribution of the modes excluded can be considered negligible. The works mentioned before never examined the convergence of the RWG Fourier transform, therefore, in this Chapter, a deep investigation on its properties will be reported.

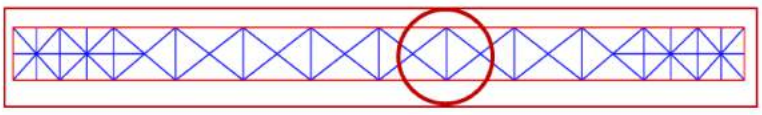

Figure 5.20: Triangular meshing of a dipole element.

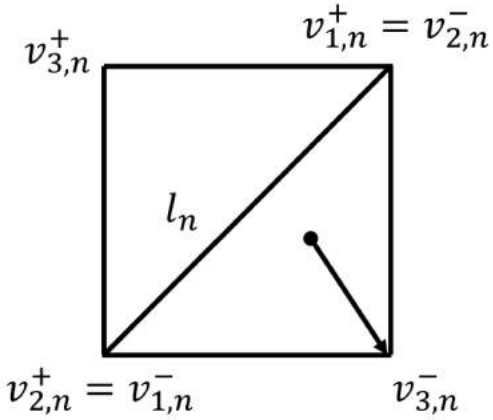

Figure 5.21: RWG basis function domain under analysis.

On the one hand, RWG basis functions allow the modeling of any arbitrary shape for the patch element of the unit cell under analysis. The formulation presented in equation (5.65) enables a non-uniform meshing, as in Fig. 5.20, where the mesh of some areas of the patch is refined. On the other hand, when implementing the spectral domain MOM, some considerations have to be made regarding the convergence of the series involving the considered RWG transform. In this regards, a study of the behavior of the Fourier transform of the RWG basis function results to be a fundamental step. Since the transform decay rate weights considerably on the the overall computational time and resources to be dedicated to the simulation, the adequate number of Floquet modes M to be considered has to be carefully studied.

A simple case of study is presented in Fig. 5.21: the sub-domain of a RWG function, composed of two adjacent square triangles, is illustrated. The Fourier transform of the RWG basis function is computed on this sub-domain. It is important to remark that, for each sub-domain, $(2M+1)^2$ transforms of the basis function have to be computed, each one corresponding to a wave-number $\mathbf{k}_{t,pq}$. In this section, the magnitude of the spectral components of the RWG basis function will be analyzed in detail, for increasing number of considered modes M.

Recalling the expression (5.51), the wave-numbers depend from the angle of incidence and the space periodicity of the unit-cell. Since the wave-number together with the mesh element dimension are found in the expression for computing the analytical Fourier transform of the RWG basis function, an investigation on the impact of these parameters on the transform convergence is carried out in this Section. In detail, parameters for which the RWG transform is studied are:

- The domain size (i.e. how fine is the mesh): l_{edge}
- The direction of incidence: θ_{inc} and ϕ_{inc}
- The cell periodicity: d_x and d_y

A metric is defined in order to obtain the minimum mode order M to be selected for achieving an accurate result. The minimum M is chosen such as:

$$\frac{E_{M+10} - E_M}{E_M} \cdot 100 < 0.5\% \tag{5.100}$$

where E_K is the energy contained in the first K modes:

$$E_K = \sum_{p,q=-K}^{K} |\tilde{\boldsymbol{J}}(\boldsymbol{k}_{t,pq})|^2 \tag{5.101}$$

In other words, the great majority of the Energy will be contained in the first M modes. The metric takes into account up to 10 modes more when checking the percentage decrease for a reason that will be explained in the following paragraphs.

Figure 5.22, shows the magnitude of the RWG transform $\hat{\mathbf{J}}(\mathbf{k}_{t,pq})$ for increasing values of mode order p, q. A large number of truncation index is chosen here, $M = 80$, in order to display the distribution of a sufficiently high number of modes. The meshing considered had an element size of $\mathrm{l}_{edge} = \frac{\lambda}{10}$ (i.e. the coarser mesh allowed in the code) for a normal incidence and a periodic spacing of $d_x = d_y = \frac{\lambda}{2}$ along both axes. According to our analysis, the minimum number of Floquet modes M for truncation is given by M = 20. The reason of the +10 addition in eq. (5.100) can be explained by observing the shape of the curve in Fig. 5.22. In fact, some ripples can be observed while the function decreases, and therefore a larger window for computing the modes energy is retained.

The mesh element size is later reduced to $\mathrm{l}_{edge} = \frac{\lambda}{20}$. The related RWG transform behavior is plotted in Fig. 5.23. It can be observed that the amplitude decrease is now slower with respect to the previous case, and around M = 30 are needed to achieve the energy constraint. This means that as the meshing finesse is increased, and consequently a better accuracy of the results can be obtained, the complexity of the system to be solved grows. Therefore, a trade-off between meshing precision and simulation time has to be established.

The cell-periodicity is now reduced along both axes: $d_x = d_y = \frac{\lambda}{4}$, for an edge length restored to $\mathrm{l}_{edge} = \frac{\lambda}{10}$. The Fourier transform for varying indexes p, q is shown in Fig. 5.24. The decrease is accelerated, and only M = 15 modes are required in this case. Finally, the cell-periodicity is reduced along only one axis: $d_x = \frac{\lambda}{4}$, $d_y = \frac{\lambda}{2}$. The effects on the curve shape are depicted in Fig. 5.25. The decrease is now accelerated only along one mode order axis (q), while along the other one it resembles the behavior of Fig. 5.22.

In conclusion, the study was not meant to provide an exact rule to follow when deciding for the order of truncation for the Floquet modes. However, the availability of a tool like the one presented in this Section, allows the designer to have a fast quantitative and qualitative help in the phase preceding the solution of the MOM equations. In fact, just by providing the basic FSS simulation parameters such as the mesh size, the angle of incidence and the element periodicity, one can have an indication about the resources and the time needed for the configuration under analysis.

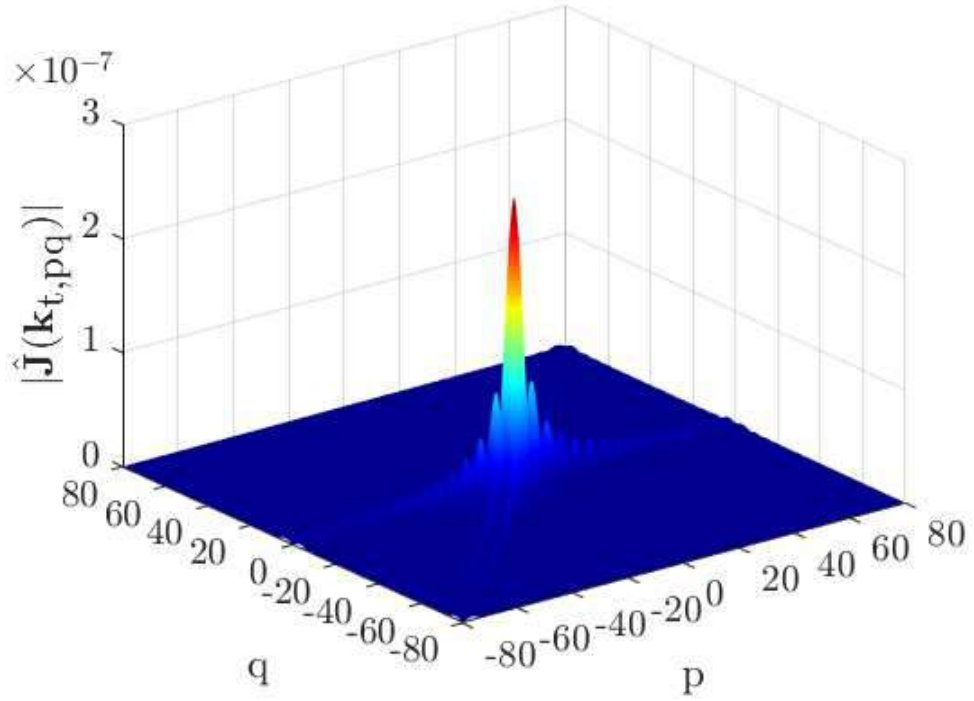

Figure 5.22: Magnitude of the RWG transform for $l_{edge} = \lambda/10$, $d_x = d_y = \lambda/2$, $\theta_{inc=0.1^\circ}$, $\phi_{inc=0.1^\circ}$ and $M = 80$.

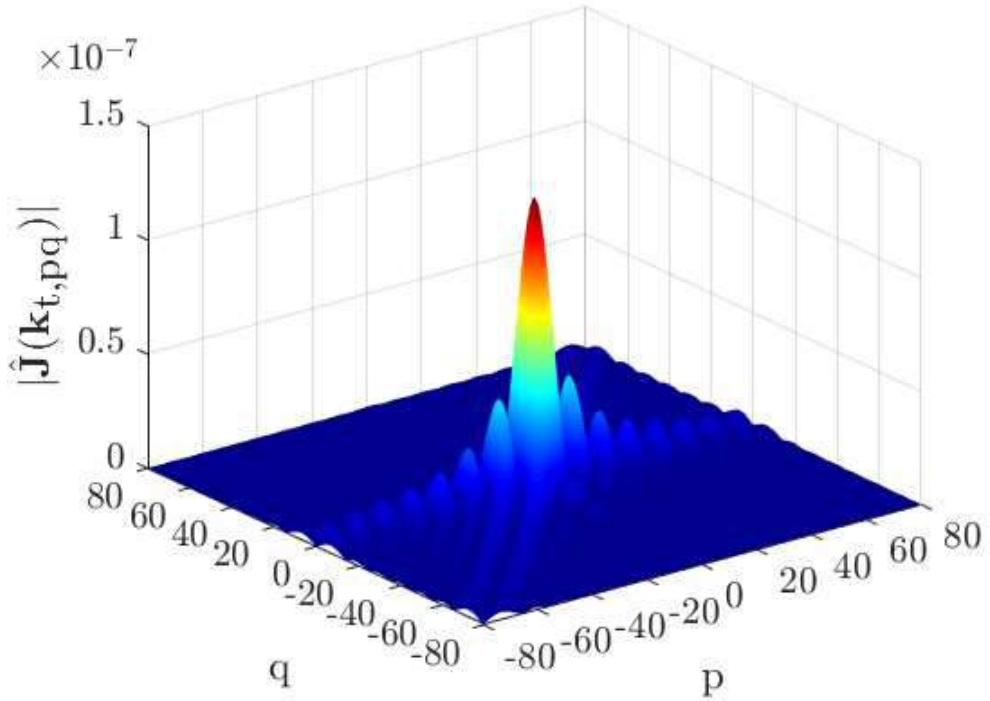

Figure 5.23: Magnitude of the RWG transform for $l_{edge} = \lambda/20$, $d_x = d_y = \lambda/2$, $\theta_{inc=0.1^\circ}$, $\phi_{inc=0.1^\circ}$ and $M = 80$.

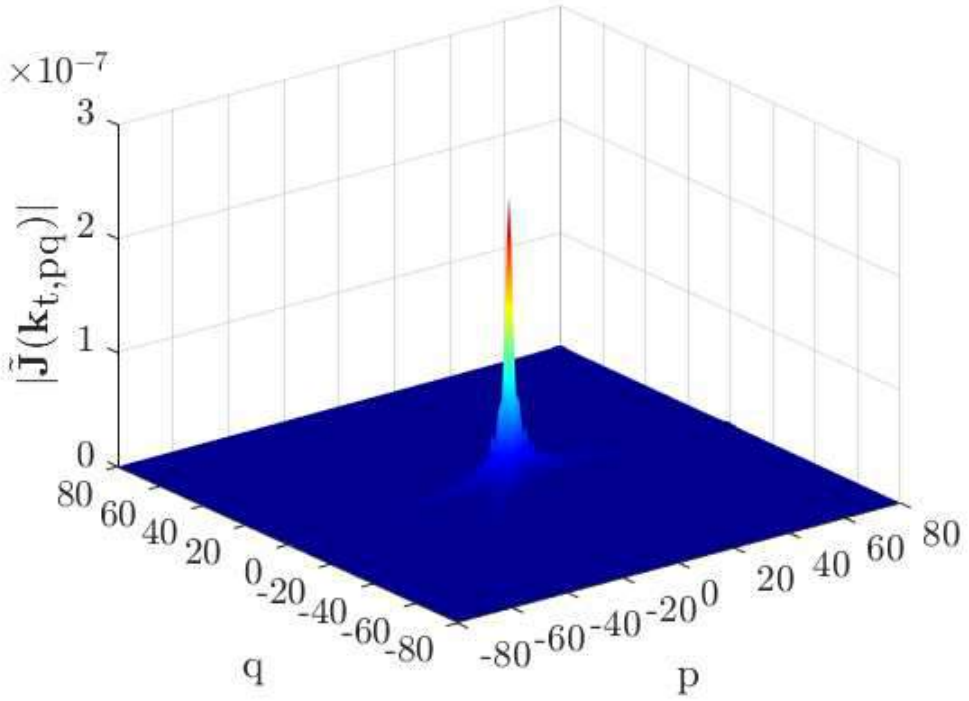

Figure 5.24: Magnitude of the RWG transform for $l_{edge} = \lambda/10$, $d_x = \lambda/4$, $d_y = \lambda/2$, $\theta_{inc=0.1^\circ}$, $\phi_{inc=0.1^\circ}$ and $M = 80$.

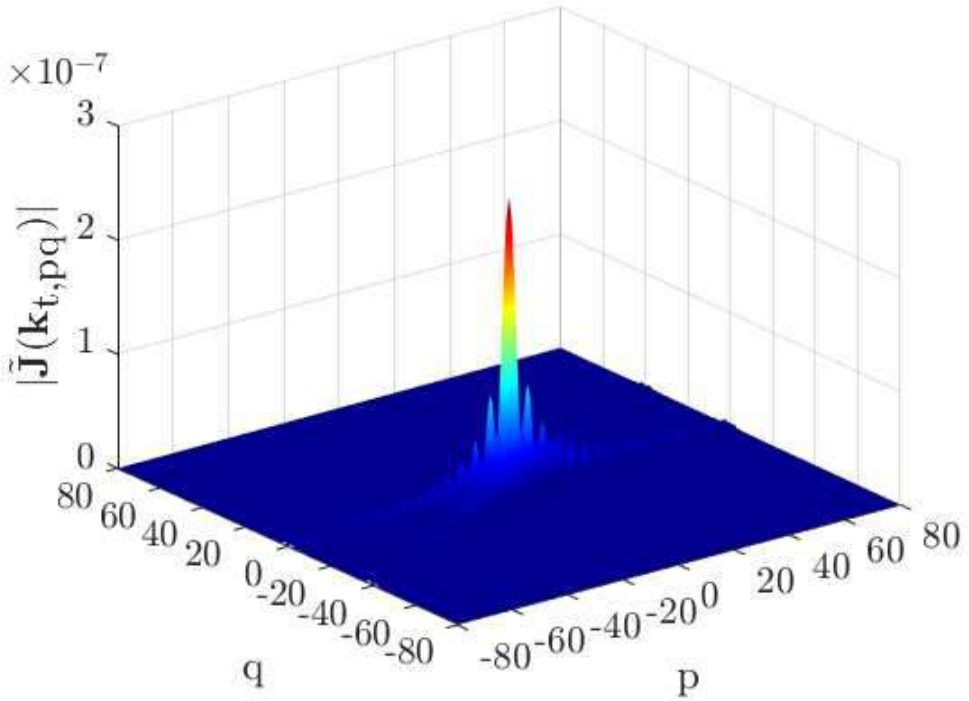

Figure 5.25: Magnitude of the RWG transform for $l_{edge} = \lambda/10$, $d_x = \lambda/4$, $d_y = \lambda/4$, $\theta_{inc=0.1^\circ}$, $\phi_{inc=0.1^\circ}$ and $M = 80$.

5.6.9 MOM Code Validation

The unit-cell depicted in Fig. 5.26 was given as an example for the validation of the code. A comparison with results obtained from CST analysis is presented in this section. The geometry of the unit-cell is described in Table 5.1: two metallic strip elements, aligned along the $x-$axis, are placed on top of a dielectric substrate of thickness h_2. This specific design was chosen as it resembles the unit-cell composing the FSS that will be used in Section 5.7 for the validation of the analysis tool developed.

Table 5.1: Geometrical parameters describing the unit-cell in Fig. 5.26.

Unit-Cell Parameters (mm)	
d_x	6.25
d_y	6.25
x_1	3.8
x_1	6
W	0.4
h_2	1.5
ϵ_{r2}	2.2
θ_{inc}	35°
ϕ_{inc}	180°

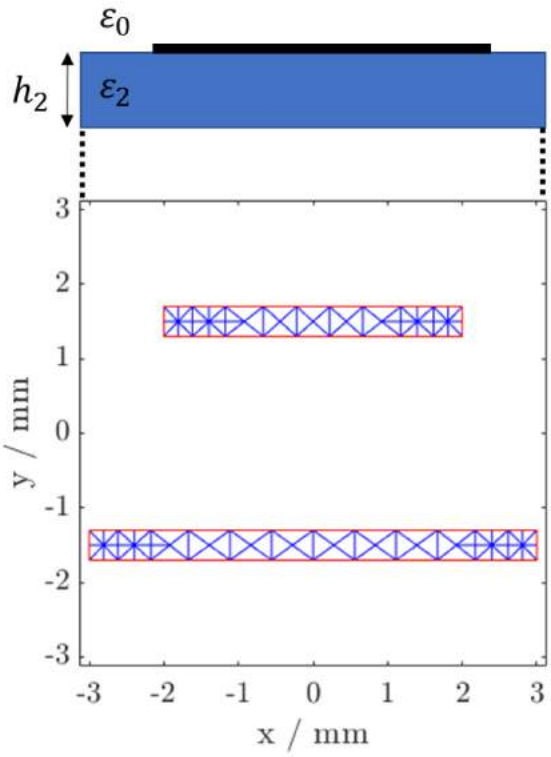

Figure 5.26: Unit-cell design for the FSS analysis tool validation.

5.6.10 Scattering Parameters

The scattering parameters for the given unit-cell are simulated using the spectral domain MOM code developed in this Chapter. The same periodic element was modeled and simulated in CST using the Floquet boundaries. A comparison between the scattering parameters of the fundamental mode, i.e. TM_{00}/TE_{00}, obtained with the two methods will be shown in this section.

TM Modes

First, the reflection and the transmission coefficient for the TM_{00} mode are shown in Fig.s 5.29-5.30, for an angle of incidence $\theta_{inc} = 35°$, $\phi_{inc} = 0°$. An excellent agreement can be observed, for both the components, in the magnitude and phase curves.

TE Modes

The reflection and the transmission coefficient for the TE_{00} mode are shown in Fig.s 5.27-5.28, for an angle of incidence $\theta_{inc} = 35°$, $\phi_{inc} = 0°$. Again, an excellent agreement can be observed, for both the components, in the magnitude and phase curves.

5.6.11 Tool Advantages Discussion

The code was shown to provide the same results of CST, thus proving to be a reliable and efficient tool. In detail, for the simulation presented, the code took around 3 minute to calculate the S-parameters on 61 frequency points, while, for the same configuration, the CST simulation took around 55 minutes. The CST simulation is used as benchmark here as the software is worldwide known and used for the unit-cell design. Furthermore, some details can be added in the CST model, for instance the metal thickness, that can not be handled with a SD-MOM. However, in order to move from the unit-cell analysis to the scattering from the whole FSS, every time a CST simulation is run, it is required to extract the results and import the data in the MATLAB code where the scattering analysis is implemented. In this regards, the code developed can be directly embedded in the code, thus allowing for instance the implementation of optimization routines that would not be possible using the CST model.

More funtionalities could be added to the code, such as the multilayer analysis, obtained through a S-matrix cascade, or including the metal losses of the patch element [110]. Those are not addressed in this thesis and are currently under development.

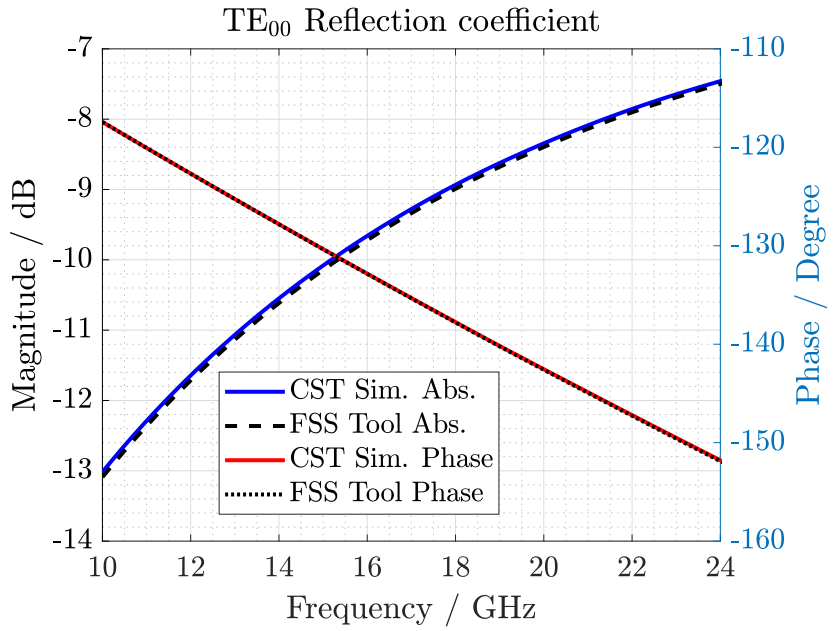

Figure 5.27: Comparison between the reflection coefficients of the unit-cell, for the TE component of the fundamental mode, simulated using CST and the Tool developed in this Thesis.

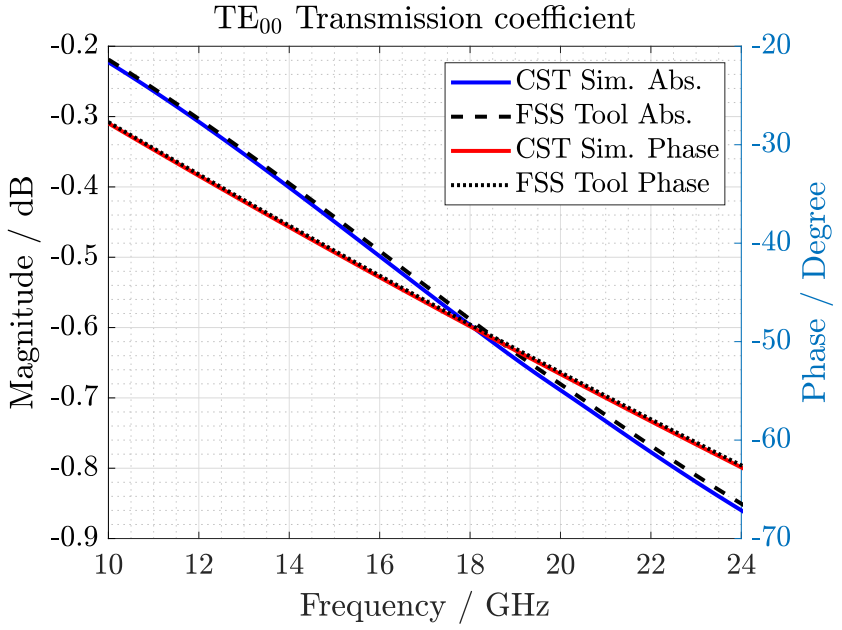

Figure 5.28: Comparison between the reflection coefficients of the unit-cell, for the TE component of the fundamental mode, simulated using CST and the Tool developed in this Thesis.

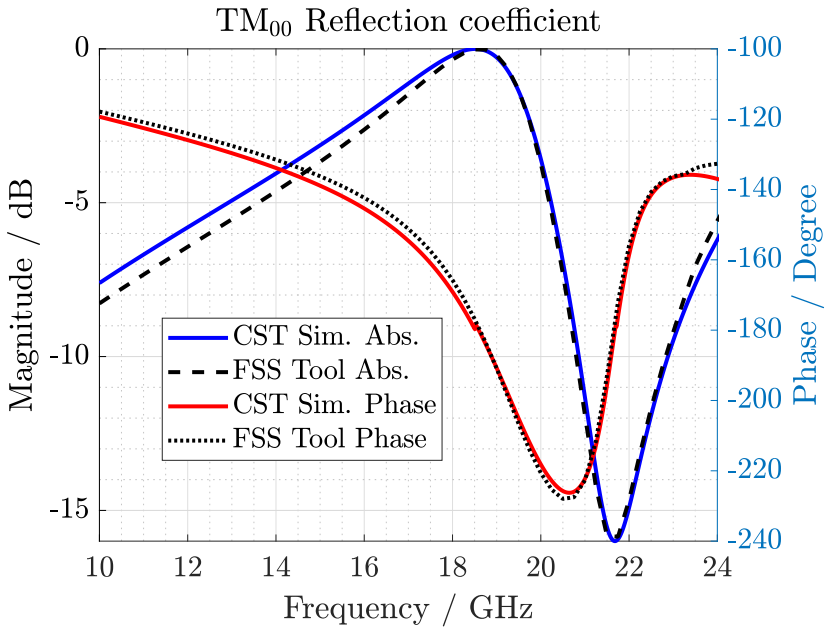

Figure 5.29: Comparison between the reflection coefficients of the unit-cell, for the TM component of the fundamental mode, simulated using CST and the Tool developed in this Thesis.

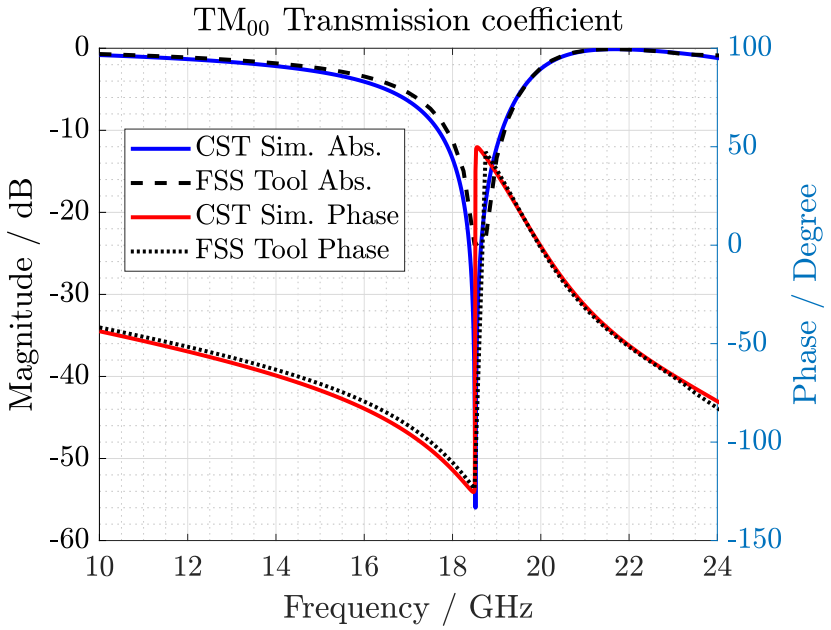

Figure 5.30: Comparison between the reflection coefficients of the unit-cell, for the TM component of the fundamental mode, simulated using CST and the Tool developed in this Thesis.

5.7 Analysis of a FSS Subreflector with Linearly Polarized Near Field Incidence

5.7.1 Problem Statement

Frequency-Selective-Surfaces (FSSs) are extensively used in reflector antennas, in order to make a more efficient use of the system resources. A subreflector, consisting of a periodic surface, can be placed between two feeds and the main reflector, in this way enabling the use of two different frequencies or polarizations at the same time. Ideally, the surface would be totally reflecting for the operating frequency (or polarization) of one feed while completely transparent for the other one. An exhaustive literature can be found on methods to analyze FSSs. The elements periodicity allows to restrict the study to the single unit-cell, and a spectral domain method of moments can be implemented in order to extract the scattering matrix.

The majority of the works approximate the feed pattern with a far field ideal model. The field illuminating the subreflector surface is computed using this modeling for the horn. However, this assumption is no longer valid if the FSS is placed in the Fresnel region with respect to the source. The accuracy of the analysis can be considerably improved if the actual incident field on the surface is considered.

In this work we provide a procedure to analyze a dual-reflector antenna system, with the subreflector positioned in the Fresnel zone of the two primary feeds. The field radiated by the feed-horn is expanded using a spherical-wave-expansion based code in order to compute the real incident near field on the FSS. Consequently, scattering parameters for the FSS along with the reflected or transmitted field on the subreflector surface are obtained using information about the actual radiation (amplitude, phase and direction of incidence). Physical optics techniques are eventually used to calculate the radiated far field from the currents distribution on the surface.

A specific application is presented in this work in order to validate our analysis approach. Two linearly polarized horn-feeds operating in a different frequency band are placed on the two sides of a subreflector that belongs to the Fresnel region of the sources. The far field pattern of the two sources is computed after transmission and reflection from the FSS and compared with experimental results in order to evaluate the accuracy of the considered analysis method. The technique can be easily adopted for handling other applications, for example to analyze periodic screens used as polarizers or beam-splitters.

Some constraints on the FSS design were given by the equipment of the facilities where the measurement campaign was intended to be performed. This issues will be described in detail in the following of the Chapter, but it has to be remarked that limitations in terms of materials and dimensions for which the FSS had to be fabricated together with restrictions on probes available for the measurement system, i.e. frequencies that could be actually measured, had to be taken into account. Therefore, it is important to clarify

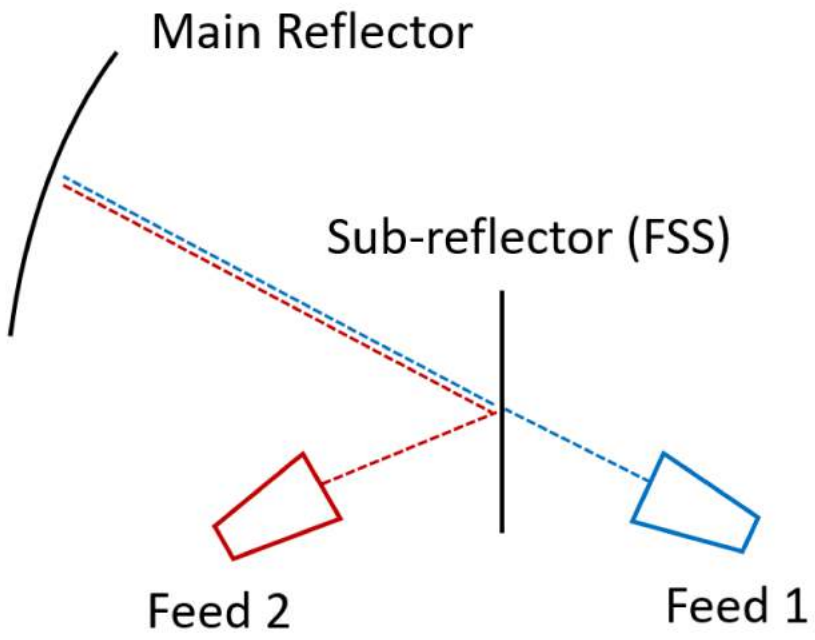

Figure 5.31: Schematic of a dual-reflector configuration adopting a frequency discriminating FSS as subreflector.

that the main intent of this study was not on the FSS design itself, but more on the validation of the analysis tool. Finally, a prototype of the FSS was fabricated and the dual configuration was measured in an anechoic chamber.

Some similarities with the work presented in [120] can be found. In that paper, the authors use the actual near field reconstruction approach in order to improve the analysis of a reflectarray. With respect to [120], in this work a FSS was used as application of interest, thus extending the analysis to the transmitted field instead of considering only the reflected radiation. Furthermore, a more precise characterization of the actual angle of incidence of the field illuminating the surface is investigated in this Chapter. It has to be remarked that this results to be a fundamental parameter when the scattering parameters of the unit-cells composing the FSS have to be extracted.

5.7.2 Scenario

The scenario considered in this work is shown in Fig. 5.31. Two primary horn-feeds are placed on the two sides of an subreflector at an offset angle θ_{off}. A periodic surface is printed on the subreflector in order to obtain frequency discrimination properties. A frequency selective surface designed to this purpose allows the radiation coming from Feed 2 to be reflected, while the radiation coming from Feed 1 is transmitted through the surface. Since the core of the analysis regards the computation of the field scattered from the subreflector, in this thesis the interest is in evaluating the far field of the configuration without considering the presence of the main reflector.

5.7.3 Incident Field on the FSS surface

The study of this kind of configuration is usually done by modeling the source with an ideal horn pattern. As long as the subreflector is placed in the far field region with respect to the source feed, information about the far field pattern is sufficient for the analysis. However, when considering near field illumination, this approximation doesn't hold anymore and therefore a different approach has to be taken. In fact, far field pattern gives information only about the tangential components of the field (θ- and ϕ- components in spherical coordinates), whereas in the Fresnel zone the radial component (ρ-component) increases in relevance and therefore can not be neglected. In this regard, the spherical-wave-expansion based code developed in Section 5.4 was used to provide a correct understanding of the incident field.

The source of radiation was a standard gain horn, Flann 20240 [119], operating in the frequency range 17.6 GHz − 26.7 GHz used as feed, both in transmission and in reflection. The PO approach described in section 5.5 does not take into account the diffraction originated by the FSS edges. In this regards, in order to preserve the validity of the technique, the taper of the feed at the subreflector edges had to be ensured to be at least 10 db lower with respect to the intensity maximum on the surface. This requirement was obtained for a square offset-fed FSS of size $D^2 = 280$ mm $\times$ 280 mm placed for a tilt angle of $\theta = 35°$ in the broadside direction of the array. The two operating frequencies were chosen to be $f_1 = 18$GHz and $f_1 = 24$GHz. In order to minimize the diffraction effects, the two feeds were positioned at a distance d from the FSS plane. The separation between the horn aperture and the center of the subreflector is around 12λ, which means, since the horn aperture dimensions are 38mm $\times$ 52mm, that the FSS surface belongs to the Fresnel zone of the source.

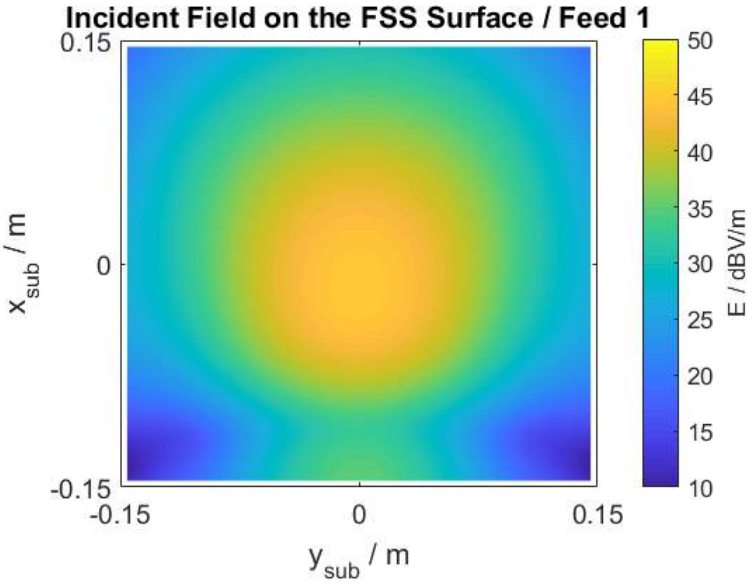

Figure 5.32: Electric field distribution across the FSS surface.

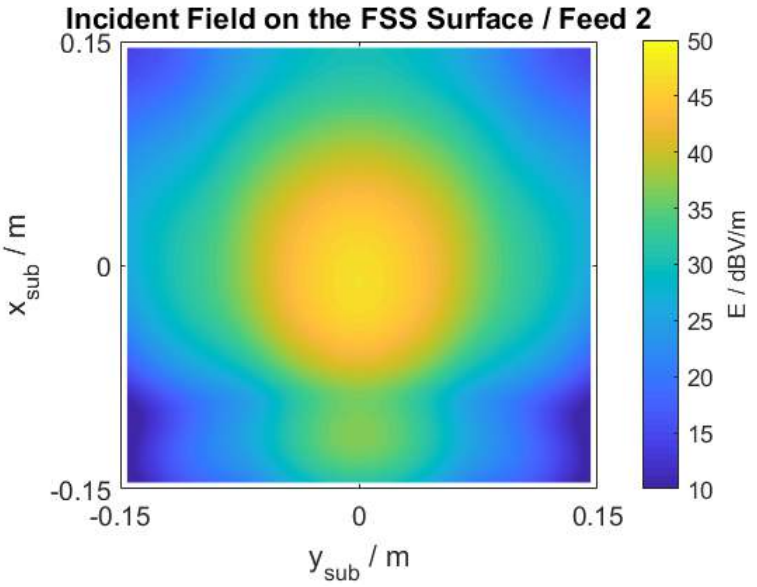

Figure 5.33: Electric field distribution across the FSS surface.

5.7.4 FSS Design

The field illuminating the surface, for both the feeds, is shown in Fig.s 5.32 and 5.33. The field distribution is symmetrical with respect to the x−axis, while a side-lobe appears along the y−direction in the lower part of the surface. The FSS design assured the secondary lobe to be at least 10dB lower with respect to the peak value.

Initially, the design of the offset fed subreflector consists in the design of the unit-cell element, which is later repeated periodically along the surface. A schematic of the proposed unit-cell is shown in Fig. 5.34. Two copper elements, aligned with the x−axis are placed above a Rogers RO4003 subtsrate of thickness $t_{sub} = 1.52$ mm and relative permittivity $\epsilon_r = 3.38$. Parameters describing the unit-cell geometry are reported in Table 5.2. The two elements are responsible for controlling the upper and lower resonance frequencies of the unit-cell. Since the main focus of this work is not on the FSS design but on the FSS analysis techniques, only linearly polarized feeds are considered

Table 5.2: Unit-Cell Geometry Description.

Unit-Cell Parameters (mm)	
D_x	6.2
D_y	6.2
x_1	4.2
x_2	5.8
W	0.4
t	1.52

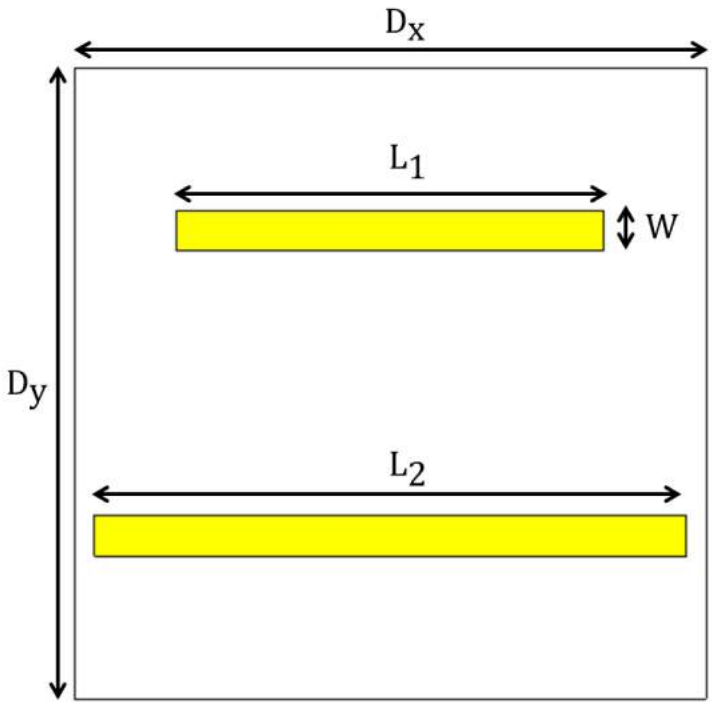

Figure 5.34: Unit-cell schematic representation. D_x and D_y represent the spatial periodicity along x and y, L_1, L_2 and W are the physical dimensions of the copper elements.

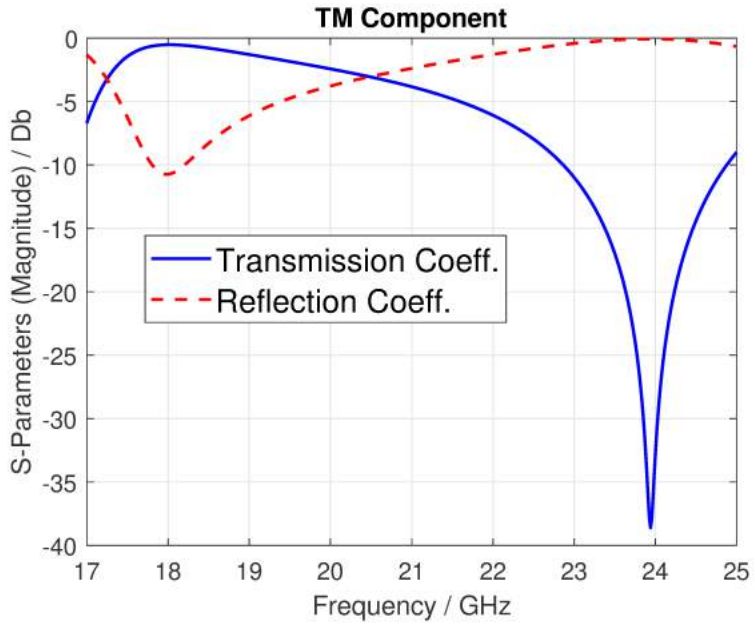

Figure 5.35: Scattering parameters of the unit-cell for TM incidence.

and, therefore, a unit-cell dealing with only one polarization, aligned with the x−axis, is designed.

The unit-cell design was optimized in order to have the best response for the offset incidence $\theta_{inc} = 35°$, $\phi_{inc} = 180°$, which corresponds, for both feeds, to the center of the subreflector surface. As linearly polarized incidence will be considered, only scattering parameters related to the TM-polarization, both in transmission and in reflection, are of interest in this case. Coefficients relative to the TM_{00} and TM_{00} have to be considered, as only the fundamental mode propagates at the selected frequencies. The frequency response of the unit-cell is represented in Fig. 5.35. Two regions of operation can be identified. The first one, around 18 GHz, where the transmission coefficient is close to 0 dB, meaning that all the radiation at that frequency gets transmitted by the FSS, and a second one, around 24 GHz, which corresponds to frequencies for which the radiation gets reflected. Therefore, two operating frequencies for the two feeds can be established: $f_1 = 18$ GHz and $f_2 = 24$ GHz.

An analysis on the angular stability of the designed unit-cell was conducted by varying the angles of incidence θ_{inc} and ϕ_{inc} respectively in the range $[25 - 45°]$ and $[160 - 200°]$. The transmission coefficient was simulated for the different angles and the results are plotted in Fig 5.36. It can be observed that the unit cell design is pretty robust to a slight incidence modification. This means that, as the horn feeds used are directive antennas and therefore the majority of energy will be concentrated around the subreflector center, all the unit-cells belonging to that region will have a substantially similar behavior.

As mentioned before, only linearly polarized incidence, aligned with the x−axis, will be considered and therefore only the scattering parameters related to the TM-component have to be computed. However, Fig. 5.37 shows that a TM-incidence gives rise to component for the orthogonal (cross-) polarization. In this case, this is given by the cross-S-parameter S_{TMTE}. This component is very low for the central unit-cell incidence, but as θ_{inc} and ϕ_{inc} move from the offset angle, a significant growth can be observed. These effects, summed for all the unit-cells across the surface, contribute to the creation of a cross-polarized component in the field transmitted or reflected by the FSS.

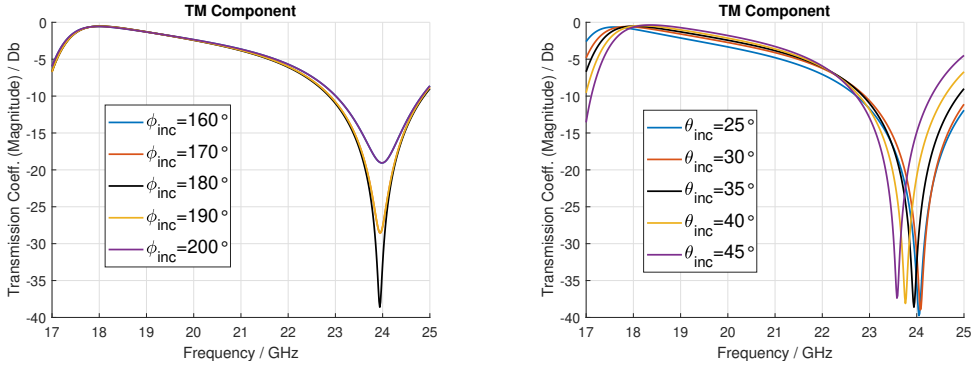

(a) (b)

Figure 5.36: Study on the angular stability of the proposed unit-cell. The frequency response of the unit-cell is evaluated while changing the angle of incidence.

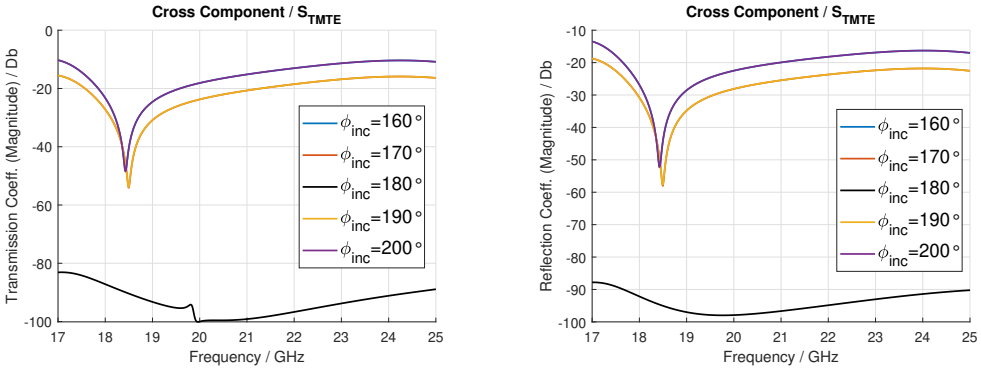

(a) (b)

Figure 5.37: Study on the angular stability of the proposed unit-cell. The cross S-parameters of the unit-cell are evaluated while changing the angle of incidence.

5.7.5 Field Scattered from the FSS Surface

The FSS analysis requires the field illuminating the surface to be approximated, within each unit cell, with a plane wave. In this way, it is possible to assign to each cell element a scattering matrix which is, following the FSS analysis theory presented in Section 5.6.7, a function of the angle of incidence. However, when considering near field incidence, the field distribution across each unit-cell can vary significantly, and a 4- or more points sampling, as suggested in [120] and shown in Fig. 5.38, has to be adopted. In conclusion, the intensity assumes discrete values, and it is constant within each unit-cell subdivision.

The reflected and the transmitted field on the subreflector surface are obtained from the incident field according to:

$$\mathbf{E}_{refl}^{TE/TM}(x_s, y_s) = \mathbf{S}_{refl} \cdot \mathbf{E2}_{inc}^{TE/TM}(x_s, y_s) \tag{5.102}$$

$$\mathbf{E}_{tran}^{TE/TM}(x_s, y_s) = \mathbf{S}_{tran} \cdot \mathbf{E1}_{inc}^{TE/TM}(x_s, y_s) \tag{5.103}$$

where E are 2-elements vectors and S are square 2×2 matrices as described in Section 5.6.7.

$$\mathbf{S}_{trans}(x_s, y_s) = \begin{pmatrix} T_{TETE}(x_s, y_s) & T_{TETM}(x_s, y_s) \\ T_{TMTE}(x_s, y_s) & T_{TMTM}(x_s, y_s) \end{pmatrix} \tag{5.104}$$

$$\mathbf{S}_{refl}(x_s, y_s) = \begin{pmatrix} R_{TETE}(x_s, y_s) & R_{TETM}(x_s, y_s) \\ R_{TMTE}(x_s, y_s) & R_{TMTM}(x_s, y_s) \end{pmatrix} \tag{5.105}$$

where the coefficients T and R are extracted from the scattering curves respectively at the frequencies f_1 and f_2.

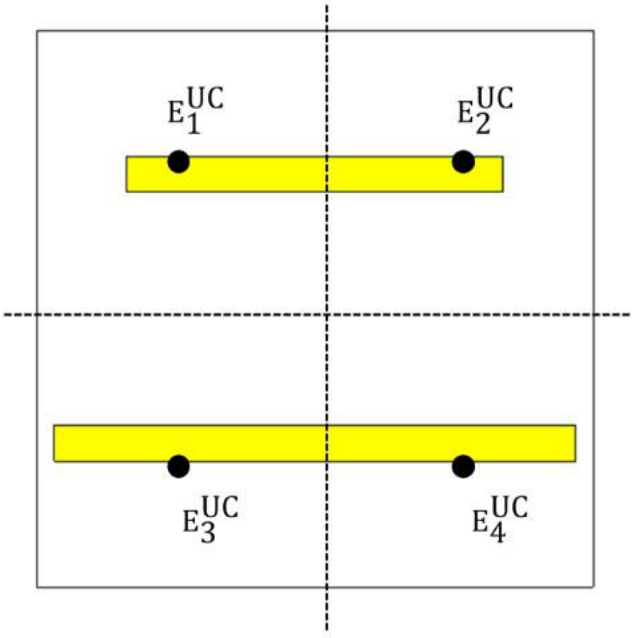

Figure 5.38: Unit-cell division in 4 sub-domains.

The actual direction of incidence is a crucial information when computing the scattering parameters all-over the surface. In fact, the angles computed assuming a far field approximation of the source are no longer valid in case of near field incidence. The actual angle of incidence, for each point on the FSS (x_s, y_s), can be obtained from the direction of the real part of the Poynting vector:

$$\mathbf{P}(x_s, y_s) = \frac{1}{2}\mathrm{Re}\{\mathbf{E}(x_s, y_s) \times \mathbf{H}^*(x_s, y_s)\} \tag{5.106}$$

Fig.s 5.39 and 5.40 show, for both feeds, a comparison between the angle of incidence of the ideal feed model and the actual angle of incidence. Dashed-lines represent the angles originated by a point source while solid lines depict the actual angles computed following 5.7.5. A noticeable difference between the two set of lines can be appreciated. The displacement gets more and more accentuated as the observation moves from the main plane of the subreflector. Although those regions correspond to a lower intensity for the incoming radiation, they still have an influence on the far field radiation scattered by the FSS, as it will be shown in the following of this Section. Therefore, since information about the angle of incidence is crucial in order to compute the scattering matrix for each unit-cell, this comparison confirms the need of a specific approach when considering near field incidence. Furthermore, it can be observed that the actual incidence does not depend only from the space displacement between source and FSS but also on the operating frequency considered. A prove of this statement can be found comparing the solid lines of Fig. 5.39 and Fig. 5.40, where the two sources, working at different frequency, are placed exactly in the same position, apart from a mirroring factor, with respect to the the FSS plane.

The far field pattern scattered by the FSS can be obtained considering the problem as a radiation from a surface illuminated by an incoming wave: electric and magnetic currents are derived on the surface as described in Section 5.5. Ideally, the scatterer has to be infinite, however, in practice, an approximation for a finite surface holds as long as the majority of the radiation is confined inside the surface and field levels at the rims are considerably lower with respect to the center.

In order to prove the improvement obtained with the analysis approach presented in this work, the transmitted and the reflected fields are computed using both the far field (FF) approximated incidence and the actual near field (NF) on the FSS surface. Comparisons between the two cases are shown in Fig.s 5.42-5.43. Some differences in the radiation pattern shapes can be observed. First of all, the peak value of the FF co-polar component is 1 to 2 dB higher with respect to the same component computed from the NF incidence. Secondly, the cross-polar component of Feed 2 results considerably lowered if the NF incidence is considered. Finally, if the shape of the main lobe for the two cases can roughly be superimposed, the same does not happen for the secondary lobes, that gets significantly smothered when the actual incidence is taken on the FSS surface.

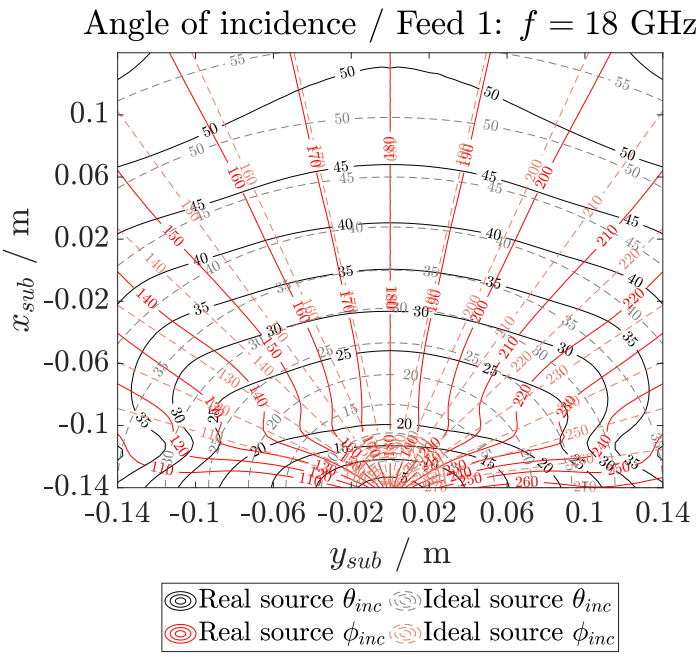

Figure 5.39: Angle of incidence across the FSS surface. NF angles obtained using the SWE code are shown to be different from those computed assuming a FF approximation.

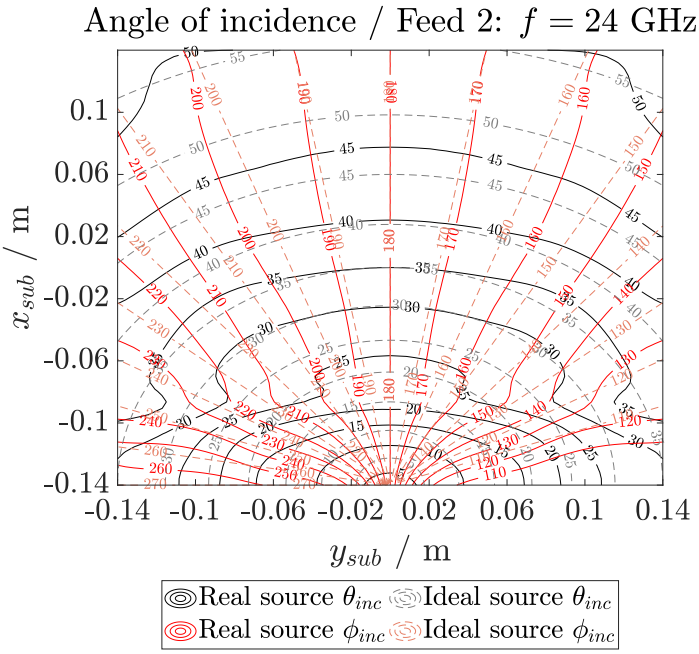

Figure 5.40: Angle of incidence across the FSS surface. NF angles obtained using the SWE code are shown to be different from those computed assuming a FF approximation.

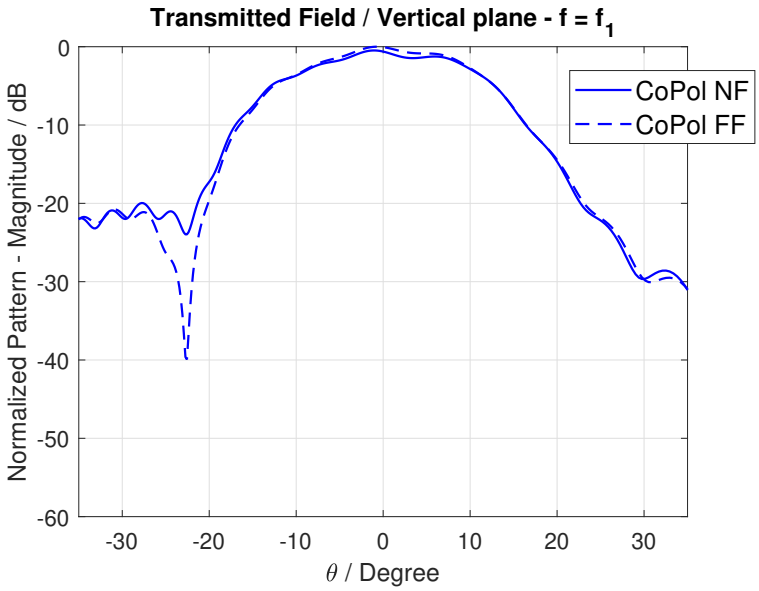

Figure 5.41: Comparison between the pattern of the field transmitted by the FSS considering far field approximated (FF) or the actual near field (NF) incidence.

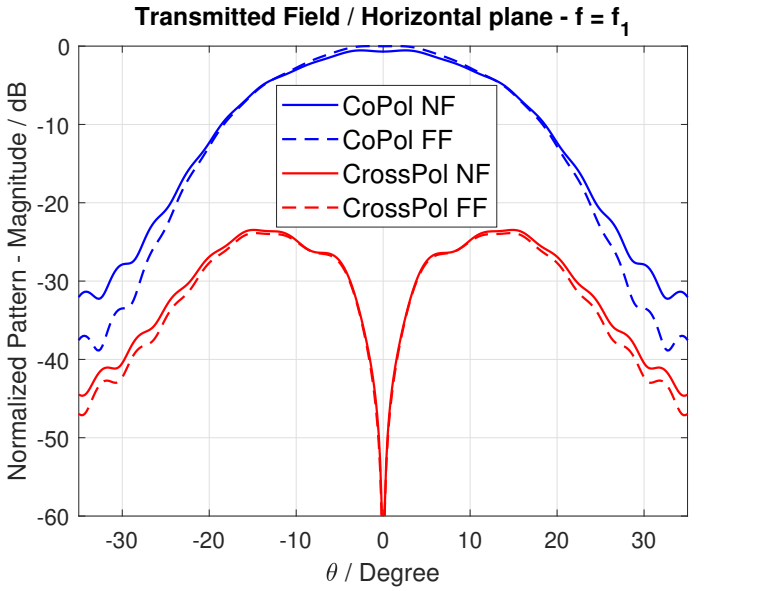

Figure 5.42: Comparison between the pattern of the field transmitted by the FSS considering far field approximated (FF) or the actual near field (NF) incidence.

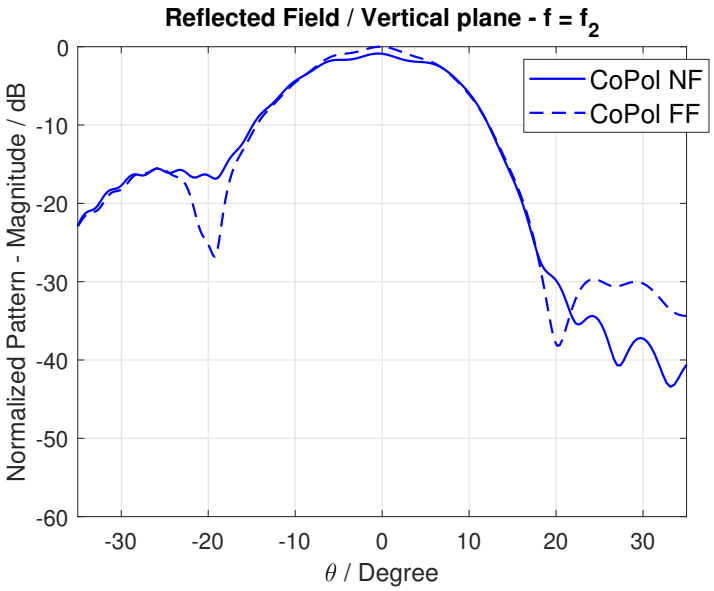

Figure 5.43: Comparison between the pattern of the field transmitted by the FSS considering far field approximated (FF) or the actual near field (NF) incidence.

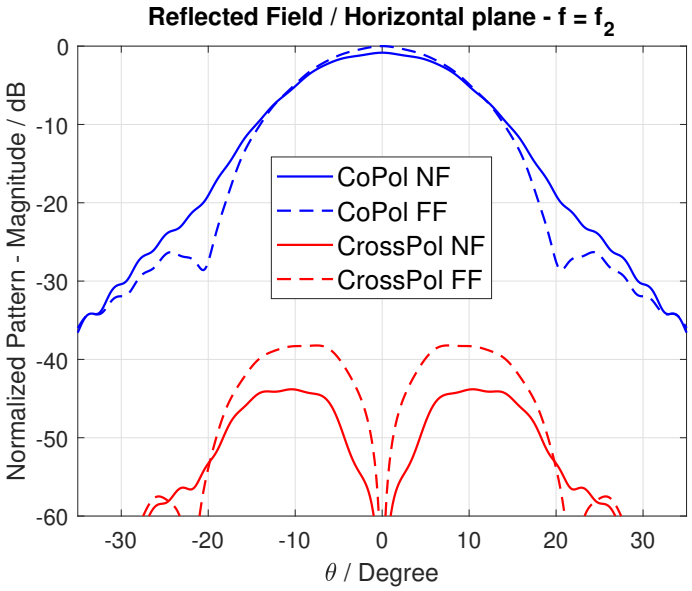

Figure 5.44: Comparison between the pattern of the field transmitted by the FSS considering far field approximated (FF) or the actual near field (NF) incidence.

5.8 Experimental Validation

A prototype of the designed frequency selective surface has been finally fabricated. The mask prepared for the etching and the actual prototype on the Rogers RO4003 substrate are shown in Fig.s 5.45 and 5.46. A strip of substrate was left below the array in order to allow the structure to be hold during the measurement campaign.

5.8.1 Measurement Setup

The preparation of the experimental setup resulted to be very challenging. A NSI near field measurement system was used in the Heriot-Watt University anechoic chamber. Referring to Fig.s 5.48 and 5.49, the setup consisted of a rectangular horn antenna used as radiation source, the FSS, used both in transmission and in reflection, and the NSI probe. The feed used was a standard gain horn, Flann 20240 [119], working in the frequency range 17.6 GHz−26.7 GHz. The three components had to be aligned and at the same time the distance between the FSS and the source antenna had to be properly set, according to the simulated configuration. This conditions revealed to be difficult to be accomplished with an excellent precision and the consequent effects on the radiation pattern will be discussed in detail along this Section.

Two measurement scenarios were prepared:

- Transmission: the FSS was rotated $\theta_{\text{off}} = 35°$ and placed in between the source antenna and the probe.
- Reflection: the FSS was placed in the same position as above and the source antenna was placed in front of the subreflector, at an offset incidence of $\theta_{\text{off}} = 35°$.

The linearly polarized horn was aligned with the FSS dipoles direction. The co-polar components of the far field were measured by aligning the NSI probe with the dipoles, while cross-polar components were obtained by rotating the probe 90° with respect to the previous case.

As it was mentioned in Section 5.7.1, the configuration chosen to validate the code developed in this work was hardly constrained by the availability of materials for the FSS fabrication and of the measurement tools. Furthermore, a critical aspect emerged as the power amplifier used at the transmitter side was not working properly at the higher frequency, i.e. the one to be reflected. Therefore, measured cross-polarization levels for the higher frequency will be highly affected by this fact and hard to detected properly.

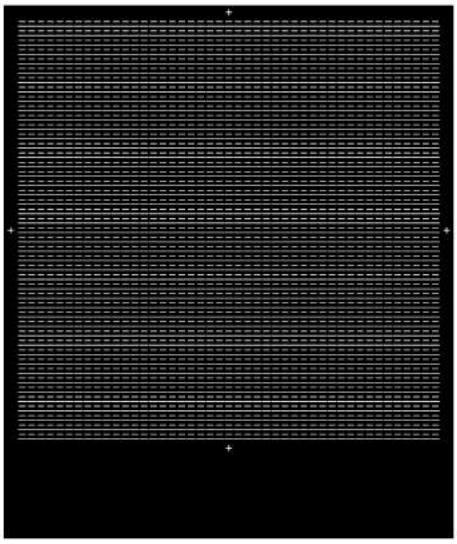

Figure 5.45: 280mm × 280mm mask for the FSS fabrication.

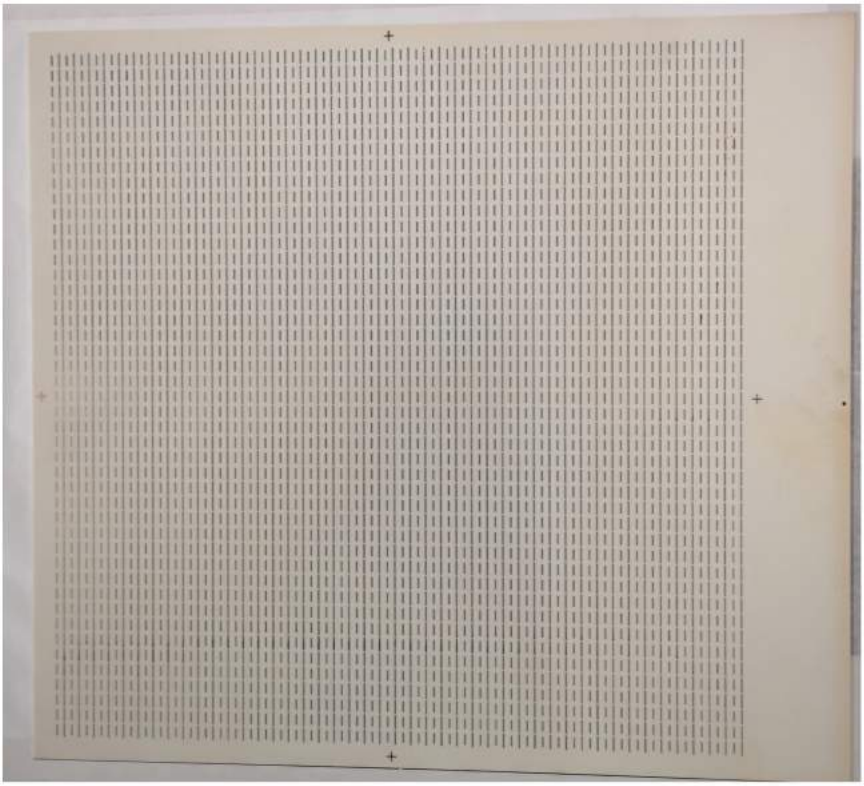

Figure 5.46: A picture of the fabricated FSS prototype.

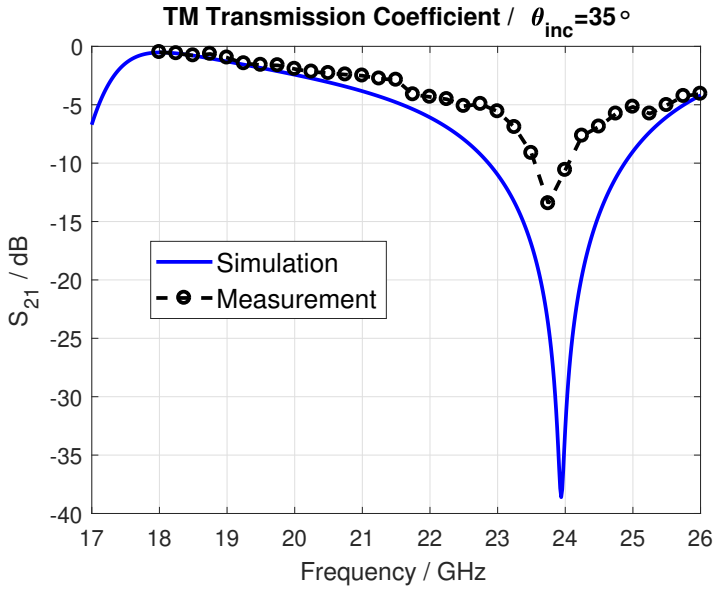

Figure 5.47: Transmission coefficient of the FSS for the considered offset configuration ($\theta_{inc} = 35°$). A comparison between simulation and measurements is shown.

5.8.2 Scattering Parameters

First, the transmission coefficient for the FSS was measured for the angle of incidence of the central unit-cell, $\theta_{inc} = 35°$, $\phi_{inc} = 180°$. As linearly polarized incidence is considered, we are interested only in evaluating the transmission coefficient for one polarization. A comparison with the same parameter obtained through simulations is shown in Fig. 5.47. A good agreement is observable in the band of interest, $18 - 25$ GHz. Referring to the configuration shown in Fig. 5.48, measurements confirmed the FSS behavior: a transmission bandwidth around 18 GHz and a reflection bandwidth around 24 GHz.

From the good agreement between measured and simulated transmission coefficient, two useful observations can be drawn. First, the proper behavior of the unit-cell was experimentally validated. Second, the correct alignment and rotation between the horn and the FSS can be proved. In fact, as shown in Section 5.7.4, a misalignment or an incorrect rotation would provoke a shift in the frequency response and, consequently, a different angle of incidence for the central unit-cell.

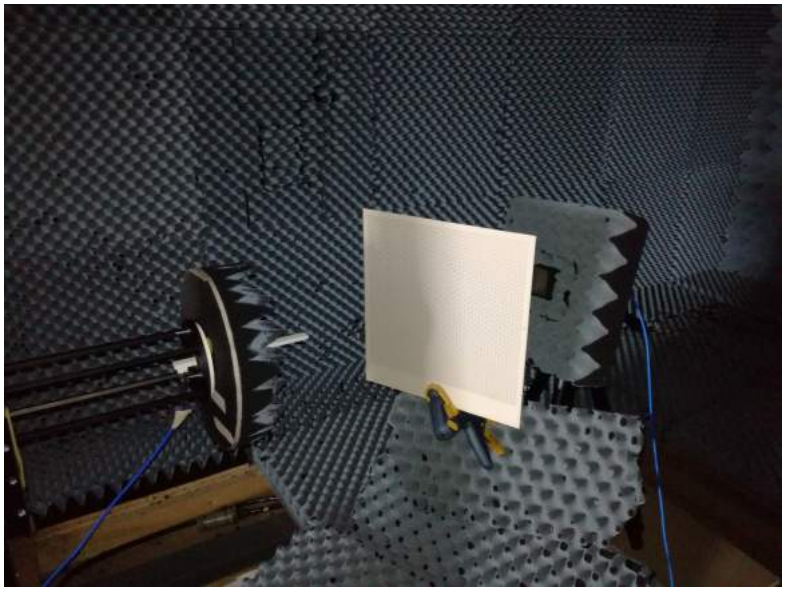

Figure 5.48: A picture of the experimental setup for the FSS acting in transmission.

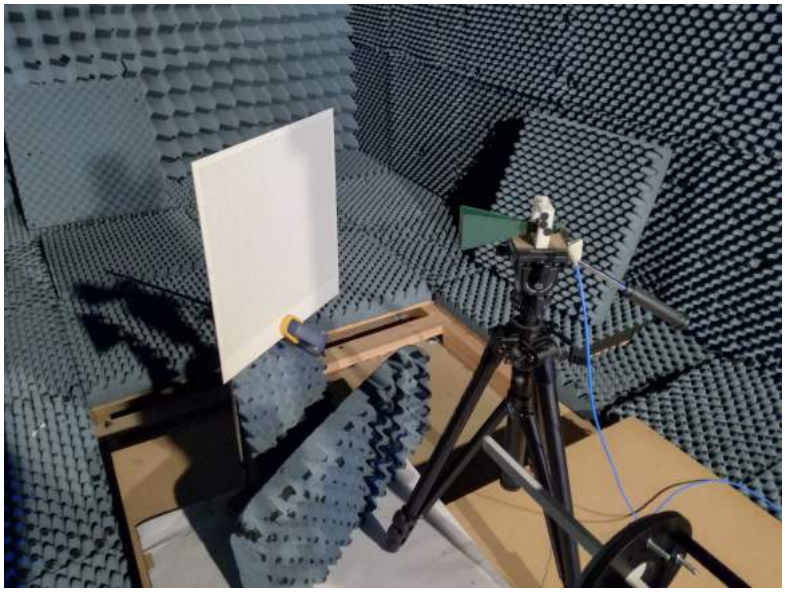

Figure 5.49: A picture of the experimental setup for the FSS acting in reflection.

5.8.3 Radiation Pattern Measurement

The radiation pattern scattered from the FSS surface was eventually measured. Experimental results are used to validate the FSS analysis tool developed and described in this Chapter: the accuracy of the proposed analysis technique has been evaluated by comparing the measured radiation pattern to the radiation pattern simulated considering the actual near field incidence on the FSS surface. Experimental results are shown in the vertical and the horizontal plane cuts, that correspond respectively to the $\phi = 90°-$ and the $\phi = 0°-$cut. Both co-polar and cross-polar components of the field have been measured, as described in Section 5.8.1.

Field Transmitted by the FSS

First, a measurement campaign was carried out in order to obtain the radiation, transmitted through the FSS, coming from Feed 1 at 18 GHz. The measured radiation pattern is shown in Fig.s 5.50 and 5.50 for the setup depicted in Fig. 5.48. A good agreement can be observed between the co-polar components, both in the vertical and in the horizontal plane. Some discrepancies can be found while moving away from the main lobe peak and as the measured pattern gets more noisy for decreasing field levels. As far as the cross-polar components are concerned, those are mainly relevant in the horizontal plane and simulations are substantially confirmed by experimental results.

Field Reflected by the FSS

Later, the field pattern of the radiation coming from Feed 2 and reflected by the FSS surface was measured. The measured co-polar component, in both planes, validates the analysis carried out with the tool developed. The main disagreement between the measured and simulated radiation patterns is caused by the shadow effect of the feed support. This appears clearly for the horizontal plane pattern in the region $\theta = [-60° - 30°]$, which corresponds roughly to the area covered by the feed and its support. The experimental setup illustrated in Fig. 5.49 highlights this issue. A considerable rise in the cross-polar component can be observed for the measured reflected pattern with respect to simulations. This might be due to a misalignment, i.e. the plane represented does not correspond exactly to the $\phi = 0°-$plane. Furthermore, power levels detected for this component were close to the noise floor of the VNA used for the measurements. In fact, as mentioned previously, the signal at 24 GHz was not amplified and therefore a sufficient value of SNR was hard to achieve. Other sources of discrepancies can be found in manufacturing errors, in the local periodicity analysis approach or in unwanted scattering effects due to the measurement setup.

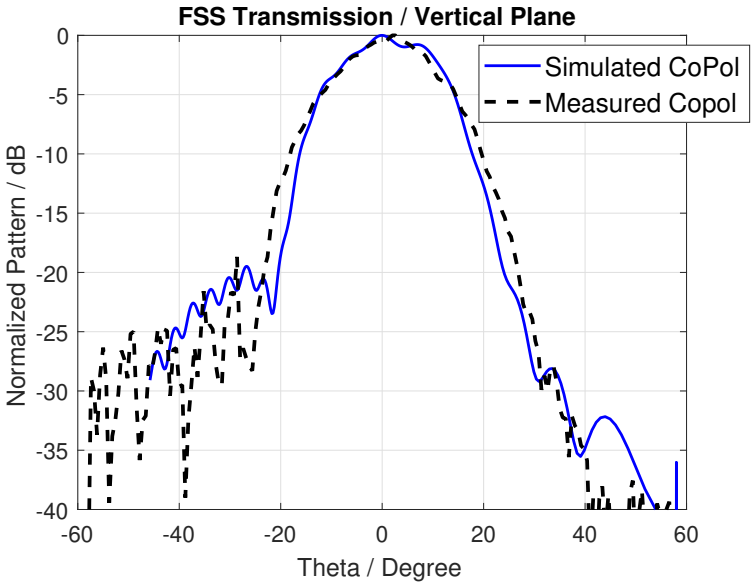

Figure 5.50: Measured radiation pattern for Feed 1 transmitted through the FSS. Co-polar and Cross-polar components are shown in the Vertical Plane.

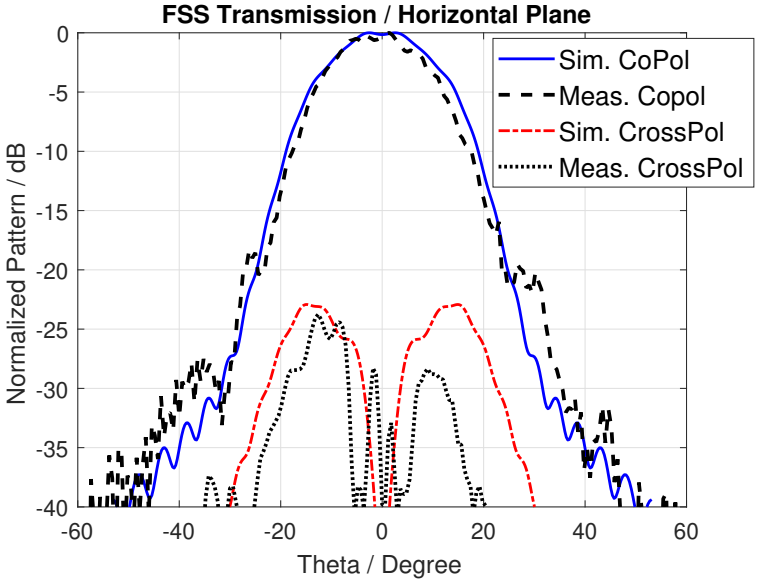

Figure 5.51: Measured radiation pattern for Feed 1 transmitted through the FSS. Co-polar and Cross-polar components are shown in the Horizontal Plane.

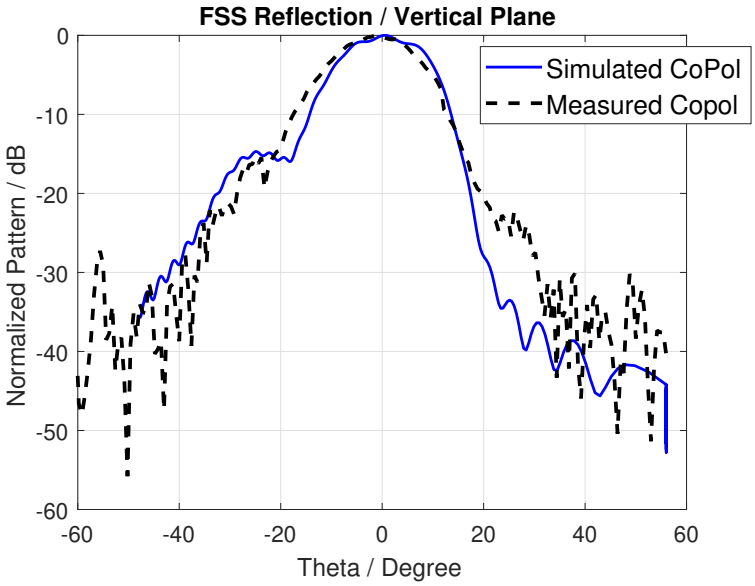

Figure 5.52: Measured radiation pattern for Feed 2 reflected by the FSS. Co-polar and Cross-polar components are shown in the Vertical Plane.

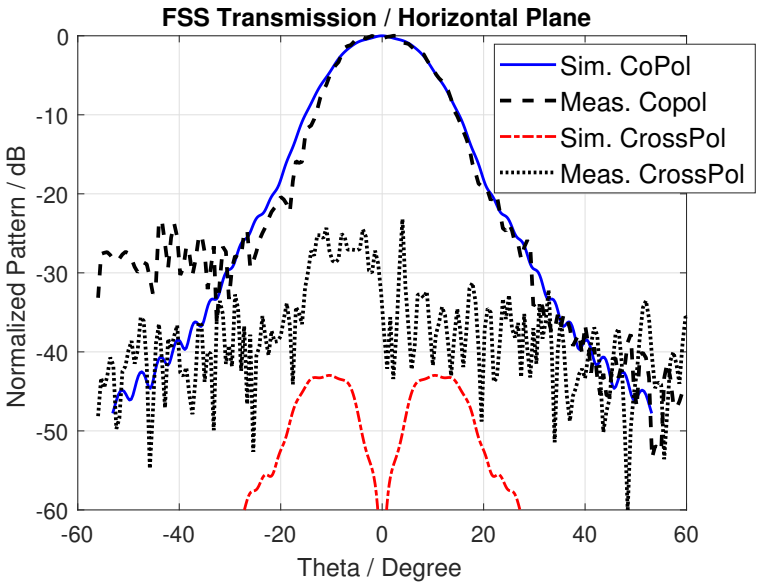

Figure 5.53: Measured radiation pattern for Feed 2 reflected by the FSS. Co-polar and Cross-polar components are shown in the Horizontal Plane.

5.9 Vanadium Dioxide Reconfigurable Unit-Cell

The last section of Chapter 4 is meant to explore an innovative solution for the reconfigurability of a reflectarray or FSS unit-cell. This work [121] was presented to the ESA Workshop on Multibeam and Reconfigurable Antennas for Space Applications

5.9.1 Introduction

Reconfigurable electromagnetic periodic surfaces, such as FSS, reflectarrays, and metasurfaces, have attracted growing interest over the last few years. The beam-forming capabilities of reflectarrays for example, together with multi-band operation and polarization flexibility, have made them very appealing for several satellite and radar applications. Innovative solutions have focused on developing reconfigurable periodic surfaces mostly by employing technologies lumped element components (i.e. PIN diodes, varactor diodes, RF-MEMS), but have also considered mechanical or hybrid approaches. More recently, liquid crystal tunable substrates have been considered, while in the past 3 years, phase change materials have demonstrated excellent reconfigurability, robustness, and linearity properties for RF and antenna applications. An exhaustive review of the literature can be found in [122].

A basic approach generally used by engineers in order to achieve reconfigurability consists either of manipulating the resonance of the scatterer, or of controlling the phase-shift induced on the incoming wave. The first can be obtained by changing the effective electrical length of the resonator. The second approach consists of coupling the incoming wave into a guided-wave and then re-radiating it with an induced phase-shift.

This work explores and introduces the new enabling technology of phase-change materials for the first of the aforementioned categories, as it allows the tuning of a reflectarray by arbitrary controlling the shape and the size of the patch element composing the unit-cell [[123],[124]].

Key advantage of the proposed technology is that the phase-change material can be integrated on-wafer with the metallic structure of each unit cell, without requiring the electrical connection to a biasing network. By taking the biasing network out of the RF design, the frequency tuning that can be achieved can be much larger than the typical 20% that is achieved by using

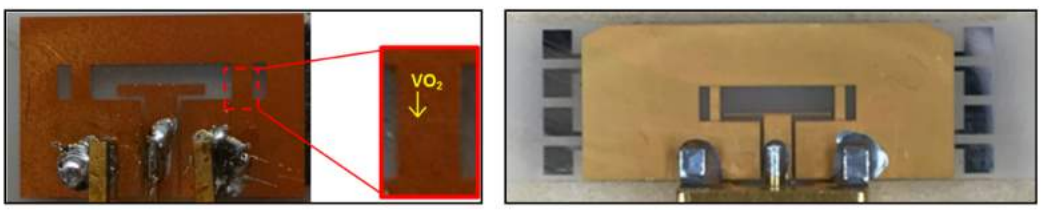

Figure 5.54: Prototypes of reconfigurable antennas using VO_2 technology presented in [123],[124].

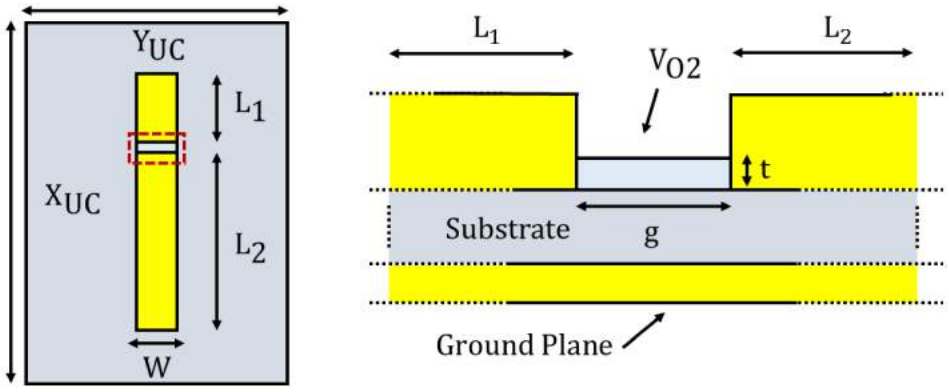

Figure 5.55: Reconfigurable Unit-Cell schematic. The element length L_2 is fixed while L_1 is different for each unit-cell across the reflectarray. The two conductive elements are connected by a thin film of VO_2.

quarter-wave stubs and quarter-wave transformers.

The phase-change material switches can be activated by using laser pulses, or integrated resistive heaters that are embedded underneath the substrate, and are not in contact with the metallic part of the unit cells. Structural advantages involve a fully planar (flush-mounted) structure, excellent robustness (no soldering required), excellent linearity, and reliability that exceeds that of typical satellite missions.

5.9.2 Enabling Technology

Vanadium dioxide VO_2 is a phase-change material that undergoes an insulator-to-semiconductor transition when subject to external stimuli. This technology has proved its effectiveness in [124], where a thin strip of VO_2 was employed in order to change the resonance frequency of a bowtie dipole. The metal-insulator transition of the VO_2 can be made extremely fast (in a few microseconds) which can enable new applications.

Many methods can be used to induce the transition: thermal via conductive heating, photo-thermal, optical excitation. The need of wired biasing is eliminated, thus allowing the achievement of reconfigurability without any of the limitations that are imposed by traditional electrically connected biasing lines [125].

5.9.3 VO_2 Reconfigurable Unit-Cell

In this work, the technique described is used to change the overall length of the metallic element of a reflectarray unit-cell. As a proof of concept, referring to [126], Fig. 5.55 shows a schematic of the proposed scenario. The considered unit cell is composed of two conductive strips: respectively of length L_1 and L_2, connected by a thin film of VO_2. The strip can have a conductive or insulating behaviour, depending on its transition status, in this way allowing an electrical connection between the two dipole elements of the unit-cell. An

insight of the VO_2 strip is shown in Fig. 5.55. The primary element of length L_2 has a fixed size, while the tuning stub length L_1 can vary in a given interval. Changing the resonator dimensions allows to tune the unit-cell response in order to achieve the desired characteristics. Therefore, a different frequency response from each unit cell can be obtained by changing the dimension L_1 when the VO_2 is in the ON status. On the other hand, when the thin film acts as an insulator, OFF status, the same response will be obtained for any length L_1 of the stub.

5.9.4 Results and Discussion

It is of interest to evaluate the frequency response of the unit cell while changing the element length L_1. For the analysis, an offset incidence of $\theta = 30°$ and an operating frequency of 5GHZ have been considered.

The polarization of the incident plane wave is aligned to the dipole direction. The simulated characteristics of the proposed reconfigurable phasing element are shown in Fig.s 5.56, 5.57 and 5.58.

For the ON-status of the VO_2 film, the element shows a phase range of approximately 300 degrees while keeping the reflection losses below 1dB. The phase response of the elements when the VO_2 in the OFF status shows that the isolated stub of length L_1 does not provide an additional phase compensation when it is not connected to the primary element. The parameters where computed for varying values of the metallic element width W, in order to prove the soundness of the cell electromagnetic design.

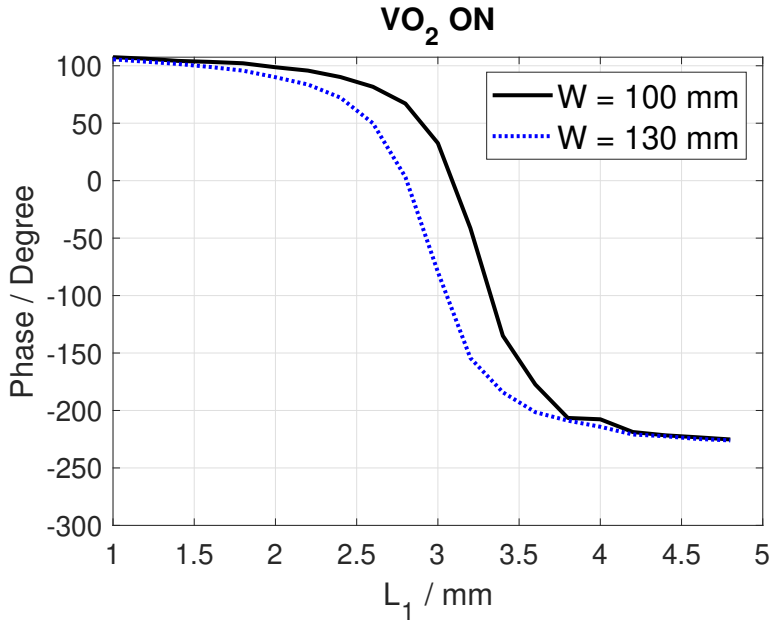

Figure 5.56: Phase of the reflection coefficient of the unit-cell for increasing values of L_1, when the VO_2 act as a conducting element. For the ON-status of the "VO_2 film, the elements show a phase range of approximately 300 degrees.

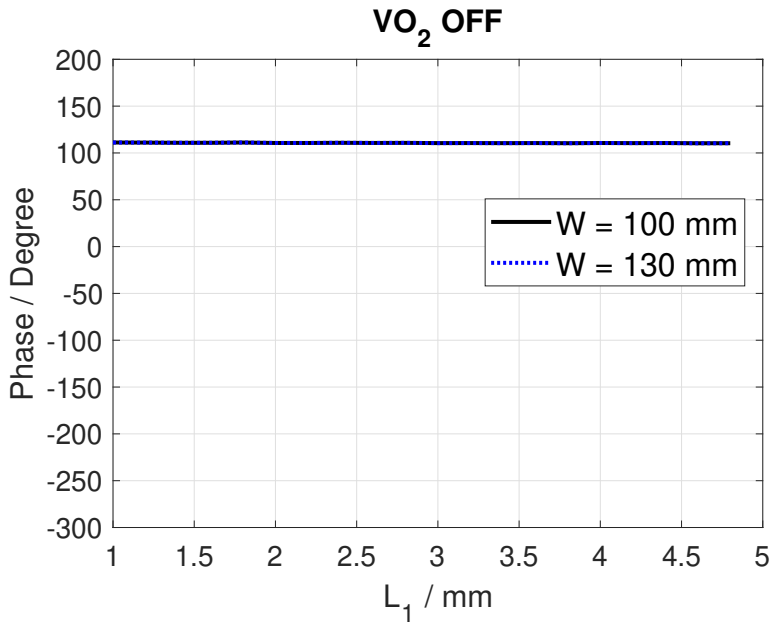

Figure 5.57: Phase of the reflection coefficient of the unit-cell for increasing values of L_1, when the VO_2 acts as a conducting element. The phase response of the elements when the VO_2 in the OFF status shows that the isolated stub of length L_1 does not provide an additional phase compensation when it is not connected to the primary element.

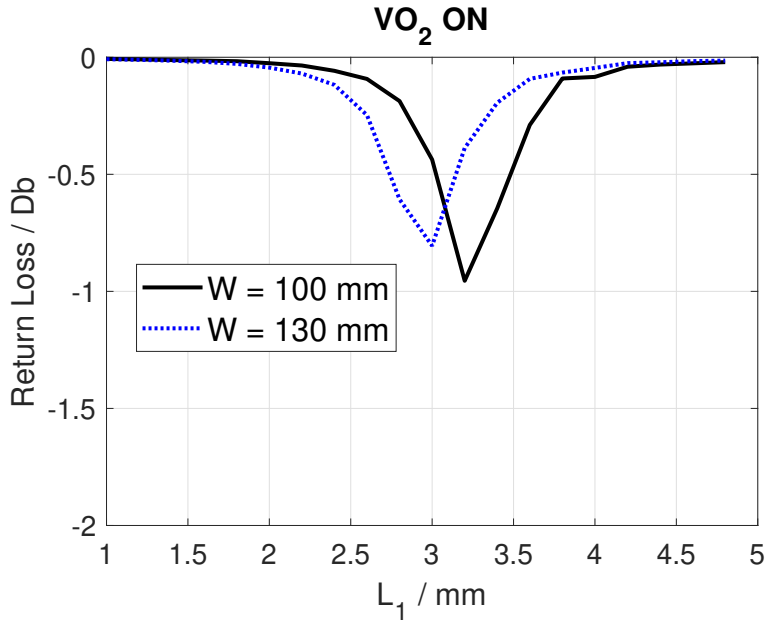

Figure 5.58: Magnitude of the reflection coefficient, when the VO_2 acts as a conducting element. The reflection losses are below 1 dB for all the considered values of L_1.

Chapter 6

Conclusion

The need of an electromagnetic simulation phase during the design process of RF applications for electric appliances was widely demonstrated throughout this thesis. Electrolux Italia was deeply interested in having a software tool for a precise modeling of the RF scenarios which are every day more breaking through the household appliance world. In fact, several issues and problematics such as the antenna positioning or the global system efficiency, could be highlighted by means of simulation without requiring an experimental phase. In this way, the whole design process of a product could be significantly accelerated and resources availability as well as prototypes could be saved. However, the preparation of electromagnetic models was not trivial and a specific approach had to be studied for each considered appliance. Two applications were analyzed in this thesis. The first one concerned an antenna system for implementing the Wi-Fi connectivity for a smart oven. The second one regarded the wireless powering of sensing devices.

The Wi-Fi system analysis described in Chapter 2 involved the characterization of the far field radiation generated by the antenna module. Several steps of validation were taken, from the standing alone antenna board to the whole appliance with the module installed in it. As far as this work was concerned, there was no relevant interest in the optimization of the system: the main scope was providing the company with accurate simulations of the RF systems. It was demonstrated that the oven structure affects considerably the radiation properties of the antennas, and several inputs were given in order to address future improvement of the whole design.

If the radiation pattern of an antenna system is not obstructed by obstacles, but still happens to be distorted, the pattern recovery technique of the projection method can be adopted. This is the case illustrated Chapter 3 where the pattern of strongly deformed antenna arrays was retrieved. Investigations on the phase sensitivity and the maximum deformation retrievable using the method were carried out, in order to prove the robustness of the method both for broad-side and beam steering arrays.

The RF application for electric appliances studied in Chapter 4 consisted in a wireless power transfer system to charge battery-less sensing devices to be positioned on pots standing on an induction hob. A model comprehensive

of both the coil antennas and the circuit components was developed. The experimental validation proved the accuracy of the model in analyzing both the field radiated around the hob and the WPT efficiency. Thanks to simulations, some critical issues were detected and properly fixed.

The research addressed in Chapter 5 was intended to improve and add new functionalities to a simulation software tool for the reflector antenna analysis, currently under development at Heriot-Watt University in Edinburgh.

First, a MATLAB code that implemented the spherical-wave-expansion technique was prepared. The field on any surface belonging to the region surrounding a feed horn could be computed from the simple knowledge of the tangential components of the far field distribution. This feature added to the tool allowed the investigation of reflector antenna systems involving reflectors or subreflectors positioned in the Fresnel region of the source. Before, this was possible only by extracting CST full-wave simulated fields on the surfaces of interest, thus requiring an external software which is not integrated with the rest of the code. CST results were used as a benchmark for validation and the SWE code proved to to be very accurate in this regards. Differences and improvements with respect to using the far field approximation of the feed were shown and discussed. Secondly, a tool for the analysis of periodic surfaces was developed, with particular interest on frequency selective surfaces applications. The analysis technique was based on the spectral domain method of moments solved on using a triangular sub-domain meshing. RWG basis functions were examined in the spectral domain and a procedure for establishing the number of relevant modes was proposed. Scattering parameters for a case study unit-cell were obtained with the investigated analysis technique and validated against CST simulation results. The major benefit of an in-house tool for the analysis of FSS or other periodic surfaces as reflectarrays consists in the possibility of using the tool in an optimization routine, which would rather be impossible by accessing to external software for the unit-cell study. Finally, a case study application involving a FSS used as subreflector for a dual feed system was designed. The simulation tool was used to analyze the configuration when the surface was positioned in the near field region of the sources. All the new features implemented could be in this way validated. The FSS was fabricated and the transmitted and reflected field scattered from the surfaces were measured in an anechoic chamber. The simulation tool proved to be efficient and accurate when compared to experimental results.

Bibliography

[1] CST, "CST Microwave Studio", 2018.

[2] Ansys, "HFSS", 2016.

[3] TICRA, "GRASP", 2017.

[4] S.Mercader-Pellicer, Analysis and Design of Linear-to-Circular Polarising Reflector Antennas Exploiting Periodic Metallodielectric Arrays, "PhD Dissertation", 2018.

[5] A. Forenza and R. W. Heath, "Benefit of Pattern Diversity via 2-Element Array of Circular Path Antennas in Indoor Clustered MIMO Channels," in *IEEE Transactions on Communications*, vol. 54, no. 4, pp. 760-760, April 2006.

[6] H.-S. Fang, C.-Y. Wu, J.-S. Sun, J.-T. Huang, "Design of a compact MIMO antenna with pattern diversity for WLAN application", *Microw Opt Technol Lett.* 2017;59:1692–1697.

[7] D. M. Pozar , "Microwave Engineering", Wiley, 2011.

[8] S. P. Hall, E. Lee, C. T. P. Song, "Planar inverted-F antennas", pp. 197–227, in Waterhouse, Rod (ed), Printed Antennas for Wireless Communications, John Wiley and Sons, 2008 ISBN 0470512253.

[9] K.-L. Wong, Y.-Y. Chen, S.-W. Su, Y.-L. Kuo, "Diversity dual-band planar inverted-F antenna for WLAN operation", *Microwave and Optical Technology Letters*, vol. 38, iss. 3, pp. 223–225, 5 August 2003.

[10] H. F. AbuTarboush, R. Nilavalan, H. S. Al-Raweshidy and D. Budimir, "Design of planar inverted-F antennas (PIFA) for multiband wireless applications," *2009 International Conference on Electromagnetics in Advanced Applications*, Torino, 2009, pp. 78-81.

[11] Z. D. Liu, P. S. Hall, D. Wake, "Dual frequency planar inverted F antenna", *IEEE Transactions on Antennas and Propagation*, vol. 45, iss. 10, pp. 1451–1458, October 1997.

[12] K. Dong-yeon Kim, J. W. Lee, C. S. C., T. K. Lee, "Design of a Compact TriBand PIFA Based on Independent Control of the Resonant Frequencies," *IEEE Transactions on Antennas and Propagation*, vol. 56, pp. 1428-1436, 2008.

[13] R. Waterhouse, D. Novak, "Wireless systems and printed antennas", Printed Antennas for Wireless Communications, John Wiley and Sons, pp. 1–36, 2008 ISBN 0470512253.

[14] B. S. Yarman, "Design of Ultra Wideband Antenna Matching Networks", Springer, 2008 ISBN 1402084188.

[15] B. Sanz-Izquierdo, J. Batchelor and R. Langley, "Multiband printed PIFA antenna with ground plane capacitive resonator", *Electronic Letters*, 28th October 2004 Vol. 40 No. 22.

[16] C. Y. Chiu, C. H. Chan, K. M. Luk, "Study of a small wide-band patch antenna with double shorting walls," *IEEE Antennas and Wireless Propagation Letters*, vol. 3, pp. 230-231, 2004.

[17] M. Huynh, W. Stutzman, "Ground plane effects on planar inverted-F antenna (PIFA) performance," in *IEE Proceedings - Microwaves, Antennas and Propagation*, vol. 150, no. 4, pp. 209-213, 8 Aug. 2003.

[18] H. Park, K. Chung and J. Choi, "Design of a planar inverted-F Antenna with very wide impedance bandwidth," *Microwave and Wireless Components Letters*, IEEE, vol. 16, pp. 113- 115, 2006

[19] J. Thaysen, "Mutual coupling between two identical planar inverted-F antennas," *IEEE Antennas and Propagation Society International Symposium*, San Antonio, TX, USA, 2002, pp. 504-507 vol.4.

[20] Z. Ying, D. Zhang, "Study of the mutual coupling, correlations and efficiency of two PIFA antennas on a small ground plane," *IEEE Antennas and Propagation Society International Symposium*, Washington, DC, 2005, pp. 305-308 vol. 3B.

[21] X. Wang, Z. Niu and Y. Liu, "Matching network design for a double band PIFA antenna via simplified real frequency technique," *International Conference on Microwave Technology and Computational Electromagnetics (ICMTCE 2009)*, Beijing, 2009, pp. 92-94.

[22] J. Malmström, H. Holter and B. L. G. Jonsson, "On the Accuracy of Equivalent Antenna Representations—A Case Study," in *IEEE Transactions on Antennas and Propagation*, vol. 66, no. 7, pp. 3251-3260, July 2018.

[23] T. M. Macnamara, "Introduction to Antenna Placement and Installation". John Wiley and Sons, 2010.

[24] L. J. Foged, L. Scialacqua, F. Saccardi, F. Mioc, D. Tallini, E. Leroux, U. Becker, J. L. Araque Quijano, and G. Vecchi, "Innovative representation of antenna measured sources for numerical simulations," in *IEEE Antennas Propag. Soc. AP-S Int. Symp.*, 2014, pp. 2014–2015.

[25] L. J. Foged, L. Scialacqua, F. Saccardi, F. Mioc, J. L. A. Quijano, and G. Vecchi, "Antenna placement based on accurate measured source representation and numerical tools," in *IEEE Int. Symp. Antennas Propag. Usn. Natl. Radio Sci. Meet.*, 2015, pp. 1486–1487.

[26] CST, "Field Source Overview", www.cst.com.

[27] L.J. Foged, L. Scialacqua, F. Saccardi, F. Mioc, M. Sorensen, G. Vecchi, J. L. Araque Quijano, "Using Measured Fields as Field Sources in Computational EMC", www.mvg-world.com.

[28] J. Huang, "Bandwidth study of microstrip reflectarray and a novel phased reflectarray concept", *Proc. of the IEEE Int. Symp. on Ant. and Propag.*, Newport Beach, CA, Jun., pp. 58-2–585, 1995.

[29] P.L. O'Donovan, A.W. Rudge, "Adaptive control of a flexible linear array", *Electronics Letters* no. 9, pp. 121-–122, 1973.

[30] T.J. Seidel, W.S.T. Rowe, and K. Ghorbani, "Passive compensation of beam shift in a bending array", *Prog. Electron. Res.* no. 29, pp. 41-–53, 2012.

[31] T. Deloues, P. Iacomme, H. Schippers, P. Knott, and M.R. Scherbarth, "Vibrating antennas and compensation techniques research in NATO/RTO/SET 0877RTG", *Proc. IEEE Aerosp. Conf.* pp. 1-–13, 2007.

[32] B.D. Braaten, S. Roy, S. Nariyal, *et al.* "A self-adapting flexible (SELFLEX) antenna array for changing conformal surface applications", *IEEE Trans. Antennas and Propagation* no. 61, pp. 655–665, 2013.

[33] B. D. Braaten, S. Roy, I. Irfanullah, *et al.*, "An Autonomous Self-Adapting Conformal Array for Cylindrical Surfaces with a Changing Radius", *IEEE APSURSI*, pp. 1784–1785, 2014.

[34] B. D. Braaten, S. Roy, I. Irfanullah, *et al.*, "Phase-Compensated Conformal Antennas for Changing Spherical Surfaces", *IEEE Transactions on Antennas and Propagation*, Vol. 62, Is. 4, pp. 1880–1887, 2014

[35] M.S. Khan, S. Asif , A.D. Capobianco, *et al.* "A frequency reconfigurable self-adapting conformal array for changing wedge- and cylindrical-shaped surfaces", *IET Microwave Antenna and Propagation* no. 10, pp 897–901, 2016.

[36] G. Mansutti, S.M. Khan, A.D. Capobianco, A. Iftikhar, S. Asif, "Self-adapting conformal phased array antennas for complex changing surfaces", *Microwave and Optical Technology Letters,* vol. 59, No. 2, Feb. 2017.

[37] B. D. Braaten, I. Ullah, S. Nariyal, A. Naqvi, M. Iskander and D. Anagnostou,"Scanning Characteristics of a Self-Adapting Phased-Array Antenna on a Wedge-Shaped Conformal Surface" *Antennas and Propagation Society International Symposium (APSURSI)*, 2013 IEEE.

[38] F. Rigobello, G. Mansutti, M. S. Khan and A. Capobianco, "Pattern recovering of conformal antenna array for strongly deformed surfaces," *2017 11th European Conference on Antennas and Propagation (EUCAP)*, Paris, 2017, pp. 869-871.

[39] G. Mansutti, F. Rigobello, M. S. Khan and A. Capobianco, "Pattern recovery of a beam-tilting phased array antenna on a doubly wedge-deformed surface," *47th European Microwave Conference (EuMC)*, Nuremberg, 2017, pp. 1353-1356.

[40] G. Mansutti, F. Rigobello, M. S. Khan, A.-D. Capobianco, A. Galtarossa "Main Lobe Control of a Beam Tilting Antenna Array Laid on a Deformable Surface", *International Journal of Antennas and Propagation*, vol. 2018, Article ID 2521953, 6 pages, 2018.

[41] Francesco Rigobello, Giulia Mansutti, Antonio-D. Capobianco, Andrea Galtarossa, "Phase Sensitivity of the Projection Method for a Beam Tilting Deformed Array", *European Conference on Antennas and Propagation*, London, 2018.

[42] F. Rigobello, G. Mansutti, S. Asif, M.S. Khan, A.-D. Capobianco, A. Galtarossa "Robustness of the projection method for an asymmetrically deformed planar antenna array". *Microw. Opt. Technol. Lett.* 2018; 1-6.

[43] Constantine A. Balanis, "Antenna Theory: Analysis and Design", John Wiley and Sons, Ltd., Hoboken, New Jersey, 2005.

[44] W.C. Brown, "Status of the Microwave Power Transmission Components for the Solar Power Satellite", *IEEE Transactions on Microwave Theory and Techniques*, vol.Mtt-29, NO.12, December 1981.

[45] A. Massa, G. Oliveri, F. Viani and P. Rocca, IEEE Transactions on Microwave Theory and TechniquesArray Designs for Long-Distance Wireless Power Transmission: State-of-the-Art and Innovative Solutions," in *Proceedings of the IEEE*, vol. 101, no. 6, pp. 1464-1481, June 2013.

[46] T. Imura, T. Uchida, Y.Hori, "Experimental Analysis of High Efficiency Power Transfer using Resonance of Magnetic Antennas for the Near Field - Geometry and Fundamental Characteristics -", *IEE Japan Industry Applications Society Conference*, No.2-62, pp.539-542, Kochi, Japan, 2008.8.

[47] Z. Bingyi, L. Hongbin, Z. Yisong, Y. Yong, F. Guihong, "Contactless Electrical Energy Transmission System Using Separable Transformer", *Proceedings of the Eighth International Conference on Electrical Machines and Systems*, Vol.3, pp.1721-1724, 2005.

[48] H. Ayano, H. Nagase, H. Inaba, "A Highly Efficient Contactless Electrical Energy Transmission System", E*lectrical Engineering in Japan*, Vol.148, No.1, 2004.

[49] A. Kurs, A. Karalis, R. Mofatt, J.D. Joannopoulos, P. Fisher, M. Soljacic, "Wireless Power Transfer via Strongly Coupled Magnetic Resonance", *Science Express*, 7 June 2007, Vol. 317. no. 5834,pp. 83-86

[50] K. M. Silay, C. Dehollain and M. Declercq, "Improvement of power efficiency of inductive links for implantable devices", 2008 Ph.D. Research in Microelectronics and Electronics, Istanbul, 2008, pp. 229-232.

[51] O. Mourad, P. Le Thuc, R. Staraj and P. Iliev, "System modeling of the RFID contactless inductive coupling using 13.56 MHz loop antennas", *The 8th European Conference on Antennas and Propagation (EuCAP 2014)*, The Hague, 2014, pp. 2034-2038.

[52] R. Xue, K. Cheng and M. Je, "High-Efficiency Wireless Power Transfer for Biomedical Implants by Optimal Resonant Load Transformation", in *IEEE Transactions on Circuits and Systems I: Regular Papers*, vol. 60, no. 4, pp. 867-874, April 2013.

[53] T. Imura, H. Okabe, T. Uchida and Y. Hori, "Study on open and short end helical antennas with capacitor in series of wireless power transfer using magnetic resonant couplings," *2009 35th Annual Conference of IEEE Industrial Electronics*, Porto, 2009, pp. 3848-3853.

[54] B. Ni, C. Y. Chung and H. L. Chan, "Design and comparison of parallel and series resonant topology in wireless power transfer," *2013 IEEE 8th Conference on Industrial Electronics and Applications (ICIEA)*, Melbourne, VIC, 2013, pp. 1832-1837.

[55] W. Zhang, S. Wong, C. K. Tse and Q. Chen, "Design for Efficiency Optimization and Voltage Controllability of Series–Series Compensated Inductive Power Transfer Systems," in *IEEE Transactions on Power Electronics*, vol. 29, no. 1, pp. 191-200, Jan. 2014.

[56] R. Jegadeesan and Y. Guo, "Topology Selection and Efficiency Improvement of Inductive Power Links," in *IEEE Transactions on Antennas and Propagation*, vol. 60, no. 10, pp. 4846-4854, Oct. 2012.

[57] L. Chen, S. Liu, Y. C. Zhou and T. J. Cui, "An Optimizable Circuit Structure for High-Efficiency Wireless Power Transfer," in I*EEE Transactions on Industrial Electronics*, vol. 60, no. 1, pp. 339-349, Jan. 2013.

[58] T. C. Beh, T. Imura, M. Kato and Y. Hori, "Basic study of improving efficiency of wireless power transfer via magnetic resonance coupling based on impedance matching", 2*010 IEEE International Symposium on Industrial Electronics*, Bari, 2010, pp. 2011-2016.

[59] J. Kim, D. Kim and Y. Park, "Analysis of Capacitive Impedance Matching Networks for Simultaneous Wireless Power Transfer to Multiple Devices," in *IEEE Transactions on Industrial Electronics*, vol. 62, no. 5, pp. 2807-2813, May 2015.

[60] M. Rütschlin, T. Wittig, F. Hirtenfelder, "A RFID system design using 3D EM simulation tools", CST European User Group Meeting, Darmstadt, March 2009.

[61] CST, "RFID Reader-Coil, 13.56 MHz", www.cst.com.

[62] H. Hirayama, Y. Okuyama, N. Kikuma and K. Sakakibara, "Equivalent circuit of induction fed magnetic resonant WPT system", *2011 IEEE MTT-S International Microwave Workshop Series on Innovative Wireless Power Transmission: Technologies, Systems, and Applications*, Uji, Kyoto, 2011, pp. 239-242.

[63] H. Hirayama, "Wireless Power Transfer - Principles and Engineering Explorations", Chapter 6, InTech, 2012.

[64] H. Hirayama, Y. Okuyama, N. Kikuma and K. Sakakibara, "An consideration on equivalent circuit of wireless power transmission," *2010 14th International Symposium on Antenna Technology and Applied Electromagnetics and the American Electromagnetics Conference,* Ottawa, ON, 2010, pp. 1-4.

[65] C. Chen, T. Chu, C. Lin and Z. Jou, "A Study of Loosely Coupled Coils for Wireless Power Transfer," in *IEEE Transactions on Circuits and Systems II: Express Briefs*, vol. 57, no. 7, pp. 536-540, July 2010.

[66] CST, "Wireless Power Transfer", CST Webminar Series, 2017.

[67] H. Kim, D. Won and B. Jang, "Simple design method of wireless power transfer system using 13.56MHz loop antennas," *2010 IEEE International Symposium on Industrial Electronics*, Bari, 2010, pp. 1058-1063.

[68] Texas Instruments, "HF Antenna Design Notes Technical Application Report", 11-08-26-003 Sept 2003.

[69] ST, "AN2866 Application Note - How to design a 13.56 MHz customized tag antenna", January 2009, www.st.com.

[70] U. Jow and M. Ghovanloo, "Design and Optimization of Printed Spiral Coils for Efficient Transcutaneous Inductive Power Transmission," in *IEEE Transactions on Biomedical Circuits and Systems*, vol. 1, no. 3, pp. 193-202, Sept. 2007.

[71] Microchip Technology Inc., "Antenna Circuit Design for RFID Applications", DS00710C, 2003.

[72] K. Fujimoto, A. Henderson, K. Hirasawa, and J.R. James, "Small Antennas", John Wiley and Sons Inc., ISBN 0471 914134, 1987.

[73] S. Mercader-Pellicer, G. M. Mederò and G. Goussetis, "Comparison of geometrical and physical optics for cross-polarisation prediction in reflector antennas," *Active and Passive RF Devices (2017)*, London, 2017, pp. 1-5.

[74] W. Tang, S. Mercader-Pellicer, G. Goussetis, H. Legay, N.J.G. Fonseca, "Low-Profile Compact Dual-Band Unit Cell for Polarizing Surfaces Operating in Orthogonal Polarizations", *IEEE Transactions on Antennas and Propagation*, 65 (3), 1472-1477.

[75] C.-A. Balanis. Antenna theory, analysis and design. Wiley, 1997, Chapter 2.

[76] I. Koffman, "Feed polarization for parallel currents in reflectors generated by conic sections", *IEEE Transactions on Antennas and Propagation*, 1966, 14, 37-40

[77] Y. Rahmat-Samii, P. Cramer, K. woo, S. W. LEE, "Realizable. Feed-Element Patterns for Multibeam Reflector Antenna Analysis", *IEEE Transactions on Antennas and Propagation*, VOL. AP-29, NO. 6, NOVEMBER 1981

[78] A.C. Ludwig, "The Definition of Cross Polarization", *IEEE Transactions on Antennas and Propagation*, JANUARY 1973.

[79] TICRA, GRASP, "Technical Description", Knud Pontoppidan, TICRA, Denmark, 2005-2008.

[80] H. E, King and J. L. Wong, "Directivity of a uniformly excited N X N array of directive elements," *IEEE Trans. Antennas Propagat.*, vol. AP-23, pp. 401-404, 1975.

[81] S. Silver, "Microwave Antenna Theory and Design", New York: Dover, 1965.

[82] A.C. Ludwig, "Near field far field Transformations Using Spherical-Wave Expansions", *IEEE Trans. Antennas Propagat.*, VOL. .e-19, NO. 2, MARCH 1971.

[83] P. D. Potter, "Application of spherical wave theory to Cassegrainian-fed paraboloids", *IEEE Trans. Antennas Propagat.*, VO . AP-15, NOV. 1967, pp. 727-736.

[84] J. E. Hansen, "Spherical near field Antenna Measurements", 1988.

[85] J. A. Stratton, "Electromagnetic Theory", John Wiley Sons, 22 gen 2007.

[86] D. S. Jones, "The Theory of Elctromagnetism". New York: Macmillan, 1964, see. 8.16.

[87] A.C. Ludwig, "Calculation of Scattered Patterns From Asymmetrical Reflectors", JPL Technical Report 32-1430.

[88] F. Jensen, "Electromagnetic near field far field correlations", Ph.D. dissertation, LD 15, Laboratory of Electromagnetic Theory, Technical University of Denmark, Lyngby, 1970.

[89] F. Jensen and A. Frandsen, "On the number of modes in spherical wave expansions", *Proc. 26th AMTA*, Stone Mountain Park, Georgia, 2004.

[90] R. E. Collin, F. J. Zucker, "Antenna Theory, Part 1", Chapter 1, McGraw-Hill Book Company, New York, 1969.

[91] Changhua Wan and J. A. Encinar, "Efficient computation of generalized scattering matrix for analyzing multilayered periodic structures," in *IEEE Transactions on Antennas and Propagation*, vol. 43, no. 11, pp. 1233-1242, Nov. 1995.

[92] R. Mittra, C. H. Chan, and T. Cwik, "Techniques for analyzing frequency selective surfaces, a review," *Proc. of the IEEE*, vol. 76, no. 12, pp. 1593-1615, 1988.

[93] C. H. Tsao and R. Mittra, "Spectral-domain analysis of frequency selective surfaces comprised of periodic arrays of cross dipoles and Jerusalem crosses," *IEEE Trans. Antennas Propagat.*, vol. AP-32, no. 5, pp. 478-486, May 1984.

[94] R. Ulrich, "Far-infrared properties of metallic mesh and its complementary structure," *Infrared Phys.*, vol. 7, pp. 37-55, 1967.

[95] M. S. Durschlag and T. A. DeTemple, "Far-IR optical properties of freestanding and dielectrically backed metal meshes", *Appl. Opt.*, vol. 20, no. 7, pp. 1245-1253, Apr. 1981.

[96] V. D. Agrawal and W. A. Imbriale, "Design of a dichroic Casegrain subreflector,", *Trans. Antennas Propagat.*, vol. AP27, no. 4, pp. 466-473, July 1979.

[97] Kipp , R. A. and C. H. Chan, "A numerically efficient technique for the method of moments solution to planar periodic structures in layered media," *IEEE Trans. Microwave Theory Tech.*, Vol. 42, No. 4, 635-643, 1994.

[98] S. M. Rao, D. R. Wilton, and A. W. Glisson, "Electromagnetic scattering by surface of arbitrary shape," *IEEE Trans. Antennas Propagat.*, vol. AP-30, pp. 409419, May 1982.

[99] T. Cwik and R. Mittra, "Scattering from a periodic array of reestanding arbitrarily shaped perfectly conducting or resistive patches," *IEEE Trans. Antennas Propagat.*, vol. AP-35, pp. 1226-1234, Nov. 1987.

[100] C. H. Tsao and R. Mittra, "Spectral-domain analysis of frequency selective surfaces comprised of periodic arrays of cross dipoles and Jerusalem crosses," *IEEE Trans. Antennas Propagat.*, vol. AP-32, pp. 478486, May 1984

[101] R. F. Harrington, "Field Computation by Moment Methods", 1993, 0780310144, Wiley-IEEE Press.

[102] M. Biscarini, "Analisi Numerica di Strutture Selettive in Frequenza Multistrato", Tesi Magistrale, A.A. 2011/2012.

[103] J. C. Vardaxoglou, "Frequency Selective Surfaces – Analysis and design", 1997.

[104] R. Tascone, R. Orta, "Frequency Selective Surfaces – Analysis and Design". Ch. 7, edited by J. C. Vardaxoglou, Research Studies Press Ltd., 1997.

[105] S. Maci, A. Cucini, "FSS-based complex surfaces". In Electromagnetic Metamaterials: Physics and Engineering Aspects. Edited by N. Engheta and R. W. Ziolkowski, Wiley InterScience, 2006.

[106] B. A. Munk, "Finite Antenna Arrays and Fss", 2003.

[107] C. C. Chen, "Transmission Through a Conducting Screen Perforated Periodically with Apertures", *IEEE transactions on Microwave Theory and Techniques*, VOL. MTT- 18, NO. 9, SEPTEMBER 1970

[108] F. Caminita, A. Cucini, S. Maci, "Fast Analysis of Stop-Band FSS Integrated with Phased Array Antennas", *Radioengineering*, VOL. 17, NO. 2, JUNE 2008.

[109] E. Newman and D. M. Pozar, "Electromagnetic modeling of composite wire and surface geometry," *IEEE Trans. Antennas Propagat.*, vol. AP-26, pp. 784-489, NOV.1978.

[110] C G. Christodoulou and J. F. Kauffman, "On the Electromagnetic Scattering from Infinite Rectangular Grids with Finite Conductivity", *IEEE Trans. Antennas Propag.*, Vol. AP-34, No. 2, February 1986.

[111] W. Zhuang, R. S. Chen, D. Z. Ding, and D. X. Wang, "An efficient analysis of frequency selective surface in spectral domain with rwg basis functions", *Microwave and Optical Technology Letters/* Vol. 51, No. 11, November 2009.

[112] A. Francavilla, S. Monni, D. Beckers, A. Neto, G. Gerini, N. Fiscante, "Multi-band Frequency Selective Surfaces: Analysis", *TNO Report*, August 2008.

[113] S.W. Lee and R. Mittra, "Fourier transform of a polygonal shape function and its application in electromagnetics", *IEEE Trans Antennas Propag* 31 (1983), 99–103.

[114] K. Mcinturff and P.S. Simon, "The fourier transform of linearly varying functions with polygonal support", *IEEE Trans Antennas Propag* 39 (1991), 1441–1443.

[115] V. Lancellotti, D. Milanesio, R. Maggiora, G. Vecchi, V. Kyrytsya, "TOPICA: an accurate and efficient numerical tool for analysis and design of ICRF antennas", *Nuclear fusion,* no. 46, pp. 476-499, June 2006.

[116] S. Rao, D. R. Wilton, A. Glisson, "Electromagnetic scattering by surfaces of arbitrary shape", *IEEE Transactions on Antennas and Propagation*, Vol. 30, no. 3, pp. 409-418, May 1982.

[117] D. R. Wilton, S. M. Rao, A. W. Glisson, D. H. Schaubert, 0. M. AI-Bundak, C. M. Butler, "Potential Integrals for Uniform and Linear Source Distributions on Polygonal and Polyhedral Domains", *IEEE Transactions on Antennas and Propagation*, Vol. 32, no. 3, pp. 276-281, March 1984.

[118] C. C. Chan, R. Mittra, "On the Analysis of Frequency-Selective Surfaces Using Subdomain Basis Functions", *IEEE Transactions on Antennas and Propagation*, Vol. 38, no. 1, pp. 40-50, January 1990.

[119] Flann Microwave, "Standard Gain Horns Series 240", Main Catalogue 2015.

[120] M. Arrebola1 Y. Alvarez, J.A. Encinar, F. Las-Heras, "Accurate analysis of printed reflectarrays considering the near field of the primary feed", *IET Microw. Antennas Propag.*, 2009, Vol. 3, Iss. 2, pp. 187–194.

[121] Rigobello, F. et al.: "Frequency Reconfigurable Single-Polarized Reflectarray Unit-Cell using Phase Change Materials", *39th ESA Antenna Workshop on Multibeam and Reconfigurable Antennas for Space Applications,* 2-4 Oct. 2018.

[122] Hum, S., Perruisseau-Carrier, J.: "Reconfigurable Reflectarrays and Array Lenses for Dynamic Antenna Beam Control: A Review", *IEEE TAP* Vol. 62, No. 1, January 2014, pp. 183–198

[123] Anagnostou, D., Goussetis, G., Torres, D., and Sepulveda, N., "Ultra-Fast Reconfigurable Antennas with Phase Change Materials", 2017 *International Workshop on Antenna Technology: Small Antennas, Innovative Structures, and Applications (iWAT).*

[124] Teeslink et. al, "Reconfigurable Bowtie Antenna Using Metal-Insulator Transition in Vanadium Dioxide", *IEEE Antennas and Wireless Propagation Letters*, vol. 14, 2015 pp. 1381-1384.

[125] Anagnostou, D., Goussetis, G., Torres, D., and Sepulveda, N., "Reconfigurable Antennas and Arrays using Phase Change Materials", *38th ESA Antenna Workshop: Innovative Antenna Systems and Technologies for Future Space Missions.*

[126] Li, Y., Abbosh, A.: "Reconfigurable reflectarray antenna using single-layer radiator controlled by PIN diodes", *IET Microw. Antennas Propag.*, 2015, Vol. 9, Iss. 7, pp. 664–671.